54th Scientific Conference for Young Students of Physics and Natural Sciences

Open Readings 2011

March 17-19, 2011

Vilnius, LITHUANIA

Programme and Abstracts

Faculty of Physics
Vilnius University
Saulėtekio Ave. 9-III, LT-10222 Vilnius
LITHUANIA

www.ff.vu.lt
www.openreadings.eu

ISSN 2029-4425

SCHEDULE OF ORAL PRESENTATIONS

Thursday, March 17

ORAL SESSION I

Auditorium: **DFA**

10:00 - 10:15	Conference opening
10:15 - 10:30	**OP-1** 5-DIMENSION OPTICAL RECORDING WITH ULTRASHORT LIGHT PULSES M. Gecevičius, M. Beresna, P. G. Kazansky *University of Southampton, Southampton, United Kingdom*
10:30 - 10:45	**OP-2** PHOTOCHROMISM DYNAMICS OF INDOLO-BENZOXAZINE-TYPE COMPOUNDS: NEW LIGHT-GATED FUNCTIONAL MOLECULES M. Vengris, L. Kontenis, K. Redeckas, V. Martynaitis, R. Steponavičiūtė, and A. Šačkus *Vilnius University, Vilnius, Lithuania*
10:45 - 11:00	**OP-3** DIRECT LASER WRITING OF MICROSTRUCTURED POLYMER SCAFFOLDS FOR TISSUE ENGINEERING APPLICATIONS P. Danilevičius, E. Balčiūnas and M. Malinauskas *Vilnius University, Lithuania*
11:00 - 11:15	**OP-4** LIGHT TWISTING WITH MICRO-SPHERES PRODUCED BY ULTRASHORT LIGHT PULSES M. Beresna, M. Gecevičius and P. G. Kazansky *University of Southampton, Southampton, United Kingdom*
11:15 - 11:30	**OP-5** 3D PHOTONIC CRYSTAL AS A SPATIAL LIGHT FILTER M. Rutkauskas, L. Maigytė, M. Peckus, K. Staliūnas, and M. Malinauskas *Vilnius University, Vilnius, Lithuania*
11:30 - 11:45	**OP-6** INTERFERENCE PATTERNS OF LASER-DRESSED STATES IN A SUPERSONIC ATOMIC/MOLECULAR BEAM M. Bruvelis, J. Ulmanis, K. Miculis, N. N. Bezuglov, C. Andreeva, and A. Ekers *University of Latvia, Riga, Latvia*

	ORAL SESSION II Auditorium: **DFA**	ORAL SESSION III Auditorium: **JR-10**
12:30 - 12:45	**OP-7** SPECTROSCOPIC STUDY OF WATER-SOLUBLE QUANTUM DOTS AND CHLORIN E6 COMPLEX FORMATION AND STABILITY IN THE PRESENCE OF ALBUMIN A.Skripka, J.Valančiūnaitė, and R.Rotomskis *Vilnius University, Vilnius, Lithuania*	**OP-13** INTERACTION OF EXCITONS IN ZnO CRYSTALS V. Tumas, E. Kuokštis, M. Karaliūnas, and E. Anisimovas *Vilnius University, Vilnius, Lithuania*
12:45 - 13:00	**OP-8** REACTIVE OXYGEN SPECIES PRODUCTION IN MITOCHONDRIA OF HUMAN LARYNX CARCINOMA CELLS E.N. Golubeva, G.G. Martinovich, I.V. Martinovich, and S.N. Cherenkevich *Belarusian State University, Minsk, Belarus*	**OP-14** QUANTUM WIRE IN ELECTRIC FIELD M. A.Belov *Belarussian State University, Minsk, Belarus*
13:00 - 13:15	**OP-9** INTEGRATION OF SELF-ASSEMBLY AND LASER TECHNOLOGIES IN FABRICATION OF TEMPLATES FOR CELL ARRAYS J. Pupkaitė, G. Račiukaitis, T. Rakickas, and R. Valiokas *Vilnius University, Vilnius, Lithuania*	**OP-15** ZnO BASED HYBRID WHITE LIGHT EMITTING DIODES T. Serevičius, I. Hussain, and M. Willander *Vilnius University, Vilnius, Lithuania*
13:15 - 13:30	**OP-10** SURFACE MODIFICATION OF SEMICONDUCTOR NANOPARTICLES FOR LIVE CELL BIOIMAGING K. Stašys, V. Karabanovas, R. Rotomskis, and M. Valius *Vilnius University, Vilnius, Lithuania*	**OP-16** KERR MICROSCOPY: HOW TO SEE MAGNETIC DOMAINS? B. Olbromska *AGH University of Science and Technology, Krakow, Poland*
13:30 - 13:45	**OP-11** CHEMICAL ASPECTS OF THE PROCESS OF BIOMASS GASIFICATION M. Sosnowska, K. Kwiatkowski, K. Bajer *Warsaw University of Technology, Warsaw, Poland*	**OP-17** STIMULATED EMISSION IN HIGH-Al-CONTENT AlGaN QUANTUM WELLS J. Jurkevičius, J. Mickevičius *Vilnius University, Vilnius, Lithuania*
13:45 - 14:00	**OP-12** GAS SENSING PROPERTIES OF HETEROPHASE NANOCOMPOSITES ON THE BASIS OF DOPED TITANIUM DIOXIDE N. Boboriko, D. I. Mychko *Belarussian State University, Minsk, Belarus*	**OP-18** OPTICAL PROPERTIES OF MBE-GROWN ZnO/CdZnO EPITAXIAL LAYERS M. Stasiūnas, M. Karaliūnas, E. Kuokštis *Vilnius University, Vilnius, Lithuania*

	ORAL SESSION IV Auditorium: **DFA**	ORAL SESSION V Auditorium: **JR-10**
14:30 - 14:45	**OP-19** THEORETICAL DESCRIPTION OF HYPERFINE STRUCTURE OF LASER-FIELD-DRESSED ATOMIC STATES A. Cinins, V. Kascheyevs *University of Latvia, Riga, Latvia*	**OP-26** APPLICATIONS OF INFRARED MICROSPECTROSCOPY FOR CHARACTERIZATION OF URINARY STONES M. Pučetaitė, T. Žalys, S. Tamošaitytė, J. Čeponkus, and V. Šablinskas *Vilnius University, Vilnius, Lithuania*
14:45 - 15:00	**OP-20** EVANESCENT WAVES (OR HOW TO MAKE A LIGHT SWORD) J.Zielinska *University of Warsaw, Warsaw, Poland*	**OP-27** HYDROCARBONS REFORMING BY PLASMA WITH CONTROLLED H2/CO RATIOS OF SYNGAS Ol. Solomenko, V. Chernyak, and O. Nedybaliuk *Kyiv National Taras Schevchenko University, Kyiv, Ukraine*
15:00 - 15:15	**OP-21** RENORMALIZATION GROUP APPROACH TO ULTRACOLD IMBALANCED FERMI GAS J. Armaitis, J. E. Baarsma, and H. T. C. Stoof *Utrecht University, Utrecht, The Netherlands*	**OP-28** FLUORESCENCE SPECTROSCOPY OF POLYSILANES CONFINED IN DIFFERENT SiO_2 AND TiO_2 NANOSTRUCTURES D. Peckus, N. Ostapenko, P. Vodolazkyy, V. Moiseenko, S. Suto, A. Watanabe, and V. Gulbinas *Center for Physical Sciences and Technology, Vilnius, Lithuania*
15:15 - 15:30	**OP-22** BLACK HOLES' ENTROPY P. Kucharski *University of Warsaw, Warsaw, Poland*	**OP-29** ELECTRICAL POWER SYSTEM OF THE ESTCUBE-1 SATELLITE M. Pelakauskas, M. Noorma *University of Tartu, Tartu, Estonia*
15:30 - 15:45	**OP-23** STATISTICAL MODELLING OF CHARGE MOBILITY IN DISORDERED MOLECULAR LATTICES USING MONTE – CARLO METHOD V. Abramavičius, D. Abramavičius *Vilnius University, Vilnius, Lithuania*	**OP-30** EXPERIMENTS ON LIQUID METAL FLOW INDUCED BY A ROTATING MAGNETIC DIPOLE T. Beinerts, A. Bojarevičs, and Y. Gelfgat *University of Latvia, Riga, Latvia*
15:45 - 16:00	**OP-24** EXCITATION ENERGY TRANSFER AND QUENCHING IN THE PHOTOSYNTHETIC MAJOR LIGHT-HARVESTING COMPLEXES J. Chmeliov, G. Trinkunas, and L. Valkunas *Vilnius University, Vilnius, Lithuania*	**OP-31** MICROSTRUCTURE AND MAGNETOTRANSPORT PROPERTIES OF GRANULAR NANOCOMPOSITE FILMS $FeCoZr-Al_2O_3$ AND IT'S APPLICATION FOR SPINTRONICS A. Maximenko, J. Fedotova, J. Kasiuk, I. Svito, and V. Bayev *Belarussian State University, Minsk, Belarus*
16:00 - 16:15	**OP-25** ANALYSIS OF EXPERIMENTAL, ANALYTICAL AND NUMERICAL MODELS OF PARALELL PATH MAGNETIC TECHNOLOGY I. Dirba, G. Arents *University of Latvia, Riga, Latvia*	**OP-32** DEVELOPMENT OF ESTONIAN "NUCLEAR ENERGETICS AND NUCLEAR SAFETY" MASTER'S PROGRAM Alan Tkaczyk *University of Tartu, Tartu, Estonia*

ORAL SESSION I

Laser physics and optical technologies

5-DIMENSION OPTICAL RECORDING WITH ULTRASHORT LIGHT PULSES

M. Gecevičius, M. Beresna, P.G. Kazansky

Optoelectronics Research Centre, University of Southampton, Southampton SO17 1BJ, United Kingdom
mg2e10@orc.soton.ac.uk

The information hunger fuels the race for continuous advances in data storage. More than a decade ago, a potential of ultrafast laser writing of isotropic modification for three-dimensional optical memory was demonstrated [1]. Later it was found that the ultrashort laser pulses could also induce anisotropic modifications related to self-assembled nanogratings formation [2]. This anisotropy can be characterized by two independent parameters: retardance and slow axis orientation, which can be rewritten with successive pulse sequences. Recently, it was suggested using these parameters to extend optical recording beyond the three dimensions [3]. As a result, femtosecond laser induced self-assembled nanostructures can be employed as a rewritable five-dimensional optical memory. Here we explore in depth this technology and demonstrate its actual implementation for multidimensional optical recording and reading.

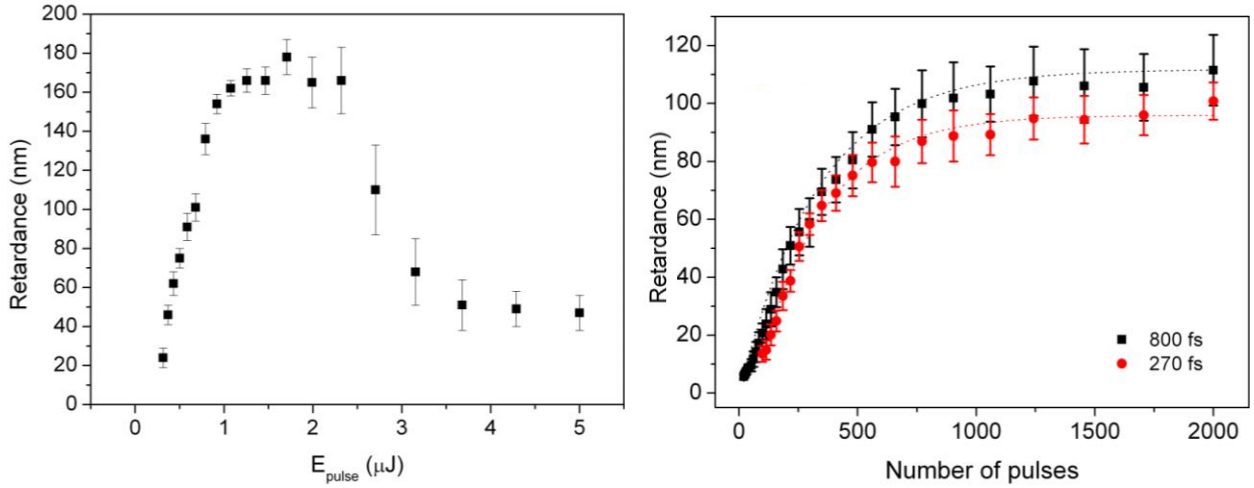

Fig. 1. Retardance dependences on pulse energy (a), with 1000 pulses exposed per single dot, and exposure (b), where the dashed lines indicate exponential approximation of experimental data.

Retardance and slow axis orientation can be independently controlled by number of pulses and azimuth of irradiated light polarization. Recording of information is performed with a mode-locked regeneratively amplified femtosecond laser system PHAROS (Light Conversion Ltd.) operating at λ = 1030 nm and delivering pulses of 270 fs at 200 kHz repetition rate. Laser beam is focused with a high-NA lens into the bulk of a fused silica sample mounted on a three-axial motion platform controlled with the SCA software (Altechna Ltd.). A successive reading of the recorded information is performed with a quantitative birefringence measurement system (Abrio,Cri Inc.) based on a conventional optical microscope Olympus BX51.

The optimization of the birefringent optical memory performance was achieved by a set of experiments. First, the retardance dependence on the number of laser pulses was measured. It

was found that this dependence can be approximated by a saturated exponential growth (Fig. 1). Next, the birefringence strength was investigated as a function of the pulse duration. Finally, as a demonstration, we recorded the portraits of two great scientists, Maxwell and Newton, in a piece of silica glass by continuously controlling exposure and polarization during the writing process (Fig.2). The Maxwell portrait was encoded with varying strength of birefringence and Newton's one by varying the slow-axis orientation. Later, using the Abrio system, we managed to decouple both images, clearly demonstrating the potential of the proposed information recording technique.

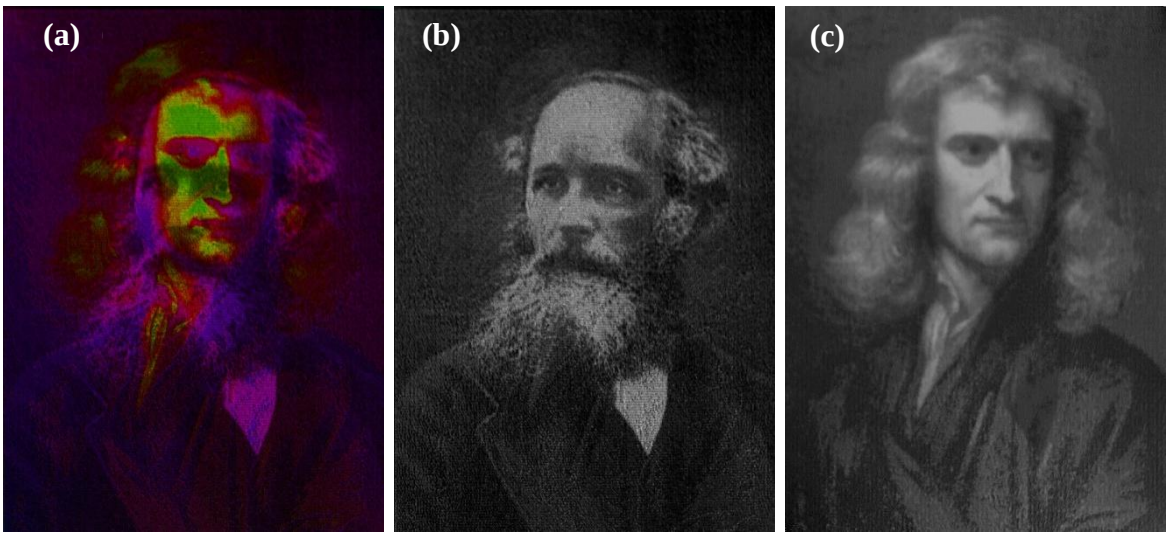

Fig. 2. Maxwell and Newton are recorded in one image (a, in pseudo colors), however, they can be easily decoupled as Maxwell is recorded in strength of retardance (b) and Newton in azimuth of the slow axis (c). Size is 1.5 × 2 mm.

In summary, by exploiting the ability of femtosecond lasers to create anisotropic modifications inside silica glass, a five-dimensional optical recording and reading has been demonstrated. The described memory multiplexing technique by polarization encoding can be successfully applied for high capacity data storage (estimated capacity 300 Gbit/cm^3).

[1] E. N. Glezer, M. Milosavljevic, L. Huang, R. J. Finlay, T.-H. Her, J. P. Callan, and E. Mazur, Three-dimensional optical storage inside transparent materials, Opt. Lett. 21, 2023-2025 (1996).
[2] E. Bricchi, B. G. Klappauf, and P. G. Kazansky, Form birefringence and negative index change created by femtosecond direct writing in transparent materials, Opt. Lett. 29, 119-121 (2004).
[3] Y. Shimotsuma, M. Sakakura, P. G. Kazansky, M. Beresna, J. Qiu, K. Miura, and K. Hirao, Ultrafast Manipulation of Self-Assembled Form Birefringence in Glass, Adv. Mat. 22, 4039–4043 (2010).

PHOTOCHROMISM DYNAMICS OF INDOLO-BENZOXAZINE-TYPE COMPOUNDS: NEW LIGHT-GATED FUNCTIONAL MOLECULES

M. Vengris[1], L. Kontenis[1], K. Redeckas[1], V. Martynaitis[2], R. Steponavičiūtė[2], and A. Šačkus[2]

[1] *Laser Research Center, Department of Quantum Electronics, Vilnius University, Saulėtekio Ave. 10, LT-10223 Vilnius, Lithuania*

[2] *Institute of Synthetic Chemistry, Kaunas University of Technology, Radvilėnų Rd. 19, LT-51270 Kaunas, Lithuania*

lukas.kontenis@ff.stud.vu.lt

Future molecular-scale devices and active mediums for holographic memories will rely on the level of fundamental understanding of the various molecular light-induced processes and the availability of subtle organic synthesis strategies, that could provide systems with the necessary physical properties. Photochromic (featuring changes in absorption due to irradiation by light) compounds, are among the best candidates for the aforementioned applications. Recently, a new class of such compounds, based on the light induced reversible opening of the indolo-benzoxazine heterocycle, was discovered [1;2] and investigated thoroughly. They exhibit excellent fatigue resistance, back-conversion lifetimes of tens of nanoseconds and have shown to support various structural modifications, that enable engineering of various electronic, chemical and optical properties.

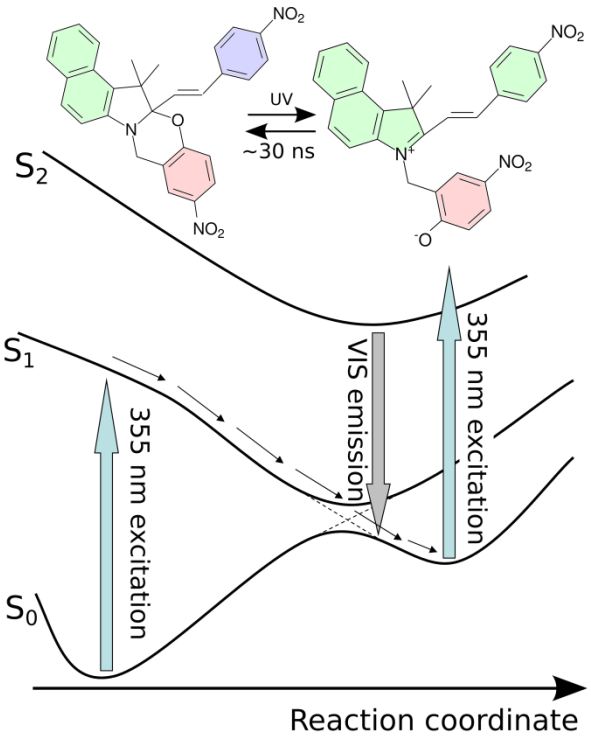

Fig. 1. A proposed energy level diagram that would explain the observed intense broadband VIS emission of only the ring-opened (top right molecule) but not the ring-closed (top left molecule) form of the investigated compound. The solid black arrows represent the photochromic reaction between the two forms. The cycles of the molecules are shaded to emphasise the different conjugated systems of the two different forms.

Here, we present an interesting group of molecules from the indolo-benzoxazine family, that develop absorbance in the visible region when exposed to UV light (Fig. 1). Two of them can be used as a short-lived (tens of nanoseconds) light-gated efficient fluorophores. After the UV light induced bond breaking of the oxazine cycle and the subsequent structural rearrangement, the conjugated systems of a benzoindole and a bromobenzene (or a nitrobenzne) groups become connected by a newly formed double bond in the indole moiety. This ring-opened form of the molecule feature an increased fluorescence quantum yield compared to the ring-closed form. Thus, for ca. 30 ns any subsequent excitation of the molecule will result in a broadband VIS emission. In the presented investigation this property is experimentally observed due to relatively long duration of 5 ns of the 355 nm wavelength excitation pulse – the same pulse forms and excites the ring-opened form (see Fig. 1).

It was also found, that a simple superposition model explaining the nature of the induced visible absorption spectrum, can only be applied to certain limited group of the indolo-benzoxazine compound family and in our case cannot account for one of the observed absorption peaks at all. More advanced techniques are thus required to gain a deeper understanding of the light-induced processes observed and few experimental directions to be taken next are suggested.

[1] A. Šačkus, Y.A. Degutis and A.G. Urbonavičius, Synthesis and study of 5a,6-dihydro-12h-indolo[2,1-b][1,3]-benzoxazines, Chemistry of heterocyclic compounds 25(5), pp. 562-565 (1989).

[2] M. Tomasulo, S. Sortino, A.J.P. White and F.M. Raymo, Fast and stable photochromic oxazines, Journal of Organic Chemistry 70, pp. 8180-8189 (2005).

DIRECT LASER WRITING OF MICROSTRUCTURED POLYMER SCAFFOLDS FOR TISSUE ENGINEERING APPLICATIONS

P. Danilevičius[1], E. Balčiūnas[2], and M. Malinauskas[1]

[1] *Laser Research Center, Department of Quantum Electronics, Vilnius University, Saulėtekio Ave. 10, LT-10223 Vilnius, Lithuania*

[2] *Vivarium, Institute of Biochemistry, Vilnius University, Mokslininkų 12, LT-08662 Vilnius, Lithuania*

mangirdas.malinauskas@ff.vu.lt

Multi-Photon Polymerization (*MPP*) is a promising direct laser writing technique which has progressed rapidly during the past decade. This technique is based on tightly focused ultrashort pulses initiating radical polymerization reaction in a spatially confined region of a pre-polymer material. By selective exposure one can create a desirable form polymeric structure which is insoluble in organic developer. The *MPP* technique allows fabrication of true three-dimensional (*3D*) structures with no geometrical restrictions [1], as well as to reaching the sub-diffraction resolution up to tens of nanometers [2]. Due to these reasons, the *MPP* is distinguished among the other high spatial resolution fabrication techniques such as UV [3] and electron beam [4] lithographies, self-organization [5], ink-jet printing [6]. MPP has already established its applications in photonics [7], microoptics [8] and microfluidics [9] as well as biological [10] applications.

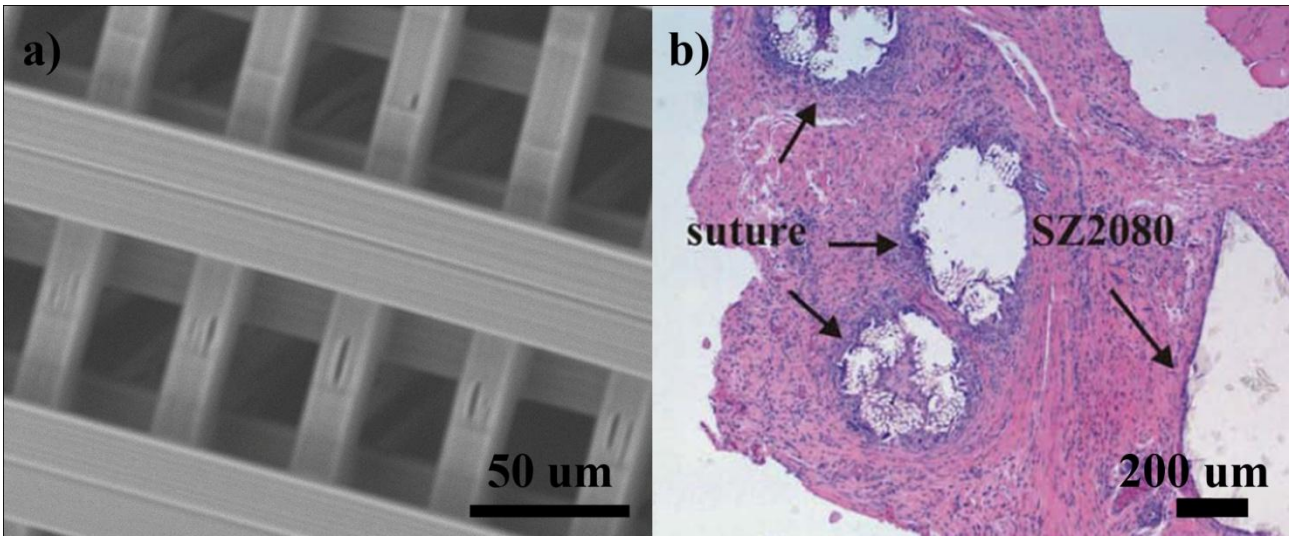

Fig. 1. a) Scanning electron microscope image of *3D* artificial scaffold with pore sizes ~25 μm fabricated out of photopolymer *SZ2080*. b) Optical microscope image of histological section of tissue surrounding *SZ2080* and surgical suture after 3 weeks of implantation.

In this work we present latest results on *MPP* application for biomedicine, by fabrication of microstructured artificial *3D* scaffolds for stem cell proliferation. Biocompatibility of non-microstructured polymers and scaffolds fabricated out of them by the *MPP* has been experimentally tested. Adult myogenic stem cell proliferation tests show polymers as well as artificial *3D* scaffolds fabricated from acrylate based *AKRE*, hybrid organic-inorganic

ORMOCORE b59 and *SZ2080* materials as well as biodegradable *PEG-DA-258* photopolymer to be applicable for biomedical practice. All these materials have been found to be at least as biocompatible as glass or polystyrene surfaces for stem cells *in vitro* and as a surgical suture judging by results of histological examination of tissues surrounding polymer implants *ex vivo*. Laboratory animals were rats and rabbits and implantation period was up to 3 weeks. Adhesion of cells was also investigated and obtained results proved the photostructurable polymers to be promising for future works for production of biocompatible *3D* scaffolds. Additional functionalization of structure surfaces is possible by covering or doping the materials with biological agents, drugs or nanoparticles. Within the limitation of our study, we conclude that the proposed direct laser writing technique offers rapid and flexible fabrication of biomedical components with required shape, pore size and general porosity. The applications could target biostable and biodegradable implants applied for bone or tissue replacement as well as drug delivery or release agents.

[1] S. Juodkazis, V. Mizeikis, H. Misawa, Three-Dimensional Structuring of Resists and Resins by Direct Laser Writing and Holographic Recording, Adv. Polym. Sci. 213, 157-206 (2008).
[2] F. Qi, Y. Li, D. Tan, H. Yang, Q. Gong, Polymerized nanotips via two-photon Photopolymerization, Opt. Express 15(3), 971-976 (2007).
[3] P. P. Naulleau, C. N. Anderson, J. Chiu, et al., 22-nm half-pitch extreme ultraviolet node development at the sematech berkeley microfield exposure tool, Microelectron. Eng. 86(4-6), 448-455 (2009).
[4] G. R. Sunne, Electron beam lithography for nanofabrication, PhD thesis, University of Barcelona (2008).
[5] S. Rousset and E. Ortega, Self-organized nanostructures, J. Phys. Condens. Matter 18(13), (2006).
[6] M. Walther, A. Ortner, H. Meier, U. Loffelmann, P. J. Smith, and J. G. Korvink, Terahertz metamaterials fabricated by inkjet printing. Appl. Phys. Lett. 95(25), 251107-251103 (2009).
[7] Q. Sun et al., Freestanding and movable photonic microstructures fabricated by photopolymerization with femtosecond laser pulses, J. Micromech. Microeng. 20(3), 035004 (2010).
[8] M. Malinauskas et al., A femtosecond laser induced two-photon photopolymerization technique for structuring microlenses, J. Opt. 12(3), 035204 (2010).
[9] D. Wu, Q. D. Chen, H. B. Sun at al., Femtosecond laser rapid prototyping of nanoshells and suspending components towards micro fluidic devices, Lab Chip 9(16), 2391-2394 (2009).
[10] A. Ovsianikov, S. Schlie, A. Ngezahayo, A. Haverich, B. N. Chichkov, Two-photon polymerization technique for microfabrication of cad-designed 3d scaffolds from commercially available photosensitive materials. J. Tiss. Eng. Regen. Med. 1(6), 443-449 (2007).

LIGHT TWISTING WITH MICRO-SPHERES PRODUCED BY ULTRASHORT LIGHT PULSES

M. Beresna, M. Gecevičius and P.G. Kazansky

Optoelectronics Research Centre, University of Southampton, Southampton SO17 1BJ, United Kingdom
mxb@orc.soton.ac.uk

Recently a property of light beams to carry angular momentum has attracted considerable attention due to numerous applications ranging from quantum optics[1] to microscopy[2] and micromanipulation[3]. Orbital angular momentum (OAM) is found in light beams with phase singularities which posses a nonzero azimuthal energy flow. Commonly used methods for generating beams with OAM are based on the exchange of orbital angular momentum with matter[4]. However, recently an efficient coupling of angular momentum carried by circular polarization with OAM was demonstrated in systems with the radial symmetry: second harmonic generation in laser induced plasma[14], liquid crystal droplets[13] and radially variant birefringent waveplates[10, 11]. Additionally, it was demonstrated that radial polarizer can introduce orbital angular momentum into the beam[12]. The advantage of this type process is that the helicity of the output wave front can be controlled by the handedness of incident light polarization. However, such systems could not be straightforwardly downsized, preventing from widespread application in integrated optics.

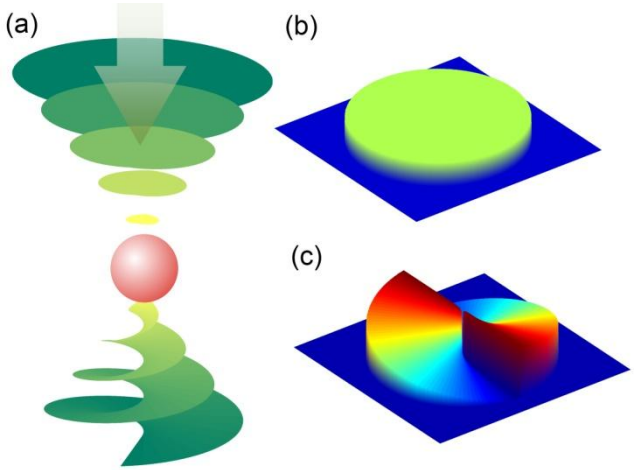

Fig. 1. (a) Optical vortex generation from an isotropic sphere. Incident circularly polarized light with plane front (l = 0) after refraction on spherical surface is partially converted into optical vortex with orbital angular momentum l = 2. (b, c) Modelled using Jones matrix formalism wave-front profiles of incident and transmitted electric field.

The system which could provide desirable compact form and also possess radial symmetry is a bubble or void. If the voids or bubbles embedded in glass have relatively high refractive index contrast, they exhibit edge birefringence[17] related to differential transmission of *s* and *p*-polarizations. In this letter, we propose and demonstrate radial polarizer based on a isotropic transparent sphere. As a result of angular momentum conservation, spherical interface leads also

to optical vortex generation, which is directly observed on microscopic bubbles produced inside the glass by femtosecond laser.

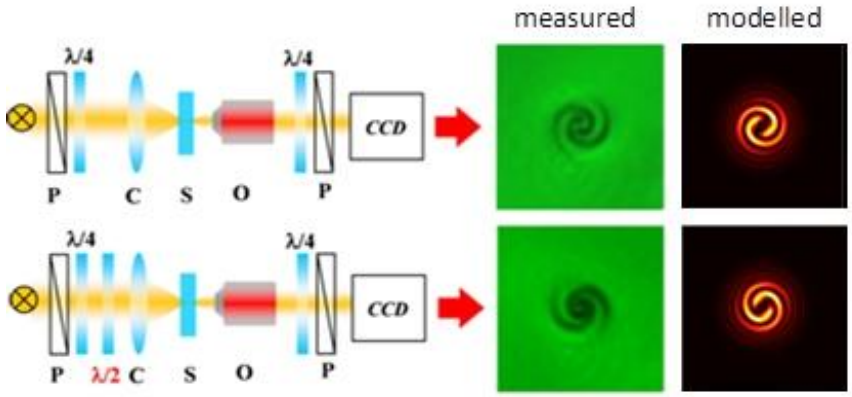

Fig. 2. Optical setups for optical vortex observation. P – polarizer, C – condenser, S – sample, O – objective. Vortex patterns (measured and modelled), observed under left and right handed polarizations, show mirror symmetry indicating reverse of orbital momentum sign.

We anticipate that the observed type of angular momentum interaction, localized in several microns and sensitive to the handedness of circular polarization, will open new opportunities in quantum optics, optical trapping and manipulation.

[1] K. Melcher, L.-M. Ng, E. Zhou et al., A gate-latch-lock mechanism for hormone signaling by abscisic acid receptors, Nature 462, 602-608 (1990).
[2] A. Mair, A. Vaziri, G. Weihs and A. Zeilinger, Entanglement of the orbital angular momentum states of photons, Nature 412, 313-316 (2001).
[3] O. G. Rodriguez-Herrera, D. Lara, K. Y. Bliokh, et al., Optical nanoprobing via spin-orbit interaction of light, Phys. Rev. Lett. 104, 253601 (2010).
[4] D. G. Grier, A revolution in optical manipulation, Nature 424, 810-816 (2003).
[5] L. Allen, M. W. Beijersbergen, R. J. C. Spreeuw and J. P. Woerdman, Orbital angular momentum of light and the transformation of Laguerre-Gaussian laser modes, Phys. Rev. A 45, 8185-8189 (1992).
[6] L. Marrucci, C. Manzo and D. Paparo, Optical spin-to-orbital angular momentum conversion in inhomogeneous anisotropic media, Phys. Rev. Lett. 96, 163905 (2006).
[7] J. A. Ferrari, W. Dultz, H. Schmitzer and E. Frins, Achromatic wavefront forming with space-variant polarizers: applications to phase singularities and light focusing, Phys. Rev. A. 76, 053815 (2007).
[8] E. Brasselet, N. Murazawa, H. Misawa and S. Juodkazis, Optical vortices from liquid crystal droplets, Phys. Rev. Lett. 103, 103903 (2009).
[9] M. Beresna, P. G. Kazansky, Y. Svirko, M. Barkauskas and R. Danielius, High average power second harmonic generation in air, Appl. Phys. Lett. 95, 121502 (2009).

3D PHOTONIC CRYSTAL AS A SPATIAL LIGHT FILTER

M. Rutkauskas[1], L. Maigytė[2], M. Peckus[1,2], K. Staliūnas[2], and M. Malinauskas[1]

[1] *Laser Research Center, Department of Quantum Electronics, Vilnius University, Saulėtekio Ave. 10, LT-10223 Vilnius, Lithuania*

[2] *ICREA, Departament de Fisica i Enginyeria Nuclear, Universitat Politecnica de Catalunya, Colom 11, E-08222 Terrassa, Barcelona, Spain*

mangirdas.malinauskas@ff.vu.lt

Photonic Crystals (PhC) have generated high interest as light flow manipulation elements due to possibility of forming photonic bandgaps in wave frequency domains [1]. Lately, it has been found out that the spatial dispersion is also modified in PhCs [2]. One example of spatial manipulation of light is a self-collimation of the beam due to the appearance of flat segments on the spatial dispersion curves [3,4]. In addition, to effects occurring inside the PhCs, crystals with particular dispersive properties show super-lensing effects [5]. However, to produce PhCs with appropriate parameters is rather a complex task. A Laser Multi-Photon Polymerization (LMPP) is the best means of fabrication of 3D photonic elements of elaborate woodpile geometry [6].

Here we present a light collimation by 3D PhCs, which were made by a LMPP technique. LMPP is a direct laser writing technique based on ultra-localized polymerization reaction initiated by nonlinear absorption of short pulsed light in the tiny volume of the photosensitive material. Moving the sample relatively to the fixed focus spot one can point by point modify the material along the scanning trace with subdiffractional resolution [7].

The produced PhCs were investigated using custom made observation setup (Fig. 1 c). The sample containing PhC was set behind the focal plane of 532 nm wavelength laser beam focused by 10x microscope objective lens. Illumination of PhC lead to appearance of well-collimated beam in the far field area and the four first order diffraction maxima (Fig.1 d). Measured diffraction angles between the central and the first maximum were 31 deg and this result correlates well with transverse period of the PhC. The beam remains well collimated even over long distances behind the sample.

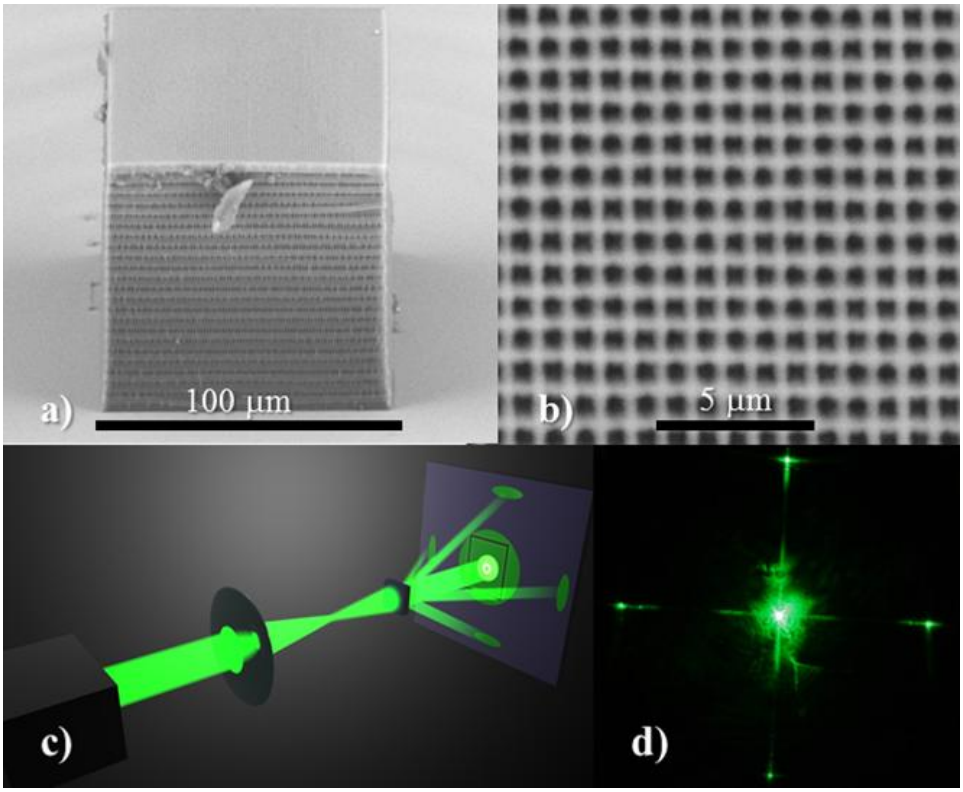

Fig.1. a), b) Scanning electron microscope images of the PhC fabricated via LMPP technique. a) Side-view of the crystal showing longitudinal period, b) PhC view from above demonstrating transversal period. c) Observation of well-collimated beam behind the PhC using laser beam. d) Transmitted intensity distribution, which is observed on the remote screen 9 cm away from the crystal, when laser beam is propagating through the PhC. This image indicates an appearance of the narrow spot of well-collimated beam and the four first order diffraction maxima.

[1] E.Yablonovitch, Inhibited Spontaneous Emission in Solid-State Physics and Electronics, Phys. Rev. Lett. 58, 2059-2062 (1987).

[2] K. Staliunas and V. J. Sánchez-Morcillo, Spatial filtering of light by chirped photonic crystals, Phys. Rev. A 79, 053807 (2009).

[3] H. Kosaka, T. Kawashima, A. Tomita, M. Notomi, T. Tamamura, T. Sato, and S. Kawakami, Self-collimating phenomena in photonic crystals, Appl. Phys. Lett. 74, 1212-1214 (1999).

[4] K. Staliunas and R. Herrero, Subdiffractive band-edge solitons in Bose-Einstein condensates in periodic potentials, Phys. Rev. E 73, 016601 (2006).

[5] E. Cubukcu, K. Aydin, E. Ozbay, S. Foteinopoulou, C. M. Soukulis, Subwavelength resolution in a two-dimensional photonic-crystal-based superlens, Phys. Rev. Lett. 91, 207401 (2003).

[6] J. Serbin, A. Ovsianikov and B. Chichkov, Fabrication of woodpile structures by two-photon polymerization and investigation of their optical properties, Opt. Express 12, 5221-5228 (2004).

[7] M. Malinauskas, H. Gilbergs, V. Purlys, A. Žukauskas, M. Rutkauskas and R. Gadonas, Femtosecond Laser-Induced Two-Photon Photopolymerization for Structuring of Micro Optical and Photonic Devices, Proc. SPIE 7366, 736622 (2009).

INTERFERENCE PATTERNS OF LASER-DRESSED STATES IN A SUPERSONIC ATOMIC/MOLECULAR BEAM

M. Bruvelis[1], J. Ulmanis[1], K. Miculis[1], N.N. Bezuglov[2], C. Andreeva[3], and A. Ekers[1]

[1] *Molecular beam laboratory, Laser Centre, University of Latvia, LV-1002, Riga, Latvia*
[2] *Faculty of Physics, St. Petersburg State University, 198904 St. Petersburg, Russia*
[3] *Institute of Electronics, Bulgarian Academy of Sciences, Sofia 1784, Bulgaria*
martins.bruvelis@gmail.com

Interference of laser-dressed states can be observed when light-induced crossings of energy levels enable the population to split between distinct excitation pathways that recombine afterwards. In this talk we present observation and interpretation of such interference patterns obtained in a Ramsey-type experiment in a supersonic Na/Na_2 atomic/molecular beam[1]. The excitation pathways are generated by applying two laser fields in an open three level ladder system g-e-f as seen in Fig. 1. In the experiment, the dressed states are spatially varying – the two lasers are cw and cross a supersonic sodium beam, coupling the g-e-f ladder. The lasers are focused in such a way that a strong and short (tightly focused) pump laser couples the two lower levels g and e , and weak and long (less tightly focused) probe laser couples the intermediate level e and the upper level f. The energy difference between the dressed states is determined by the pump field Rabi frequency and its detuning off from resonance. This particular arrangement produces the excitation spectra of level f consisting of oscillatory patterns with distinct maxima and minima that are characteristic to interference patterns. Detailed numerical calculations based on the dressed-state picture show that this particular arrangement of dressing fields can be used to vary the spatial distribution of highly excited atoms, which can be precisely controlled by varying the frequencies and intensities of both laser fields.

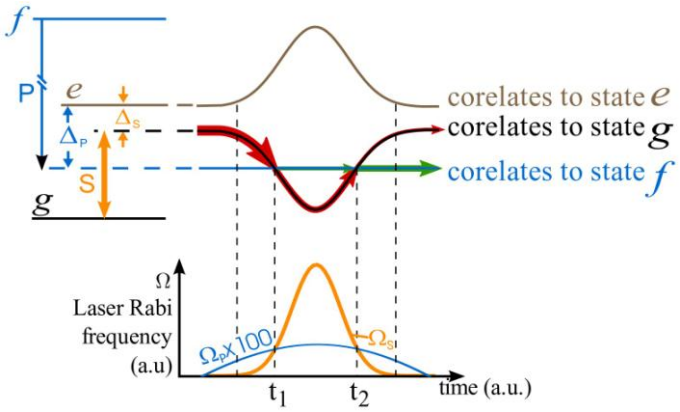

Fig. 1. Excitation in an open three level ladder system g-e-f. At t_1 population can evolve through two pathways. At t_2 phase dependent interference can happen when pathways cross for the second time.

[1] N. N. Bezuglov, . Garcia-Fernandez, A. Ekers, K. Miculis, L. P. Yatsenko and K. Bergmann, Consequences of optical pumping and interference for excitation spectra in a coherently driven molecular ladder system, Phys. Rev. A 78, 05380 (2008).

ORAL SESSION II

Biophysics, medical and environmental physics

Chemistry and chemical physics

SPECTROSCOPIC STUDY OF WATER-SOLUBLE QUANTUM DOTS AND CHLORIN e_6 COMPLEX FORMATION AND STABILITY IN THE PRESENCE OF ALBUMIN

A. Skripka[1, 2], J. Valančiūnaitė[1], and R. Rotomskis[1, 2]

[1] *Institute of Oncology, Vilnius University, Santariškių 1, LT-08660 Vilnius, Lithuania*
[2] *Vilnius University, Physics faculty, Saulėtekio Ave. 9-III, LT-10222 Vilnius, Lithuania*
Artiom.Skripka@ff.stud.vu.lt

Quantum dots (QD), luminescent semiconductor nanoparticles, have received considerable interest due to their potential application in various biological and biomedical fields. Several years ago it was suggested that QDs could also be used in the photodynamic therapy (PDT) of cancer to enhance the efficiency of PDT by using them as energy donors for conventional porphyrin-type photosensitizers (PS) [1]. Although there are numerous studies on different QD-PS systems in organic and aqueous solutions reported until now [2], little is still known about the QD-PS complex formation and stability in biological medium.

Our earlier research with commercially available CdSe/ZnS QDs and a second-generation photosensitizer chlorin e_6 (Ce_6) showed that upon the formation of QD-Ce_6 complex the QD PL band intensity decreased and the intensity of the fluorescence band of Ce_6 increased simultaneously. Moreover, in the presence of QDs, the fluorescence of Ce_6 shifted bathochromically from 660 nm to 670 nm. The fluorescence excitation spectrum of QD-Ce_6 complex recorded at λ_{em}=670nm showed the significant contribution of QD to the fluorescence of bound Ce_6. These results indicated that the energy transfer from QD to Ce_6 in the QD-Ce_6 complex occured. [3].

In this work we present the spectral study on the formation and stability of complex between CdSe/ZnS-amino(PEG) (545 nm) QDs and Ce_6 in the presence of protein, bovine serum albumin (BSA).

The emission spectra of QD, Ce_6 and QD-Ce_6 solutions in the absence and presence of BSA are shown in Fig. 1. The excitation wavelength at 465nm was used for the emission spectra measurements so that only QDs but not Ce_6 could be excited. The peak of the PL spectrum of QD was at 545 nm. Addition of BSA changed neither the intensity nor the position of the QD PL band. Meanwhile, in the presence of BSA, the fluorescence band of Ce_6 experienced a bathochromic shift from 660 nm to 670 nm the same as observed with QDs. The addition of BSA to QD-Ce_6 solution caused the decrease in the intensity of Ce_6 fluorescence by 14% while the intensity of QD PL band increased by 13%. Such changes indicate that the QD-Ce_6 complex was not disrupted and could further undergo the energy transfer in the presence of BSA. Similar results were obtained by changing the sequence of compound mixing. The fluorescence excitation spectrum recorded at λ_{em}=670 nm either adding Ce_6 to QD-BSA solution or QD to Ce_6-BSA solution, showed the spectrum Ce_6 on the intensive slope of QD spectrum. The

intensities of 545 nm and 670 nm bands in the emission spectrum were similar to those as in the case of adding BSA to already formed QD-Ce_6 complex solution. Obtained fluorescence emission and excitation spectra indicates that QD-Ce_6 complex still forms in the presence of BSA and can successfully undergo energy transfer.

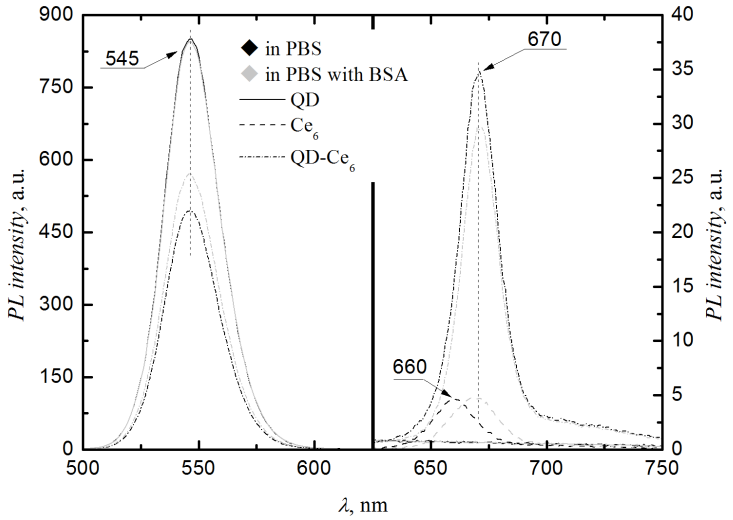

Fig. 1. Emission spectra of QD (0.05μM), Ce_6 (0.5μM) and QD-Ce_6 (QD-Ce_6 molar ratio 1:10) solutions in PBS and in the presence of BSA (QD:BSA 1:20, Ce_6:BSA 1:2, QD:Ce_6:BSA 1:10:20). Measurements were carried out with λ_{ex}=465 nm.

We conclude that the photosensitizer Ce_6 can form a stable complex with CdSe/ZnS-amino(PEG) quantum dots in the presence protein at studied concentrations. The energy transfer from QD to bound Ce_6 molecules occur in the presence of BSA, however with lower efficiency.

Acknowledgments. This work was supported by the Lithuanian Science Council Student Research Fellowship Award (A.S).

[1] Samia, A.C.S., Chen, X.B.,Burda, C. Semiconductor quantum dots for photodynamic therapy. Journal of the American Chemical Society 125(51), 15736-15737 (2003).

[2] Juzenas, P., Chen, W., Sun, Y.P., Coelho, M.A.N., Generalov, R., Generalova, N.,Christensen, I.L. Quantum dots and nanoparticles for photodynamic and radiation therapies of cancer. Advanced Drug Delivery Reviews 60(15), 1600-1614 (2008).

[3] Valanciunaite, J., Skripka, A., Streckyte, G., Rotomskis, R. Complex of water-soluble CdSe/ZnS quantum dots and chlorine e6: interaction and FRET. SPIE Proceedings 7376, 737607 (2010).

REACTIVE OXYGEN SPECIES PRODUCTION IN MITOCHONDRIA OF HUMAN LARYNX CARCINOMA CELLS

E.N. Golubeva, G.G. Martinovich, I.V. Martinovich, and S.N. Cherenkevich

Belarusian State University, Minsk, Republic of Belarus

golubeva.ln.87@gmail.com

Apoptosis, or programmed cell death, is a physiological cell process essential for normal tissues. It is associated with mitochondrial membrane depolarization and the loss of the electrochemical gradient on the inner mitochondrial membrane. Excessive calcium influx is supposed to be a typical cell death stimulus where mitochondrial membrane depolarization precedes the cytochrome c release. It has been also observed that the inner mitochondrial membrane may undergo a transient hyperpolarization and rapid matrix alkalinization in response to various stimuli during apoptosis. Eventually hyperpolarization and matrix alkalinization are followed by mitochondrial membrane depolarization and equilibration of mitochondrial and cytosolic pH, leading to mitochondrial permeability transition pore opening [1]. Cytoplasmic acidification is required for pro-apoptotic proteins caspases to function properly [2]. Furthermore, the loss of the mitochondrial membrane potential results in the production of reactive oxygen species (ROS) [3]. Most anticancer drugs kill their target cells at least in part through the generation of elevated amounts of intracellular ROS. It is worth mentioning that cytosolic pH values in tumors are above normal levels, which is likely to be due to the activation of one of the major cytosolic pH regulator Na^+/H^+ exchanger (NHE) in cancer cells. Activation of NHE may lead to inhibition of apoptosis and provide cancer cells survival [2]. Recent findings indicate that either the presence of excessive ROS or the collapse of the mitochondrial membrane potential opens the mitochondrial permeability transition pore, which is accompanied by the release of pro-apoptotic molecules such as cytochrome c into the cytoplasm. Understanding the molecular basis of electron transport chain functioning in tumors will lead to the investigation of novel cancer cell death activation mechanisms by apoptotic signalling pathways controlled by mitochondria and will favour the development of more effective therapies that selectively kill cancer cells with little or no harm to normal cells.

In our investigations the production of reactive oxygen species in human larynx carcinoma cells HEp-2 was observed. In order to reveal possible sources of ROS (HADPH oxidase or mitochondria) the influence of external pH and $[Ca^{2+}]$ on the ROS production in HEp-2 cells was investigated. External calcium and pH did not appear to change the ROS production revealing that HADPH oxidase was unlikely to be a source of the ROS production in HEp-2 cells. The major sites of superoxide formation within the mitochondrial respiratory chain are linked to respiratory complexes I and III [4]. In our experiments both rotenone (complex I inhibitor) and

antimycin A (complex III inhibitor) were ascertained to enhance the ROS production in HEp-2 cells. Superoxide production by complex I is supposed to occur during the reverse electron transport (RET) from succinate to NAD^+ and during the forward electron transport (FET), the former being faster than the latter. Recent investigations have led to the conclusion that rotenone enhances the ROS formation during the forward electron transport and inhibits it during the reverse electron transport [4]. Moreover, the RET-induced ROS production is regulated by the amplitude of the mitochondrial electrical membrane potential so that a 10% decrease in the membrane potential inhibits the ROS production by 90%. The inhibition of electron transport by antimycin A causes a collapse of the proton gradient across the mitochondrial inner membrane, thereby breaking down the mitochondrial membrane potential [3] but leading to the ROS formation even after rotenone treatment (Fig.1).

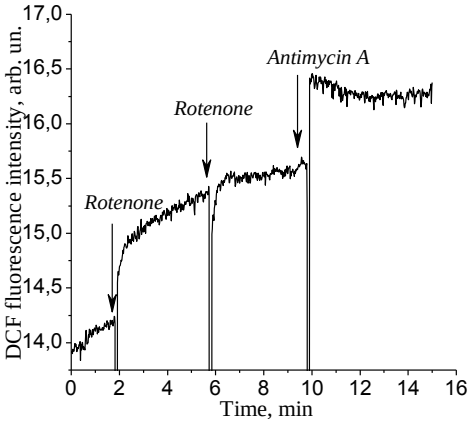

Fig. 1. DCF fluorescence in HEp-2 cells. Concentrations: rotenone – 50 μM, antimycin A – 10 μM.

The facts mentioned above indicate that the major source of ROS in HEp-2 cells is mitochondria and the ROS formation is not connected with the reverse electron transport in complex I. Cytosolic pH values in cancer cells are above cytosolic pH values in normal cells. This shift in the cytosolic pH value in cancer cells may lead to a decreased electrochemical gradient on the inner mitochondrial membrane in HEp-2 cells. This, in turn, may result in constant ROS production in HEp-2 cells mitochondria.

[1] S. Matsuyama, J.-C. Reed, Mitochondria-dependent apoptosis and cellular pH regulation, Cell Death and Differentiation 7, 1155-1165 (2000).
[2] D. Konstantinidis et al., Inhibition of the Na+-H+ exchanger isoform-1 and extracellular signal-regulated kinase induces apoptosis: a time course of events, Cell. Physiol. Biochem. 18, 211-222 (2006).
[3] Y.-H. Han et al., Antimycin A as a mitochondrial electron transport inhibitor prevents the growth of human lung cancer A549 cells, Oncology Reports 20, 689-693 (2008).
[4] G. Lenaz, M.-L. Genova, Structure and organization of mitochondrial respiratory complexes: a new understanding of an old subject, Antioxid. Redox. Signal. 12, 961-1008 (2010).

INTEGRATION OF SELF-ASSEMBLY AND LASER TECHNOLOGIES IN FABRICATION OF TEMPLATES FOR CELL ARRAYS

J. Pupkaitė[1], G. Račiukaitis[2], T. Rakickas[3], and R. Valiokas[3]

[1] *Faculty of Natural Sciences, Vilnius University, M.K.Čiurlionio g. 21/27, LT-03101 Vilnius, Lithuania*
[2] *Department of Laser Technology, Center for Physical Sciences and Technology, A. Goštauto 11, LT-02300 Vilnius, Lithuania*
[3] *Department of Nanoengineering, Center for Physical Sciences and Technology, A. Goštauto 11, LT-02300 Vilnius, Lithuania*

j.pupkaite@ftmc.lt

Structured monolayers of organic molecules can be a useful tool in controlled cell growth and adhesion experiments. Genome and proteome analysis is another area where such microarrays can be used. Naturally occurring chemical gradients are important for cell growth, adhesion and other biological processes. To study them at a lab, one needs to create controlled chemical gradients [1]. Most of the methods that have been applied to date have disadvantages which prevent efficient manufacturing of complex structures that maintain the function of the biomolecules. D. Rhinow and N.A. Hampp [2] proposed a method of submerged laser ablation which allows fabrication of complex multimolecular self-assembled monolayer (SAM) structures on gold surfaces from various molecules with surface-selective thiol groups. The aim of this work was to investigate the effect of laser radiation on thiol monolayers and to fabricate structures made up of self-assembled monolayers terminated with different functional groups.

In our experiments, a SAM (for instance, HS-C_{11}-EG_3-OH) is grown from solution on a gold-covered silicon chips. Initially, the experiments were performed with the specimen put into a small Petri dish filled with ethanolic HS-C_{11}-EG_3-biotin solution and covered with glass. Later, a special fluid cell was designed. It makes it possible to change the solutions without moving the specimen, so structures from different molecules (HS-C_{11}-EG_3-biotin and HS-C_{15}-COOH) or different concentrations of the same molecule (HS-C_{11}-EG_3-biotin) could be formed with greater precision. Pulsed laser NL 640 (Ekspla) was used as irradiation source (wavelength of 532 nm, with an impulse duration of approximately 10 ns). The laser beam was directed using galvanometric scanner, focused using a flat-field lens (100 mm). After sample irradiation, the obtained microstructures were visualized using streptavidin-conjugated quantum dots which selectively bind to biotin groups. The –COOH areas were visualized via non-specific binding of the same quantum dots (an epifluorescence microscope Olympus BX51 was used).

When the HS-C_{11}-EG_3-OH SAM is irradiated, the gold-sulfur bonds are broken, molecules (HS-C_{11}-EG_3-biotin or HS-C_{15}-COOH) adsorb from the solution and form a new monolayer. Quantum-dot-conjugates revealed that HS-C_{11}-EG_3-biotin and HS-C_{15}-COOH molecules form fluorescent spots whose radii depend on the dose of irradiation and laser fluence (Fig. 1 a, b).

Using the fluid cell, the formed structures had a more regular circular shape than those fabricated using a Petri dish.

To check whether, in principle, it is possible to form gradient SAM structures using this method, we performed experiments with HS-C_{11}-EG_3-OH SAM in ethanolic HS-C_{11}-EG_3-biotin / HS-C_{11}-EG_3-OH solutions of different molar ratios. We found that a 70mol% HS-C_{11}-EG_3-biotin solution produces more intense fluoresescence of the formed structures than 10mol% HS-C_{11}-EG_3-biotin solution, which suggests higher concentration of HS-C_{11}-EG_3-biotin (Fig. 1 c, d).

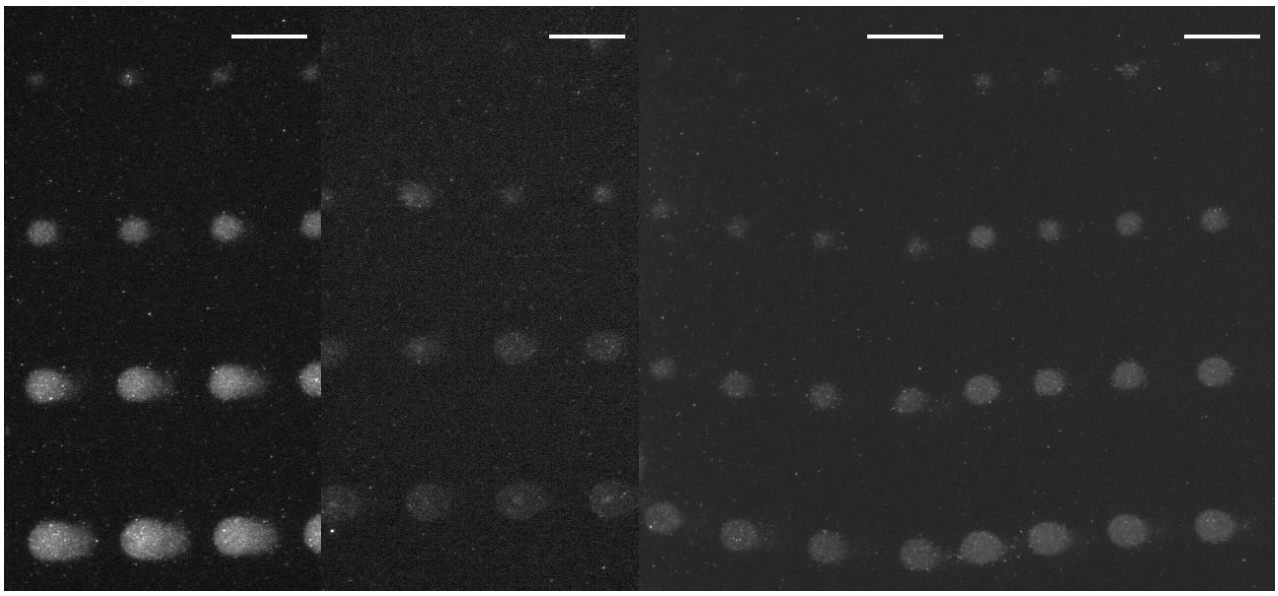

a) b) c) d)

Fig. 1. Fluorescence microscopy images. HS-C_{11}-EG_3-OH SAMs with fabricated microstructures from: a) HS-C_{11}-EG_3-biotin; b) HS-C_{15}-COOH; c) 10%mol HS-C_{11}-EG_3-biotin; d) 70%mol HS-C_{11}-EG_3-biotin. Laser power was changed for scanning lines from top to bottom: 0,06W, 0,07W, 0,08W, 0,09W. Scale bars are 50 μm.

In conclusion, we have confirmed that by irradiating self-assembled thiol monolayer on a gold surface we can form monolayer structures from different molecules. Our experiments show that pulsed laser technologies and SAM chemistry can be integrated to produce biological microarrays. In particular, SAM gradients can be obtained for use in cell growth and adhesion experiments.

[1] S. Morgenthaler, C. Zink, N. D. Spencer, Surface-chemical and -morphological gradients, Soft Matter, 4, 419-434 (2008).

[2] D. Rhinow, N.A. Hampp, Solid-Supported Multicomponent Patterned Monolayers, Advanced Materials 19, 1967-1972 (2007).

SURFACE MODIFICATION OF SEMICONDUCTOR NANOPARTICLES FOR LIVE CELL BIOIMAGING

K. Stašys[1], V. Karabanovas[1], R. Rotomskis[1], and M. Valius[2]

[1] *Laboratory of Biomedical Physics, Institute of Oncology, Vilnius University, Santariškių 1, LT-08660 Vilnius, Lithuania*

[2] *Department of Developmental biology, Institute of Biochemistry, Vilnius University, Mokslininkų 12, LT-08662 Vilnius, Lithuania*

Karolis.Stasys@ff.stud.vu.lt

Colloidal semiconductor nanocrystals, often referred to as ‘‘quantum dots’’ (QD), have attracted considerable interest in cell labelling due to their unique size-dependent optical properties and high emission stability against bleaching. These unique properties allow them to be used in many applications such as molecular biology, hybrid nanobiosensors and drug delivery systems. Tuneable emission wavelength, broad absorption and sharp emission spectra, high quantum yield (QY), resistance to chemical degradation, versatility in surface modification makes QD very promising fluorescent markers. However, QD synthesized in organic solvents are insoluble in water which is a necessity for biological application and thus further modification is required.

QD solubilisation requires replacing hydrophobic trioctylphosphine oxide (TOPO) surface with a hydrophilic coating. In this work CdSe(ZnS)-TOPO QD surface was modified using thiol group bifunctional ligands: 2-mercaptopropionic acid (MPA), mercaptoacetatic acid (TGA) and cysteamine (CYS). Then the effects on optical properties of QD were observed using spectroscopic methods. Differences in absorption and PL spectra after modification are presented in Fig.1A,B respectively. The decrease of absorbance at the interval ranging from 400 up to 630nm was detected in both QD-MPA and QD-CYS solutions (Fig.1A).

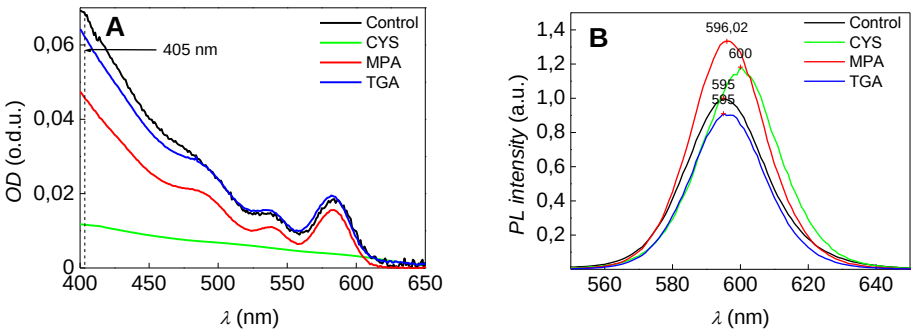

Fig. 1. (CdSe)ZnS QD (c=100nM) after modification with MPA, TGA and CYS. Absorption spectra (A) and PL spectra (B). PL spectra is normalised at excitation wavelength (405 nm) due to different absorption.

QD-MPA and QD-TGA photoluminescence (PL) intensity increased in comparison with QD-TOPO (control) while the PL intensity for QD-TGA slightly decreased (Fig.1B). Also a red shift was visible for QD-CYS in PL spectra. QD PL spectral position depends on nanoparticle size,

therefore the red shift of QD-CYS might be caused by particle aggregation. The increased QD-CYS PL intensity compared with QD-TOPO implies that the surface coating of QD with CYS molecules the quantum yield of PL but reduces the stability.

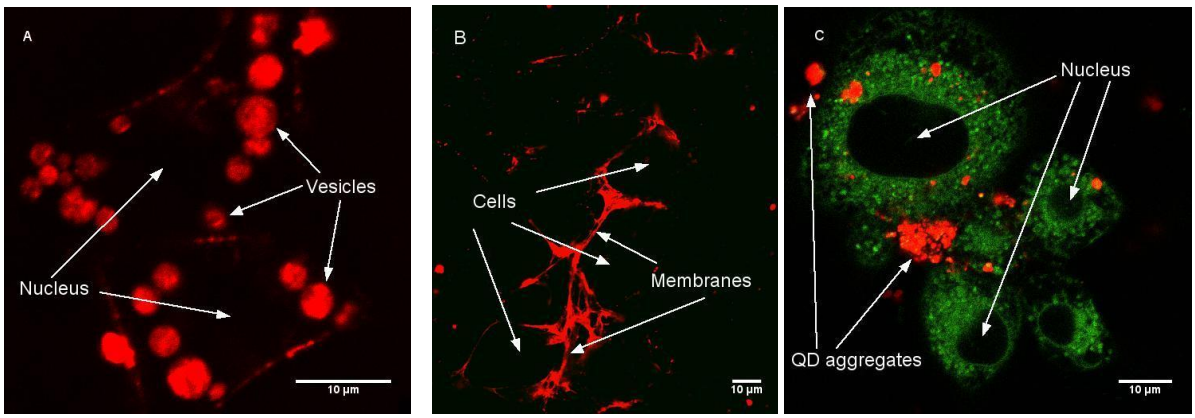

Fig. 2. Fluorescence imaging of NIH3T3 cells taken after 24 h incubation with different functional groups coating QD at 40nM concentration. A – QD-MPA, B – QD-TGA, C – QD-CYS. NIH3T3 cell endoplasmic reticulum and membranes were marked using DIOC6 dye. Scale bar - 10 µm.

From confocal microscopy experiments was observed, that different ligands on QD surface could determine these nanoparticles uptake and localisation in cells (Fig. 2). QD coated with MPA access the cells and accumulate in vesicles, which after 24 h. of incubation fuse each other into multivesicular bodies. QD-TGA do not pass cells plasma membrane and stuck within also marking membrane structures. QD-CYS aggregates in cell media and do not internalize into cells.

All facts considered, it can be stated that QD properties highly depend on surface chemistry and coating quality. Using surface coating ligands with different functional groups greatly alters both photophysical and biological QD properties. This understanding opens a path for better QD functionalization which allows controlling their localization in cells. In this manner, a new powerful tool for cell probing and biomedicine application could be created.

[1] Karabanovas, V.; Rotomskis, R.; Beganskiene, A.; Kareiva, A.; Bagdonas, S.; Grigaravicius, P.; Greulich,; Degradation related cytotoxicity of quantum dots IEEE-NANO 2009. 454 – 457

[2] Pong B,; Trout B.L., Modified ligand-exchange for efficient solubilization of CdSe/ZnS Quantum Dots in Water: A Procedure Guided by Computational Studies; Langmuir 2008, 24, 5270-5276

CHEMICAL ASPECTS OF THE PROCESS OF BIOMASS GASIFICATION

M. Sosnowska[1], K. Kwiatkowski[2], K. Bajer[2]

[1] *Warsaw University of Technology, Faculty of Chemical and Process Engineering*
[2] *University of Warsaw, Faculty of Physics, Institute of Geophysics*
m.j.sosnowska@gmail.com

The lack of appropriate waste management is currently one of the major environmental concerns of the world. An average citizen of a developed country produces annually 300 kg of waste that is mostly disposed on landfills. The population is growing and so is the amount of produced wastes. It is therefore crucial to shift from waste disposal to more sustainable waste management methods. By means of the recent directive on waste (2006/12/EC) the European Council encourages the Member States to reduce the waste production by developing clean technologies and to enhance changes in current waste management, especially by introducing "the recovery of waste by means of recycling, re-use or reclamation or any other process with a view to extracting secondary raw materials or to make use of waste as a source of energy" [1].

One of the methods of dealing with organic waste is to convert it into a flammable gas by means of anaerobic digestion or thermal gasification. Thermal gasification is a complicated physicochemical process that takes place in reducing (oxygen-deficient) environment and requires heat. The object of this paper is to present the process taking place in an up-draft air gasifier and briefly discuss its chemical aspects.

The process consists of four distinct phases, which are: drying, pyrolysis, combustion and reduction (actual gasification). Though there is a considerable overlap between those phases, it can be assumed for the purpose of modelling that each of them occupies a separate zone of the gasifier, where fundamentally different chemical reactions take place [2]. The final product of the process is a flammable gas consisting essentially of N_2, H_2, CO, CH_4.

In the first zone the biomass dries. Wood, which is the most common substrate for the process, usually consists of about 10 – 60 % water. The following process is pyrolysis which is a thermal decomposition of the organic compounds in absence of oxygen. At common gasifiers the process takes place in temperatures from 500 to 700°C and is driven by the energy released during the combustion of the previous load of biomass. The chemistry of the process is not well understood [4]. The products of the decomposition are in three phases: solid (char), liquid (tar – gaseous at the process conditions, liquid after cooling to 25°C) and gaseous (CO, CO_2, H_2 and CH_4).

The third phase is combustion when the char is partially oxidized according to the formulas (1) and (2), releasing energy:

$$C + O2 = CO2 (+ 393 \text{ MJ/kg mole}) \quad (1)$$

$$2H2 + O2 = 2H2\,O\ (-\ 242\ MJ/kg\ mole) \quad (2)$$

Finally the gasous products of the previous processes and the hot char react in the reduction phase according to the formulas (3), (4), (5), (6) and (7):

$$C + CO2 = 2CO\ (-\ 164.9\ MJ/kg\ mole) \quad (3)$$

$$C + H2O = CO + H2\ (-\ 122.6\ MJ/kg\ mole) \quad (4)$$

$$CO + H2O = CO + H2\ (+\ 42\ MJ/kg\ mole) \quad (5)$$

$$C + 2H2 = CH4\ (+\ 75\ MJ/kg\ mole) \quad (6)$$

$$CO2 + H2 = CO + H2O\ (-\ 42.3\ MJ/kg\ mole) \quad (7)$$

The spacial configuration of the above described phases in an up-draft gasfier is presented in the figure 1 [3].

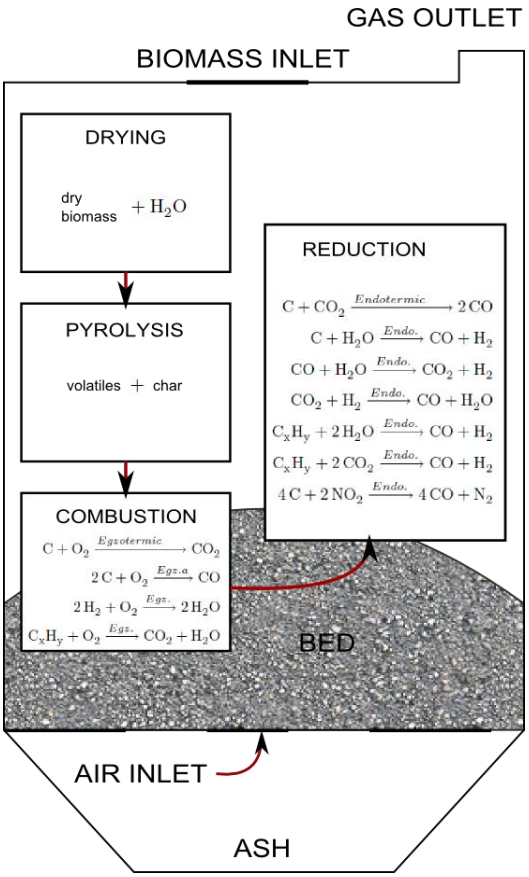

Fig. 1. Diagram of an up-draft air gasifier.

Acknowledgements. The authors wish to express gratitute for the financial support from the National Centre for Research and Development, Poland (project „Advanced Technologies for Energy Generation“). One of the objectives of the working group is to create a mathematical model of thermal gasification of biomass with special focus on wastes from poultry industries.

[1] Directive 2006/12/EC of the European Parliament and of the Council of 5 April 2006 on waste.
[2] P. Basu, Biomass Gasification and Pyrolisis. Practical Design and Theory (Elsevier Inc., UK, 2010).
[3] A.K. Rajvanshi, Alternative Energy in Agriculture (CRC Press, 1986).
[4] C.de Blasi, Modeling chemical and physical processes of wood and biomass pyrolysis, Progress in Energy and Combustion Science 34, 47–90 (2008).

GAS SENSING PROPERTIES OF HETEROPHASE NANOCOMPOSITES ON THE BASIS OF DOPED TITANIUM DIOXIDE

N. Boboriko, D.I. Mychko

Belarussian state university, Chemistry department

natchem@tut.by

Permanent monitoring and control of under explosive concentrations of burning gases, such as methane, hydrogen, hydrogen sulfide, carbon monoxide, petrol vapor, jet engine and diesel fuel vapor demand development of new stable and selective gas sensing materials. Semiconductor and thermocatalytic chemical gas sensors are promising devices for this effect as their main advantages are small size, simplicity in device structure, high sensitivity, robust performance and low price. Moreover sensitivity and selectivity of sensors can be changed by gas sensitive layer material variation. The operating principle of these devices is based on the measurement of sensor output signal, which is affected by the oxide film or ceramics electroconductivity change under the influence of the gaseous atmosphere. The main scientific aspect of works in this area is revelation of the ways of chemical gas sensor sensitivity and selectivity regulation by investigation of the mechanisms of the detecting gas molecules interaction with gas sensing material surface and the processes of sensors' output signal generation.

In our research heterophase nanocomposites on the basis of doped titanium dioxide were established to be perspective materials for gas sensing layer formation. Sensitive elements of gas sensors were fabricated in monoelectrode variant as hollow cylinders. Sol-gel method comprising colloidal solution hydroxides deposition on platinum wire with twelve coils (wire diameter 20 μm) was applied with subsequent thermal dehydration and treatment at 800 °C. Gas-sensing properties of the sensors were measured in steady-state conditions by applying flow-through technique. All measurements were performed in a temperature-stabilized sealed chamber at 20 °C under controlled humidity. Electrical characterization was carried out by voLT-amperometric technique. The sensor output signal (ΔU) was controlled, where ΔU - voltage change on the sensor under atmosphere composition change. Sensors on the basis of TiO_2-Ga_2O_3 and TiO_2-In_2O_3 were established to operate as thermocatalytic detectors under hydrogen-air and hydrogen-methane-air atmosphere, and as semiconducting detectors under methane-air atmosphere. Sensors on the basis of individual oxides TiO_2 and Ga_2O_3 are unresponsive to methane under investigated conditions. It was shown that minimal response of the nanocomposites on the basis of TiO_2-Ga_2O_3 and TiO_2-In_2O_3 to methane and their high sensitivity to hydrogen allow considering them as perspective systems for fabrication of selective to hydrogen gas sensors in methane-hydrogen-air medium. It was shown that the value of the

output signal of multioxide based sensors depends on kind of the doping oxide and on its quantity. The optimal content of gallium oxide in TiO_2-Ga_2O_3 system, which provides the best operating characteristics of the sensor, is 10mol.%. In TiO_2-In_2O_3 system the value of the output signal rises with molar ratio In_2O_3/TiO_2 increase in the explored range of the doping oxide concentration.

According to the data obtained with the employment of XRD analysis, thermal analysis, IR-spectroscopy, scanning electron microscopy and transmission electron microscopy improvement of gas sensing characteristics of titanium dioxide correlates with structural chemical changes which take place with multioxide system formation. It was established that the dominant phase in TiO_2-Ga_2O_3 system is titanium dioxide, however, its crystal lattice distortion is possible. Formation of crystal phase of gallium oxide in the multioxide system was not observed. Improvement of gas sensing characteristics of titanium dioxide under the hydrogen-air atmosphere after its doping with indium oxide is possibly specified by In_2TiO_5 crystal phase formation after heat treatment and by the absence of individual indium oxide crystal phase. Investigation of individual and multioxide sols by methods of differential thermogravimetry and differential scanning calorimetry makes it possible to assert that the defectiveness of the structure increases, which in turn affects electrical properties of the system, i.e. its gas sensing characteristics. Using multihydroxide sols for sensors formation allows obtaining highly developed surface of sensing elements for gas molecules adsorption and catalytic reaction passing. Changes in structural characteristics of the materials were fixed by IR-spectroscopy. The shift of Ti-O vibration bands and appearance of new bands after titanium dioxide doping reveals TiO_2 crystal structure distortion and multioxide phase formation.

ORAL SESSION III

Semiconductor and condensed matter physics, material sciences

INTERACTION OF EXCITONS IN ZnO CRYSTALS

V. Tumas[1], E. Kuokštis[1], M. Karaliūnas[1], and E. Anisimovas[2]

[1] *Department of Semiconductor Physics, Faculty of Physics, Vilnius University, Saulėtekio Ave. 9-III, LT-10222 Vilnius, Lithuania*

[2] *Department of Theoretical Physics, Faculty of Physics, Vilnius University, Saulėtekio Ave. 9-III, LT-10222 Vilnius, Lithuania*

vytautas.tumas@ff.stud.vu.lt

Zinc oxide (ZnO) is a promising material for modern optoelectronics. Recently interest in investigation of ZnO and ZnO-based structures increased essentially due to achievements in growing technology of high quality of quantum-size structures along with unique electrical, optical and crystal structure properties of ZnO itself. It is important not only for industry, medicine and other industries, including novel optoelectronic devices, but for fundamental investigation, too. The oneness of ZnO among other semiconductors is due to large direct energy gap, which ranges from 3.44 to 3.38 eV in temperature interval from 0 to 300 K, and unusually large (60 meV) exciton binding energy. These properties make ZnO a promising material for optoelectronics and are almost ideal for LEDs and laser diodes operating in the blue and near ultraviolet spectra region.

In this paper, various interactions of excitons responsible for optical properties of material are taken into consideration. Usually, inelastic interactions of excitons are very important for optical properties including luminescence mechanisms in highly excited crystal, when colliding excitons annihilate eradiating photons and break down into pairs of electrons and holes, or moves to higher kinetic energy and/or higher excited states. The various possible interactions determine the properties of different fluorescent lines: different peak position and shape of distribution of luminescence spectra. In order to correctly determine the nature of the luminescence all kinds of interaction between excitons have been taken into account.

The excitonic luminescence intensities maxima are shifted from ground state of free exciton to lower energy side by E_b, ¾E_b, ½E_b and 0E_b respectively for these interactions (Fig. 1): a) (E_{1s}^{K}, $E_{1s}^{K'}$) → (ħω, e-h), b) (E_{1s}^{K}, $E_{2s,\,2P}^{K'}$) → (ħω, e-h), c) (E_{1s}^{K}, $E_{1s}^{K'}$) → (ħω, $E_{2s,\,2P}^{K''}$) and d) (E_{1s}^{K}, $E_{1sK'}$) → (ħω, $E_{1s}^{K''}$).

At low temperatures, interactions of excitons form narrow luminescence lines, but increase of temperature leads to broadening of these lines and shift of their maxima, except for interaction (E_{1s}^{K}, $E_{1s}^{K'}$) → (ħω, $E_{1s}^{K''}$).

We suggest e new luminescence mechanism of exciton collisions, namely interaction between free and localized excitons. Interaction of localized exciton with a free exciton at low temperatures forms a narrow line, which broadens rapidly when the temperature is increased (Fig. 2).

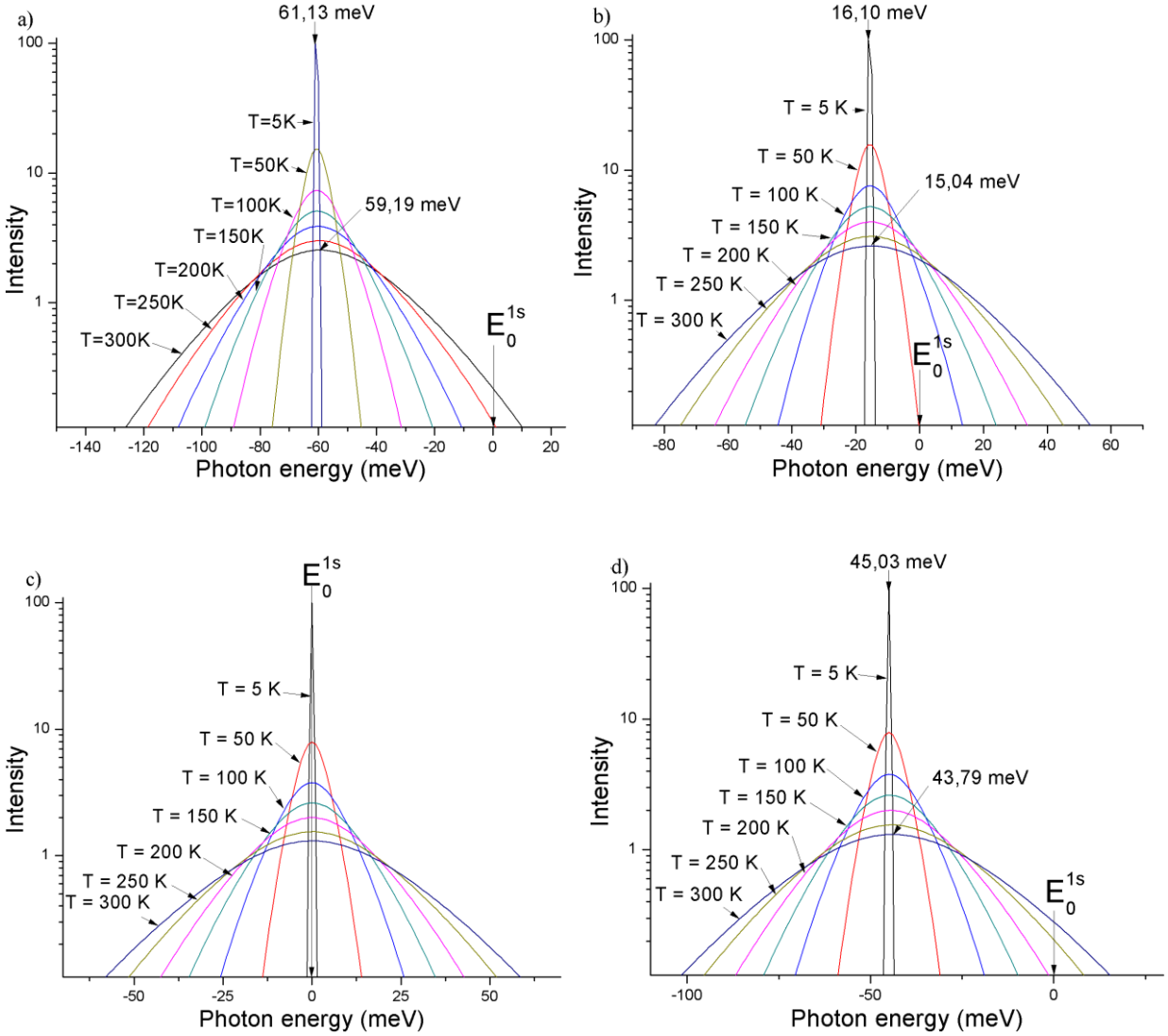

Fig. 1 Luminescence spectra formed by different exciton interactions in ZnO crystal.

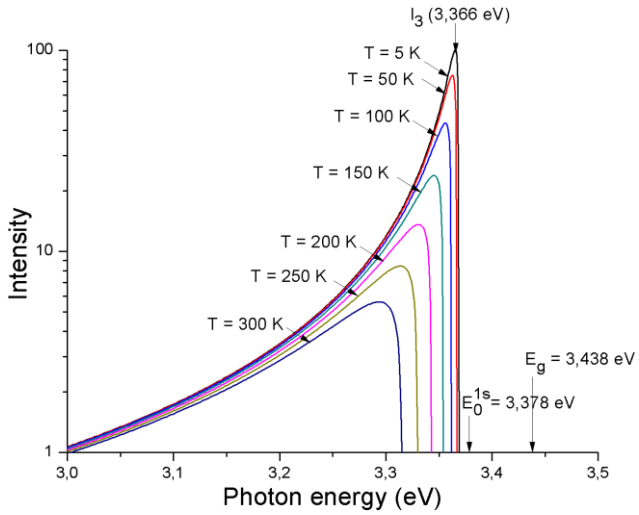

Fig. 2 Luminescence spectra formed by free and localized exciton interactions in ZnO crystal

QUANTUM WIRE IN ELECTRIC FIELD

M.A. Belov

Belorussian State University, Physics Faculty

mpui@tut.by

Development and miniaturization in the field of electronic components has achieved the stage, when devices make use of quantum coherent effects. There are two actual development directions, namely, the design of new nanoscale digital electronics components and the development of new media and systems. Materials with anomalously high Fermi surface anisotropy are commonly referred to as one-dimensional ones. Their properties are described in terms of one or two dimensional zone structure, while the rest dimensions are spatially localized. It's evident, that transport characteristics of these systems are highly anisotropic, so while conductivity in chosen directions has typical metallic behavior, in localized dimensions we deal with jumps between layers, or even transport is denied. Analytical description of quantum transport on disordered wires in external electric field is discussed in [1]. Landauer approach is used there along with first approximation of controlling field with perturbation theory. In this paper we give numerical analysis of controlling electric field effect on one-dimensional chain represented with a curve. Also, we will consider the same system represented with narrow plain waveguide of finite length and the same shape as the above mentioned curve.

We give numerical analysis of controlling electric field effect on one-dimensional atom chain represented with a curve. Also, we will consider the same system represented with narrow plain waveguide of finite length and the same shape as the above mentioned curve. Curve shape is defined as $y(z) = a \exp(-\beta x^2)$, curve length is 30 nm and curve height a is 2.4 nm.

In the first model we followed [2], where Kronig-Penney model with disorder is used to calculate conductivity. Then, as in [2,3], time-independent Schrodinger equation was represented as Poincare map due to the properties of scattering potential. It's known [4] that a distinguishing feature of one-dimensional models is abnormal conductivity fluctuation. We used uniformly-distributed random potential and a geometric mean of 100000 realizations for each point to cease fluctuations and make dispersion less than 10%. We applied longitudinal accelerating electric field with potential $U_x = 0.01 – 0.1$ eV and transverse controlling field U_z of same strengths.

Due to the absence of non-coherent scattering in the system we observed nonlinear, almost exponential transparency dependencies on both fields intensities. The dependence of transparency versus field intensity can render a possible use in high-frequency switches. However the considered system is rather simplified. That's why we also consider a a plain channel of finite width.

The second model represents a nanoscale curved channel (quantum waveguide) of a finite width and previously defined shape with one electron passing through. We used Split-Step Fourier (SSF) method [5], a simplectic integrator of error $O(dt^3)$ on a step. High amount of calculations requires supercomputer usage. Supercomputer implementation of SSF is described in [6,7]. We simulated the same modes as in the first model and compared the results (fig. 1). One can see that transparency in both models can be controlled by transverse field.

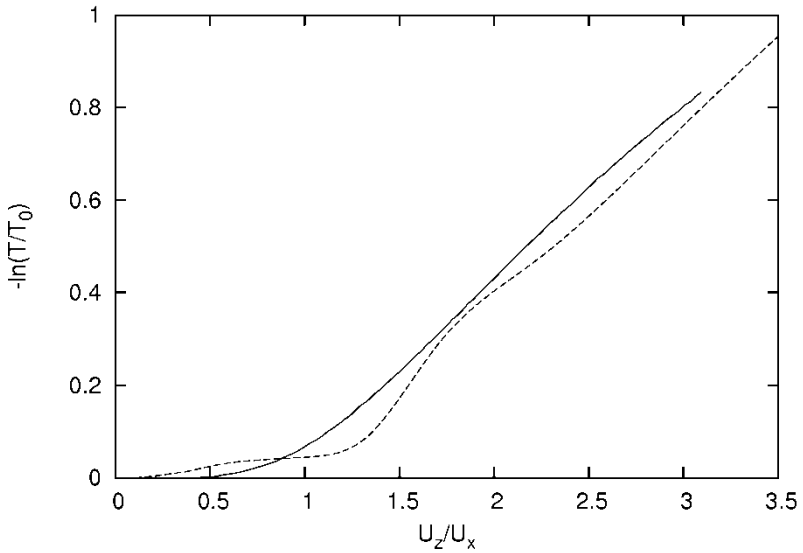

Fig. 1. One-dimensional (solid line) and quasi-one-dimensional (dashed line) models compared.

We have demonstrated the existence of field control in one-dimensional and quasi-one-dimensional systems. Fields of relatively small intensities can be used to control conductivity of these systems in coherent quantum transport mode. Localization phenomena become exponentially sensitive to the field magnitude. Both considered models have given qualitatively compliant results.

[1] E. Domany et al. Solutions to the Schrodinger equation on some fractal lattices. Phys. Rev. Vol. B28. P. 3110-3123 (1983).
[2] R. Quasti J. Phys. Cond. Matt. Vol. 7. P. 811-820 (1995).
[3] N. Zekri et al. Compensation effect of one-dimensional disordered potential wells and barriers in the presence of an electric field J. Phys. Cond. Matt. Vol. 7. P. L275 (1995).
[4] B. Shapiro. Phys. Rev. Vol. B34, no. 6. P. 4394-4397 (1986).
[5] Wilfredo Rodriguez. Solution of the time-dependent Schrodinger equation using a continuous Fourier transform. Int. J. Quant. Chem. Vol. 40, no. S25. P. 107-111 (1991);
[6] S. Zoldi. Parallel Implementation of the Split-step Fourier Method for Solving Nonlinear Schrodinger Systems. SIAM News. Vol. 32, no.1 (Philadelphia, 2005)
[7] M. A. Belov. Accuracy Estimation of Split-step Fourier method BSU News. S. 1 N. 2 P. 45-50 (2010).

ZnO BASED HYBRID WHITE LIGHT EMITTING DIODES

T. Serevičius[1], I. Hussain[2], and M. Willander[2]

[1] *Institute of Applied Research, Vilnius University, Saulėtekio Ave. 9-III, LT-10222 Vilnius, Lithuania*
[2] *Department of Science and Technology, Linkoping University, SE-601 74 Norrkoping, Sweden*
tomas.serevicius@ff.stud.vu.lt

An improvement of lightning technologies is a great challenge for scientists and engineers, as it has a direct impact on everybody's life. Good source of light should be effective, small, cheap and should have long lifetime, together with low price. Light emitting diode (LED) is the most efficient light emitting device that can be used nowadays. ZnO is excellent candidate for LED's, because it poses perfect optical properties, high mechanical stability, piezoelectric features and, most important for LED's, possibility to grow nanostructured ZnO using simple growth techniques on cheap substrates [1]. Aqueous chemical growth (ACG) is excellent technique for nano – ZnO growth. It requires low temperatures, ordinary chemicals and simple substrates without any need of special treatment [2]. The only drawback of ZnO is poor quality of p – type layers. This problem is solved by using hybrid inorganic – organic semiconductor heterostructures of n-ZnO and p – type organic semiconductor. Organic semiconductors can be easily doped and they can be easily introduced into various semiconductor structures.

In this work, we report on growth and characterization of hybrid ZnO white LED's on plastic substrate. Nanostructured ZnO nanorods (see fig. 1) of 2 – 3 mm length and average 150 nm diameter were grown utilising ACG method on the top poly (3,4-ethylenedioxythiophene) poly-styrenesulfonate (PEDOT:PSS) and poly (9, 9-dioctylfluorene) layer system. Detail growth steps are described in ref. 3.

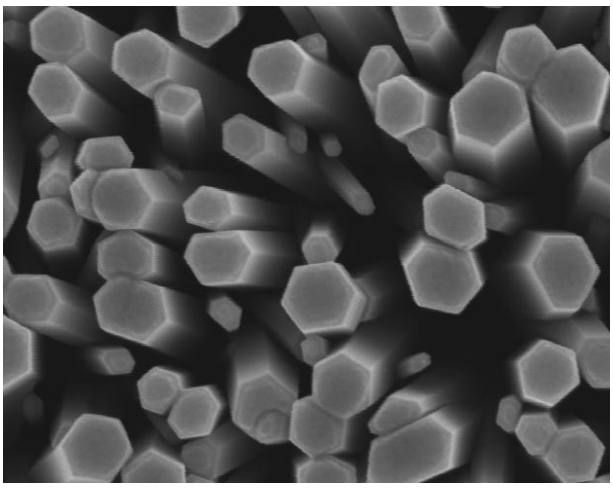

Fig. 1. Scanning electron microscope picture of ACG grown ZnO nanorods array. The average diameter of nanorods is in range of 100-200 nm.

PEDOT:PSS layer is used as an electrode and PFO is used for the light emission at blue – green range. White light in ZnO LED's is being produced by mixing blue – green -red light

from PFO layer and UV, blue and red light from ZnO nanorods (see fig. 2). The usage of PFO layer improves the intensity of light emission in visible range.

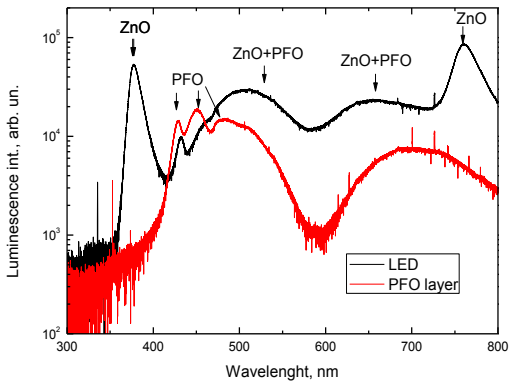

Fig. 2 Photoluminescence spectra of ZnO LED structure (black curve) and PFO layer (red curve). Excitation density is about 2 mW, CW, room temperature.

Room temperature electroluminescence spectra (not shown here) consist of three bands at 448, 469 and broad band at about 541 nm. Calculated colour rendering index (CRI) and correlated colour temperature of white ZnO LED's were calculated 68 and 5800 K [3].

In this work, a model of hybrid ZnO based white LED on flexible plastic substrate was demonstrated. The quality of white light is described by the CRI index of 68, which later can be improved by tuning spectral properties of LED.

[1] H. Morkoc, U. Ozgur, Zinc Oxide (Wiley VCH, Weinheim, 2009).
[2] B. Postels, H-H. Wehmann , A. Bakin , M. Kreye, D Fuhrmann, J. Blaesing , A. Hangleiter, A. Krost, A. Waag, Controlled low-temperature fabrication of ZnO nanopilars with a wet-chemical approach, Nanotechnology 18 195602 (2007).
[3] N. Bano, S. Zaman, A. Zainelabdin, S. Hussain, I. Hussain, O. Nur, M. Willander, ZnO-organic hybrid white light emitting diodes grown on flexible plastic using low temperature aqueous chemical method, J. of App.Phys., 108, 043103 (2010).

KERR MICROSCOPY: HOW TO SEE MAGNETIC DOMAINS?

B. Olbromska

AGH University of Science and Technology, Faculty of Physics and Applied Computer Science, Department of Solid State Physics, Krakow, Poland

basia.olbromska@gmail.com

Research done in some last decades shows an interesting property of very thin layers of some materials. It seems that for properly low thickness of the layer, materials exhibit behavior like a two - dimensional objects. It results a new features, phenomenon and subsequently novel application.

Materials, called Artificial Antiferromagnets (AAF), consist of films made with properly selected substances and with specified thickness [1]. AAF behave like natural antiferromagnets: elementary magnetic moments in material are antiparallel ordered. Moreover, thanks to careful selection of preparation parameters, such substances show new, important features: perpendicular magnetic anisotropy and interlayer exchange coupling. Both of them are really useful in magnetic recording information, especially in so-called *spin valves* [2].

Unfortunately, measurement of magnetic properties such films is extremely difficult, because of their low value: about 10^{14} μ_B. Magnetooptical Kerr Effect (MOKE) is one of the best method for thin films investigation [1]. It causes changes in polarization and intensity of light reflected from magnetic substance. It is possible to watch in real time, with rather simple equipment, changes in magnetization using *Kerr Microscopy*.

How make such MOKE measurement? How special AAF samples are prepared? Some experimental results and a little of theoretical base of phenomena will be presented.

[1] Grünberg P. A. & Pierce D. T., Multilayer: interlayer coupling, (Encyclopedia of Materials: Science and Technology, Elsevier Science, 2001)

[2] Wolf S. A. et al., Spintronics: A Spin-Based Electronics: vision for the Future, Science, vol. 294, no. 5546 (2001)

STIMULATED EMISSION IN HIGH-Al-CONTENT AlGaN QUANTUM WELLS

J. Jurkevičius, J. Mickevičius

[1] *Department of Semiconductor Physics, Faculty of Physics, Vilnius University, Saulėtekio Ave. 9-III, LT-10222 Vilnius, Lithuania*

getjonas@gmail.com

III-nitride wide bandgap semiconductors are essential in the creation of solid-state ultraviolet (UV) light sources and detectors. These devices are expected to have a wide application range in medicine diagnostics, therapy, detection of biological and chemical agents, water purification and data storage.[1]

UV lasers are based on AlGaN materials and decreasing the emission wavelength requires high-aluminum-content AlGaN layers in active region. Although recently AlGaN epitaxial layers have received much attention and investigative efforts, observation of stimulated emission has been complicated even under optical excitation and data on it is very scarce. Situation is even worse for high aluminum content AlGaN/AlGaN multiple quantum well (MQWs) structures. Also, the development of AlGaN-based UV laser faces technological growth problems, which cause low quality of layers and result in an increase of the threshold of stimulated emission or even in the vanishing of it.

In this report, we present the study of stimulated emission and its properties in AlGaN MQWs structures with different well width: the well width in different samples varied from 2.5 to 5.0 nm. Aluminum content in the wells and barriers was equal to 35 % and 49 %, respectively. The samples were investigated by photoluminescence (PL) spectroscopy; measurements were carried out in a wide temperature range of 20 – 300 K under various excitation power densities (0.2-10 MW/cm^2). Stimulated emission was measured in edge emission configuration.

We demonstrate stimulated emission threshold dependences on temperature for different samples. While stimulated emission threshold increases with temperature as expected, the threshold temperature dependence is somewhat different for structures with different quantum well width. Additionally, we show that the peak position of stimulated emission band does not exhibit obvious shift with increasing temperature, once spectra are shifted along *x* axis to compensate temperature dependence of bandgap (see Fig. 1). This behavior of stimulated emission may be explained by non-equilibrium carrier recombination from states localized near mobility edge.

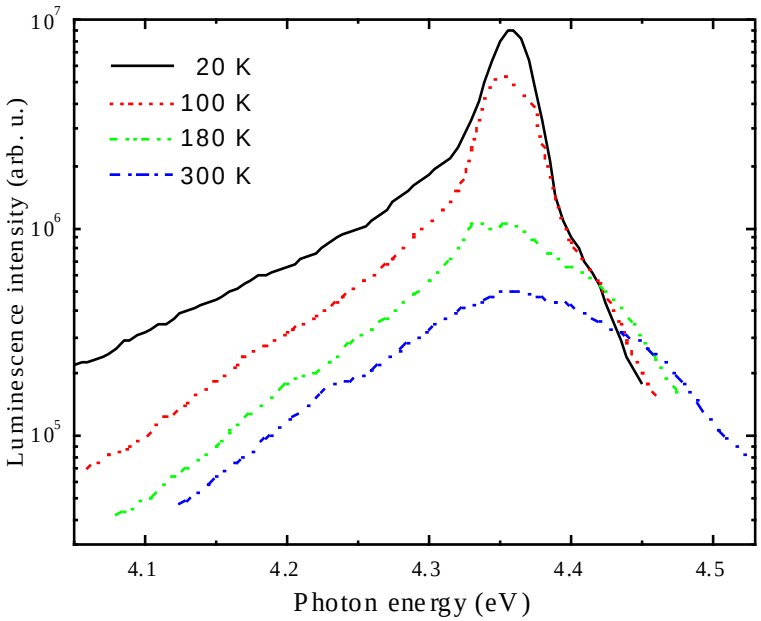

Fig. 1 PL spectra of AlGaN/AlGaN MQWs sample with 5 nm wide quantum well at different temperatures (indicated) under excitation power density of 6 MW/cm^2. The positions of spectra are shifted along *x*-axis by respective energy value to compensate temperature-dependent bandgap change, calculated form *Varshni* formula.

[1] S. Nakamura, S.F. Chichibu, Introduction to Nitride Semiconductor Blue Lasers and Light-Emitting Diode (CRC Press, London, 2000).

OPTICAL PROPERTIES OF MBE-GROWN ZnO/CdZnO EPITAXIAL LAYERS

M. Stasiūnas, M. Karaliūnas, E. Kuokštis

Department of Semiconductor Physics, Faculty of Physics, Vilnius University, Saulėtekio Ave. 9-III, LT-10222 Vilnius, Lithuania

marstas@gmail.com

Researches of epitaxial ZnO layers and ZnO-based ternary compounds, such as CdZnO are of increasing interest due to large exciton binding energy of around 60 meV in zinc oxide and recent technological achievements in fabrication of various ZnO-based structures [1]. The unique exciton features lead to efficient radiative transitions of excitonic nature for ZnO-based light emitting devices working at elevated temperatures. Temperature dependent photoluminescence (PL) spectra of the samples helps to determine the quality of epitaxial layers as well as to derive parameters that might help to describe the behavior of future devices based on these layers.

The PL of the four MBE-grown ZnO/CdZnO quantum structures samples were investigated using 10 mW continues-wave He-Cd laser with emission wavelenght of 325 nm as an excitation source. The temperature dependent PL spectra were measured utilizing the closed-circuit He cryostat, which allows the stabilization of the sample temperature in the range from 8 K to 300 K. Structures of all the samples are depicted in Fig. 1. Multi-layer sample structures resulted in more complex interpretation of observed PL peaks nature.

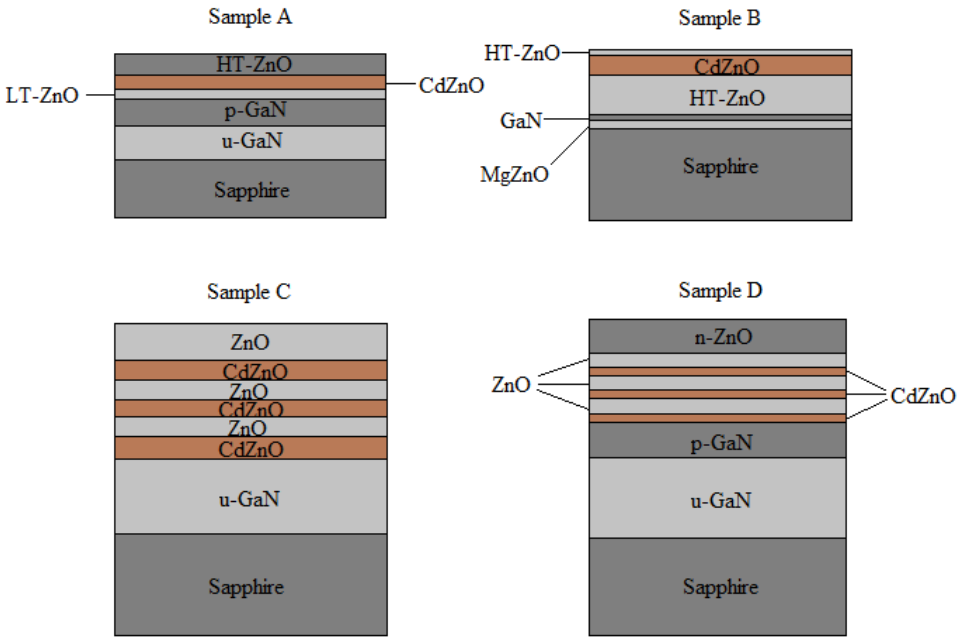

Fig. 1. Sample structures. HT marks layer, grown at high temperature, LT marks layer, grown at low temperature.

The dependences of the PL peak energies, which where all attributed to near-band-edge (NBE) emission, on temperature were fitted using empirical Varshni [Eq. (1)] and Bose-Einstein [Eq. (2)] relations [2]:

$$E_g(T) = E_g(0) - \frac{\alpha T^2}{T + \beta} \quad (1)$$

$$E_g(T) = E_g(0) - \frac{k}{\exp\left(\frac{\theta}{T}\right) - 1} \quad (2)$$

Fitting parameters α, β and θ where evaluated for both free exciton and bound exciton PL peaks of ZnO epilayers as well as CdZnO NBE emission peak.

Cd molar fraction in CdZnO epitaxial layers where estimated to be around 15%, 9%, 19% and 16% for samples A – D respectively.

PL intensity and full width at half maximum (FWHM) dependences on sample temperature were in good agreement with the ultraviolet ZnO PL peak being of excitonic nature. Large FWHM values for CdZnO epilayers of all the samples refers to worse crystalline quality whereas NBE PL peak is red-shifted with incorporation of Cd. Nevertheless, formation of muptiple quantum well structures (CdZnO well layers separated with ZnO barrier layers) helps to improve the efficiency of excitonic transitions by increasing their localization preventing carriers/excitons from nonradiative recombination.

[1] Hadis Morkoç, Ümit Özgür, Zinc Oxide, 1-7, 12 (2009)
[2] Z. Yang, L. Li, Z. Zuo, J. L. Liu, Journal of Crystal Growth 312, 68-70 (2009)

ORAL SESSION IV

Theoretical physics

THEORETICAL DESCRIPTION OF HYPERFINE STRUCTURE OF LASER-FIELD-DRESSED ATOMIC STATES

A. Cinins[1], V. Kascheyevs[2, 3]

[1] *Laser Centre, University of Latvia, LV-1002 Riga, Latvia*
[2] *Faculty of Physics and Math, University of Latvia, 8 Zellu street, Riga LV-1002, Latvia*
[3] *Laboratory of Theoretical Physics and Computer Simulations, Institute for Solid State Physics, University of Latvia, 8 Kengaraga street, Riga LV-1063, Latvia*
ac06014@lanet.lv

It is well known fact that a weak electromagnetic field can induce transitions between quantum states. The states are said to be coupled by external field. In presence of a strong electromagnetic field both coupled states are mixed together, forming two so called dressed states. Atomic states before mixing are therefore called bare states. The dressed states are split apart according to transition's Rabi frequency and external field's detuning from atomic transition resonance frequency [1]. Splitting of the dressed states is called Autler–Townes effect.

If atomic nucleus has a nonzero spin value, electronic states of the atom are split into hyperfine levels due to electron – nuclear spin interactions. Properties of hyperfine atomic levels at presence of strong external electromagnetic field are studied in our present work. An atomic system with both hyperfine and Autler–Townes effect present should be treated as a multilevel system, in which detuning of external field frequency may be different for every pair of coupled levels, therefore hyperfine structure of dressed states differs from hyperfine structure of bare atomic states. In my presentation theoretical aspects of the problem will be explained, and most recent results of theoretical calculations will be presented.

[1] H. R. Gray and C. R. Stroudr, Jr., Autler-Townes effect in double optical resonance, Opt. Comm. 25, 359-362 (1978).

EVANESCENT WAVES (OR HOW TO MAKE A LIGHT SWORD)

J. Zielinska

Faculty of Physics, University of Warsaw
jz276093@okwf.fuw.edu.pl

As it turns out, investigating such a well known phenomenon as the total internal reflection of the electromagnetic wave can still lead to interesting conclusions.

If we consider a plane wave, that undergoes total internal reflection on a flat border between two media, the first surprising fact that arises is that the reflected wave is shifted with respect to the incident wave on the border between the media (Goose–Hanchen shift). Moreover, in the second medium (that apparently should not be penetrated) appears the evanescent wave – an exponentially disappearing wave that carries no energy.

I will present the results of my attempts to tackle the following question:

What shape and spectrum of the incident wave do we have to use to obtain the thinnest and disappearing as slowly as possible evanescent wave?

In other words, my purpose is to manipulate the shape of an evanescent wave so as to make it look like a ‘light sword’.

It turns out that the desired shape cannot be achieved using only monochromatic light. If the beam with spectrum is considered, it can be done, but some interesting phenomena arise, since the shape of the evanescent wave in this situation depends on time.

RENORMALIZATION GROUP APPROACH TO ULTRACOLD IMBALANCED FERMI GAS

J. Armaitis, J.E. Baarsma, and H.T.C. Stoof

Institute for Theoretical Physics, Utrecht University, Leuvenlaan 4, NL-3584 CE Utrecht, The Netherlands

jogundas@gmail.com

Ultracold atomic gases are among the systems, where the quantum nature of particles is most pronounced. Moreover, ultracold gases are under great experimental control. Not only can they be cooled down to extremely low temperatures, but there is also precise control of the interaction strength. These features bring ultracold quantum gases to the prime focus of both experimental and theoretical physicists [1].

Fermi mixtures in the strongly interacting regime have been recently shown to possess a rich phase diagram both experimentally [2] and theoretically [3]. In addition to normal and superfluid phases, the mass-imbalanced case demonstrates a supersolid phase [3].

Supersolid is an exotic kind of superfluid, which shares the properties of both a solid and a superfluid. Even though the existence of the supersolid phase in the said system has been well established by mean-field calculations, which give qualitatively good results, the exact transition temperature is still to be computed. Determining the temperature of the phase transition is extremely important, since it will answer the question if the observation of the supersolid phase is experimentally plausible. Our group is tackling this problem by utilizing the renormalization-group, which is the tool of choice for calculations beyond mean-field calculations, such as needed for strongly interacting systems. Thus far, we have been able to obtain the exact chemical potential of an extremely spin-imbalanced Fermi gas with strong interactions at zero temperature. This result perfectly matches the experiment [4], as well as Monte Carlo calculations [5]. In the future, we plan to include screening effects due to density fluctuations and map out the full phase diagram.

[1] H.T.C. Stoof et al., Ultracold Quantum Fields (Springer, 2009).
[2] Y. Shin et al., Phase diagram of a two-component Fermi gas with resonant interactions, Nature 451, 689-693 (2008).
[3] J.E. Baarsma et al., Population and mass imbalance in atomic Fermi gases, Physical Review A 82, 013624 (2010).
[4] A. Schirotzek et al., Observation of Fermi Polarons in a Tunable Fermi Liquid of Ultracold Atoms, Physical Review Letters 102, 230402 (2009).
[5] C. Lobo et al., Normal State of a Polarized Fermi Gas at Unitarity, Physical Review Letters 97, 200403 (2006).

BLACK HOLES' ENTROPY

P. Kucharski

Faculty of Physics, University of Warsaw
pjkucharski@gmail.com

The famous equation

$$S = k \log W \tag{1}$$

invented by Ludwig Boltzmann is well known as a connection between macroscopic and microscopic world. Not until the discovery of quantum mechanics, had it turned out that a volume in a phase space was a number of microstates, that conserved the macroscopic quantities of the system.

Black holes have to have entropy, because once matter falls into them, the entropy of the rest of the Universe lowers. We are even able calculate that entropy, hoping that studying it will prove helpful in understanding the role of quantum microstates in the theory of gravity.

Thermodynamics of black holes seems extremely odd, because the only parameters we have are *M, Q, J*. Consequently, the entropy must expressed by nothing but mass, charge and angular momentum of the black hole. Furthermore, the formula looks very similar to the formula describing the area of the event horizon. We can obtain this formula from calculating action of the gravitational field, integrating not on the event horizon, but on the sphere of infinite radius. What does it really mean? Where are those microstates?

And what are they?

EXCITATION ENERGY TRANSFER AND QUENCHING IN THE PHOTOSYNTHETIC MAJOR LIGHT-HARVESTING COMPLEXES

J. Chmeliov[1,2], L. Valkunas[1,2], and G. Trinkunas[1,2]

[1] *Department of Theoretical Physics, Faculty of Physics, Vilnius University, Sauletekio Ave 9, build. 3, LT-10222 Vilnius, Lithuania*

[2] *Institute of Physics, Center for Physical Sciences and Technology, Savanoriu Ave 231, LT-02300 Vilnius, Lithuania*

jevgenij.chmeliov@ff.vu.lt

The life evolved on Earth strongly depends on the sunlight harvesting occurring in all photosynthetic organisms. In green plants the light reaction of photosynthesis is related to the photosystem II – the huge pigment–protein supercomplex located in the thylakoid membrane in the chloroplasts. Structurally it consists of the light-harvesting antenna, where the major part of the chlorophyll (Chl) molecules can be found, and the reaction centers, to which the excitation energy from the antenna is finally transfered, initiating the process of charge separation.

Another physiologically important process also related to the light-harvesting antenna is a very effective regulation of the amount of the absorbed light energy. At high light intensity not all the energy of the absorbed photons can be used in photochemical reactions, which can result in the production of the singlet oxygen – a very strong oxidant which can damage the whole photosynthetic unit. In order to avoid such a photodamage, plants have developed several protective mechanisms. One of them, acting on the molecular level and dissipating the excess energy as heat, is known as non-photochemical quenching (NPQ) and, as was recently shown in the time-resolved spectroscopy measurements [1], takes place in the major light-harvesting complexes (LHCII). It is commonly agreed that the increasing intensity of the sunlight causes some configurational changes within the LHCII which lead to the generation of additional excitation trapping centers (probably related to the carotinoid molecules) converting the excess excitation energy to heat. However, despite recent extensive studies in this field and several suggested models, a common consensus about the origin of the NPQ-traps has not been achieved so far.

Since experimentally observable excitation decay kinetics in the LHCII aggregates under NPQ conditions are mostly bi-exponential, there are 2 principle ways to qualitatively describe such results [2]. In the *'migration-limited'* case the excitation slowly migrates through the antenna until it reaches the NPQ-trap, and then quickly relaxes (the so-called slow/fast (SF) regime). In the converse *'trap-limited'* regime the excitation lifetime is dominated by the trapping in the NPQ-center, whereas the migration can be assumed to be relatively fast.

In order to determine the key parameters defining the excitation kinetics and thus to get an insight into the origin of the NPQ, in the present work the excitation energy transfer and quenching in LHCII aggregates was considered in terms of a coarse-grained model, in which

only the transfer of excitons between separate pigment–protein subunits is treated explicitly, with all intra-monomer kinetics 'integrated out' of the calculation (Fig. 1). Excitation dynamics in such a system can be calculated by solving the Pauli master equations [3]

$$\frac{\mathrm{d}p_i}{\mathrm{d}t} = \sum_{j \neq i} \left(k_{ij} p_j - k_{ji} p_i \right) - k_{\mathrm{dis}} p_i - \delta_{i,\mathrm{NPQ}} k_{\mathrm{NPQ}} p_i, \quad i, j = 1, ..., N, \tag{1}$$

where p_i is the time-dependent probability for the excitation to be found in the ith complex; k_{ij}, k_{dis} and k_{NPQ} stand for the rates of the transfer from the jth to the ith complexes, intrinsic dissipation processes or non-photochemical trapping, respectively.

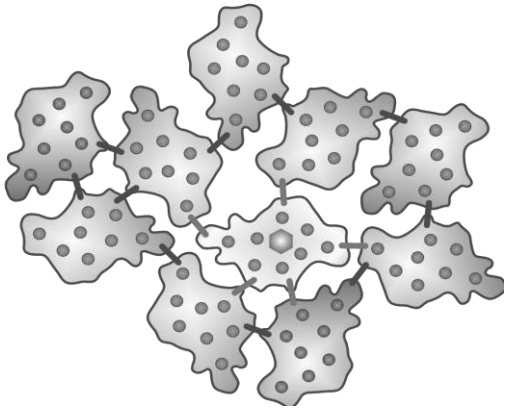

Fig. 1. Coarse-grained model for the LHCII aggregate with a NPQ-trap in one of LHCII monomers (represented by hexagon; circles stand for Chl molecules; thick bars depict possible excitation transfer paths between different LHCII monomers). While modelling, only excitation transfer between different LHCII is taken into account whereas their internal structure is neglected.

As follows from the calculations, this model can be well-fitted to the experimental kinetics assuming different values for the excitation hopping rate between different LHCII monomers. However, certain problems are encountered while assuming FS regime: the LHCII aggregate should be rather small, and excitation will be mainly localized on the NPQ-trap. Moreover, if considering NPQ excitation dynamics at higher excitation conditions when singlet–singlet annihilation starts to dominate, in the FS regime the excitation kinetics of the aggregate are almost insensitive to the initial excitation density. Conversely, the excitation kinetics in the SF regime display strong sensitivity to the changes in excitation density. Since the experimentally observed kinetics reveal a similar dependence, it can be concluded that the SF regime is a more appropriate description for the physical origin of the NPQ-trap: the excitation dynamics is mainly determined by the excitation migration within antenna, whereas the relaxation in the NPQ-center takes just several ps.

[1] N. E. Holt, D. Zigmantas, L. Valkunas et al., Carotenoid cation formation and the regulation of photosynthetic light harvesting, Science **307**, 433-436 (2005).

[2] M. G. Müller, P. Lambrev, M. Reus et al., Singlet energy dissipation in the photosystem II light-harvesting complex does not involve energy transfer to carotenoids, ChemPhysChem **11**, 1289-1296 (2010).

[3] L. Valkunas, G. Trinkunas, J. Chmeliov et al., Modeling of exciton quenching in photosystem II, Phys. Chem. Chem. Phys. **11**, 7576-7584 (2009).

STATISTICAL MODELLING OF CHARGE MOBILITY IN DISORDERED MOLECULAR LATTICES USING MONTE – CARLO METHOD

V. Abramavičius, D. Abramavičius

Department of Theoretical Physics, Faculty of Physics, Vilnius University, Saulėtekio Ave. 9-III, LT-10222 Vilnius, Lithuania

vytautas.ab@gmail.com

During the last few decades a broad class of organic molecular materials was investigated extensively both theoretically and experimentally. Nevertheless, a general theory explaining all essential electrical and optical phenomena in such materials has not yet been developed. For different temperatures, electric and magnetic field strengths, various phenomenological and semi-phenomenological models have been developed [2]. Difficulties arise from the great variety and complexity of internal structures of organic molecular materials and weak intermolecular forces between different molecules. The former property introduces anisotropy and the latter restricts in most cases the usage of one-electron approximation and thus the band model for description of electronic phenomena in organic molecular materials.

The aim of this work is to simulate the charge transfer in a disordered organic molecular material using the dispersive hopping model [2], [5], [6] and obtain charge mobility dependencies on electric field strength, temperature, energy disorder in a sample of finite dimensions. Furthermore, charge mobility dependency on the sample thickness is also to be investigated.

The following physical model of disordered organic molecular material is used for achieving the above-mentioned goals: a cubic three dimensional lattice constructed from stationary point-like nodes. Disorder of material is included by assigning random energies from Gaussian distribution to every node in addition to potential energy from electric field $\boldsymbol{F}$ applied across the sample as shown in Fig. 1.

Charge transfer is simulated by letting a single charge to hop from one site to a neighbouring site in the lattice with applied electric field. Hopping rates are calculated using Miller – Abrahams equation:

$$\nu_{\mathrm{nm}} = \nu_0 \exp\left(-2\gamma a \frac{R_{\mathrm{nm}}}{a}\right) \begin{cases} \exp\left(-\dfrac{(E_{\mathrm{m}} - E_{\mathrm{n}})}{k_{\mathrm{B}}T}\right) & E_{\mathrm{m}} > E_{\mathrm{n}} \\ 1 & E_{\mathrm{m}} < E_{\mathrm{n}} \end{cases}, \qquad (1)$$

where E_n and E_m are the energies of nodes n and m respectively, R_{nm} – distance between nodes n and m, γ – electronic wave function overlap factor, ν_0 – frequency prefactor, a – lattice constant.

These rates are renormalized into probabilities of charge hops. Knowing the thickness of the sample *d* and finding the time *t* needed for a charge to cross the sample one can derive charge mobility from the equation relating it with the electric field strength *F* and charge drift velocity $v = \frac{d}{t}$:

$$\mu = \frac{d}{tF}. \tag{2}$$

This simulation is repeated many times and the average mobility is calculated for different disorder realizations.

We observe strong dependence of mobility on the sample thickness.

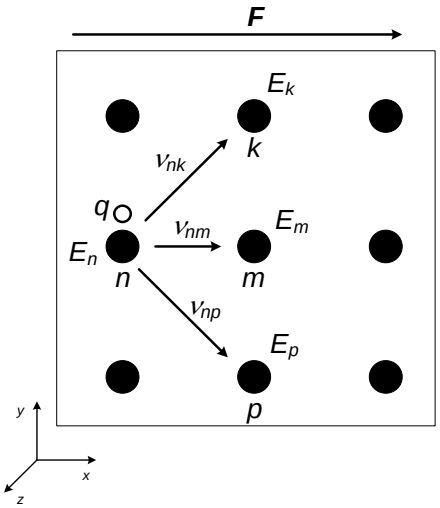

Fig. 1. Illustration of physical model of disordered organic molecular material.

[1] Э. А. Силинш, М. В. Курик, В. Чапек, Электронные процессы в органических молекулярных кристаллах: Явления локализации и поляризации. (Зинатне, Рига, 1988).

[2] M. Pope, Ch. E. Swenberg, Electronic processes in organic crystals and polymers – 2nd ed., (Oxford University Press, New York, Oxford, 1999).

[3] S. Juršėnas, Organiniai puslaidininkiai (Vilniaus universitetas, Vilnius, 2008).

[4] W. H. Press, S. A. Teukolsky, W. T. Vetterling, B. P. Flannery, Numerical Recipes. The Art of Scientific Computing – 3rd ed. (Cambridge University Press, Cambridge, New York, Melbourne, Madrid, Cape Town, Singapore, Sao Paulo, 2007).

[5] V. Coropceanu, J. Cornil, D. A. da Silva Filho, Y. Olivier, R. Silbey, J. L. Bredas, Charge Transport in Organic Semiconductors, Chem. Rev. 107, 926-952 (2007).

[6] D. Abramavičius, V. Gulbinas, A. Ruseckas, A. Undzėnas, L. Valkūnas, Geminate charge pair recombination in sensitized photoconducting polymer, Journal of Chemical Physics, Volume 111, Number 12, (1999).

ANALYSIS OF EXPERIMENTAL, ANALYTICAL AND NUMERICAL MODELS OF PARALLEL PATH MAGNETIC TECHNOLOGY

I. Dirba[1], G. Arents[2]

[1] *Institute of Solid state Physics of University of Latvia*
[2] *Riga Technical University*
imants.dirba@gmail.com

Nowadays electric motors are used everywhere: at home, on the street, at work. Although electricity has been known for more than 2000 years and an electric motor at least 200 years, their construction and materials are being improved continuously. Parallel Path Magnetic Technology (PPMT) is an advanced magnetic force control technology that is applicable to motors, rotary actuators, linear actuators, and generators. PPMT uses two or more permanent magnets positioned in parallel [1]. The basic magnetic circuit consists of a flux steering coil on each flux path. If there is no current in the coils, the magnetic circuit then acts as if the coils does not exist (Figure 1). However if current flows in the flux steering coils to produce a magnetic polarity, the magnetic flux produced by the coils couples with the permanent magnet's flux and the result is four units of force at one pole of the device (four units, not two, is due to the squared force law of the combined permanent magnet flux).

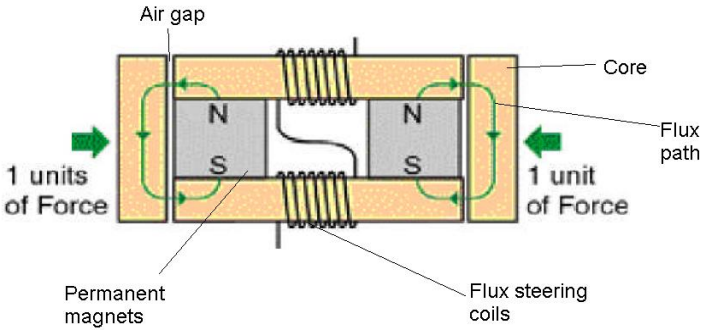

Fig. 1. Basic PPMT actuator (flux steering coils off).

In our work the design for PPMT device is performed using finite- element (FE) analysis. This model is based on reduction of 3D problem to 2D problem which is considered as accurate for design aspects. In our research we describe theoretical, numerical and experimental model of PPMT device. Air gap magnetic flux density, field lines, vectors, saturation, magnetic force of the PPMT device are simulated using FEMM 4.2 software (Figure 2).

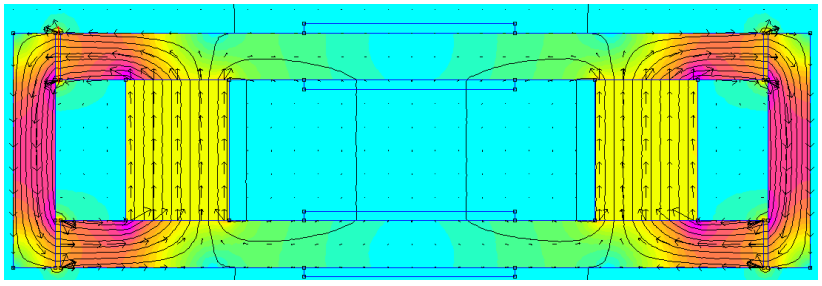

Fig. 2. Calculated magnetic field density, fieldlines and vectors.

Approximate theoretical analysis was made for assessment of air gap magnetic field density using Circulation Theorem of magnetic field and Biot – Savart law. Magnetic force was calculated using Maxwell's stress tensor (Eq. (1)).

$$T_{ik} = \varepsilon_0 E_i E_k + \frac{1}{\mu_0} B_i B_k - \frac{\delta_{ik}}{2}\left(\varepsilon_0 \vec{E}^2 + \frac{1}{\mu_0} \vec{B}^2 \right), [N/m^2] \quad (1)$$

An experimental model of basic PPMT actuator is manufactured and tested in dynamo - bench. Obtained experimental results are compared with output from analytical and numerical models.

[1] C.J. Flynn, N.B. Talsoe, J.J. Childress, Parallel Path Magnetic Technology for High Efficiency Power Generators and Motor Drives. SPACE TECH.& APPLIC.INT.FORUM-STAIF 2006: 3rd Symp on New Frontiers & Future Concepts. AIP Conference Proceedings, University of New Mexico, February 13, 2006; Volume 813, pp. 1205-1212.

ORAL SESSION V

Interdisciplinary

APPLICATIONS OF INFRARED MICROSPECTROSCOPY FOR PREVENTION OF URINARY STONES

M. Pučetaitė, J. Čeponkus, and V. Šablinskas

Department of General Physics and Spectroscopy, Faculty of Physics, Vilnius University, Saulėtekio Ave. 9-III, LT-10222 Vilnius, Lithuania

milda.pucetaite@ff.stud.vu.lt

Kidney stone disease which causes the formation of urinary stones is very common. However, the formation factors and processes are still not properly understood. Structural and morphological analysis of urinary stones enables to determine the underlying causes of the disease prescribe treatment and prevent recurrences.

The quantitative and qualitative analysis of urinary calculi is challenging due to their usually small size, fragility and heterogeneous composition. In this work we used two spectroscopical techniques. (I) Fourier transform infrared spectroscopy (FTIR) combined with KBr (potassium bromide) pellet technique allowed us to elucidate chemical composition of the stones. 106 urinary stones received from Vilnius university hospital *Satariskiu klinikos* have been studied in this work. As it can be seen in figure 1, the most abundant components are calcium oxalate and phosphates – apatite and brushite.

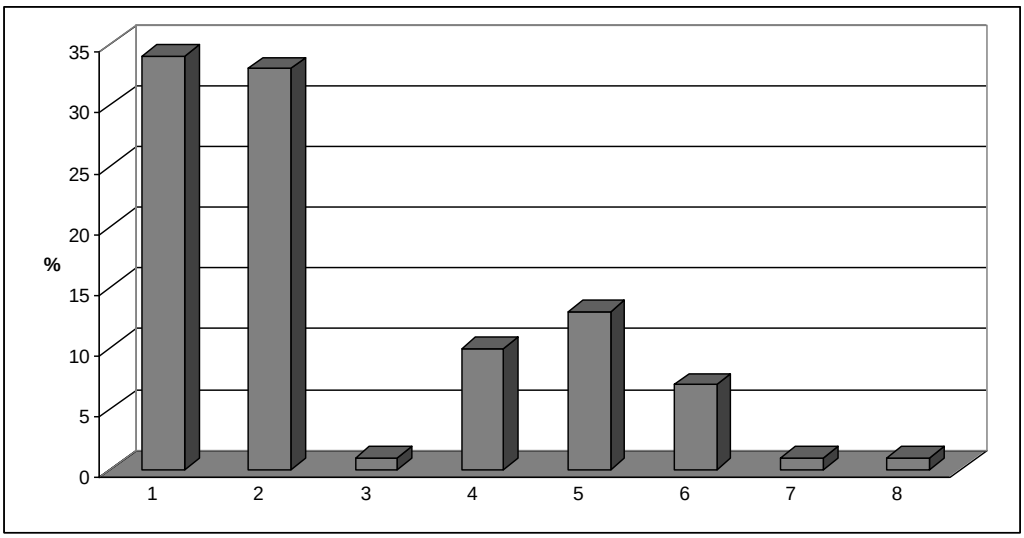

Fig. 1. Composition of urinary stones: 1-calcium oxalate (CaOx)+apatite, 2-CaOx+brushite, 3-pure uric acid (UA), 4-CaOx+UA, 5-three component stones (including struvite), 6-pure $CaHPO_4*H_2O$, 7-pure CaOx, 8-CaOx+ $CaHPO_4*H_2O$

(II) Infrared microspectoscopic surface reflectance imaging allowed us to analyse morphology of the cross-sectioned stones [1]. Integral intensities of the *restrahlen* bands obtained in the specular reflection spectra are directly proportional to the concentration of particular chemical component in the stone (Fig. 2). Distribution of the components in the stones is determined by processes of formation of the stones. In this work, we have experimentally confirmed that stones can be formed in at least two ways: (I) loose stone grows in the urinary

system from oversaturated salt solution without fixation to the walls of the system, (II) the stone formation is initiated on the walls. In this case the grow starts with formation of calcium phosphate crystal on the wall of the system. Later, this crystal is being covered by calcium oxalate.

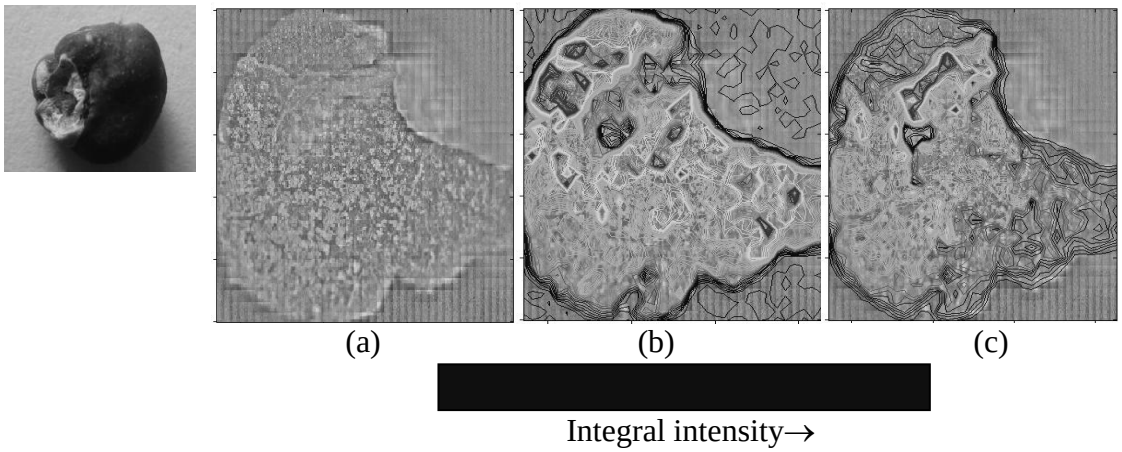

Fig.2. Optical (a) and false-color infrared images of the stone constituted from calcium oxalate (b) and brushite (c). Integral intensities of ν_{as}(C-O) band at 1318 cm^{-1} for calcium oxalate and ν_{as}(P=O) at 1120 cm^{-1} for brushite are used for the false-color images. Dark grey color represents areas with high concentration of the chemical component and light grey color – areas with low concentration or absence of the corresponding component.

[1] J. C. Anderson et al, Analysis of urinary calculi using an infrared microspectroscopic surface reflectance imaging technique, Urol.Res. 35 (2007) 41-48

HYDROCARBONS REFORMING BY PLASMA WITH CONTROLLED H_2/CO RATIOS OF SYNGAS

Ol. Solomenko, V. Chernyak, and O. Nedybaliuk

Kyiv National Taras Shevchenko University, Faculty of Radiophysics, Department of Physical Electronics, Kyiv, Ukraine

elanka@ukr.net

Technologies with using syngas are very relevant today. Synthesis gas (or "syngas"), is a mixture of carbon monoxide and hydrogen, it is an important intermediate for various synthesizing chemicals and environmentally clean fuels, such as ammonia, methanol (MeOH), acetic acid, methyl formate, dimethyl ether (DME), synthetic gasoline, and diesel [1] or nanomaterials. Generally, it is required for various H_2/CO ratios of syngas to synthesize different products. For example, H_2/CO ratio of 2/1 is needed to synthesize methanol, and 1/1 one to synthesize acetic acid or methyl formate. Also, it is known, that the addition of syngas to fuels improves the efficiency of its combustion: less time, triggering the rapid spread of the combustion wave, the stabilization of combustion, more complete combustion of the mixture and decreases the amount of hazardous emissions (NO_x).

Synthesis gas can be produced from coal, petroleum coke, natural gas, biomass and even from organic wastes. The most promising is obtaining syngas from renewable hydrocarbon sources nowadays. Various types of discharges for reforming syngas: corona discharge, dielectric barrier discharge (DBD), microwave discharge, atmospheric pressure glow discharge (APGD), gliding arc discharge extensively studied. Of particular interest in reforming of liquid hydrocarbons constitute discharge that does not require an additional gasification, such as tornado discharge with liquid electrode (TD LE) [2].

Adding CO_2 in the reforming system for change and management H_2/CO ratios of syngas is the standard approach. CO_2 was used as a working gas, distillate and ethanol – as a working liquid in this work. The gas flow was changing in range of 110-220 cm^3. The discharge current was changing in the range 260-340 mA. Adding NaOH to the working liquid leads to the stabilization of the discharge. The sign of the differential resistance become negative in these conditions. Emission spectra of the plasma between the electrodes were investigated. Emission spectra of investigated plasma are multicomponent and contain intensive OH bands, C_2 bands, atomic lines O, H, C, Na. It was found that electronic temperature T^*_e (T^*_e ~ 3800 K, T^*_r ~ 4000 K, T^*_v ~ 4500 K), vibration T^*_v and rotation T^*_r temperatures is constant.

[1] Xumei Tao, Meigui Bai, Xiang Li, Huali Long, Shuyong Shang, Yongxiang Yin, Xiaoyan Dai, CH4-CO2 reforming by plasma – challenges and opportunities, Progressin Energy and Combustion Science XXX. (2010).

[2] O.A. Nedybaliuk, V.Ya. Chernyak, S.V. Olszewski, Plasma-liquid system with reverse vortex flow of “tornado” type (Tornado-LE), Problems of atomic science and technology, № 6. Series: Plasma Physics (16), p. 135-137. (2010).

FLUORESCENCE SPECTROSCOPY OF POLYSILANES CONFINED IN DIFFERENT SIO_2 AND TIO_2 NANOSTRUCTURES

D. Peckus[1], N. Ostapenko[2], P. Vodolazkyy[2], V. Moiseenko[3], S. Suto[4], A. Watanabe[4], and V. Gulbinas[1]

[1] *Center for Physical Sciences and Technology, A. Goštauto 11, LT-02300 Vilnius, Lithuania*
[2] *Institute of Physics of NASU, pr. Nauki 46, Kiev 03028, Ukraine*
[3] *Dnipropetrovsk National University, Prospect Gagarina 72, Dnipropetrovsk 49050, Ukraine*
[4] *Tohoku University, 980-8578 Sendai, Japan*
domantas@ar.fi.lt

Potential application of nanosize polymers in different technologies such is transport and luminescent layers in electroluminescent diodes, sensors, and photoresistors stimulates investigation of their optical and electrical properties. Recently the possibility to manipulate properties of nanosize polysilanes by incorporating them in mesoporous silica has been demonstrated. It was shown that we can control the number of embedding polymer chains, their conformation and orientation, and their optical properties by simply changing diameter of nanopores. These investigations revealed new polymer conformational states with different degree of disordering, which are not present in polymer solutions and solid films [1, 2].

In this work four novel composite films based on photoconducting silicon-organic polymer poly(di-n-hexylsilane)-PDHS incorporated into different SiO_2 and TiO_2 nanostructures, namely in nanoporous SiO_2 and TiO_2 films, silica photonic crystals and silica gel, have been fabricated. Photoelectronic properties of these composites have been studied using photoluminescence (FL), absorption, FL excitation spectra as well as FL decay measurements in the wide temperature range (5-330) K. The analysis of the FL spectra of the composites shows three different polymer conformations coexisting inside a pore: gauche-, trans- conformation and aggregates. The aggregate fluorescence intensity in photonic crystal and in silica gel gradually decreases by increasing temperature, while in porous SiO_2 and TiO_2 films the temperature dependences are more complex: the fluorescence intensity gradually decreases by increasing temperature below trans-gauche transition, while at higher temperatures it increases until 310 K, when aggregates are thermally destroyed (Fig. 1).

Fig.1. Temperature dependence of FL spectra of: a) PDHS/SiO_2 porous film; b) PDHS/TiO_2 porous film. λ_{ex}= 280 nm.

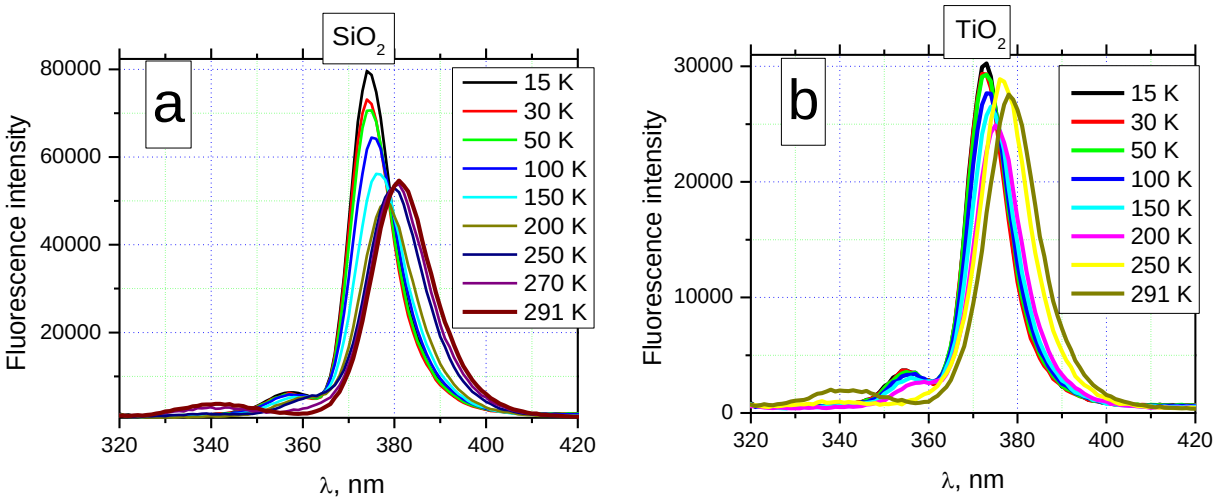

Fig.1. Temperature dependence of FL spectra of: a) PDHS/SiO_2 porous film; b) PDHS/TiO_2 porous film. λ_{ex}= 280 nm.

[1] A. Dementjev, V. Gulbinas, L. Valkunas, N. Ostapenko, S. Suto and W. Watanabe, J. Phys. Chem. 111 (2007), 4714-4721.

[2] K. Kazlauskas, A. Dementjev, V. Gulbinas, L. Valkunas, P. Vitta, A. Zukauskas, N. Ostapenko and S. Suto, Chem. Phys. Lett. 465 (2008) 261-264.

ELECTRICAL POWER SYSTEM OF THE ESTCUBE-1 SATELLITE

M. Pelakauskas, M. Noorma

University of Tartu, Faculty of Science and Technology, Tähe 4-111, 51010, Tartu, Estonia
martynas@ut.ee

ESTCube-1, the first Estonian student satellite (www.estcube.eu), is a student project which is aiming to create, build and launch a CubeSat specification satellite. The satellite's primary mission will be to test the concept of the electric solar sail (www.electric-sailing.com) in space for the first time. The novel electric propulsion technology based on the interaction of charged particles with a microscopic tether will be tested together with partners from the Finnish Metrological Institute (FMI), Jyväskylä University and Helsinki University (all from Finland), and the German Space Agency (DLR).

The Electrical Power System (EPS) subsystem of the satellite is responsible for generating, storing and distributing the electrical power to other subsystems of the satellite. For other tasks, it is also responsible for the initial startup of the satellite, beacon control, watching over other subsystems and power consumption monitoring and control. Its correct and reliable operation is critical to the success of the whole mission.

The projected power production of the solar cells is to be at around 2 W with an estimated efficiency of around 75 % at the 3,3 V, 5 V and 12 V output rails. Several designs with and without an additional battery charging and discharging control step are being tested for best efficiency and robustness.

Battery choice is also being investigated very thoroughly. 4 different off-the-shelf batteries from different manufacturers are being tested for best space-readiness. The tests involve various current tests at various temperatures, cycling, vacuum and vibration tests and radiation resistance testing.

EXPERIMENTS ON LIQUID METAL FLOW INDUCED BY A ROTATING MAGNETIC DIPOLE

T. Beinerts, A. Bojarevičs, and Y. Gelfgat

Institute of Physics of University of Latvia

toms.beinerts@gmail.com

Permanent magnet (PM) rotors are very successfully used for pumping and stirring of liquid metals [1] due to fact that they are non-invasive and do not loose energy in windings as it is in 3-phase inductors classically used for such tasks. Though in practice PM systems are being used only in metals that are relatively cool like Li, Na, Hg or some eutectics like In-Ga-Sn due to fact that PM produce relatively high fields only at small distances, but hot-liquid metals like Iron or Aluminium requires significant thermal isolation layer and therefore magnets can be put only at significant distance from metal making them ineffective. So there was set task to optimize PM configuration to achieve higher fields at further distances. Considering the optimization task regarding the most efficient stirring and/or pumping efficiency it was proposed that, if the distance of the liquid metal region from the surface of the magnetic rotor is not very small, a single cylindrical permanent magnet may turn out the best option [2] in respect to traditionally used multipolar designs (Fig.1.).

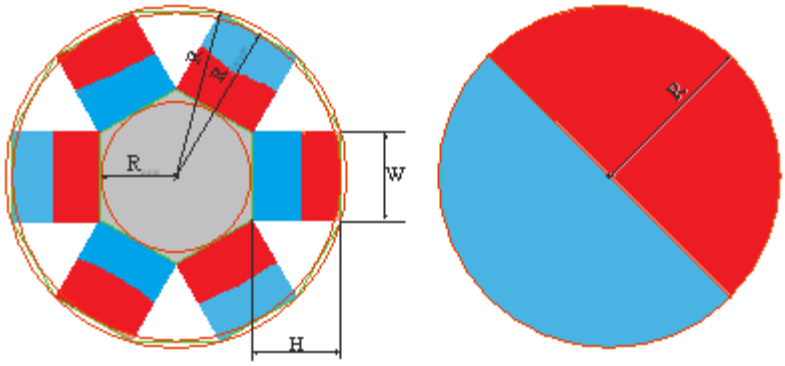

Fig. 1. Magnetic rotor with arbitrary number of magnetic pole pairs N (left) and a single magnetic dipole cylinder (right).

Rotating magnetic cylinder produces alternating magnetic flux in the surrounding space and induces vortical electrical field. Induced current in conducting media, interacting with the magnetic field, results in electromagnetic force proportional to a square of magnetic field induction and first order of the frequency. It is obvious that a single cylindrical PM, a magnetic dipole, would produce maximum of induction comparing to any other rotor with higher number of magnetic poles. Therefore a small scale model was built to test experimentally the feasibility of such a stirrer for practical tasks of metallurgy.

Modern rare-earth permanent magnets tend to ideal when magnetization is nearly uniform all over the volume and relative magnetic permeability is nearing 1. Therefore, two dimensional

magnetic field of a cylindrical magnet with remanence B_r transverse to the axis of a cylinder, and radial extent $R >> W$ (W - axial length of the magnet) at a distance L from the axis of the magnet may be given by a simple expressions (1) in polar coordinates

$$B_{rad} = \frac{B_r}{2} \cdot \left(\frac{R}{L}\right)^2 \cdot \cos(\omega \cdot t)$$
$$B_{\varphi} = \frac{B_r}{2} \cdot \left(\frac{R}{L}\right)^2 \cdot \sin(\omega \cdot t) \qquad (1)$$

These simple expressions allowed us to calculate also analytically output parameters of such system. As these results were close to ones obtained experimentally, it was possible also to compare results with multipolar rotors and calculate if similar systems could be used in real metallurgical applications.

After first experimental tests it seems that a cylindrical magnetic dipole rotor may be a promising option to consider for practical tasks in metallurgy for stirring or even transporting molten metal, moreover when high temperature and/or erosive action of the melt require thick refractory wall thickness of the melt containing enclosure. There were also proposed more complex systems with two, three and more rotating PM cylinders in series coupled magnetically or mechanically which gives possibility to create more powerful systems and systems that create completely different flow patterns, which are more perspective rather for stirring than metal transport.

[1] Bucenieks I.: Perspectives of increasing efficiency and productivity of electromagnetic induction pumps… 14th international conference on nuclear engineering, Miami, Florida, USA, July 17-20, 2006.
[2] Bojarevics A., Bucenieks I., Gelfgat Yu.: Flow at the Liquid Metal Surface Subject to Rotating Magnetic Field. PAMIR 2008, pp.273-275.

MICROSTRUCTURE AND MAGNETOTRANSPORT PROPERTIES OF GRANULAR NANOCOMPOSITE FILMS FeCoZr-Al_2O_3 AND IT'S APPLICATION FOR SPINTRONICS

A. Maximenko[1], J. Fedotova[1], J. Kasiuk[1], I. Svito[2], and V. Bayev[1]

[1] *NC PHEP Belarusian State University, 53 M.Bogdanovich str., 220040 Minsk, Belarus*
[2] *Belarusian State University, 4 Nezavisimosti str., 220030 Minsk, Belarus*
alexeymaximenko@gmail.com

Granular metal-dielectric nanocomposites have become quite attractive materials to develop spintronic devices (magnetic sensors, high frequency nano-oscillators, spintronic transistors, magnetic storage devices etc.) because of their unusual physical properties. The advantage of such nanocomposite materials that contain soft ferromagnetic nanogranules coated with dielectric matrix is related to the appropriate properties combination, such as high saturation magnetization M_S (≈ 200 emu/g), low coercive force *Hc* (less than 100 Oe), high electrical resistivity ρ and high negative magnetoresistance ($MR=\Delta\rho/\rho=(\rho(H)-\rho_0)/\rho_0$~5 %). It has been shown experimentally that physical properties of granular films depend on chemical composition of nanogranules and matrix, the shape and size of nanogranules, their structural order and possible surface oxidation, thickness of insulator layers and state of the interface between nanogranules and matrix. In this work we present a study of the magnetic and magnetotransport properties of granular $(FeCoZr)_x(Al_2O_3)_{1-x}$ **(**35 at. % ≤ *x* ≤ 64 at. %) thin films with respect to their structure. Two kinds of samples were synthesized by ion-beam sputtering in pure Ar (Ar series) or mixed Ar + O_2 (Ar + O_2 series) atmosphere. The electron transport in such nanocomposites proceeds by intergranular tunneling when the concentration of metallic granules is below the percolation threshold (~ 52% for films of Ar series). Granular fims of Ar+O series do not reveal percolation (formation of metallic current-conductive cluster) even at metallic contribution as high as 64 %.

Complementary study of the magnetic structure characteristic of $(FeCoZr)_x(Al_2O_3)_{100-x}$ covering different concentrations of metallic phase was performed using combination of atomic-force (AFM)-magnetic force microscopy (MFM) method. MFM topography images of the films of Ar and Ar+O_2 series with three studied compositions $(FeCoZr)_{33}(Al_2O_3)_{67}$, $(FeCoZr)_{45}(Al_2O_3)_{55}$ and $(FeCoZr)_{64}(Al_2O_3)_{36}$ differ greatly. For the films of Ar series MFM study of x=33 at.% composition showed no magnetic interactions between the isolated nanoparticles, for x=45 at.% the labyrinth-like structure of ferromagnetically interacting nanoparticles and for x=36 at.% it was shown the stripe-like structure that confirmed the formation of magnetically ordered net of the metallic granules. The study of MFM images of Ar +O_2 films series showed no evidence to ferromagnetic interaction between nanoganules and that proves the oxidation of FeCoZr nanoparticles during the fabrication of nanocomposite films.

This conclusion is strongly confirmed with direct observation of metallic core-oxide shell structure with transmision electron microscopy. The same should be deduced basing on the field dependencies of magnetization M(H) as a function of temperature (50-300 K) for three studied compositions from Ar series (x=42,47,50 at.%) and Ar +O_2 series (x=35, 55, 59 at.%). For all studied compositions of Ar +O_2 series FeCoZr granules should rather be considered as non-interacting and superparamagnetic (SP). This is evidenced from their unsaturated state as at T = 300 K as at quite low temperature (50 K) and from close to zero coercive force. For Ar series M(H) of film $(FeCoZr)_{42}(Al_2O_3)_{58}$ at T = 300 K showed no ferromagnetic interaction between matellic nanogranules that should be assigned to their SP state. Granular films of $(FeCoZr)_{47}(Al_2O_3)_{53}$ composition revealed similar M(H) behavior, while $(FeCoZr)_{50}(Al_2O_3)_{50}$ film evidenced partial magnetic interaction between FeCoZr granules. The magnetization curves of nanoparticles in SP state can be analyzed within the framework of the Langeven theory of paramagnetism. For nanogranules of Ar + O_2 series and neglecting their metal core-oxide shell structure their medium diameters <D> could be roughly estimated by of Langevin approximation of M(H) curves as 2,9 nm for the composition x=36 at.%, 5,6 nm for x=55 at.%, 6,2 nm for x=61 at.%. For granular films of Ar series the same tendency of <D> growth with metal concentration has been observed, particularly <D>=6,2 nm for x=42 at.%, <D>=11,4 nm for x=47 at.%. This tendency in a good agreement with MFM data that detected the increasing of magnetic contribution with metal concentration growth in studied films.

MR of nanocomposite films from both Ar and Ar+O_2 series were investigated with different FeCoZr concentration (x=42,47,50 at.% for Ar series) and (x=35, 55, 61 at.% for Ar+O_2). Concentration dependency of MR at $H_{max} \approx 3$ kOe revealed twice higher effect for oxidized film as compared to non-oxidized one. It should to mention that oxidized films have much higher magnetic sensitivity S (S is equal to variation of MR when magnetic field H is changed on 10 kOe) and much higher resistivity. Obtained absolute values of negative MR effect at higher magnetic field ($H_{max} \approx 80$ kOe), values of resistivity and magnetic sensitivity for oxidized and non-oxidized granular films as a function of metallic contribution are summarized in the Table 1. This evidences that incorporation of chemically active impurities like oxygen during preparation procedure of the FeCoZr-Al_2O_3 has a great approach for tuning it's magnetic and magnetotransport properties.

Table 1

Composition, x % Non-oxidized	**MR,%**	**ρ, mOhm·m**	**S, 1/Oe**	**Composition, x % Oxidized**	**MR,%**	**ρ, mOhm·m**	**S, 1/Oe**
42	3	1,20	2,4	35	5,5	540	1,3
47	0,8	0,16	0,5	55	6,3	3,16	4,2
50	0, 5	0,08	0,2	61	5,4	4,6	3,2

DEVELOPMENT OF ESTONIAN "NUCLEAR ENERGETICS AND NUCLEAR SAFETY" MASTER'S PROGRAM

A. H. Tkaczyk

University of Tartu, Institute of Physics, Tähe 4-105, Tartu 51010, Estonia

alan@ut.ee

In 2009 Estonia approved the National Development Plan for the Energy Sector, including the nuclear energy option. This can be realized by construction of a nuclear power plant (NPP) in Estonia or by participation in neighboring nuclear projects (e.g., Lithuania and/or Finland). Either option requires the availability of competent personnel. It is necessary to prepare specialists with expertise in all aspects related to nuclear infrastructure and to meet workforce needs (e.g. energy enterprises, public agencies, municipalities). Estonia's leading institutions of higher education and research with the support of the European Social Fund have announced in this context a new nuclear master's curriculum to be launched in September 2011. The language of instruction will be English.

Since April 2009 a committee at the University of Tartu (UT) has been working with partners at Tallinn University of Technology (TUT) to develop and introduce the completely new joint master's program "Nuclear Energetics and Nuclear Safety." The committee members include: Alan H. Tkaczyk, Arvo Kikas, Enn Realo, Marco Kirm, Madis Kiisk, Kadri Isakar, Siiri Suursoo, Rein Koch, Eduard Feldbach, Aleksandr Lushchik, and Kaido Reivelt. This new degree curriculum complies with the European Atomic Energy Community (EURATOM) treaty and takes into account International Atomic Energy Agency (IAEA) and European Nuclear Education Network (ENEN) recommendations. It is based on consultations with the premier Estonian energy company Eesti Energia, the Environmental Board Radiation Department, and international scientific contacts.

The curriculum consists of the following modules:

1) General subjects module which provides students the basic knowledge on nuclear physics and technology.

2) Nuclear energetics module providing a theoretical and applied fundamental knowledge of nuclear fuel cycle. This module includes hands-on nuclear reactor training.

3) Nuclear safety module which handles nuclear and radiation safety, including radiological assessment.

4) Electives for quality management, economics, measurements, reactor dynamics and practical experience.

5) Free electives to broaden horizons or complement specialized knowledge according to needs and interests.

6) Master's seminar including literature reviews, oral presentations, and excursions.

7) Master's thesis, which develops knowledge and skills related to independent research in the specialty.

Fig. 1. Promotional flyer for the new curriculum.

Upon completion of the curriculum the graduate is expected to have systematic knowledge of the physical and chemical basis of nuclear energetics and the technologies used in nuclear power plants; has acquired an overview of the management of nuclear safety and emergency preparedness; understands nuclear safety assessment methods, international nuclear regulatory requirements on construction, operation, monitoring and control; understands nuclear safety culture and safety requirements; is able to assess risks associated with nuclear energetics; has expertise in measuring ionizing radiations and doses, analyzing measurement results, and assessing radiological impacts; is able to participate and defend his/her scientific views in discussions related to the profession, and communicate with both specialists and non-specialists; is competent to be employed in the nuclear field, or to pursue doctoral studies. Students from all countries are encouraged to apply to the program at the website www.ut.ee/nuclear and there are some scholarships available.

POSTER PRESENTATIONS

FORSTER RESONANT ENERGY TRANSFER FROM TWO-PHOTONS EXCITED QUANTUM DOTS TO CHLORIN e_6

G. Dauderis[1], A. Skripka[2], J. Valančiūnaitė[2], S. Bagdonas[1], and R. Rotomskis[1, 2]

[1] *Department of Quantum Electronics, Faculty of Physics, Vilnius University, Saulėtekio Ave. 9-III, LT-10222 Vilnius, Lithuania*

[2] *Institute of Oncology, Vilnius University, Baublio 3[B], LT-08408 Vilnius, Lithuania*

Artiom.Skripka@ff.stud.vu.lt

Semiconductor quantum dots (QDs) are intensively studied for different applications. Size-dependant photoluminescence (PL) spectra, broad and intensive absorption spectra, high photostability and flexible surface modification make QDs attractive as energy donors for different biological fluorophores [1], including porphyrin-type molecules [2]. Porphyrins are typical light activated drugs for the photodynamic therapy of cancer (PDT) with the high singlet oxygen quantum yield and preferential accumulation in tumour. However, the small two-photon (TP) action cross section limits their application in TP-PDT. This problem can be solved by using QDs as energy donors to activate the porphyrin sensitizers.

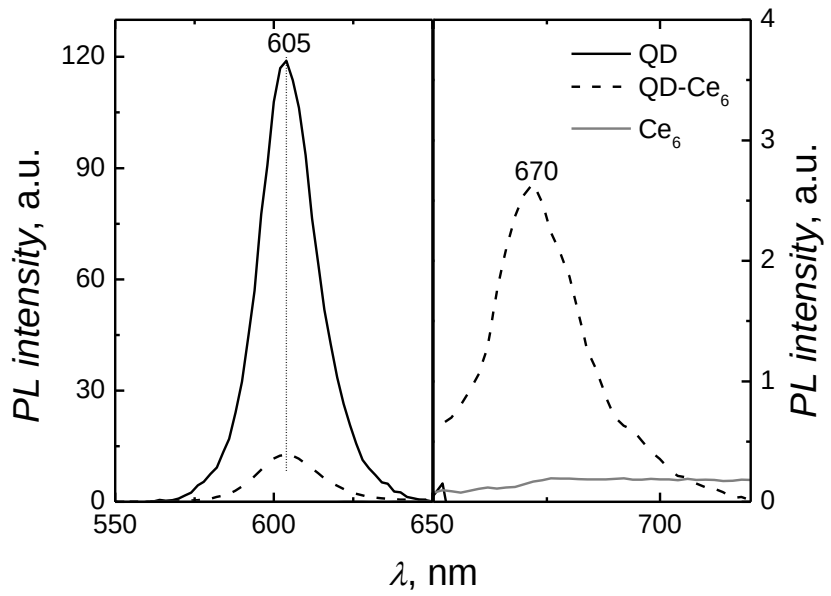

Fig 1. The photoluminescence spectra of $4x10^{-8}$ M QDs, $2.5x10^{-6}$ M Ce_6 and QD-Ce_6 ($4x10^{-8}$ M:$3.6x10^{-7}$ M) solutions using two-photon excitation at 810 nm. The region from 650nm to 720nm is shown in different scale.

Here we present the study on Forster resonant energy transfer (FRET) from two photon excited CdSe/ZnS QDs to photosensitizer chlorin e_6 (Ce_6).

For TPE of the samples 810 nm pulsed radiation of Ti-sapphire laser was used. TPE fluorescence spectra of QDs, Ce_6 and mixed QD-Ce_6 solutions are shown in Fig. 1. The sample of QDs displayed an intensive TPE PL at 605 nm. Meanwhile, the intensity of Ce_6 fluorescence at 660 nm, which is usually observed by single-photon excitation, was negligible. The absence of

TPE fluorescence indicated the small TP cross section of Ce_6. An addition of Ce_6 to QDs solution caused the quenching of QDs PL as well the formation of the new fluorescence band at 670 nm was observed. Similar fluorescence band at 670 nm was obtained in QD-Ce_6 solutions using single-photon excitation. This band was attributed to Ce_6 molecules localized in the lipid-based coating of QDs [3]. Close localization of Ce_6 to QD core ensured the effective energy transfer. The hydrophobic environment of QDs coating resulted in 10 nm bathochromic shift of Ce_6 fluorescence band. Similar appearance of the intensive fluorescence band at 670 nm in QD-Ce_6 solution confirmed the energy transfer from TPE QDs to bound Ce_6. The most intensive TPE fluorescence at 670 nm was observed when QD:Ce_6 molar ratio was 1:10. The obtained results demonstrated the evidence of indirect PS activation via TPE of QDs, which shows the primary perspectives of using such QD-Ce6 complex for TP-PDT.

Acknowledgment:This work was supported by the Lithuanian Science Council Student Research Fellowship Award (A.S) and "Multifunctional nanoparticles for specific non-invasive early diagnostics and treatment of cancer" (No. 2004-LT0036-IP-1NOR).

[1] Medintz, I.L., Uyeda, H.T., Goldman, E.R.,Mattoussi, H. Quantum dot bioconjugates for imaging, labelling and sensing. Nature Materials 4(6), 435-446 (2005);
[2] Samia, A.C.S., Chen, X.B.,Burda, C. Semiconductor quantum dots for photodynamic therapy. Journal of the American Chemical Society 125(51), 15736-15737 (2003);
[3] Valanciunaite, J., Skripka, A., Streckyte, G., Rotomskis, R. Complex of water-soluble CdSe/ZnS quantum dots and chlorine e6: interaction and FRET. SPIE Proceedings 7376, 737607 (2010).

PERCH (*Perca fluviatilis*) STOCK EXPLOITATION BY GREAT CORMORANTS (*Phalacrocorax carbo sinensis*) AND FISHERY IN THE CURONIAN LAGOON

E. Jakubavičiūtė[1], Ž.Pūtys[1], L.Ložys[1], H. Gorfine[1,2], R. Repečka[1], R. Bukontaitė[1]

[1] *Nature Research Centre, Laboratory of Marine Ecology, Akademijos st. 2, LT–08412 Vilnius–21, Lithuania*

[2] *Department of Primary Industries, Queenscliff Research Centre, PO Box 114, 2A Bellarine Hwy, Queenscliff VIC 3225, Australia*

ejakubaviciute@ekoi.lt

Perch is an important fish species in the Curonian Lagoon fishery as well as prey species in the diet of Great Cormorant (*Phalacrocorax carbo sinensis)*. Fishermen often consider Cormorants as competitors and a necessity appears to evaluate how these two mortality factors interact with each other and affect perch population in the Curonian lagoon. Aiming to evaluate the interaction, age structure of perch population in the Curonian Lagoon was assessed. Fish were aged using otoliths collected in 2009 and 2010 (N=744). Otoliths have been processed by cutting and submerging into polyester resin on microscopes slides; annual rings were identified and counted using light microscope. Back-calculation was performed by measuring growth zones; different mean temperatures of the past growth seasons were used for age correction.

The obtained size-at-age data were used for estimation of growth and mortality parameters of perch population by employing FAO FISAT II software [1]. The analysis of length-at-age data showed an asymptotic total length (L_∞) of 49.99 cm and growth curvature (K) of 0.13 yr^{-1}.

The selectivity of Cormorants' diet and commercial 40 – 45 mm gillnet fishery was evaluated in 2009 and 2010. Cormorant diet was studied by analysing pellets (for detail description see [2]), collected at the Juodkrantė colony (N=560). Perch was one of the most important fish species by biomass and numbers contributing to the diet 19.7% and 18.7% respectively. Sets of various mesh size (14-17-21.5-25-30-33-38-45-50-70 mm) gillnets were used for fish sampling, perch length distribution and fishery selectivity evaluation.

Comparison of different cohorts in catches obtained as the result of the research surveys in 2009 and 2010 revealed that survival of 4, 5, 6-year old individuals was 53.4, 19.5 and 13 %, while instantaneous mortality rate (Z) was 0.27, 0.7 and 0.88 respectively. Increasing mortality rates from age group 4 did not fit with Cormorants' selectivity, which showed clear preference on 1 – 3 years old perch individuals (Fig. 1). In contrast to Cormorants' preferences, commercial 40 – 45 mm gillnet fishery targets and eliminates 4 – 6 years old perch.

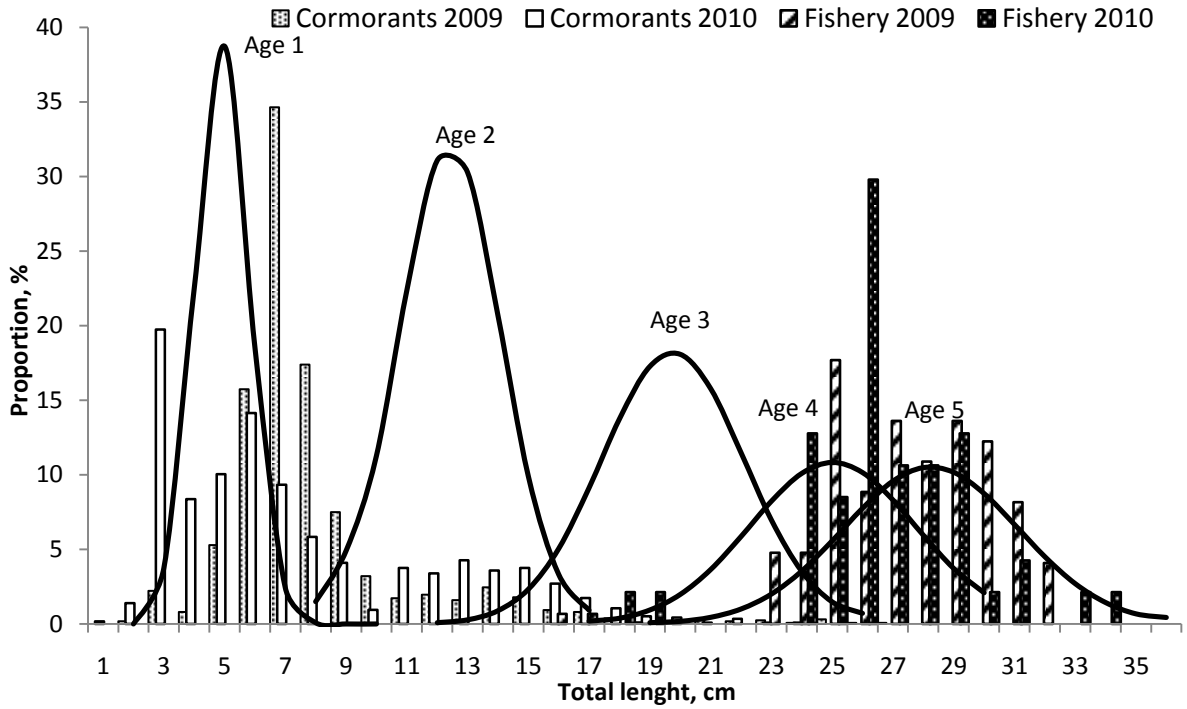

Fig. 2. Length distribution of perch in the Cormorants' diet and commercial fishery (40 – 45 mm gillnets) in contrast to length-at-age distribution (solid line).

Our study demonstrates that direct competition between Cormorants and commercial fishery for perch stock is weak. On the other hand, Cormorants consume large amount of perch – approximately 140–160 tones in 2010 according to the diet study exceeding reported commercial landings by fivefold. However, Cormorants exploit young age, mostly premature perch and mortality caused by the predation might be compensated by lower intraspecific competition and reduced natural mortality caused by other factors. Evaluation of Cormorants' impact on perch stock needs further studies on the dynamics of fish cohorts, including such parameters as a recruitment and production.

Acknowledgements. The study was granted by Research Council of Lithuania (grant No. LEK-24/2010).

[1] Gayanilo F.C., Sparre P., Pauly D. FISAT II FAO-ICLARM stock assesment tools II. User's guide. Rome, 2005.

[2] Pūtys, Ž., Zarankaitė, J. 2010. Diet of the Great Cormorant *(Phalacrocorax carbo sinensis*) at the Juodkrantė colony, Lithuania. Acta Zoologica Lituanica 20(3): 179-189.

AEROSOL SPECTROMETRY: PARAMETERIZATION OF SUB-MICROMETER AEROSOL PARTICLE SIZE DISTRIBUTION DURING NUCLEATION EPISODES IN PREILA

V. Ulevicius, S. Kecorius

Center for Physical Sciences and Technology, Savanoriu ave. 231, LT-02300, Vilnius, Lithuania

simolas2000@yahoo.com

Atmospheric aerosol particles, which are very small and suspended in the air, affect the Earth's climate by directly scattering and absorbing the atmospheric radiation and indirectly by acting as cloud condensation nuclei and modifying the optical properties of clouds. Furthermore, human exposure to fine particulate matter is associated with adverse impacts on human health [1] and the environment [2]. Because of the high variability of the properties of atmospheric aerosol particles, simplification are needed before the parameterized particle number size distribution can be used as input data in global climate models. [3].

In this work we focus on the strongest nucleation episodes:

2009-04-06, 2009-04-19, 2009-04-21, 2009-05-10, 2009-05-13, 2009-05-23, 2009-05-26, 2009-06-12, 2009-07-27, 2009-08-04, 2009-09-20, 2009-10-10, 2009-11-23, 2009-12-01. The aerosol particle concentration measurements were performed at the Preila environmental pollution research station (55°55'N, 21°00'E, 5 m above sea level) in the coastal/marine environment. Scanning Mobility Particle Sizer (SMPS) spectrometer, manufactured by IfT, Germany and Condensation Particle Counter 1500 (CPC), manufactured by Institute of Physics, Lithuania were deployed at the site and provided real-time, continuous measurements of aerosol size distribution and aerosol concentration.

Aerosol particle size distribution was parameterized by fitting multi log-normal distribution:

$$f\left(D_p, \bar{D}_{pg,i}, N_i, \sigma_{g,i}\right) = \sum_{i=1}^{n} \frac{N_i}{\sqrt{2\pi}\log\left(\sigma_{g,i}\right)} \times \exp\left[-\frac{\left[\log\left(D_p\right) - \log\left(\bar{D}_{pg,i}\right)\right]^2}{2\log^2\left(\sigma_{g,i}\right)}\right] \quad (1)$$

presented by Whitby [4]. The main objective of the fitting is to obtain the log-normal parameters: geometric mean diameter D_g, mode number concentration N_i and standard deviation σ_g, that best fit the measured particle number size distribution and thus describe the properties of the atmospheric aerosol particle formation.

In this study, we used DistFit™ (Chimera Technologies, USA) software that parameterizes aerosol particle number size distributions with the multi log-normal distribution functions. DistFit™ software revealed that there were three modes in aerosol particle number size distribution during nucleation episodes in Preila. Selected size ranges for modes were: Nucleation: 3 - 20 nm, Aitken: 20 – 100 nm, Accumulation: 100 – 1000 nm. Parameterization showed that main multi log-normal distribution parameters are: N_i=6.67E+04, σ=1.57, D_g=14

nm., N_i=9.18E+04, σ= 1.77, D_g=43.6 nm., *N_i=13.94+04, σ=1.83, D_g=114 nm.*, for nucleation, Aitken, and accumulation modes respectively.

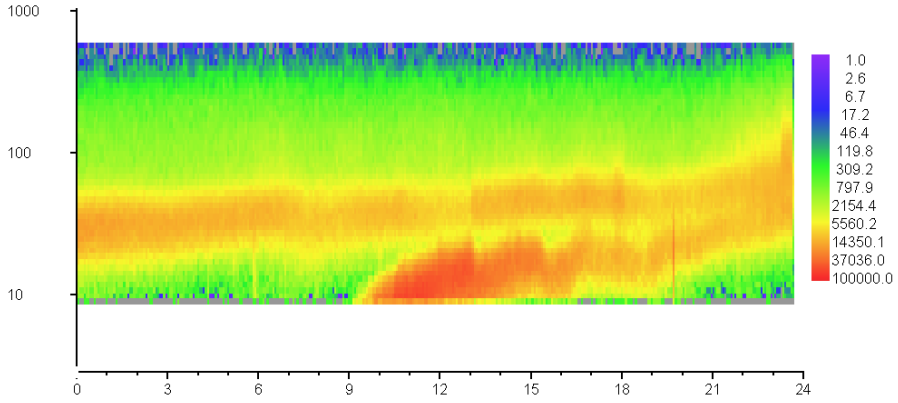

Fig. 1. Aerosol particle number size distribution spectrum. Y axis – particle size, X – time of the day, color – aerosol particle concentration ($dN/dlogD_p$).

[1] Schwarz, J. P., Spackman, J. R., Fahey, D. W., Gao, R. S., Lohmann, U., Stier, P., Watts, L. A., Thomson, D. S., Lack, D. A., Pfis- ter, L., Mahoney, M. J., Baumgardner, D., Wilson, J. C., Reeves, J. M. (2008). J. Geophys. Res., 113.

[2] Ramanathan, V. Li, F., Ramana, M. V., Siva, P. S., Kim, D., Corrigan, C. E., Nguyen, H., Stone, E. A., Schauer, J. J., Carmichael, G. R., Adhikary,

[3] Hussein, T., Dal Maso, M., Petaja, T., K. Koponen, Ismo., Paatero, P., P. Aalto, P., Hameri, K., Kulmala, M. (2005). Borel Environ.Res., 10: 337-355.

[4] Whitby, K.H. (1978). Atmos.Environ. 12: 135-159.

NON-LINEAR MULTIMODAL OPTICAL MICROSCOPE BASED ON CARS MICRO-SPECTROMETER

J. Kiškis, A. Dementjev

Center for Physical Sciences and Technology, A. Goštauto 11, LT-02300 Vilnius, Lithuania
juris.kiskis@ff.stud.vu.lt

Light microscopy has greatly advanced our understanding of the world on the micro-scale. Various light-matter interactions are used to investigate different physical properties of the specimen, e.g. in bright field microscopy, image contrast is based on absorbance and scattering of light. As developments in optical techniques progress, more specific and contrast mechanisms are used, the higher spatial resolution and higher sensitivity levels are achieved. In particular, the use of non-linear light-matter interactions in microscopy has emerged as a powerful research tool for biology [1]. In the past few years, there had been number of aproaches to combine multiple non-linear contrast mechanisms in one microscope [2,3,4,5].

In this work we present non-linear multimodal optical microscope based on coherent anti-Stokes Raman scattering (**CARS**) micro-spectrometer [6] and multimodal imaging of some biological objects (i.e. green algae, starch granules). A fundamental beam of picosecond laser operating in a cavity dumping regime (Nd:YVO_4, 1064 nm) at the 1MHz repetition rate is used to pump optical parametric generator, which serves as a two-color, signal beam (850-1040 nm) and idler beam (1060-1395 nm), excitation light source. Excitation beams are directed to the standard inverted microscope (Olympus IX71) and focused on the sample with an oil-immersion objective (Olympus, Plan Apochrom., 60×, NA 1.42). This experimental setup can be used for imaging with multiple non-linear contrast mechanisms: coherent anti-Stokes Raman scattering, two-photon excitation fluorescence (**TPEF**), and second harmonic generation (**SHG**).

Vibrational origin of CARS signal allows us chemically selective imaging without chemical labeling. In biology, high intensity CARS signals arising from CH_2 vibrations are frequently used for lipid membranes, elastin and collagen fibrils imaging. SHG signal arises from non-centrosimetric structures. This characteristic of SHG signal can be used to determine the orientation of molecules in the specimen. TPEF from auto-fluorescent components gives information about the distribution of the fluorophores. Combining information from images of different contrast mechanisms lead to better understanding of the sample under investigation.

Imaging green algae *Nostoc commune* with CARS and TPEF contrast mechanisms are shown in Figure 1. The green algae *Nostoc commune* has two types of cells: normal cells which have chlorophyll and heterocyst cells which do not have chlorophyll. Figure 1A shows CARS image tuned to CH_2 vibration contrast where both types of cells are visualized. Figure 1B shows TPEF image of chlorophyll fluorescence. In this figure heterocyst cell is not visible.

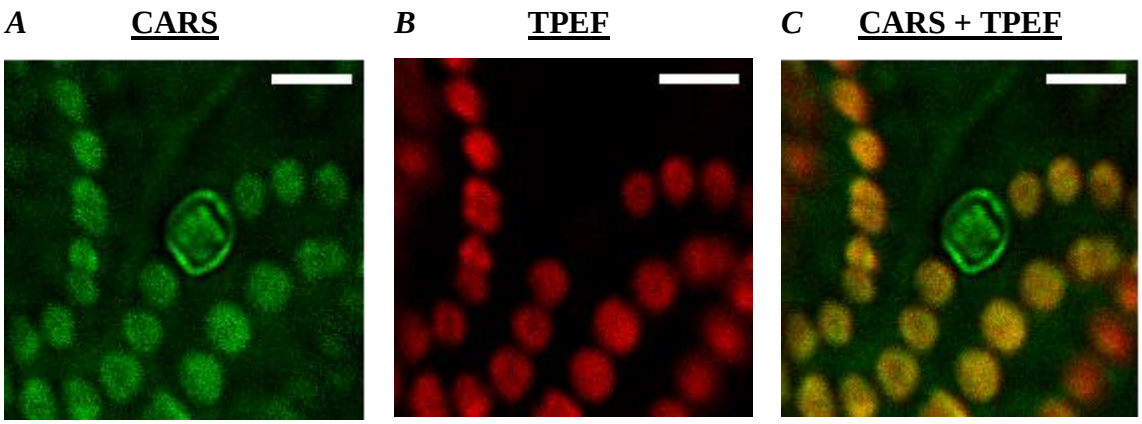

Fig. 1. Pseudo color images of green algae *Nostoc commune* using different contrast mechanisms: coherent anti-Stokes Raman scattering (***A***), two-photon excitation fluorescence (***B***) and overlay of CARS and TPEF images (***C***). Scale bar - 10 μm length.

Acknowledgements. Jūris Kiškis acknowledges Student Research Fellowship Award from the Lithuanian Science Council.

[1] F. Helmchen and W. Denk, Deep tissue two-photon microscopy, Nature Methods 2 (12), 932-940 (2005).
[2] H. Chen et al., A multimodal platform for nonlinear optical microscopy and microspectroscopy, Optics Express 17 (3), 1282-1290 (2009).
[3] D. Li, W. Zheng and J. Y. Qu, Integrated multiplex CARS and two-photon fluorescence microscopy for imaging biological systems, Proceedings SPIE 7903, 790315 (2011).
[4] R. Zadoyan et al., CARS module for multimodal microscopy, Proceedings. SPIE 7903, 79030Z (2011).
[5] D. Slepkov et al., Multimodal CARS microscopy of structured carbohydrate biopolymers, Biomedical Optics Express. 1 (5): 1347-1357 (2010).
[6] Dementjev et al., Coherent anti-Stokes Raman scattering spectroscope/microscope based on a widely tunable laser source, Journal of Modern Optics 57, 503-509 (2010).

METHODS OF COLOR CORRECTION AND OBJECT IDENTIFICATION IN SEAFLOOR VIDEO MOSAIC

M. Lukas, O. Ramašauskas

[1] *Department of Informatics, Faculty of natural science and mathematics, University of Klaipėda, H.Manto st. 84, LT-92291 Klaipėda, Lithuania*

ggarsas@gmail.com

The combination of new underwater technology as remotely operating vehicles (ROVs), high-resolution video imagery, and seafloor mosaics creating provides new opportunities for marine geological or biological studies. While these underwater techniques are now well-engineered, there is still a lack of methods for the automatic analysis of the acquired image data. Such data are mostly analysed manually at present, which is a very labour-intensive and time-consuming task [1].

Research was started to create video mosaic image analyses methods, which would reduce time-costs and human labor and increase precision in obtained data.

Mosaic is made from individual video frames merged together through similar points [2]. That creates problems in image color and contrast integrity. SCC *(Segmentation, Color and Contras correction)* algorithm was made to divide image in to segments and adjust color and contras each frame separately (Fig. 1).

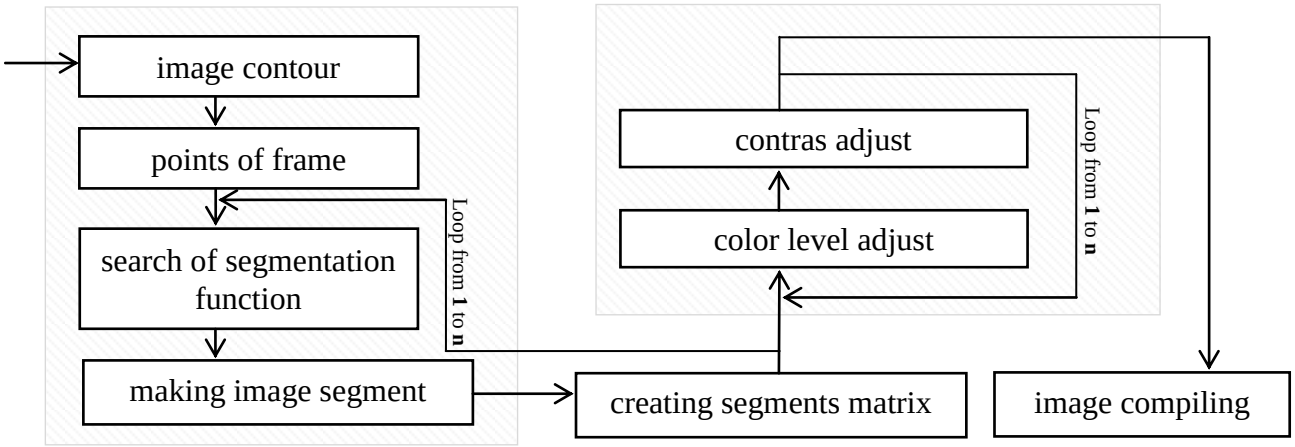

Fig. 1. SCC algorithm operation sequence.

This segmentation method is based on searching and detecting two video frames connecting points on image and calculating function between them. Frames connecting points` detection works only with standard video mosaic forms. Functions are lines separating individual segments.

Underwater images typically wind up looking far more green or blue and less red as we move away from the object being imaged. [3]. So SCC algorithm color correction method nearly removes water effect from video mosaic by adding red and subtracting green or blue colors (Fig. 2.). Method will be improved adding color intensity leveling algorithm.

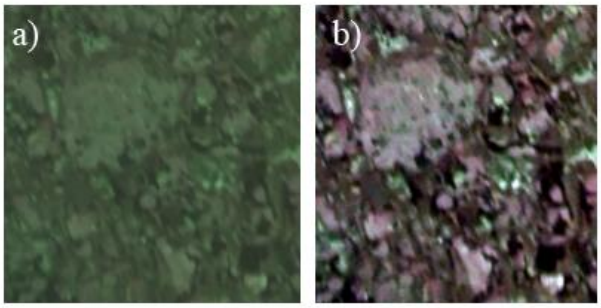

Fig. 2. Video mosaic a) before and b) after SCC algorithm was used.

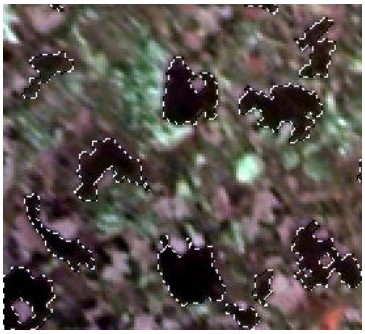

Fig. 3. Object identification

Video mosaic is usually analyzed manually, and obtained data isn`t accurate. So there was created identification method witch is semiautomatic, based on color tolerance and made on PhotoShop (PS) as it`s plug-in. Object color interval is define manually using PS tool – "magic wand" and its` tolerance parameter. It is easy to fine objects` color specter and won`t need to create a pattern before image analyze as it is usually used in identification software [4]. After defining one object software finds all similar color objects (Fig. 3).

Using SCC algorithm can increase image color contras and quality very noticeable and help to analyze video mosaic more accurately for human and computer software. Semiautomatic image analyze saves time and obtains better quality data. Also it not requires preparation (making patterns) for image analyzes.

[1] K. Jerosch, A. Ludtke, M. Schluter, G.T. Ioannidis, Automatic content-based analysis of georeferenced image data: Detection of Beggiatoa mats in seafloor video mosaics from the Hakon Mosby Mud Volcano, Computers & Geosciences, 202-206 (2007).

[2] Chiou-Ting Hsu, Tzu-Hung Cheng, Rob A. Beukers and Jyh-Kuen Horng, Feature-based video mosaic, Image Processing, 2000. Proceedings. 2000 International Conference on. Vancouver, 10-13 September, 2000, p. 887-890.

[3] V.L. Ferrini, H. Singh, M. E. Clarke, W. Wakefield and K. York, Computer-Assisted Analysis of Near-Bottom Photos for Benthic Habitat Studies, Oceans **2006**, 1-4 (2006).

[4] Frank Beuchel, Raul Primicerio, Ole Jørgen Lønne, Bjørn Gulliksen, and Sten-Richard Birkely, Counting and measuring epibenthic organisms from digital photographs: A semiautomated approach, Limnology and Oceanography: Methods 8, 229–240 (2010).

PREVALENCE AND BIOLOGICAL PROPERTY OF THE MEDICAL PLANTS IN THE GIRULIAI FOREST

G. Mikalauskas

Klaipeda University
giedriusm3@gmail.com

The purpose of work was to assess variety and distribution of medicinal plants in the Giruliai forest. Researches were performed in of 2006 and 2009 in the Giruliai forest which is in the territory of Klaipeda town. To get more accurate results were chosen 160 plots in different locations. The width of each plot was one hundred square meters. The 12 types of medicinal plants were found in the researched plots: *Dryopteris filix-mas, Linaria vulgaris, Tanacetum vulgare, Thymus serpyllum, Urtica dioica, Melampyrum nemorosum, Melampyrum pratense, Silene vulgaris, Achillea millefolium, Viola tricolor, Centaurea cyanus* and *Calluna vulgaris* species. All these species are very frequent in Lithuania.

During researches was measured heigh of plant, weigh mass of plants, establish phenological phase and status. During research, was apply coefficient of correlation and linear regression analysis.

The most prevalent herbal was *Calluna vulgaris* (frequency of occurrence 37,57 %) and *Melampyrum pratense* (frequency of occurrence 24,86 %). The least prevalent herbal was *Viola tricolor* individs (frequency of occurrence 0,55 %). The most of medical plants status was good, there was no injuring. Only *Centaurea cyanus* status was at an average, with insignificant injuries.

There was a very strong positive correlation between heigh and weigh of medical plants (r reached from 0,82 to 0,99; $p \leq 0,05$).

MERCURY CONCENTRATION MEASUREMENTS IN LAKE SEDIMENTS AND WATER IN WESTERN LATVIA

A. Svagere

Institute of Atomic Physics and Spectroscopy, University of Latvia, Skunu street 4, Riga, Latvia, LV – 1050

anda.svagere@gmail.com

Water is very important for all living organisms but it also plays an important role in the transport and cycling of toxic elements, including Hg, in nature, so it is necessary to control concentration rates in order to prevent pollution, especially in drinking water.

Mercury was analyzed in sediments from Engures lake and water samples from Liepājas lake and several rivers located in western Latvia (Venta, Slocene). The mercury concentration in samples was analyzed using mercury analyzer RA-915+ and its attachments RP-91C (for sediments) and RP-91 (for water).

Method used for the mercury determination in sediments is based on the atomization of mercury contained in the sample in an RP-91C attachment and subsequent mercury determination by flameless Atomic Absorption Spectroscopy (AAS) in a mercury analyzer RA-915+. Using mercury analyzer RA-915+ together with attachment RP-91C allows determination of mercury in soil and other similar samples without specific sample preparation and mercury accumulation on a sorbent.

Mercury concentration in water was determined by atomization of mercury contained in the sample in an RP-91 attachment and subsequent mercury determination by Cold Vapour Atomic Absorption Spectroscopy (CV-AAS) in analyzer RA-915+. Chemically pretreated (mineralized) and untreated samples were analyzed. The comparison of the results will be shown.

Profile of concentration distribution depending on depth is obtained for Engures lake's sediments. Determination of sediments layers' age allows us to get insight into Hg concentration changes in time and sedimentation velocity.

For water samples detected mercury concentrations varied between 0 and 1,5 ng/l and thus they were below analyzer's detection limit (10 ng/l), so we can conclude that water in these water bodies is free of mercury.

Acknowledgments: The work was partly supported by European Social Fund project Nr. 2009/0210/1DP/1.1.1.2.0/09/APIA/VIAA/100.

INFRARED SPECTROMETRY METHOD FOR THE PREVENTION OF KIDNEY STONE DISEASE

S. Tamošaitytė, V. Šablinskas, and M. Pučetaitė

Department of General Physics and Spectroscopy, Faculty of Physics, Vilnius University, Saulėtekio Ave. 9-III, LT-10222 Vilnius, Lithuania

sandra.tamosaityte@ff.stud.vu.lt

Kidney stone disease affects about 10 percent of the people [1]. Therefore, emerging kidney stones should be found as early as possible. However, usually kidney stones are only found when they have already formed, mainly big and cause severe pain. To suggest a solution to this problem the hypothesis was set: infrared (IR) spectrometry method could be informative enough to investigate human urinary sediment composition and identify the crystals in the urinary sediment which are highly responsible for the kidney stone formation. Urine which is saturated with these materials usually signal about highly anticipated or already existing kidney stone in organism [2]. Continuous monitoring of the patients' urinary sediment composition and its changes could be a way to predict the formation of the kidney stones and then take certain preventive measures to stop kidney stones from growing further.

The urinary sediment samples of Santariskes clinics patients' were tested during the experiment. All spectra were registered using Fourier transform IR spectrometer (FTIR) Bruker Vertex 70. Firstly, centrifuged urine was evaporated until only crystals of urine sediment were left on permeable for IR plate. Then, the IR absorption spectra were registered of these samples. Using the same method the urea sample was prepared and its IR absorption spectrum registered. Recording of the IR absorption spectrum of urea was necessary as it was immediately noticed that urine sediment contains mainly urea. Knowing exactly in which wavelenght values urea molecules absorb, it was possible to reject the influence of urea molecules absorbtion. Then it has been analysed what other low concentration crystal materials could be found in urinary sediment samples.

It was found that excluding urea urinary sediment also contains uric acid. This material is one of the main kidney stones forming substances. Fig. 1. shows uric acid absorbance at 1670 cm^{-1}, 1348 cm^{-1}, 1305 cm^{-1} wavenumber values. Although uric acid also has characteristic spectral absorption bands in 3160 cm^{-1} - 2550 cm^{-1} region, it is likely that because uric acid molecules concentration is low these bands are disguised in the inclined part of the spectrum of the corresponding interval. By forming urine sediment and urea differential spectra, other low concentration crystalline substances were found in the urine sediment.

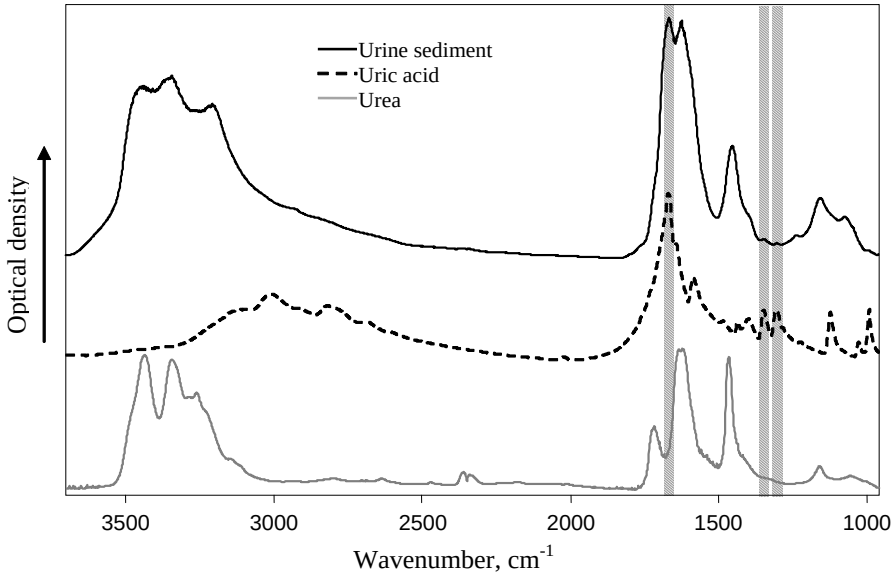

Fig. 1. Urine sediment, uric acid and urea spectra

Thus, the selected spectral method is sensitive and informative enough to identify low concentration crystal materials in the urine. Analysis and proper interpretation of patients' urine sediment composition changes could make this method a viable technique for kidney stones surveillance and prevention.

[1] N. Bullock, A. Doble, W. Turner, P. Cuckow, Urologijos vadovas (Vaistų žinios, Lietuva, 2008).
[2] J.H. Parks, M. Coward, F. L. Coe, Correspondence between stone composition and urine supersaturation in nephrolithiasis, Kidney Int. 51, 894-900 (1997).

THE GROWTH OF THE EASTERN ATLANTIC HARBOR SEALS PUP'S *(PHOCA VITULINA)* IN THE LITHUANIAN MARITIME MUSEUM

S. Trumpytė

Department of Ecology, Faculty of Natural Sciences and Mathematics, University of Klaipėda, H. Manto 84, LT - 92294 Klaipėda, Lithuania

trumpytee@gmail.com

The eastern Atlantic harbor seal occurs around Svalbard, Iceland, the British Isles and Ireland, in Norway up to Finnmark, in the southwestern part of the Baltic, in the Wadden Sea, and on the North Sea coasts of Denmark, the Netherlands, and Brittanny (France) [1]. Generally, the length of males ranges from 1.5 to 1.8 m and weight from 55 to 130 kg, while the slightly smaller adult females measure 1.2-1.5 m in length and weigh 45-105 kg. Pups measure 70-90 cm at birth and weight 9-11 kg [2].

Sexual maturity is reached at an age of 3-5 years for female and 4-6 years for male [3]. Gestation lasts 10.5-11 month, including a 2-month delayed implantation. Lactation lasts 4-6 weeks. The annual pregnancy rate of adult females in on average 87%. Pups are able to swim and dive within hours of birth, and they grow quickly on their mothers' milk [4, 5].

On average, harbor seal milk is about 45% fat, 9% protein, and 45.8% water, with traces of lactose (milk sugar). The extremely high fat content of the milk helps the pups more than double their weight by the time they are weaned. This species grew rapidly (0.56 ± 0.01 kg day^{-1}) over the ~25 day lactation period and body condition increased from 10% at birth to 39.4 ± 0.1% at weaning, before falling to an average value of 25.1 ± 1.3% in yearling and adults [6, 7, 8].

The aim of this study was to evaluate the growth rates of five harbour seals pup`s during the breeding season by the female harbour seal in captivity. Three adult harbour seals (one male and two females) were housed together in non-flowing water tanks (8 x 3 x 3 m) at the Lithuania maritime museum. Harbour seals give birth in the second half of June or July, nursing lasts for approximately 30 days. The rate of mass gain is directly related to the duration of the lactation period. Pups less than 7 days old had an elevated or reduced body mass compared with their gain growth. Pups grew from 10.6 ± 0.3 kg to 27.7 ± 1.6 kg (means ± S.D.) over the duration of lactation period. Male pups body condition increased 9% more then female.

The effect of maternal age and condition on the date of parturition and the duration of the perinatal period were investigated over three consecutive breeding seasons. Although females may first pup at three years old, they did not attain full adult size until six years of age; older females (≥ 6 years) tended to be heavier, longer, and in better condition than younger females (3–5 years) [9]. Maternal body condition and age influence the physical development of offspring and thereby their reproductive success. Younger females` pups are nursed for about 6 days shorter during which time they will gain 15% more than older females pups.

Analysis of dive and surface durations indicates that young pups need more rest between dives than older ones. They spend a smaller proportion of time submerged than older. Pups haul-out less frequently as they grow older.

[1] G. B. Corbet, S. Harris, British Mammals, The Mammal Society **3**, 632–642 (1991).

[2] J. J. Burns, Harbor Seal and Spotted Seal Phoca vitulina and P. Largha, Encyclopedia of Marine Mammals **12**, 552-560 (2002).

[3] C. Lydersen, K. M. Kovacs, Worlds' northernmost population of harbour seals, Ottan **5**, 34-40 (2001).

[4] M. A. Bigg, Harbor seal *Phoca vitulina* Linnaeus, 1758, and *Phoca largha*, Pallas, 1811. In: S.H. Ridgway & R.J.Harrison (eds), Handbook of Marine Mammals **2**, 1-77 (1981).

[5] P. J. H. Reijnders, Recruitment in the harbor seal *(Phoca vitulina)* population in the Dutch Wadden Sea, Netherlands Journal of Sea Research **122**, 164-179 (1978).

[6] J. M. Burns, C. A. Clark, J. P. Richmond, The impact of lactation strategy on physiological development of juvenile marine mammals: implications for the transition to independent foraging, International Congress Series **1275**, 341-350 (2004).

[7] Y. Dubé, M. O. Hammill, C. Barrette, Pup development and timing of pupping in harbour seals (Phoca vitulina) in the St.Lawrence River estuary, Canada, Canadian Journal of Zoology **81**, 188-194 (2003).

[8] W. D. Bowen, D. J. Boness, S. J. Iverson, Estimation of total body water in Harbor seals: how useful is bioelectrical impedance analysis? Marine Mammal Science **14**, 765-777 (1998).

[9] H. D. Fisher, Delayed Implantation in the Harbour Seal, Phoca vitulina L., Behavioral Ecology and Sociabiology **173**, 879-880 (2008).

ESTIMATE OF LIVE AND DEAD ZOOPLANKTON INDIVIDUALS IN CURONIAN SPIT AND BALTIC SEA COAST

N. Usanova[1], E. Grinienė[2]

[1] *Klaipėda University, Klaipėda, Lithuania*
[2] *Coastal research and Planning institute, Klaipėda, Lithuania*
neringa.usanova@gmail.com

Mortality is known to be one of the principal factors that determine the dynamics of natural populations. Traditionally researchers collect, preserve and enumerate zooplankton samples without knowledge of the health status of the zooplankton. Zooplankton could suffer from non-consumptive mortality due to starvation, environmental stresses, diseases, pollution, injuries, parasites, and harmful algal blooms.

The research was performed on the 10th and 20th of April and 4th of September, 2009, as well as on the 20th of April, 2010 in Klaipėda along the cruise ship terminal; on the 22nd of September, 2009 in Nida and Nemunas; on the 11th of May, 2009 in Palanga; on the 4th of September and 20th of April, 2010 in Melnragė, Palanga and Liepaja.

During the research Procion dyes was tested, however when the expiration date was over, the paint did no longer affect the deceased individuals. Therefore, the comparison between Procion and the Neautral red and the Aniline blue dyes failed.

The Neutral Red method was applied in the Baltic Sea, dead copepods were not stained whereas live copepods were stained red; the Aniline Blue – in Curonian Lagoon, dead copepods were stained blue, live – not stained.

The mortality of zooplankton species in the Curonian Lagoon and the Baltic Sea coast at Melnragė, Palanga and Liepaja was investigated. There were 24 samples investigated in total. *Eudiaptomus graciloides, Mesocyclops leuckartii,* Rotatoria sp. dominated in the Curonian Lagoon; *Cyclopoida* representatives and their Nauplii – at Melnragė; *Acartia bifilosa* species dominated in Palanga. Low species diversity was observed in Liepaja, however, the most dominant were Rotatoria sp. and Nauplii.

On the 4th of September, the mortality in the Curonian Lagoon was 7.3 ± 4.3%, 15.1% in Nida, 6.6 ± 4.6% at the Baltic Sea coast along Melnragė, 4.67 ± 2.0% in Palanga, and 3.85 ± 2.9% in Liepaja.

However, this study did not observe a significant relationship between percent dead copepods and environmental factors, that this factors varied within a rather narrow range in this field study.

MEASURING Be-7, Cs-137 AND Pb-210 ACTIVITY CONCENTRATIONS IN THE NEAR-GROUND LEVEL ATMOSPHERE

A. Vinčiūnas[1], A. Gudelis[2]

[1] *Faculty of Physics, Vilnius University, Saulėtekio Ave. 9-III, LT-10222 Vilnius, Lithuania*
[2] *Center for Physical Sciences and Technology, Savanoriu ave. 231, LT-02300, Vilnius, Lithuania*
antanas.vinciunas@ff.stud.vu.lt

The aim of this work is to measure and compare the variation of the recent activity concentrations of three radionuclides - cosmogenic Be-7, artificial Cs-137 and terrestrial Pb-210 – in the near-ground level atmosphere at two different sites– in the Ignalina Nuclear Power Plant (further – INPP) impact zone (3.5 km southeast of the INPP) and in Vilnius - and to estimate how these radionuclides contribute to the annual committed effective dose for the members of public.

The measurements of the activity concentrations were carried out using gamma-spectrometers with HPGe detectors for the non-destructive analysis of FPP-15 filters. The filters used in Vilnius (sampling time – 2 weeks) were analysed using a well-type detector and the ones from the INPP impact zone (sampling time – 1 week) were analysed using a coaxial detector. Three peaks of the gamma-ray spectra were analysed: 46.5 keV (Pb-210), 478 keV (Be-7) and 661.7 keV (Cs-137).

The variations of the Be-7, Pb-210 and Cs-137 activity concentrations in Vilnius and in the INPP impact zone from May to December 2010 were measured and the results are shown in figures 1, 2 and 3, respectively. The vertical dashes in the figures denote the 68% confidence intervals. Assuming that the radionuclides get into the human (adult) body via the inhalation pathway and the mean breathing rate is 6.5 l/min, the contribution of each radionuclide to the annual committed effective dose was estimated. The results are shown in Table 1.

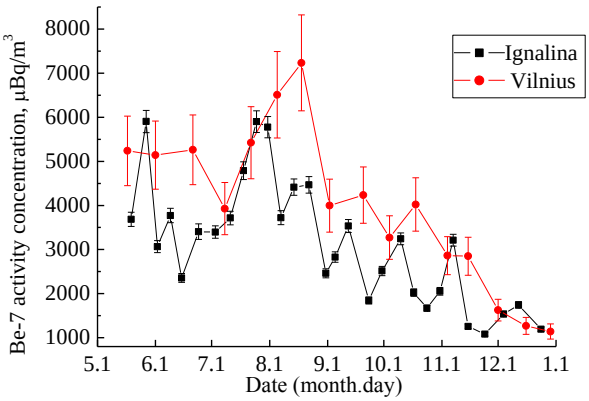

Fig. 1. The variation of the Be-7 activity concentrations

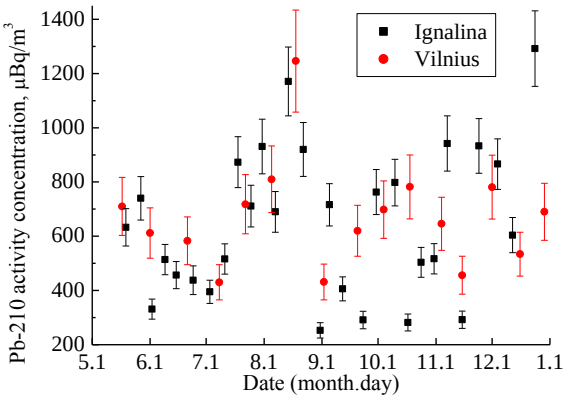

Fig. 2. The variation of the Pb-210 activity concentrations

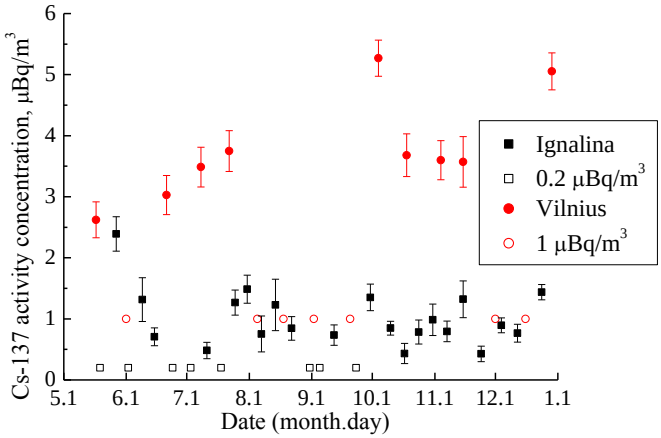

Fig. 3. The variation of the Cs-137 activity concentrations (hollow squares and circles denote the Cs-137 detection limits of coaxial and well-type detectors, respectively)

Tab. 1. The mean activity concentrations of Be-7, Cs-137 and Pb-210 and the estimation of the annual committed effective doses for the members of public

Nuclide	Conversion coeff. [Sv / Bq]	Vilnius		The INPP impact zone	
		Activity conc. [Bq / m^3]	Effective dose [Sv]	Activity conc. [Bq / m^3]	Effective dose [Sv]
Be-7	5.5 E-11	4.0 E-03	7.5 E-10	3.1 E-03	5.9 E-10
Cs-137	3.9 E-08	2.6 E-06	3.4 E-10	7.9 E-07	1.1 E-10
Pb-210	5.6 E-06	6.7 E-04	1.3 E-05	6.5 E-04	1.2 E-05

The activity concentrations of Be-7 in Vilnius and in the INPP impact zone are highest in July and August because of the tropopause changes in spring [1].

The Cs-137 activity concentrations in both sites represent the global distribution of this radionuclide.

The activity concentrations of Pb-210 in both sites are similar with a mean value of 660 μBq/m^3. These are typical for the continental locations.

The annual committed effective dose for the members of public due to Pb-210 makes up about 1.2 – 1.3% of the annual limit effective dose (1 mSv). The annual committed effective doses for the members of public due to Be-7 and Cs-137 are insignificant.

Acknowledgements. We acknowledge Student Research Fellowship Award from the Lithuanian Science Council.

[1] Sýkora, I., Ješkovský, M., Merešová, J. Radioactivity of Bratislava atmosphere. *Acta Physica Universitatis Comenianae*. 2009-2010, 50-51 (1-2), 125-132.

NMR MONITORING OF NONEQUILIBRIUM AGGREGATION IN IONIC SOLUTIONS

V. Klimavičius

Faculty of Physics, Vilnius University, Saulėtekio Ave. 9-III, LT-10222 Vilnius, Lithuania
vytautas.klim@gmail.com

It is known that some mesoscopic structures appear in aqueous solutions [1]. The complex shaped ^{1}H NMR signal of 1-decyl-3-methyl imidazolium bromide (in shorter version [C10mim][Br]) has been observed after it was mixed with water in different concentrations. Within time of minutes the contour of a signal caused from C-H···Br - hydrogen bridge was transformed into Voigt function profile with Gauss contribution as dominant and started to evolve towards Lorentz function line shape while the contour from water signal remained Lorentz shaped during all the waiting time. Relative half width (w_G/w_L) contribution in Voigt profile (fig. 1) was introduced as the measure of nonequilibrium aggregation in mesoscopic/supramolecular scale.

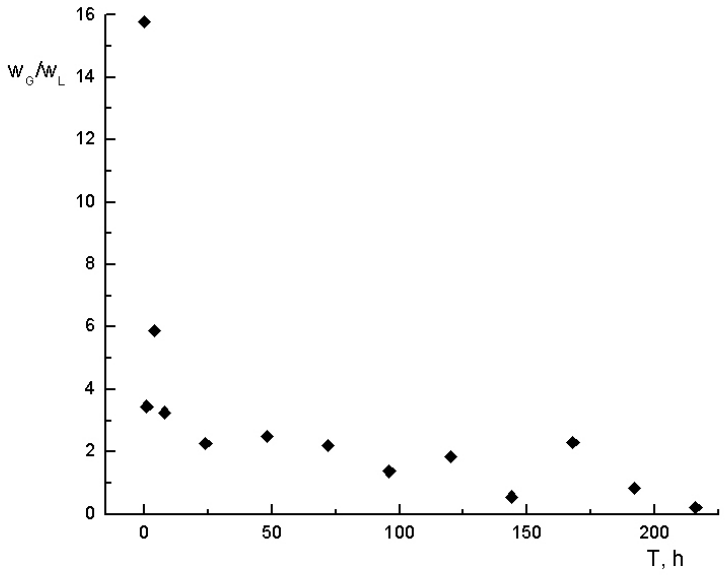

Fig. 1. Kinetics of eqiuilibration in [C_{10}mim][Br]/water solution (ionic liquid molar concentration 0,003) using the parameter w_G/w_L of a fitted Voigt function.

The equilibration kinetics was monitored by time dependence of the half-widths Gauss/Lorentz with waiting time up to 10 days. The 'nonequilibrium' covers only certain degrees of freedom of the guest (ionic liquid) molecules, whereas the matrix, i.e. the hydrogen-bonded network of water, is equilibrated.

Acknowledgments. Vytautas Klimavičius acknowledges Student Research Fellowship Award from the Lithuanian Science Council.

[1] A. F. Kostko; M. A. Anisimov; J. V. Sengers. Physical Review E. 2004, 70, 026118-1 - 026118-11.

SPECTROSCOPIC PROPERTIES OF CARBAZOLE-FLUORENE-BENZOTIADIAZOLE COMPOUNDS

R. Karpicz, S. Puzinas, V. Gulbinas

Center for Physical Sciences and Technology, A. Goštauto 11, LT-02300 Vilnius, Lithuania
Skomantas.Puzinas@ff.stud.vu.lt

Fundamental issue in rapidly developing field of organic optoelectronic is a research for derivatives possessing desired optical, electrical, thermal and chemical properties. Consequently incorporation of different organic functional groups in molecular structure leading to arise of novel characteristics plays a key role in molecular design. Due to unique physical properties carbazole (C), fluorene (F) and benzotiadiazole (B) moieties are preferred from a remarkable variety of functional groups.

This report presents spectroscopic properties of novel organic multifunctional compounds CFC, FFBC, CBFBC and CBC. It is evident from experimental results that fluorescence and absorption properties for these molecules are determined by charge transfer state related with presence of carbazole - benzotiadiazole chromophore and excited state delocalized over entire molecule for CFC. Time-resolved fluorescence spectra reconstructed from fluorescence transients for FFBC, CBFBC and CBC suggests that exciton migration induced fluorescence quenching takes place resulting in decrease of quantum yield in neat films. Furthermore, we propose that conformational relaxation taking place in solutions is suppressed in close-packed structures contributing to a decrease of fluorescence efficiency.

In order to investigate ultrafast excited state relaxation processes of studied compounds tetrahydrofuran, pentane solutions and neat films were investigated by means of pump – probe spectroscopy.

L-ASCORBATE AND MENADIONE COMPLEX: EFFICIENCY OF INTERMOLECULAR ELECTRON TRANSFER

K. Šarka, N. Galikova, A. Gruodis

Department of General Physics and Spectroscopy, Faculty of Physics, Vilnius University, Saulėtekio Ave. 9-III, LT-10222 Vilnius, Lithuania

Karolis.Sarka@gmail.com

This work is devoted to the theoretical study of oxidation-reduction (redox) reaction of vitamin K_3. Mentioned reaction is very important in medical chemistry due to possibility to generate the derivatives containing active oxygen forms. Initial assumption describing the catalytic properties of vitamin C in K_3 redox reaction was formulated in Ref. [1]. According to this assumption, vitamin C could significantly increase the rate and product yield of K_3 redox reaction.

Mentioned task was solved using quantum chemical study of dynamical processes between vitamin complexes containing C (L-ascorbate, two forms) and K_3 (menadione, one form). Fig. 1 represents all molecular systems.

Optimization of the ground state complex geometry was provided by means of GAUSSIAN03 package using HF/6-311G and HF/6-311G(2df.2pd) basis. Optimized structure of complex is presented in Fig. 2. Following simulation of intermolecular electron transfer (IET) was done using NUVOLA package [2] in the framework of molecular orbitals (MO) expressed as linear combination of atomic orbitals (AO). Rate of IET *k* was calculated using Fermi Golden rule:

$$k = \frac{2\pi}{\hbar}\langle\alpha|\hat{H}\,|\beta\rangle^2\delta\left(E_\alpha - E_\beta\right) \qquad (1)$$

Results of simulations allow us to create the model of reaction pathway. Several possibilities are presented and discussed.

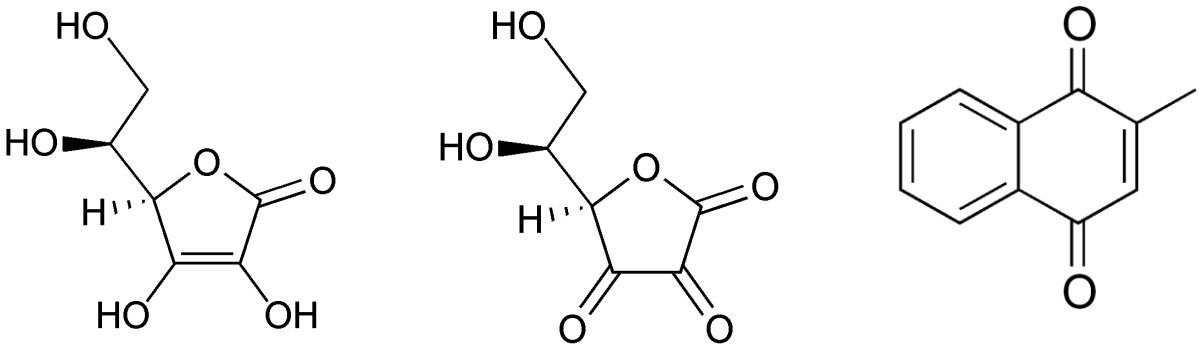

Fig. 1. Two forms of vitamin C (left, center) and vitamin K_3 (right).

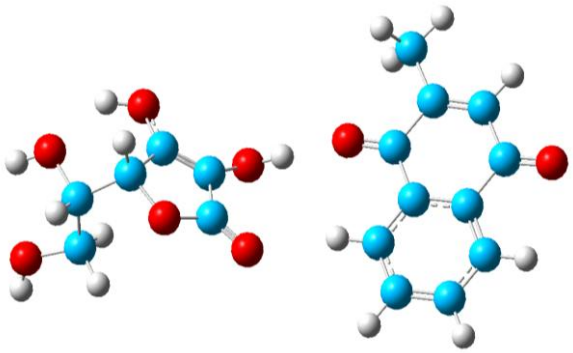

Fig. 2. C..K_3 complex.

[1] J. Verrax, J. Cadrobbi, M. Delvaux, J.M. Jamison, J. Gilloteaux, J.L Summers, H.S. Taper, P.B. Calderon. The association of vitamins C and K3 kills cancer cell mainly by autoschizis, a novel form of cell death. Basis for their potential use as coadjuvants in anticancer therapy, European Journal of Medicine Chemistry 38 (2003) 451-457.

[2] NUVOLA. Quantum chemistry package. Vilnius university, 2007.

SIMULATION OF INTERMOLECULAR ELECTRON TRANSFER IN Ag..Pyr COMPLEX USING DALTON PACKAGE

K. Šarka, N. Galikova, A. Gruodis

Department of General Physics and Spectroscopy, Faculty of Physics, Vilnius University, Saulėtekio Ave. 9-III, LT-10222 Vilnius, Lithuania

Karolis.Sarka@gmail.com

Aromatic derivative containing heteroatoms – pyridine – is well known as a model compound for simulations of adsorption on metal surface. Quantum chemical modeling of adsorption processes includes several significant factors: i) ground state geometry simulation; ii) intermolecular electron transfer simulation.

This work is devoted to exact quantum chemical study of intermolecular electron transfer (IET) between donor (pyridine) and acceptor (Ag surface). Ref. [1] (containing different geometry optimization tasks as well as excitation energy distribution tasks) allows us to take attention to the IET processes between pyridine and neighboring Ag atoms. Fig. 1 shows two structures which were used for IET simulation.

DALTON2 package was used for vector generation in the molecular orbital (MO) framework using linear combination of atomic orbitals (AO). Density functional (DFT) method CAMB3LYP (α=0.190, β=0.460, μ=0.330) by means of the effective core potential basis set ecp-sdd-DZ was used for such purposes. Following simulation of intermolecular electron transfer (IET) was done using NUVOLA package [2]. Results of simulation allow us to discuss the role of *p*- and *d*-electrons.

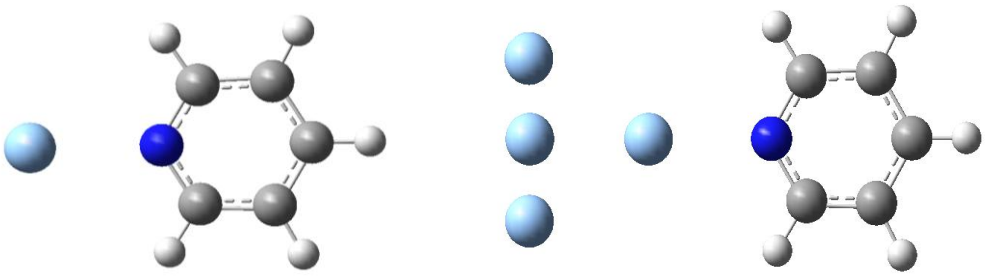

Fig. 1. Ag..Pyr (left) and Ag_4..Pyr complexes.

[1] V. Arcisauskaite, J. Kongsted, T. Hansen, and K. V. Mikkelsen. Charge transfer excitation energies in pyridine-silver complexes studied by a QM/MM method. Chem. Phys. Lett. **470 (**2009) 285.

[2] NUVOLA. Quantum chemistry package. Vilnius university, 2007.

ACTIVATED OXYFLUORIDES FOR SOLID-STATE LIGHTING

I. Brice, U. Rogulis, E. Elsts, A. Šarakovskis, J. Grūbe, G. Doķe

Institute of Solid State Physics, University of Latvia

inga02@inbox.lv

White LEDs are more energoeffective and serve longer than conventional light bulbs. Therefore investigations of new phosphors for solid-state lighting are in progress [1] to find an appropriate phosphor with wide enough spectrum for higher quality lighting. In our work, the luminescence of oxyfluoride samples activated by Ce^{3+}, Eu^{2+} and Ce^{3+}/Eu^{2+} have been compared together and discussed from the point of view of solid-state lighting applications.

[1] A. A. Setlur, Phosphors for LED-based Solid-State Lighting, The Electrochemical Society Interface, Winter 2009, pp 32-36.

PHOTOELECTRICAL PROPERTIES OF DMABI DERIVATIVES IN THIN FILMS

R. Grzibovskis, I. Muzikante, J. Latvels, M. Rutkis

Institute of Solid State Physics, University of Latvia, Latvia

raitis1898@gmail.com

Organic thin films with semiconducting properties have been intensively studied in nowadays due to very promising applications in organic electronics, for example, organic photovoltaic. Among organic semiconductors, group of indandiones with their electrical properties, thermal and chemical stability are good candidates for use in design of novel molecular electronic devices.

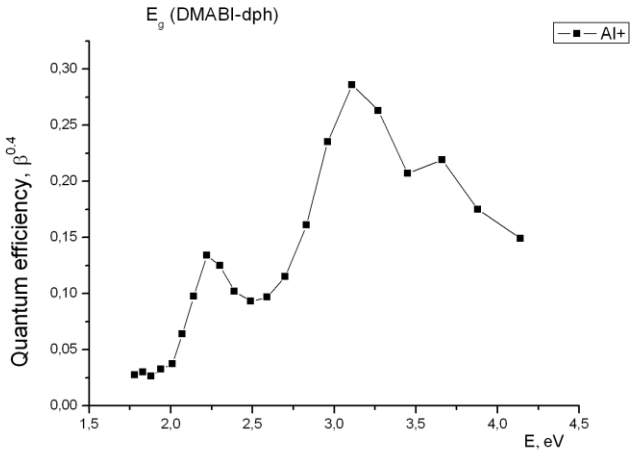

Fig.1 Spectral dependence of quantum efficiency

We have investigated photoconductivity and its spectral dependence of two different dimetilaminobenziliden-1,3-indandion (DMABI) derivatives- DMABI-dph and DMABI-JU. Value of the threshold energy E_{th} from spectral dependence of quantum efficiency of photoconductivity is obtained. The values of the surface potential of thin films of DMABI derivatives are compared with oxidation potentials and shifted highest occupied molecular level (HOMO) and lowest unoccupied molecular level (LUMO) values according to the RHF *ab initio* calculations. Also photocurrent-voltage characteristics are measured.

Acknowledgements. This work is supported by the ERAF Project No. 2010/0252/2DP/2.1.1.1.0/10/APIA/ VIAA/009.

BROADBAND DIELECTRIC SPECTROSCOPY OF Fe_3O_4–$BaTiO_3$ CERAMICS

A. Kuprevičiūtė[1], J. Banys[1], R. Grigalaitis[1], D. Lupascu[2]

[1] *Department of Radiophysics, Faculty of Physics, Vilnius University, Saulėtekio Ave. 9-III, LT-10222 Vilnius, Lithuania*

[2] *Institute for Materials Science, University Duisburg-Essen, Essen, Germany*

a.kupreviciute@ff.stud.vu.lt

Ceramic composites containing ferroelectric and ferromagnetic phases have recently drawn scientists' attention because of their possible applications. The aim of this research was to characterize multiferroic Fe_3O_4–$BaTiO_3$ composites by means of dielectric spectroscopy. This enables us to describe conductivity and dielectric relaxation phenomena in the material and make predictions about its intrinsic structure. Measurements were made in wide temperature (150–450 K) and frequency (20 Hz–1,2 GHz) range.

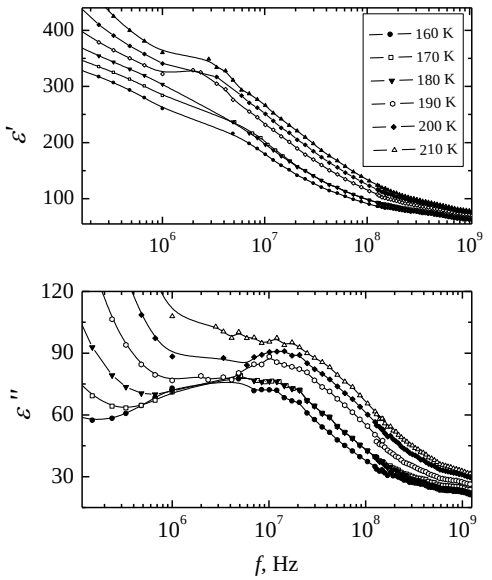

Fig. 1. Spectra of complex dielectric permittivity.

Dielectric measurements indicated that in high temperatures and low frequencies the dielectric response of the composite is governed by conductivity. Evaluation showed that conductivity satisfies the Arrhenius law and the activation energy of this process agrees with the value of electron hopping between different valence states of Fe ions. Further measurements in low temperatures and high frequencies, where the influence of conductivity is smaller, revealed dielectric relaxation (Fig. 1.). It can be said that both phases, conducting Fe_3O_4 and dielectric $BaTiO_3$, have influence to the dielectric spectra of the composite so this opens the possibility for the multiferroic response.

ENERGY TRANSFER IN POROUS SILICON AND POLYMER COMPOSITES

V. Pranculis, R. Karpič, V. Gulbinas

Institute of Physics, Center for Physical Sciences and Technology, A. Goštauto 11, LT-01108, Vilnius, Lithuania

vytenis.pranculis@ff.stud.vu.lt

Porous silicon (PS) and polymer composites are particularly interesting because of their visible luminescence, which has greater stability and emission efficiency compared to plain PS [1]. What is more, different polymers allow tuning of luminescence spectra to match specific requirements [2]. However, the processes taking place during fluorescence of these composites and their properties aren't sufficiently examined.

In our work we used time-resolved fluorescence measurements to investigate energy transfer in PS/polymer composites. THF solutions of mLPPP and MEH-PPV polymers were spin-coated onto porous silicon substrate to create the composites. After close examination of fluorescence spectra and decay kinetics of the composites as well as constituens, we can conclude that energy transfer from PS to polymer takes place during fluorescence of the composites.

Acknowledgements. This work was partly supported by the Lithuanian Science Council Research Fellowship Award (V.P.).

[1] D. Li, D. Yang, C. Zhou, D. Que, Excitation transfer from porous silicon to polymer, Mater. Sci. Eng. B 121, 229-231 (2005).

[2] H. A. Lopez, X. L. Chen, S. A. Jenekhe, P. M. Fauchet, Tunability of the photoluminescence in porous silicon duo to different polymer dielectric environments, J. Lumin. 80, 115-118 (1998).

ENERGY STRUCTURE OF THIN FILM WITH CARBAZOLE DERIVATIVES DETERMINATION IN LIGHT EMITTING DIODE STRUCTURE

K. Pudzs[1], A. Vembris[1], I. Muzikante [1], J. V. Grazulevicius[2]

[1] *Institute of Solid State Physics of University of Latvia, 8 Kengaraga str, Riga, Latvia*
[2]*Department of Organic Technology of Kaunas University of Technology, Radvilenu plentas 19, Kaunas, Lithuania*

kaspars.pudzs@cfi.lu.lv

Modeling the organic light emitting diode structure, it is necessary to study electrical properties and energy structure of organic layer. Bi-polar organic material (electron and hole mobility is of same order) is very important for organic light emitting diodes (OLED). Carbazole derivatives are one of them.

In this work, we have studied electrical properties and energy structure of novel carbazole derivatives (JS97 and JS100) thin films. We used "sandwich" type samples *(see Fig.1.)* consisting of derivative of carbosole oligomer as an active layer sandwiched between top contacts of different metals and gold bottom contacts. The organic films were prepared by spin-coating method with the thickness of the order of 0.5μm and vacuum evaporating method with the thickness of order of 0.5 to 0.9 μm. It allows applying space charge limited current method to characterize charge carrier injection and energy distribution of traps in the thin films. For injection of holes ITO, Au, Pd, Cu electrodes and for injection of electrons Al electrodes were applied.

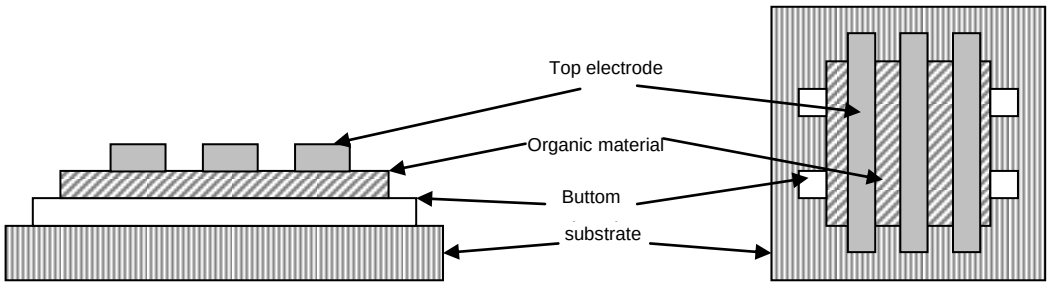

Fig. 1. "sandwich" type sample

Acknowledgement: This work is supported by the Latvian-Lithuanian-Taiwan project „Design, Synthesis and Studies of New Effective Materials for Organic (Opto)electronics"

REPLICATION OF MICRO/NANOSTRUCTURES USING POLYDIMETHYLSILOXANE SOFT LITHOGRAPHY

E. Balčiūnas[1, 2, 3], S. Rekštytė[1], L. Jonušauskas[1] and M. Malinauskas[1]

[1] *Laser Research Center, Department of Quantum Electronics, Vilnius University, Saulėtekio Ave. 10, LT-10223 Vilnius, Lithuania*

[2] *Vivarium, Institute of Biochemistry, Vilnius University, Mokslininkų 12, LT-08662 Vilnius, Lithuania*

[3] *Department of Chemistry and Bioengineering, Faculty of Fundamental Sciences, Vilnius Gediminas Technical University, Saulėtekio ave. 11, LT-10223 Vilnius*

nanopolimerizacija@gmail.com

With the growing need for micro and nano-scale objects, fabrication methods that are low cost, high throughput and simple to operate are in an increasing demand. We present replica molding by PDMS (polydimethylsiloxane) soft lithography (Fig. 1 (a)).

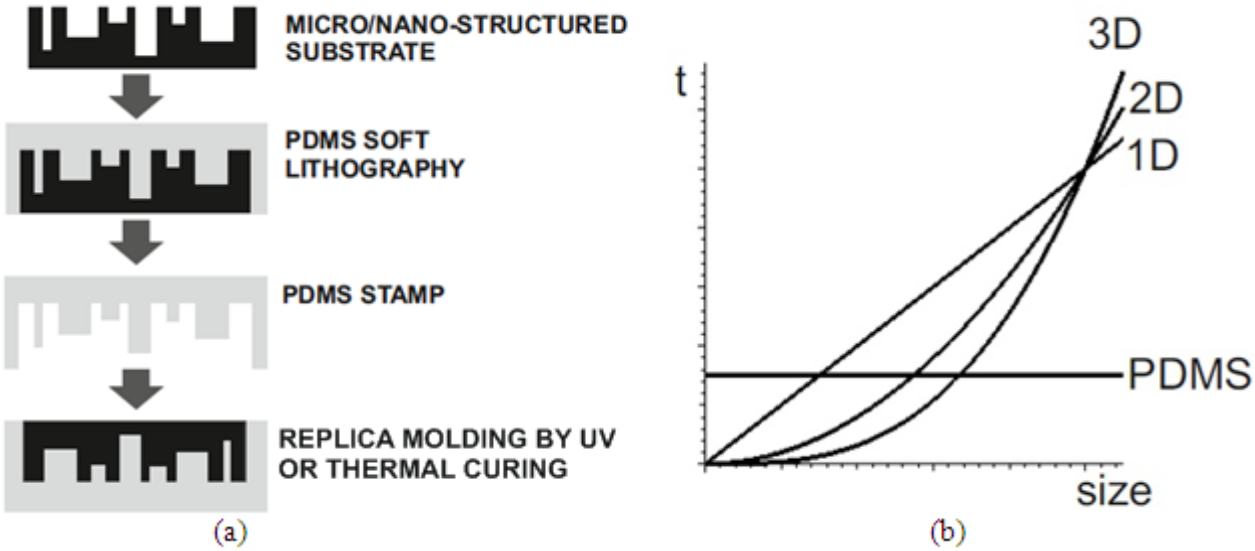

Fig. 1. (a) - schematics of micro/nano-structured object replication using PDMS; (b) Replication by PDMS soft lithography is independent of structure dimensions, because it is cured all at once. Fabricating a structure using multi-photon polymerization requires time consuming serial writing.

Compared to other fabrication techniques, like laser multi-photon polymerization (Fig. 2 (a)), PDMS soft lithography is attractive because of its area (volume) – independent fabrication time (Fig. 1 (b)) and a relatively low cost/quality ratio.

PDMS is a substantial elastomer and stamps made of it may be used up to a thousand times without significant loss of quality. It also allows usage of new materials, that would otherwise not be susceptible to structuring, e.g. PEG-DA (poly (ethylene glycol) diacrylate).

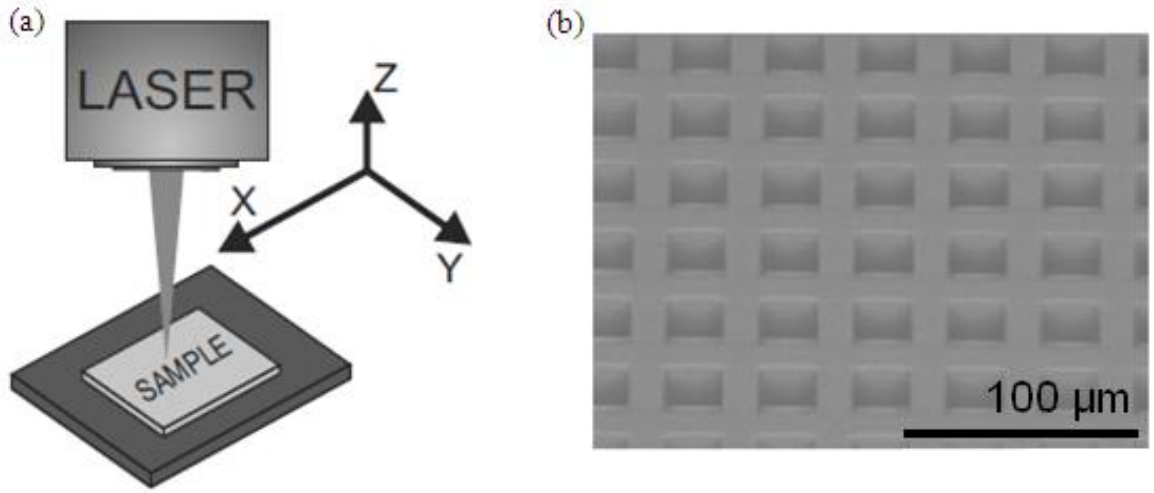

Fig. 2. (a) - The principle of direct-laser writing using multi-photon polymerization. (b) – SEM micrograph of a scaffold out of SZ2080 photopolymer, fabricated using multi-photon polymerization.

We have successfully replicated scaffolds for stem-cell growth (Fig. 3 (b)), reducing fabrication time twentyfold, as well as elements of micro-optics.

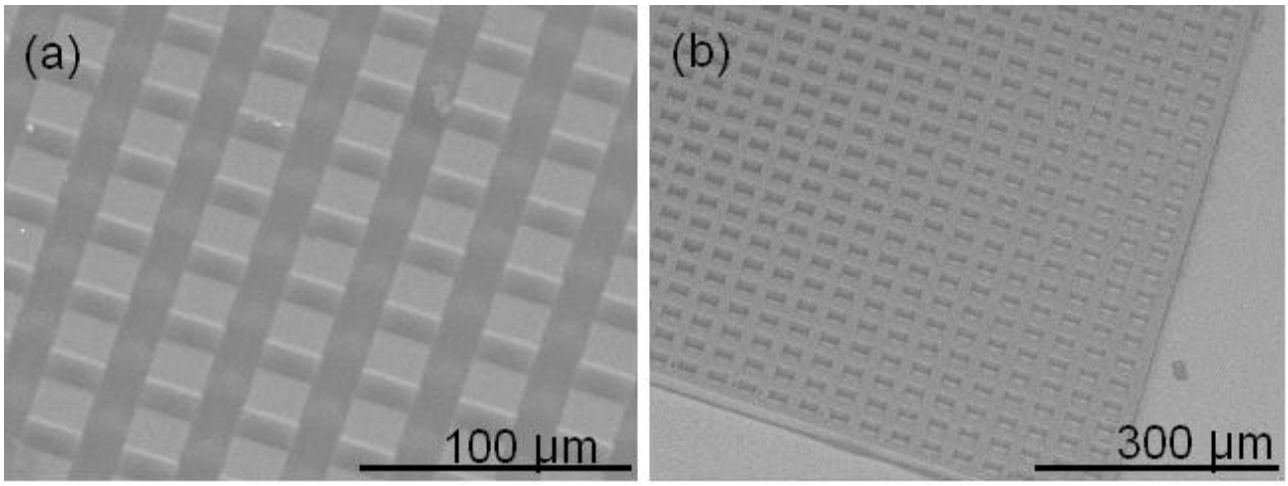

Fig. 3. (a) – a PDMS stamp, made using a SZ2080 master . (b) – a replica of the laser fabricated SZ2080 scaffold, made of PEG-DA-258 polymer.

There is a wide spectrum of other applications which would benefit from this replica molding technique, such as microfluidics, photonic components, plasmonic metamaterials, etc.

[1] M. Malinauskas et al., Large Scale Laser Two-Photon Polymerization Structuring for Fabrication of Artificial Polymeric Scaffolds for Regenerative Medicine, Proc. AIP **1288**, 12-7 (2009).
[2] M. Malinauskas et al., Femtosecond laser polymerization of hybrid/integrated micro-optical elements and their characterization, J. Opt. **12**, 124010 (2010).
[3] G. Kumi et al., High-speed multiphoton absorption polymerization: fabrication of microfluidic channels with arbitrary cross-sections and high aspect ratios, Lab Chip **10**, 1057-60 (2010).

ACOUSTOOPTIC INTERACTION OF LEAKY SURFACE ACOUSTIC WAVES IN YX –$LiTaO_3$ CRYSTALS

J. Belovickis

Department of Radiophysics, Faculty of Physics, Vilnius University, Saulėtekio Ave. 9-III, LT-10222 Vilnius, Lithuania

jaroslavas.belovickis@ff.vu.lt

The acoustooptic interaction provides many possibilities for light control and probing of the acoustic wave properties. Bulk wave acoustooptic devices have found numerous applications as light deflectors, modulators, and tunable filters [1]. The leaky surface acoustic waves (LSAWs) have many advantages as compared to the conventional Rayleigh waves, such as higher velocity and electromechanical coupling coefficient values. In given geometry, the leaky surface wave strongly radiates energy into the substrate in the form of a bulk wave, allowing for efficient acoustooptic interaction. In the present work, the acoustooptic interaction using the LSAW radiation in YX - $LiTaO_3$ has been investigated. The interdigital transducers (IDTs) deposited on the crystal surface were used for acoustic wave excitation.

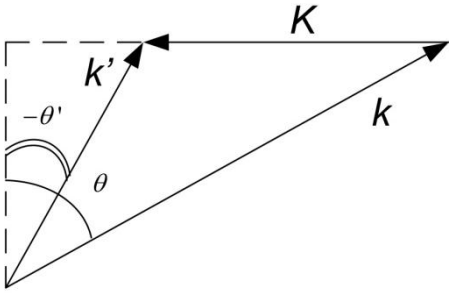

Fig. 1. Wave – vektor diagram of anisotropic light diffraction

The acoustooptic interaction is described using the momentum conservation law [2]:

$$\vec{\mathbf{k}}' = \vec{\mathbf{k}} + \vec{\mathbf{K}}, \tag{1}$$

where $\vec{\mathbf{K}}$ is the acoustic wave vector, $\vec{\mathbf{k}}$ and $\vec{\mathbf{k}}'$ are the wave vectors of the incident and diffracted light. Angles θ and θ' in Fig. (1) define the directions of incident and diffracted light beams with respect to the acoustic wave vector normal.

The dependencies of these angles on the acoustic frequency can be derived from Eq. (1) :

$$\gamma = \arcsin \frac{\lambda f}{2V_{\mathrm{B}} n_{\mathrm{e}}} \left[1 + \left(\frac{V_{\mathrm{B}}}{\lambda f} \right)^2 \cdot \left(n_{\mathrm{e}}^2 - n_{\mathrm{o}}^2 \right) \right] - \frac{\pi}{6}, \tag{2}$$

$$\gamma' = \arcsin \frac{\lambda f}{2V_{\mathrm{B}} n_{\mathrm{o}}} \left[1 - \left(\frac{V_{\mathrm{B}}}{\lambda f} \right)^2 \cdot \left(n_{\mathrm{e}}^2 - n_{\mathrm{o}}^2 \right) \right] + \frac{\pi}{6}, \tag{3}$$

where $\gamma = \theta - \pi/6$ and $\gamma' = \theta' + \pi/6$, λ is the optical wavelength in a free space , f is the acoustic frequency, V_{B} is the velocity of bulk acoustic wave, n_{o} and n_{e} are the ordinary and

extraordinary refraction indices, respectively. The dependencies $\gamma(f)$ and $\gamma'(f)$ calculated from Eq. (2, 3) for the case of YX-$LiTaO_3$ are shown in Fig. (2). The same dependencies, measured experimentally, are also shown in Fig. (2). As seen, the experimental and theoretical curves are in perfect agreement. It follows that the propagation angle of the radiated bulk acoustic wave equals to 30 degrees with respect to the crystal X-axis on the substrate surface and its velocity is 3530 m/s.

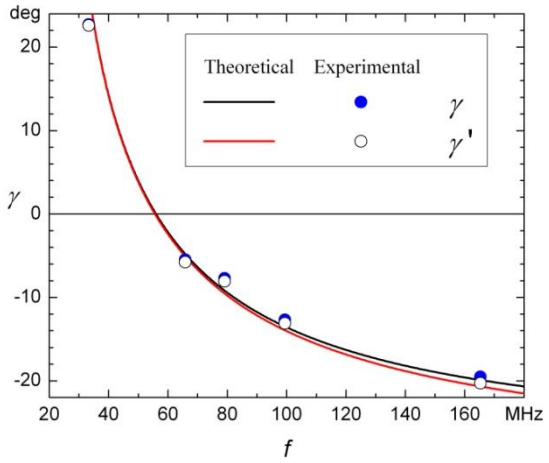

Fig. 2. The experimental (dots) and theoretical (lines) dependencies of angles of incidence (γ) and diffraction (γ') on the acoustic wave frequency in YX – $LiTaO_3$ crystal

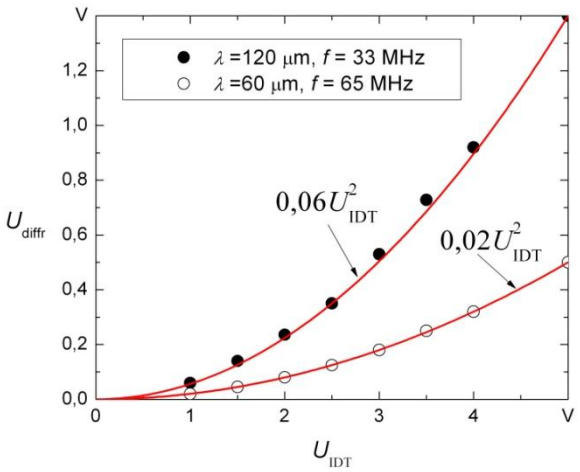

Fig. 3. Dependencies of diffracted light intensity on IDT voltage amplitude at different IDT periods

The dependencies of the diffracted light intensity on the amplitude of radio-frequency (RF) voltage applied to the interdigital transducer are shown in Fig. (3). The curves exhibit quadratic dependencies, in accordance with the theory of acoustooptic interaction. Our experiments revealed that the efficiency of acoustooptic diffraction was different for different IDT periods. In particular, the efficiency increases 3 times when the IDT period is increased from 60 μm to 120 μm.

[1] R. Rimeika, D. Čiplys, P. Každailis, M. S. Shur, Anisotropic acousto - optic diffraction by leaky wave radiation in ZX - $LiNbO_3$, Appl. Phys. Lett., 90, 181935, (2007).

[2] В. В. Леманов, О. В. Шакин, Рассеяние света на упругих волнах в кристаллах, ФТТ, том. 14, *в.* 1, с. 229 - 236, (1972).

GRAPTOLITES FROM SILURIAN ERRATIC BOULDERS OF MOKRZESZÓW QUARRY (LOWER SILESIA, POLAND)

A. Kojelė[1], K. Pluta[2], P. Raczyński[2], S. Radzevičius[1]

[1] *Department of Geology and Mineralogy, Faculty of Natural Sciences, Vilnius University, M.K.Čiurlionio g. 21/27, LT-03101 Vilnius, Lithuania*

[2] *Wroclaw University, Department of Stratigraphy, Institute of Geological Sciences, ul. Cybułskiego 30, 50-205 Wroclaw, Poland, 2.*

andrius.kojele@gmail.com

Graptolites from erratic boulders are known since the 19th Century.

Graptolites from Baltic erratic boulders serve as a tool for taxonomic, morphological, phylogenetic and evolutionary investigations, as well as for population dynamic studies and partly for stratigraphy and Quaternary geology which documents the significance of their investigation.

Mokrzeszów quarry is located in Lower Silesia, Southwest Poland, about 80 km southwest of Wrocław or 60km east of Jelenia Góra, between Wałbrzych and Swidnica towns.

Mokrzeszów quarry is located in the area of the Cenozoic tectonic graben Roztoka-Mokrzeszów, which separates here Świebodzice depression from the Fore-Sudetic Block. The thickness of Cenozoic sediments exceeds 400 m. There are tens of meters composed of glacial grave originating from the Saalian glacier. Lower Palaeozoic limestone is dominating (35–45%) together with Scandinavian crystalline rocks (32–39%). The minor part consists of quartzite, white sandstones, Mesozoic limestones, flints and grey granites. Some of them might originate from the Sudetes.

"Baltic limestone" are found in Central Europe Lowland from Netherlands in the West to West Lithuania in the East, from Rügen Island and the South coast of the Baltic Sea north of Lower Silesia in the South. The southern distribution border of Silurian gechiebes with graptolites coincides with their maximum distribution in Pleistocene (Saalian) glaciers.

Silurian Graptolites variety is enough wide both species quantity and age. *Monograptus flemingi* and *Pristiograptus pseudodubius* are the oldest graptolites, found in Mokrzeszów quarry. They are from the middle Wenlock (*radians – lundgreni* biozones). *Gothograptus nassa* and *Pristiograptus parvus* (*parvus – nassa* biozones), *P. praedeubeli, P. deubel*i (*praedeubeli – deubeli* biozones) are found in the upper Wenlock. P. parvus and G. nassa (parvus biozone) were on the one side of the boulder, and the younger P. praedeubeli (praedeubeli biozone) species – on the other side. Mostly the boulders with the lower Ludlow graptolites are found: *Neodiversograptus nilssoni, Colonograptus colonus, Saetograptus varians, S. chimaera, Bohemograptus bohemicus, Monograptus uncinatus, P. dubius frequens, Lobograptus progenitor, L. scanicus*.These graptolites are from *nilssoni – scanicus* biozones. *Slovinograptus balticus* from *balticus* biozone (Uppermost Ludlow) was found in Mokrzeszów quarry. So, in

Mokrzeszów quarry the middle Wenlock – uppermost Ludlow (the lower Ludlow graptolites dominate) graptolites are found.

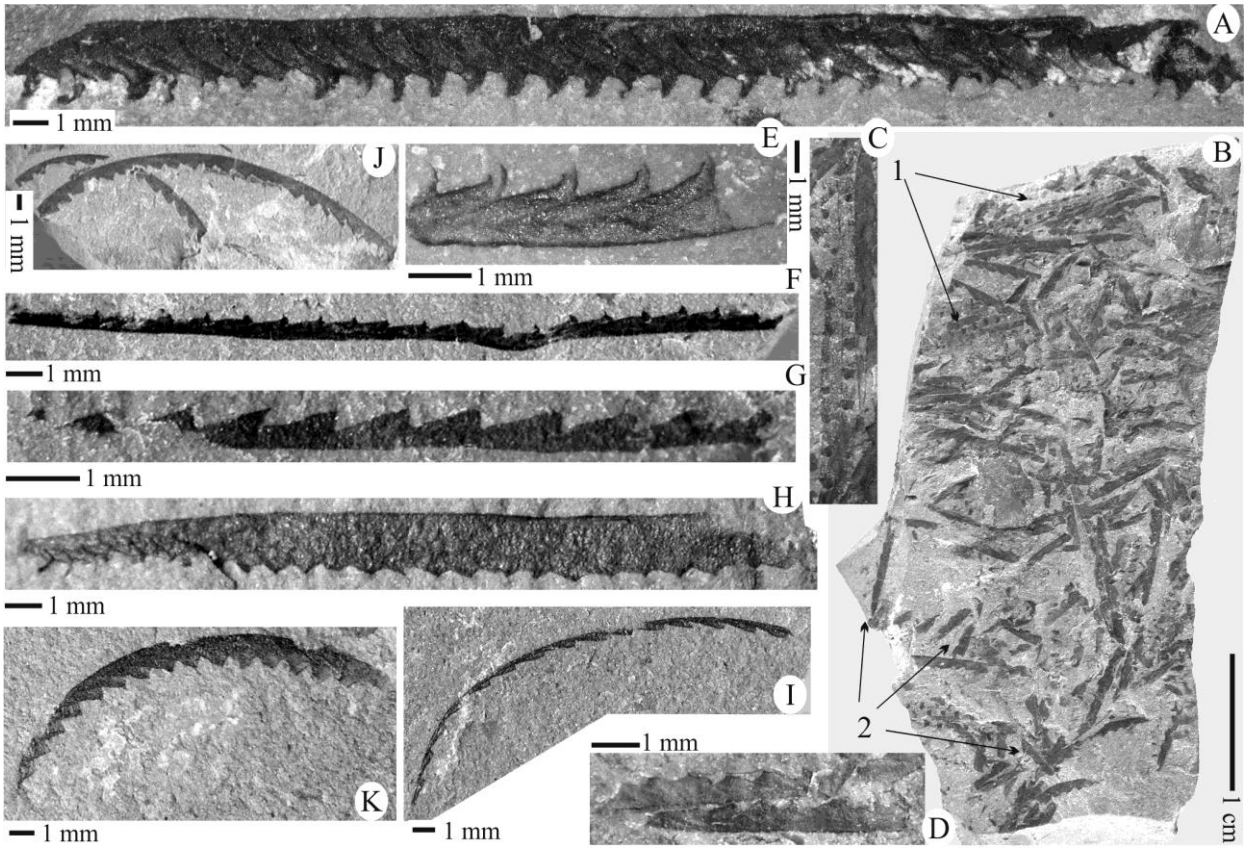

Fig. 1. Some graptolites of erratic boulders from Morkzeszów quary; A – *M. flemingi*, *lundgreni* biozone; B – *G. nassa* (1) and *P. parvus* (2), *parvus–nassa* biozones; C – *G. nassa*, *parvus–nassa* biozones; D – *P. parvus*, parvus–nassa biozones; E – *S. balticus*, balticus biozones; F – *L. scanicus*, scanicus biozone; G – *N. nilssoni*, *nilssoni* biozone; H – *S. varians*, nilssoni biozone; I – *B.* cf. *garrati* scanicus biozone; J – *B. bohemicus*, scanicus biozone; K – *B.* cf. *praecornutus*, leintwardinensis biozone.

The number of investigated samples may not be identical with the real number of glacial erratic boulders, since some of the samples could be fragments of larger boulders. However, it is obvious that boulders with graptolites from the lower Ludlow dominate. The oldest Silurian boulders from that locality refer to the belophorus–lundgreni biozones, while the youngest come from the bohemicus tenuis–kozlowskii biozones. The latter represent the youngest Silurian erratic boulders in Europe yet known. Whether or not this quarry yield even younger Silurian graptolite-bearing erratic boulders needs further investigations.

DESIGNING AND MANUFACTURING OF THE AMPERATOR

A.Matelis

Students' Scientific Association, Faculty of Physics, Vilnius University, Saulėtekio Ave. 9-III, LT-10222 Vilnius, Lithuania

matelis@fidi.lt

The Amperator is a powerful step-down transformer. It was made to present the Joule's law and show how much of energy is being lost in transfer lines.

The Amperator has a very low output impedance, that makes him a powerful current source. Even though the output voltage is approximately 3V AC, it can deliver up to 700Amps of current on short circuit. If we put a nail in between output clamps due to Joule's law it will heat up and melt. The current on the nail can be determined using Ohms law:

$$I = \frac{U}{R + r} \qquad (1)$$

Here U – output voltage, R – samples resistance (typical resistance of a nail is 0.01Ohms), r – inner resistance of the device that is many times less then the resistance of the sample, so all of the voltage drops across the sample. Then, using Joule's law we can determine how much of heat is being exceeded.

$$Q = R \cdot I^2 \cdot t \qquad (2)$$

Here I – current that flows through the sample, t – time. The Power that is dissipated in the sample:

$$P = R \cdot I^2 \qquad (3)$$

Even though Amperator is basicly a step-down transformer it can help a lot of people to understand where is the energy loss in transfer lines, what is inner resistance and what does it do.

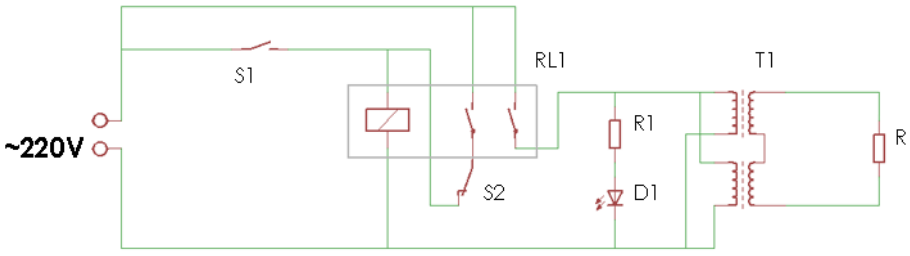

Fig. 1. Schematic of the device

The switch S1 turns on the relay RL1, that enables current flow through the step-down transformer T1. Transformer changes voltage from 220AC to approximately 3V AC. If sample

resistance R is low, a high current will flow through the circuit and a lot of ohmic heat willd be created.

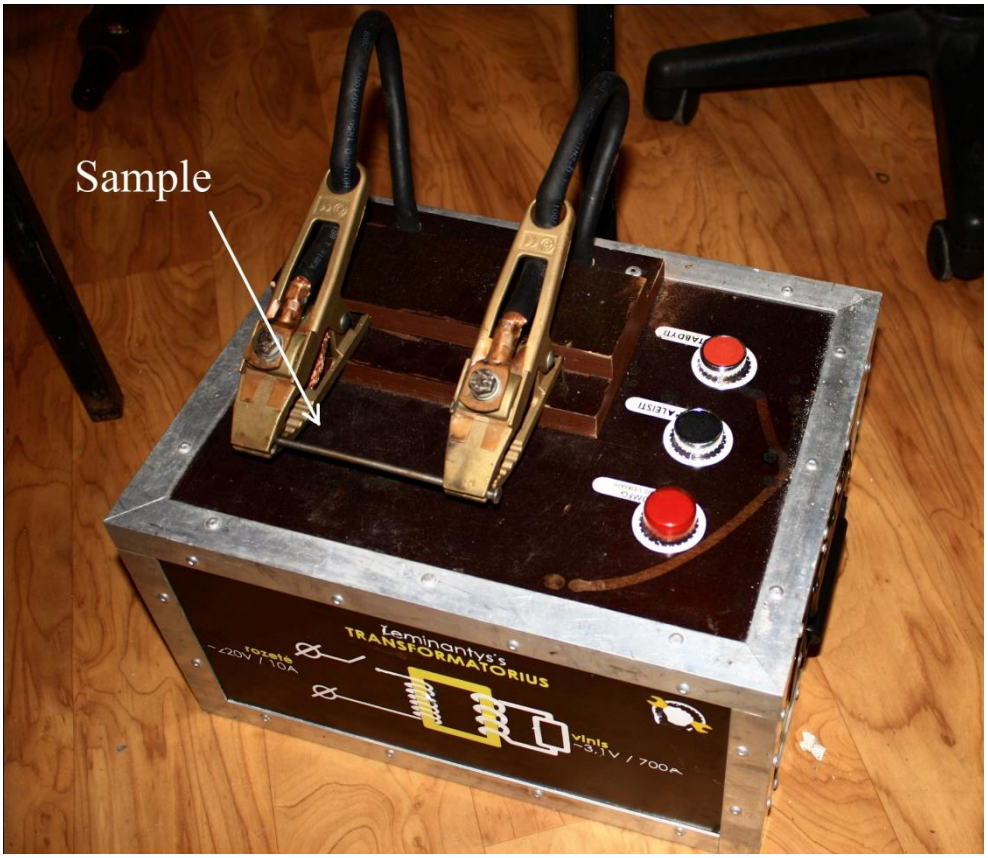

Fig. 2. A nail as a sample in the device

Figure 2 shows a device itself. A nails is usually used as a sample. After couple of seconds after switching on the device nail starts to glow brightly yellow and melts.

ON THE DEVELOPMENT OF IONISING RADIATION DETECTOR - CLOUD CHAMBER

G. Medzevičius

Students' Scientific Association, Faculty of Physics, Vilnius University, Saulėtekio Ave. 9-III, LT-10222 Vilnius, Lithuania

giedrius.medzevicius@ff.stud.vu.lt

Cloud chamber is a device, invented by C. T. R. Wilson in the beginning of 20th century, used for detecting paths of charged particles and other ionising radiation [1]. It can be called the cornerstone of the experimental particle physics, because it gave discoveries of a positron and muon – first discovered elementary particles, which are not, by direct means, a part of an atom.

The operating principle of the cloud chamber is based on the nucleation (formation of droplets) of supersaturated (more than it should be under given conditions) vapour around the condensation nuclei – when a charged particle passes through vapour, it ionises vapour atoms alongside its path and the ionised atoms act as condensation nuclei, forming a cloud.

The original cloud chamber, as developed by C. T. R. Wilson, used the process of adiabatic expansion to form supersaturated vapour, but because of discontinuous operation the active time of track formation was less than a second [2]. However Patrick Blackett partly solved it by making rapid expansions a few times per second. Another great developer of the cloud chamber was Alexander Langsdorf, who developed diffusion cloud chamber – a continuously sensible cloud chamber in 1939 [3].

Since 20th century technologies have greatly advanced and more sophisticated particle detectors were created, pushing cloud chambers out of the research field. Currently, semiconductor devices are being used to detect paths of elementary particles. However, due to its simple construction, diffusion cloud chambers are still being built. Their complexity varies from simple home made to enough technically equipped to produce fairly accurate measurements. Since this device has such a straightforward display of subatomic particles, the goal of this research is to share the experience of building and testing diffusion cloud chamber.

The particular diffusion cloud chamber, which was used in experiment, is shown schematically in Fig. 1. Container walls (and top) [W] are made out of 125x125x4mm Plexiglas plates. The bottom is 1mm thick steel plate [M] with folded sides. It was painted black, for better contrast of particle tracks. Walls, top and bottom of the chamber have been fixed together using adhesive sealant [F]. The heating wire [H] was wrapped on two plastic trays [S], which were connected to the top of the chamber using metal rods [R].

During the experiment, trays were filled with pure isopropanol (2-propanol) and the heating was turned on by supplying power to the metal rods. When the cloud chamber is saturated with isopropanol vapour the bottom is then cooled to temperature, les than 200K.

Bright white tangential light is applied to the side of the cloud chamber to make the isopropanol mist visible. After 2 min. of cooling, a layer of supersaturated vapour [L] starts to form at 2-3 cm above the bottom of the chamber. Obscured trails can be observed at this time, however, it takes approximately 10-15 minutes until the supersaturated layer fully forms.

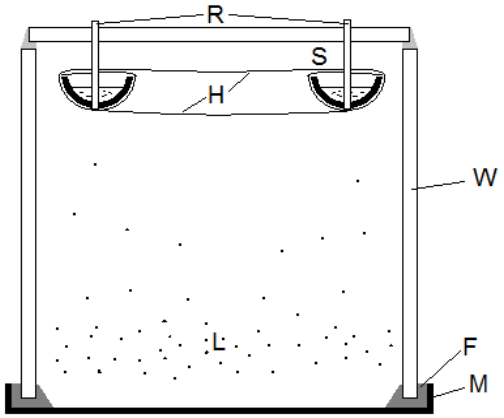

Fig. 1. Scheme of the diffusion cloud chamber used in the experiment

Observed natural background radiation consisted mainly of beta particles, which formed thin (less than 1mm) and relatively long (5-10cm) tracks. However, due to greatly varying energy (in range from keV to MeV), beta particle tracks had different forms, from short and curly (due to interaction with vapour molecules) to straight long lines, although less energetic beta particles were more common. Another common radiation was alpha particles, occurring a few times per minute, compared to several tracks of beta radiation every second. Alpha particle tracks are thick (5-10mm), short (up to 4cm) straight lines. Besides of common tracks, several rare events were also observed. High energy cosmic alpha particles had enough energy to pass through the whole cloud chamber (12cm). High energy alpha particle collision with a molecule was also observed. There were other cosmic ray events, which are not discussed here.

It is important to discuss problems, which occurred during the experiments. The most common problem is setting up the right heating and cooling. Underheating and incorrect cooling resulted in depletion of the supersaturated layer, while overheating caused vapour condensation on the walls. Optimal bottom temperature was found out to be 200-220K. Other problems were cracking of Plexiglas, sealant and paint detaching due to chemical and physical reactions to isopropanol and very low temperatures.

[1] C. T. R. Wilson, On a Method of Making Visible the Paths of Ionising Particles through a Gas, Proc. R. Soc. Lond. A **85(578)** , 285-288 (1911).
[2] C. T. R. Wilson, On an Expansion Apparatus for Making Visible the Tracks of Ionising Particles in Gases and Some Results Obtained by Its Use, Proc. R. Soc. Lond. A **87(595)**, 277-292 (1912).
[3] Langsdorf, A Continuously Sensitive Diffusion Cloud Chamber, Rev. Sci. Instrum. **10**, 91 (1939).

DESIGNING AND CONSTRUCTION OF A "CAN-CRUSHER"

M. Velička, R. Skaisgiris, G. Medzevičius, and V. Čeledinas

Students' Scientific Association, Faculty of Physics, Vilnius University, Saulėtekio Ave. 9-III, LT-10222 Vilnius, Lithuania

velicka.m@gmail.com; rokas.skaisgiris@gmail.com

This device was created to show the abilities of inductive force to students and to explain the basic principles of electric and magnetic fields. Alternating electric current through a can induces a very strong magnetic field, which results in crushing of the can.

The main components of the can-crusher are:

- Microwave oven transformer;
- Four capacitors;
- Trigatron;
- A couple of resistors;
- Diode bridges;
- Electromagnet.

This device is powered by 220V alternating current, which is a standard in Europe. When the device is turned on, the voltage is increased to approximately 2.1 kV in the transformer T1. Then the high voltage current passes through the diode bridge, which was made from 15 cheaper diodes, and we have a direct current of 3kV. Resistor R1 is used to reduce the current, so that the conductors C1,C2,C3,C4 would be charged slower, preventing overcharge and explosion. Then when a special switch, which is covered in oil to prevent short circuiting, is turned on, the current travels through wires and starts charging four parallel connected conductors. In about one minute the conductors are charged to their full capacitances, containing about 2,5kJ of energy. The switches are then turned off to stop the current flow to capacitors. At this point the can-crusher is charged and ready. A thick wire from one end of a capacitor is wound into a coil L1 and connected to special switch called “trigatron”. When a trigger is pressed an alternating current flow through separate wires into the “trigatron” which closes in the two ends of the wire connecting capacitors. When an air gap is reduced, the 3kV electricity ionize air (“fires”) thus the circuit is then closed. When the spark gap fires, current rapidly climbs in the work coil and it creates a rapidly increasing magnetic field within the work coil. Through electromagnetic induction a huge circulating current is induced within the can which then creates a magnetic field of the can. These magnetic fields are of the same polarity and push each other. Because the can is thin it can’t hold the magnetic force that is applied, resulting in the crushing of the can.

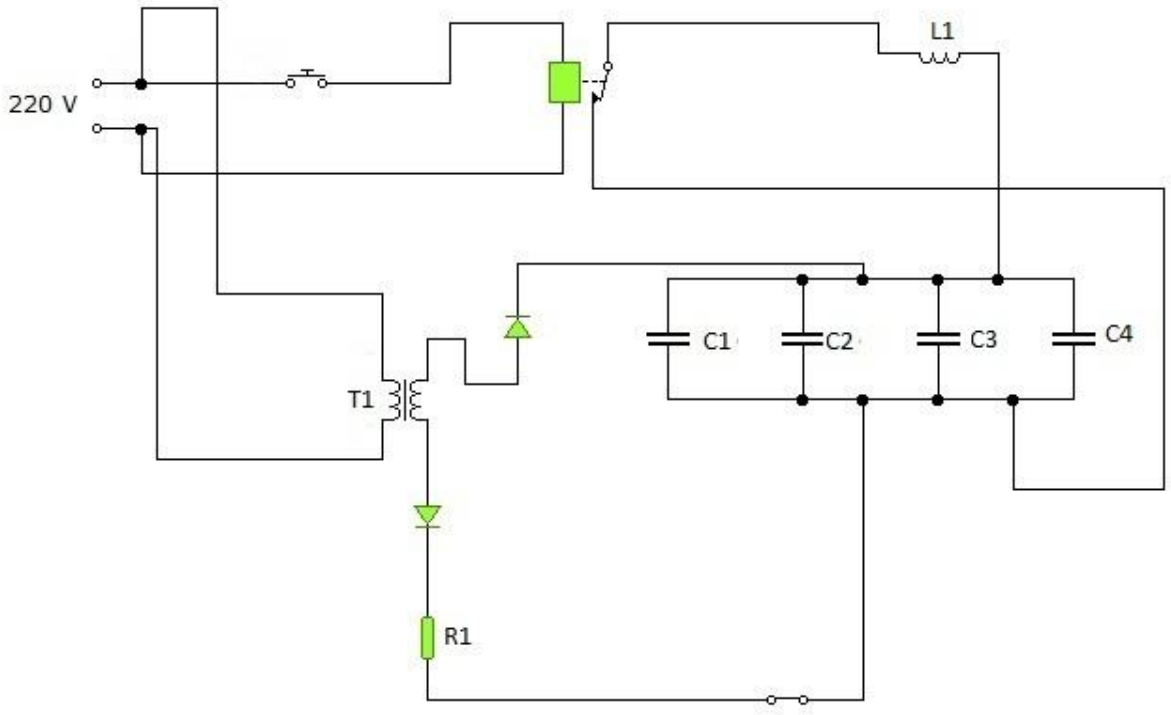

Fig 1. Electric wiring diagram of the can-crusher.

INFLUENCE OF LASER STRUCTURING OF TiO_2 SURFACE TO OPTOELECTRIC FEATURES OF ORGANIC SOLAR CELL

V. Sabonis[1, 3], G. Juška[1], V. Getautis[2], K. Arlauskas[1]

[1] *Department of Solid State Electronics, Faculty of Physics, Vilnius University, Saulėtekio Ave. 9-III, LT-10222 Vilnius, Lithuania*

[2]*Department of Organic Chemistry, Kaunas University of Technology, Radvilenų pl. 19, LT-50254 Kaunas, Lithuania*

[3]*Altechna Co. Ltd., Konstitucijos ave. 23C, LT-08105 Vilnius, Lithuania*

vytautas.sabonis@ff.stud.vu.lt

Recently Grätzel type organic solar cells (GOSC) demonstrated relatively high external quantum efficiency (> 6%), which stimulated interest of their further research. The efficiency of GOSC significantly depends on roughness and porosity of TiO_2 sub-layer, on which the organic dye is deposited. The TiO_2 surface can be formed of different structures: nanowires and nanotubes [1], annealed nano-spheres [2], by laser ablation [3, 4].

The objective of this research is to investigate the influence of TiO_2 layer roughness formed by laser ablation to I-V characteristics of Grätzel type organic solar cells.

For experiments a Yb:KGW femtosecond laser "PHAROS" (Light Conversion GmbH Lithuania) has been used. The light pulse duration τ=280 fs, λ=1064 nm has been used, and the pulse repetition rate can be tuned from 1 kHz up to 350 kHz at average power up to 6W. The harmonics generator "HIRO" (Light Conversion GmbH Lithuania) has been used to generate third harmonic (λ=343 nm) pulses of light. For beam XY positioning the "IntelliSCAN 14" and for Z coordinate the "VarioSCAN 20" (SCANLAB AG Germany) have been used. SCA (Altechna Co Ltd Lithuania) software has been used to compile and execute fabrication algorithms. For beam focusing the F-theta objective field size 160x160 mm, and f=255 mm, has been used. Surface was mapped using profiler, AFM and SEM. Fig. 1 demonstrates an example of TiO_2 ablation.

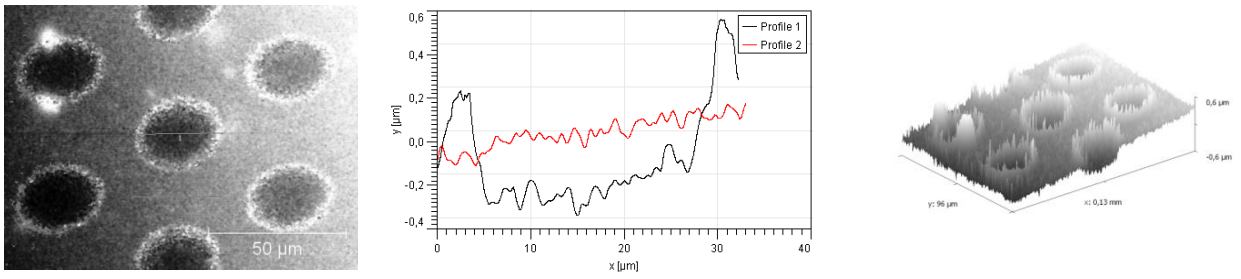

Fig. 1. Ablation mapped using optical profilometer. Profile 1 - ablated region, profile 2 – not ablated region.

Organic layers were vacuum deposited on TiO_2 layers. Metal electrodes were vacuum deposited onto the top of the OSC structures on unaffected and laser ablated TiO_2 regions.

The electric features of formed GOSC structures were investigated by measuring I-V characteristics in the dark and under illumination by AM1.5 light source. The optoelectric

features of GOSC have been investigated and discussed taking into account an influence of TiO_2 sub-layers of various roughness.

[1] Craig Grimes, Karthik Shankar, SPIE 10.1117/2.1200806.1148.
[2] Rui Zhu, Chang-Yun Jiang, Appl. Phys. Lett., **93** 013102 (2008).
[3] H. Kim, G.P. Kushto, Appl. Phys. Lett., **85** 464 (2004).
[4] S.K. Das, K. Dasari, Nanotechnology, **21** 155302 (2010).

ELECTROMAGNETIC WAVE ATTENUATION DUE TO RAIN: EVALUATION OF THE "WORST-MONTH" MODEL

M. Tamošiūnaitė, A. Gruodis

Faculty of Physics, Vilnius University, Saulėtekio Ave. 9-III, LT-10222 Vilnius, Lithuania
milda.tamosiunaite@ff.stud.vu.lt

Atmospheric humidity attenuates the propagating electromagnetic waves. Water molecules scatter (undirected reradiation) and absorb (heating) electromagnetic wave's energy. Therefore, on purpose to design reliable and efficient communication systems, it is necessary to estimate the specific electromagnetic wave attenuation, α.

In calculations of the α-value, a very important parameter is the rain rate, R (mm/h), which is the thickness of a rain precipitation layer, which felled down over the time period of one hour in case when rain precipitation is not evaporated, not soaked into the soil, and is not blown off by the wind [1]. In most of the α-value calculation models, one-minute rain rate values, $R_{(1\text{min.})}$ (mm/h), are required. The $R_{(1\text{min.})}$-value is a R-value, measured with interval of 1 minute and multiplied by 60.

Usually the reliability of communication system must be 99.99%. It means, that system may be unreliable only 0.1% of a year (52.56 minutes a year). Therefore, the $R_{(1\text{min.})}$-value, which is exceeded no more than 52.56 minutes a year, must be known. In Lithuania, the $R_{(1\text{min.})}$-value for 99.99% system reliability is 60.23 mm/h [2].

In cases, when required communication system's reliability is other than 99.99%, the "Worst-month" model can be used. The "Worst-month" model is suggested by the International Telecommunication Union's Radiocommunication sector (ITU-R) [3]. The concept of the worst-month can be applied in terms of rain rate for a period of 12 consecutive calendar months. The annual worst-month for a selected threshold (the $R_{(1\text{min.})}$-value) is described as a month (or 30 days period) with the highest probability of exceeding that threshold. According to the ITU-R's „Worst-month" model, the average annual time percentage of excess, p (%), is proportional to the average annual worst-month's time percentage of excess, p_{m} (%):

$$p = \frac{p_{\text{m}}}{Q}, \tag{1}$$

where Q is the conversion factor; p and p_{m} correspond the same threshold's value $R_{(1\text{min.})}$.

The conversion factor Q is dependent on parameters Q_1 and β. In cases, when a high reliability communication system is required (reliability none less than 97%), the dependency is [3]:

$$Q = Q_1 p^{-\beta}. \tag{2}$$

Considering Lithuania's climate conditions, the ITU-R's recommended Q_1 and β values are 2.85

and 0.15 respectively.

In this work, the ITU-R's "Worst-month" model was estimated for Vilnius city. According to (1) and (2), and using the ITU-R's recommended values $Q_1 = 2.85$ and $\beta = 0.15$, the theoretical *p*-values were calculated. Those values were calculated for thresholds till $R_{(1\text{min.})} = 60.23$ mm/h. The theoretical *p*-values were compared to the measured *p*-values. According to the results, the ITU-R's recommended values $Q_1 = 2.85$ and $\beta = 0.15$ are proper only for thresholds $R_{(1\text{min.})} \geq 34$ mm/h. For thresholds $R_{(1\text{min.})} < 34$ mm/h, the measured *p*-values are double the calculated *p*-values. Therefore, for thresholds lower than $R_{(1\text{min.})} = 34$ mm/h, the Q_1 and β values must be corrected according to measured *p*-values.

[1] R.L. Freeman, Radio System Design for Telecommunications (JOHNWiley&SONS, INC, New Jersey, 2007).

[2] M. Tamošiūnaitė, M. Tamošiūnienė, A. Gruodis, S. Tamošiūnas, Prediction of electromagnetic wave attenuation due to water in atmosphere. 1. Attenuation due to rain, Innovative infotechnologies for science, business and education, Vol. **2 (9)**, 3-10 (2010).

[3] Conversion of annual statistics to worst-month statistics, RECOMMENDATION ITU-R P.481-4 (Question ITU-R 201/3). – 1992-1999-2001-2003-2005.

METHOD OF CERVICAL SMEARS MATERIAL AUTOFLORESCENCE SPECTRA FILTRATION FOR CERVICAL PRE-CANCER DIAGNOSTICS

V. Gėgžna[1, 2], D. Varanius[1, 2], A. Vaitkuvienė[1], R. Kurtinaitiene[3], J. Vaitkus[1]

[1] *Institute of Applied Research, Vilnius University, Saulėtekio Ave. 9-III, LT-10222 Vilnius, Lithuania*
[2] *Faculty of Natural Sciences, Vilnius University, M.K.Čiurlionio g. 21/27, LT-03101 Vilnius, Lithuania*
[3] *Santariškių Klinikos, Vilnius University Hospital, Vilnius, Lithuania*
Darius.Varanius@tmi.vu.lt

Cervical cancer is one of the most frequent forms of cancer in women and more than a half of cases of this disease are lethal [1]. Usually methods of cytology and histology are used for diagnostics of the cancer and its pre-cancer states. Unfortunately, these methods can be realized only by qualified specialists in specialized laboratories. So the purpose of our investigation was to search for supplementary or alternative diagnostic methods based on cervical smear material autofluorescence.

In this research we had samples of cervical smears which were classified into normal and precancerous CIN2+ (cervical intraepithelial neoplasia of 2nd degree or higher) groups according to diagnostic (cytological and histological) tests. Ultraviolet radiation (355nm) of microlaser STA-01-TH was used to excite the samples *in-vitro* and fluorescence spectra were registered. Method of spectra filtration was developed to analyze individual regions of fluorescence spectra. The main procedures of this method are spectra normalisation, rectangular function (i.e. rectangular filter) creation and filtration (Fig.1). This sequence of procedures was repeated 4524 times with different parameters (stat position and width) of filter. Then areas under the curves of filtered spectra were calculated and compared between normal and CIN2+ groups using analysis of ROC curves. Source codes have been developed in order to perform this analysis automatically. In several spectral regions statistical parameter AUC (area under the ROC curve) of 0.71 has been achieved. According to literature [2], this indicates diagnostic value of the test as ‘good’.

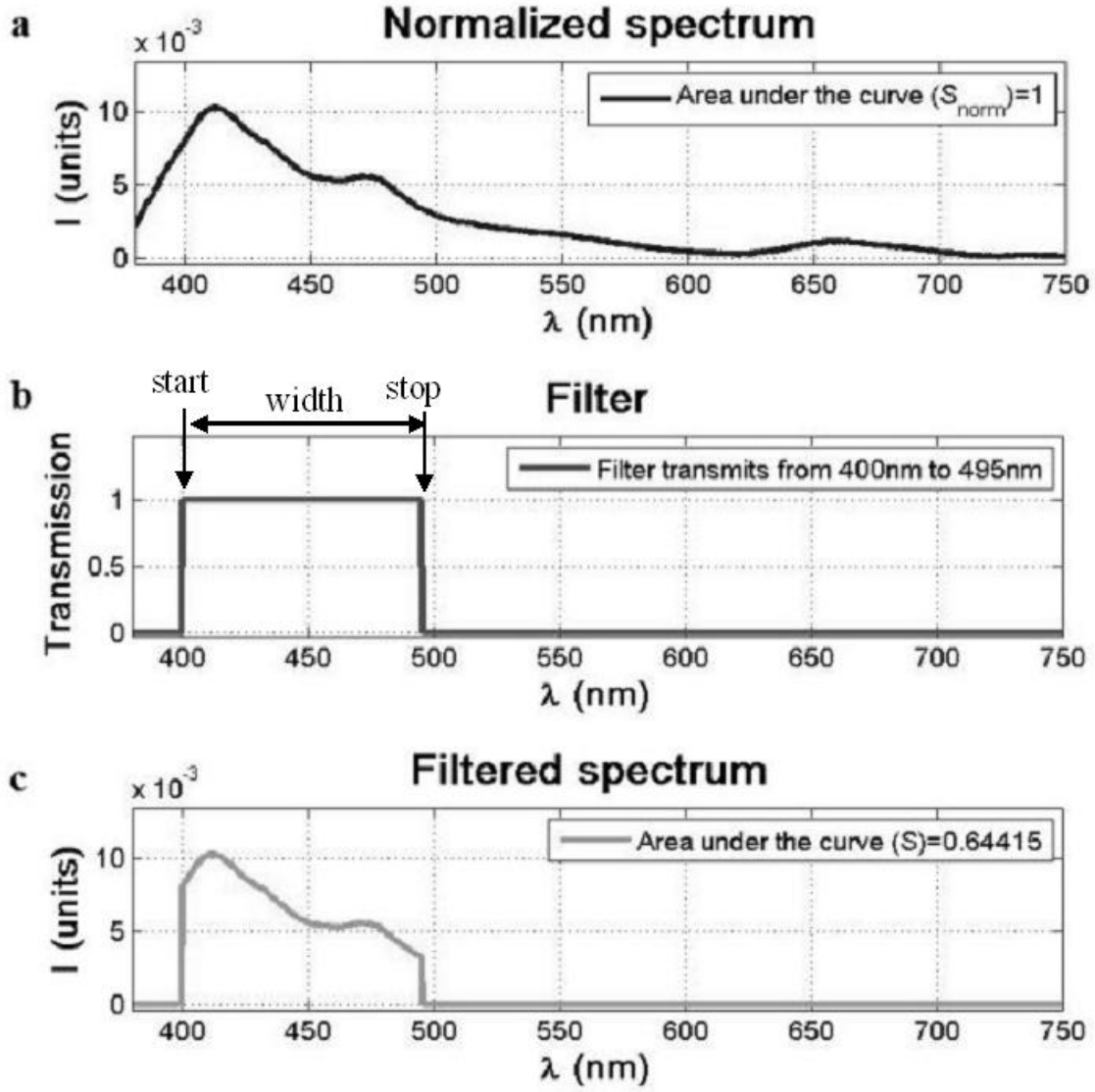

Fig. 1. The main procedures of fluorescence spectra analysis: (a) normalization, (b) creation of filter and (c) filtration. Legend: I – intensity (in arbitrary units), S_{norn} – normalized area under the curve from the baseline, S – area under the curve of filtered spectrum from the baseline, start (stop) – position at which filter begins (stops) transmitting fluorescence signal.

[1] Sankaranarayanan R. Cervical cancer prevention strategies in the developing world. Cytopathology **18** (Suppl 1), 1 (2007).

[2] J. Kurtinaitis, A. Gulbinas, Klinikinių tyrimų metodologija (Vilniaus universiteto leidykla, Vilnius, 2008) pp.13-44.

FEMTOSECOND SOLID-STATE UV LASER SYSTEM FOR THE REFRACTIVE EYE SURGERY

E. Gabrytė[1,2], M. Vengris[1], R. Danielius[2], O. Rukšėnas[3], A. Vaičeliūnaitė[3] and E. Danielienė[4]

[1] *Laser Research Center, Department of Quantum Electronics, Vilnius University, Saulėtekio Ave. 10, LT-10223 Vilnius, Lithuania*
[2] *Light Convertion Ltd, Saulėtekio Ave. 10, LT-10223 Vilnius, Lithuania*
[3] *Faculty of Natural Sciences, Vilnius University, M.K.Čiurlionio g. 21/27, LT-03101 Vilnius, Lithuania*
[4] *Private Practice, Krokuvos 13, LT-09314 Vilnius, Lithuania*

Egle.Gabryte@ff.stud.vu.lt

Laser refractive surgery using excimer ultraviolet (UV) laser was first performed on a human eye in 1990 by Pallikaris et al. [1] and applied in the clinics by Buratto and Ferrari [2]. Ever since, the corrective eye surgery was dominated by ArF excimer laser systems. They ensure an effective and predictable ablation since the absorbance of corneal tissue at ArF laser wavelength (193 nm) is high. However, excimer laser technology has several essential disadvantages. The active medium of the laser is toxic gas, the laser is maintenance-intensive and expensive, the system is sensitive for the environment conditions. The alternatives for the excimer laser in the refractive eye surgery have been actively researched for some time. Utilization of solid-state lasers is very promising since it guarantees stability and a good beam quality. Femtosecond lasers are becoming the routine tools in many ophthalmic procedures, for example, as the replacement of a microkeratome for flap creation in the LASIK surgery; in cataract surgery, corneal transplantation, presbyopia correction, etc. In this study we present a femtosecond all-solid-state system with capabilities of both deep UV laser source and standard IR femtosecond laser, as well as discuss results of the first *in vivo* applications.

A laser system for corneal ablation must meet several requirements. Firstly, energy density at wavelengths of corneal tissues absorption must be high enough for the effective ablation to be ensured. Secondly, the duration of the surgery has to be comparable to that when an excimer laser is used. Our deep UV laser system is based on femtosecond high power Yb:KGW laser "Pharos" (Light Conversion Ltd., Lithuania). When appended with the fifth harmonic generator, the laser provides ~300 fs, 206 nm pulses in a Gaussian beam. The efficiency of the fifth harmonic generator is about 7.7 %, and the output pulse energy is 11.5 μJ (230 mW at 20 kHz repetition rate).

Our previous experiments using 206 nm 300 fs pulses gave excellent results of ablation on model materials such as poly(methyl-methacrylate), gelatin and freshly enucleated porcine eyes [3]. Here we present our first results of *in vivo* experiments on rabbit corneas. Corneas were mechanically debrided and received photoablation at an average power of 100-160 mW and repetition rate of 5-20 kHz with variable spot size. The duration of treatment for a 12 D refraction change within the optical zone of 6 mm was about 100 s with the laser duty cycle of

70%. Fig. 1 shows the progress of flat ablation of the cornea until perforation, performed at a 20 kHz repetition rate and an average laser power of 125 mW. From the cross sections one can see that the cornea keep its shape until it becomes very thin, which indicates gentle action of low energy femtosecond pulses.

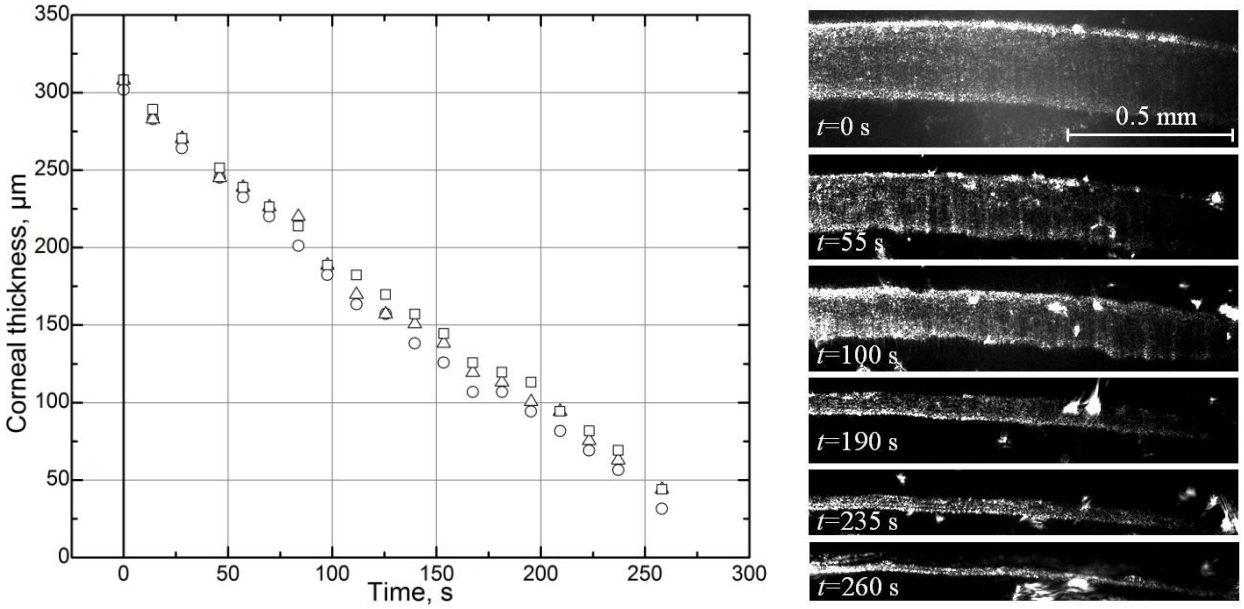

Fig. 1. Change of cornea thickness vs ablation time (left panel) and cross-sections of cornea at different stages (right panel). Different symbols denote measurements at different spots.

In conclusion, the presented laser system has a potential of becoming a versatile ophthalmic laser system due to its high power and wide range of wavelengths. Further research is aimed towards investigation of the safety of short UV pulses, collection of more extensive statistical data is in progress.

[1] I. G. Pallikaris, M. E. Papatzanaki, E. Z. Stathi, O. Frenschock, A. Georgiadis, Laser in situ keratomileusis, Lasers in Surgery and Medicine **10**, 463-468 (1990).

[2] L. Buratto, M. Ferrari, Excimer laser intrastromal keratomileusis: case reports, Journal of Cataract & Refractive Surgery **18**(1), 37-41 (1992).

[3] M. Vengris, E. Gabryte, A. Aleknavicius, M. Barkauskas, O. Ruksenas, A. Vaiceliunaite, R. Danielius, Corneal shaping and ablation of transparent media by femtosecond pulses in deep ultraviolet range, Journal of Cataract & Refractive Surgery **36**(9), 1579-1587 (2010).

MODELLING AND CHARACTERIZATION OF DIFFRACTION GRATING BASED BEAM SPLITTERS

I. Gražulevičiūtė[1], A. Jurkevičiūtė[1], T. Tamulevičius[2], R. Šeperys[1,2], V. Morkūnas[1,2]

[1] *Department of Physics, Kaunas University of Technology, Studentų st. 50, LT-51368 Kaunas, Lithuania*
[2] *Institute of Materials Science of Kaunas University of Technology, Savanorių Ave. 271, LT-50131 Kaunas, Lithuania*

ieva.grazuleviciute@stud.ktu.lt, ausrine.jurkeviciute@stud.ktu.lt

Optical properties of the diffraction grating based laser beam splitters depend on the chosen materials, linear dimensions and profile of the grating. Appropriate set of grating parameters allows controlling intensity and spatial distribution of diffraction spectra. Diffraction optical elements are most efficient only in a narrow wavelength range and are designed and manufactured for every application individually. In this work we present experimental results and simulations of optical properties of visible light diffraction grating based beam splitters.

Diffraction gratings that were used as beam splitters were fabricated in 15x15 mm^2 fused quartz substrates employing optical-contact lithography and plasma chemical etching, that was performed in PK-2430PD unit with mixture of CF_4 (80 %) and O_2 (20 %) gases. The depth of structures was controlled by changing etching duration (18 - 40 min) and it was measured by an atomic force microscope NT-206. Linear dimensions of the formed structures were measured by a scanning electron microscope (SEM) FEI Quanta 200 FEG. The optical properties were evaluated by measuring white light reflection and transmission spectroscopy (spectrometer AvaSpec-2048). More experimental details can be found elsewhere [1]. Numerical simulations of diffraction efficiencies (transmission and reflection spectra) were performed with a standard software ("PCGrate" based on the integral equation method) and additionally calculated using analytical model of a rectangular profile phase diffraction grating, which ridge (*a*) and groove (*b*) are of equal width.

The fabricated phase diffraction gratings of greater depth (etching time 40min) revealed a disagreement between the experimental and simulated diffraction efficiencies. From the obtained SEM micrographs it was found that the profile of diffraction grating is sine trapezoidal (Fig.1.). The change of the initial rectangular profile could be addresses to the anisotropy of plasma chemical etching. Depth of the fabricated structures was estimated from the white light transmission spectroscopy measurements using the (1) equation [2]:

$$h = (2k+1)\frac{\lambda}{2}\Bigg/\left(\frac{n_2^2}{\sqrt{n_2^2 - n_1^2 \sin^2\alpha}} - \frac{n_1}{\cos\alpha}\right) \qquad (1)$$

where α is the angle of incidence, n_1, n_2 – refractive indexes of the incidence media and diffraction grating respectively, $k = 0, 1, 2\ldots$

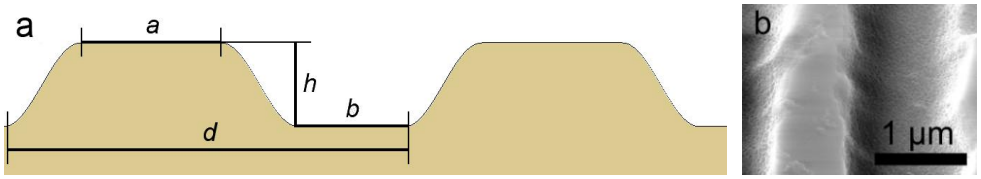

Fig. 1. a) "PCGrate" model of sine trapezoidal profile diffraction grating: *d* – grating period, *h* – groove depth, *a*, *b* – width of the ridge and groove respectively; b) SEM micrograph of the diffraction grating

Numerical diffraction efficiency (reflection) simulations obtained with the "PCGrate" software using sine trapezoidal grating profile are in good correlation with the experimental results (Fig. 2.).

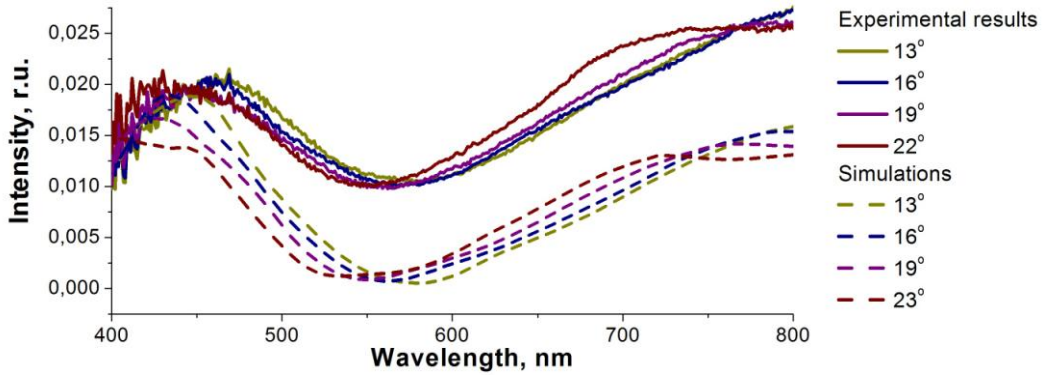

Fig. 2. Experimental and simulation results of absolute diffraction efficiency (reflection) of diffraction grating of period *d*=2 μm, depth *h*=468 nm, *a*=701 nm, *b*=530 nm measured for different angles of incidence.

Results:

- We have shown that our produced beam splitters demonstrate high diffraction efficiencies (73.4%, λ=405nm);
- The disagreement between experimental and theoretical diffraction efficiencies of the fabricated beam splitters was explained by the anisotropy of plasma chemical etching, which causes sine trapezoidal profile of the grating.
- We have demonstrated that depth of the grooves can be evaluated from the white light transmission spectroscopy measurements.

[1] Tamulevičius T.; Šeperys R.; Morkūnas V.; Kopustinskas V.; Andrulevičius M.; Tamulevičius S. Diffraction Grating Based Beam Splitters: Calculations and Implementation *3rd International Conference Radiation Interaction With Material and Its Use In Technologies 2010 materials*. 2010, 357-360 psl.

[2] Tamulevičius T.; Tamulevičius S.; Andrulevičius M.; Janušas G.; Guobienė A. Optical Evaluation of Geometrical Parameters of Micro-Relief Structures *Mater. Sci.-Medzg.* 2006, 12(4), 360-365 psl.

IN-CORE PUMPED Yb-DOPED FIBER AMPLIFIER AND ITS APPLICATION FOR THE AMPLIFICATION OF PICOSECOND PULSES

E. Karpavičiūtė[1,2], N. Rusteika[2], A. Kaušas[2]

[1] *Faculty of Physics, Vilnius University, Saulėtekio Ave. 9-III, LT-10222 Vilnius, Lithuania*
[2] Laboratory for Applied Research, *Center for Physical Sciences and Technology, Savanoriu ave. 231, LT-02300, Vilnius, Lithuania*
Egle.Karpaviciute@ff.stud.vu.lt

Recently a huge progress was achieved in development of ultrashort pulse (<ps) fiber laser technologies [1]. However, due to the nonlinear effects in the core of fiber, producing high energy ultrashort pulse fiber oscillator is complicated [2]. One of the simplest way to solve this problem is to generate low energy pulses with fiber oscillator, and further increase their power in fiber amplifier (MOPA – master oscillator power amplifier - scheme).

In this experiment, the diode pumped fiber amplifier was constructed. The picoseconds pulses from all-normal dispersion fiber oscillator were amplified. Amplifier gain media was glass doped Ytterbium ions (Fig. 1). One of its properties – small quantum defect (~5%), that leads to potentially very high power efficiency.

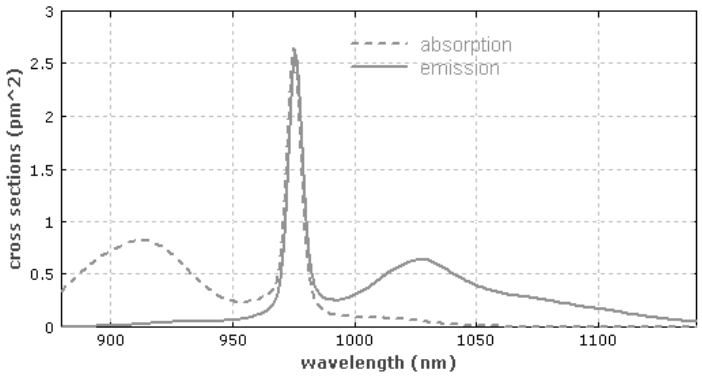

Fig. 1. Absorption and emission cross sections of ytterbium-doped germanosilicate glass, as used in the cores of ytterbium-doped fibers [3].

Measurements were made for several values of pump and input signal powers. It was noticed, that the amplified spontaneous emision (ASE) dominates while having low input powers. With higher powers, the saturation was observed, the gain was increasing slowly (Fig. 2). After shortening Ytterbium-doped fiber, output power increased (Fig. 3).

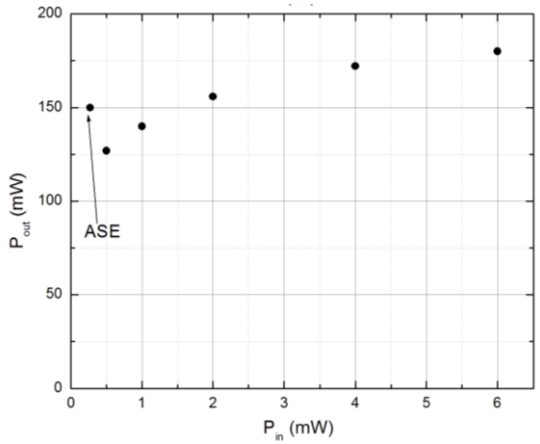

Fig. 2. Dependence of output power P_{out} from input power P_{in}, when P_{pump}=400 mW

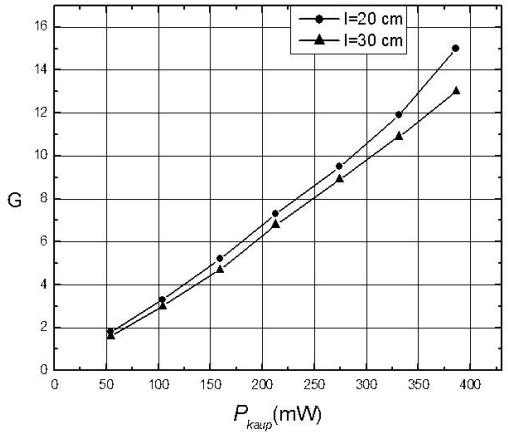

Fig. 3. Amplifier gain G from pump power P_{pump}, with diferent yb-doped fiber lengths. P_{in}=10 mW.

[1] F. Ö. Ilday, J. Buckley, L. Kuznetsova, and F. W. Wise, Generation of 36-femtosecond pulses from a ytterbium fiber laser, Optics. Express **11**, 3550-3554 (2003).

[2] J. R. Buckley, F. W. Wise, F. Ö. Ilday, and T. Sosnowski, Femtosecond fiber lasers with pulse energies above 10 nJ, Optics. Letters. **30**, 1888-1890 (2005)

[3] http://www.rp-photonics.com/ytterbium_doped_gain_media.html (2011-02-21)

THE SPATIAL SHAPE OF THE SPIRAL ZONE PLATE FOCI

A. Kubica[1], P. Migdał[2]

[1] *College of Inter-Faculty Studies in Mathematics and Natural Sciences, University of Warsaw,Żwirki i Wigury 93, 02-089 Warsaw, Poland*

[2] *Institute of Photonic Sciences, Mediterranean Technology Park, Av. del Canal Olimpic s/n, 08860 Castelldefels (Barcelona), Spain*

a.kubica@student.uw.edu.pl

We present a study of optical properties of Spiral Zone Plates (SZPs) [1]. The SZPs are apertures which not only focus light, as well-known (Fresnel) Zone Plates, but also modify its angular momentum. The emphasis of the research is put on the spatial shape of foci, as well as on the behaviour of the beam near a focus.

In the experiment we use a binary SZP, that is a mask [2] consisting of transparent and opaque parts – one/zero transmission (Fig. 1). Such an aperture gives a series of foci with focal lengths *f/n* (where *f* is the major focal length and *n* is an integer). The number of arms indicate the topological charge of the vortex for the major focus. The nth focus has the topological charge *n* times that of the major focus.

The SZP foci have unique properties. The light in the focal plane forms a thin ring with radial fringes (Fig. 2). The radial fringes bend as the plane is moved towards or away from the aperture.

Our experimental findings are supported by both a numerical simulation and a theoretical model based on the Ref. [3].

Fig. 2: Spiral Zone Plate with 3 arms.

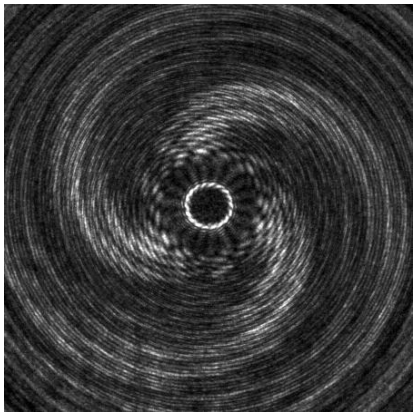

Fig. 3: Image (3mm x 3mm) of a near-focal region of a SZP with 3 arms. The intersection plane is near the 6th focus.

[1] . R. Heckenberg, R. McDuff, C. P. Smith, and A. G. White. Generation of optical phase singularities by computer-generated holograms. Opt. Lett. 17, 221-223 (1992).

[2] P. Migdał, P. Fita, C. Radzewicz, Ł. Mazurek. Wavefront sensor with Fresnel zone plates for use in an undergraduate laboratory. Am. J. Phys. 76, 229-235 (2008).

[3] V.V. Kotlyar et al. Diffraction of a plane, finite-radius wave by a spiral phase plate. Opt. Lett. 31, 1597-1599 (2006)

MODELING OF SELF-ORGANISATION IN THIN METAL LAYERS UNDER LASER IRRADIATION

V. Kučikas, M. Gedvilas, and S. Grubinskas

Center for Physical Sciences and Technology, Savanoriu ave. 231, LT-02300, Vilnius, Lithuania

vytautas.kucikas@gmail.com

Theoretical model is developed of self-organsation effects in chromium layer under incident laser beam. In the actual experiment the beam of a nanosecond pulse laser tightly focused to a line was applied for the back-side ablation of the chromium thin film on a glass substrate. The stripe ablated with a single laser pulse had sharp edges on both sides and ridges of the melted metal around it. Subsequent partially overlapping pulses formed a wide cleaned area with a complicated structure made of the metal remaining from the ridges. Regular structures, ripples, were developed when the shift between pulses was less than half width of the line ablated with a single laser pulse. The ripples were located periodically (4 μm) and were orientated perpendicularly to the long axis of the beam spot. Different theories of the ripple formation in the thin metal film were considered. One of the most probable reason for such metal layer behaviour appears to be surface tension of the boundary air-liquid metal dependence on temperature. This model is developed to estimate the influence of this effect.

The theorem, which describes surface tension dependence on temperature influence to fluid flow near the free surface is known as Marangoni effect. It states that surface tension σ depends on temperature T. Expanding surface tension up to the first order in temperature, we obtain

$$\frac{\partial \sigma}{\partial x} = \frac{\partial \sigma}{\partial T}\frac{\partial T}{\partial x} \tag{1}$$

We omit surface tension dependence on concentration. This equation is applied to boundary condition of air – liquid metal boundary

$$\eta \frac{\partial v_x}{\partial y} = \frac{\partial \sigma}{\partial T}\frac{\partial T}{\partial x} \tag{2}$$

Where η is dynamic viscosity of liquid material, v_x is the tangential component of velocity and y is the normal coordinate.

Full Navier – Stokes equation system needs to be considered because of significant non-linearity effects of the fluid flow:

$$\rho\left(\frac{\partial \mathrm{v}}{\partial t} + \mathrm{v}\cdot\nabla\mathrm{v}\right) = -\nabla\rho + \mu\nabla^2\mathrm{v} + \mathrm{F} \tag{3}$$

$$\nabla\cdot\mathrm{v} = 0 \tag{4}$$

The standard diffusion equation was used for temperature dissipation.

Comsol Multiphysics 3.5 was used for a computational scheme. Moving mesh is also required to model this situation. Calculations to this fully coupled multiphysics simulation was carried out for a wide range of parameters. Typical results are represented in Fig.1 and Fig. 2

Fig.1 The process of ripples formation.

Fig.2 Cooled ripple

[1] K.Regelskis Ripple formation in the chromium thin film during laser ablation. *Applied Surface Science 253 (2007) 6584–6587*

[2] D.Isvoranu Marangoni convection basic mechanism explanation using the two-point theory of mass and heat transfer. *International Journal of Heat and Mass Transfer 47 (2004) 3769-3782*

MODELING OF OPTICAL POLING OF POLYMERS

L. Kučinskaitė[1,2], R. Petruškevičius[2]

[1] *Faculty of Physics, Vilnius University, Saulėtekio Ave. 9-III, LT-10222 Vilnius, Lithuania*
[2] *Center for Physical Sciences and Technology, Savanoriu ave. 231, LT-02300, Vilnius, Lithuania*
Lina.Kucinskaite@ff.stud.vu.lt

All-optical poling of azo-dye polymers is carried out by inducing the second order nonlinearities by means of polychromatic interference of first and second harmonic waves. The optical poling of azo-dyes in the polymer matrix is going through so-called reorientational hole burning and molecular reorientation mechanisms. This is a complex mechanism consisting of three parts:

- photo excitation of azo-dye and isomerization of trans state transforming to cis state;
- cis state relaxation back to trans state of azo-dye;
- molecular thermal induced orientational diffusion.

Kinetic equations for the optical poling model were proposed by J. - M. Nunzi [1], where only the trans state of azo-dye was taken into consideration in the optical poling process. Later, this model has been improved by including into the overall balance of kinetics the molecules in the cis-state [2]. Our simulations are based on this more general model. We obtained infinite system of coupled differential equations for order parameters T_j and C_j, which define 1D all-optical poling model [3]. This system was truncated to 10 equation system and solved for case of CW laser excitation by numerical methods using MATLAB software. It is assumed that before poling process, all azo-dye molecules are in unexcited state (trans state) and oriented isotropically. The parameters needed for modeling of optical poling are found out by fitting to be near to real parameters of materials used for optical poling experiments [4]. The fitting of the theoretical modeling with the measured relaxation of induced second harmonic generation in the "dark" regime is presented on the Fig.1 for azo phenylcarbazole V-628 in polycarbonate polymer matrix. This fitting was obtained with model parameters: single photon excitation rate $4*10^{-5}$ s^{-1}, two photon excitation rate $2*10^{-2}$ s^{-1}, azo dye orientational diffusion coefficient $11*10^{-5}$ s^{-1} and cis isomer relaxation time 400s.

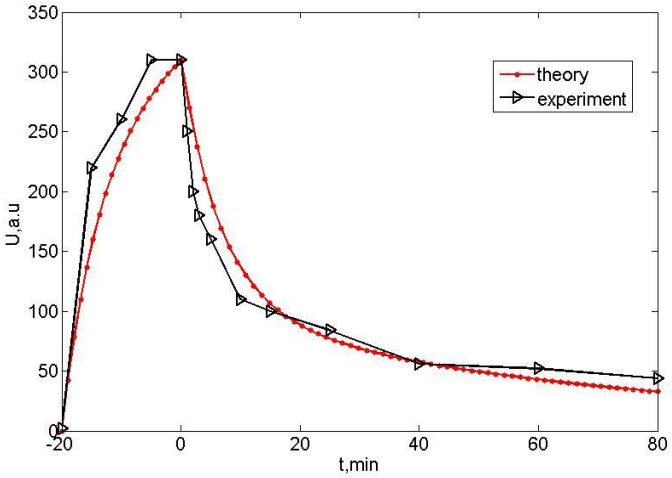

Fig.1. Amplitude of generated second harmonic in phenylcarbazole V-628 versus seeding and reading time in all-optical poling process. Curve with dots is theoretical modeling, with triangles - experimental results.

It is shown that the relaxation kinetics of optical poling can be divided into short – and long – time relaxation kinetics. Long time relaxation kinetics is fully described by diffusion coefficient D_t for the trans isomer. The short time relaxation kinetics depend on the conditions of the micro - texture grating writing and is mainly caused by the relaxation kinetics of the cis isomer and parameters for the reorientation probabilities.

[1] C.Fiorini, F.Charra, J.-M.Nunzi, P.Raimond, Quasi-permanent all-optical encording of noncentrosymmetry in azo-dye polymers, *J.Opt. Soc. Am. B* **14**(8), 1984-2003 (1997).
[2] G. Xu, X. Liu, J. Si, P. Ye, Zh. Li, Yu. Shen, Modified theory of photoinduced molecular polar aliggnment in azo polymers, Opt. Lett., 25(5), 329-331 (2000).
[3] R. Petruskevicius, L. Kucinskaite, G. Navickaite, G. Seniutinas, R. Tomasiunas, Photoinduced Molecular Polar Alignment in E-O Polymers by All-Optical Poling Holographic Methods, IEEE Proc., 4p., (2010).
[4] G. Seniutinas, L. Laipniece, J. Kreicberga, V. Kampars, J. Gražulevičius, R. Petruškevičius, R. Tomašiunas, J. Opt. A: Pure. Appl. Opt. **11**, 034003 (2009).

OPTIMIZATION OF SHORT Er-Yb CO-DOPED DIODE PUMPED LASER

L.G. Krylova

Belarusian State University, Minsk, Belarus

krylova_lubou@mail.ru

The spectral region of $1.5\,\mu m$ is very attractive, as it is supposed to be eye-save and has wide technical and technological applications. The configurations of such lasers are rather different. There are short length resonators and fiber optical amplifiers of different lengths (from few cm up to several meters); different variants of glass lasers and crystal active media lasers, which use end or transverse pumping scheme, laser diode pumping or pumping by Ti: sapphire laser. Nowadays, the most popular system of this type is a diode pumped laser system with glass media co-doped with erbium and ytterbium ions [1, 2].

The question about geometrical and power parameters optimization for this laser type remains actual. In the literature optimizations (for threshold, media length, slope) are done mostly for fiber optical amplifiers; short active media lasers optimization is mostly abandoned.

We held out numerical simulation of short laser. It revealed [2], that optimal geometric and power characteristics can also be determined for this type of lasers.

We consider one-dimensional short-laser model with an active medium been a glass matrix co-activated by Er and Yb ions. We use the four-level schema for the descriptions of the dynamics of populations Yb^+ and Er^+ ions (the up-conversion processes has been neglected).

For the evolution of dimensionless intensities has been used the propagation equation:

$$\frac{\partial f_{\pm}(x,t)}{\partial t} \pm \frac{\partial f_{\pm}(x,t)}{\partial x} = \left(k_{g1} n_4(x,t) - k_{g2}(1-n_4(x,t))\right) \cdot f_{\pm}(x,t) - k_l \cdot f_{\pm}(x,t) + R_{lum}^{\cdot} n_4(x,t) \qquad (1)$$

Polarization and inhomogeneous media issues were not taken into consideration.

Here we discuss results of research towards optimal threshold and slope values. Threshold power dependence on active media length is given on fig.1a for several pump absorption coefficient lp (that is, for several Yb ion concentrations). An qualitative explanation for minimum can be given.

In case of short active media amount of absorbed energy is rather small, so higher puming power level is required to reach generetion threshold. With the increase of media length L amount of absorbed energy raises, so threshold value lowers down to some minimal value. In the case of long active media most power is absorbed near input mirror and the other media part is excited relatively low. This part introduces neglectable amplificcation, and increases losses that lead to threshold value increase.

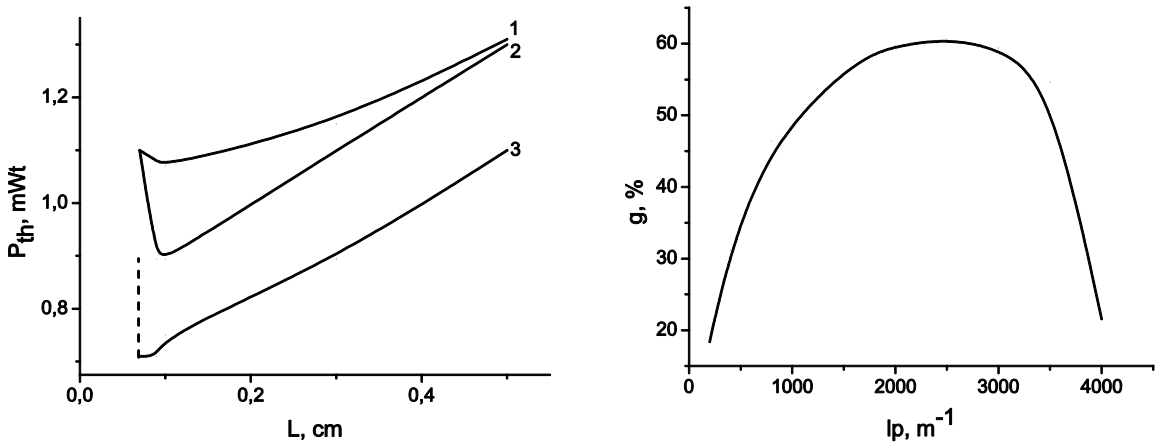

a) b)

Fig.1.a) Threshold vs. active length $l_p = 75\ м^{-1}(1),\ 150\ м^{-1}(2),\ 225 м^{-1}(3)$ $(r_1 = 0.95, r_2 = 0.7, N_{Er} = 3 \cdot 10^{27}\ м^{-3})$; b) Slope vs. pump absorption coefficient $(L_{res} = 2mm,\ N_{Er} = 3 \cdot 10^{28} m^{-3}, r_1 = 0.999,\ r_2 = 0.7)$.

Maximum on fig. 1b in slope versus lp dependence can be explained in the same way. However we point out that despite the same explanation, regions of optimal threshold and slope values differ.

[1] S. Liu, F. Song, H. Cai, T. Li, X. Zang, Z. Wu, J. Tian, , J. of Appl. Phys., 103101 – 103104 (2007)
[2] L.I. Burov, G.G. Krylov, L.G. Krylova, Influence of spatial inhomogeneity of pump energy distribution on output characteristicsof Yb:Er laser with end pump. Nonlinear Phenomena in Complex Systems, № 13, v. 4., 368-380 (2010)

MEASUREMENT OF SCATTERING LOSSES OF LASER COMPONENTS BY TOTAL INTEGRATED SCATTERING METHOD USING DIFFERENT BEAM DIAMETERS

S. Liukaitytė, V. Sirutkaitis

Department of Quantum Electronics, Faculty of Physics, Vilnius University, Saulėtekio Ave. 9-III, LT-10222 Vilnius, Lithuania

Simona.Liukaityte@ff.stud.vu.lt

The scattering of the optical component is caused by : surface topography, surface contamination, bulk index fluctuations, and bulk particulates [1]. Coefficient of the reflection of optical component is decreased and losses of the optical laser system increased due to the scattering [2]. That is the reason why scattering losses must be minimized as much as possible. It is more usual to measure the total integrated scattering (TIS) from a component than to measure the scatter as a function of angle of incidence. The measurement principle of TIS described in International Standard ISO 13696:2001 is based on an Ulbricht sphere as the integrating element for scattered radiation and cw laser [3]. The Ulbricht sphere is standard scattering sphere coated with suitable scattering surface and fitted with a suitable detector for the wavelength of interest. This work explores modified TIS measurement scheme based on repetitively Q-switched laser source. Usage of the repetitively Q-switched laser source allows easier measurements at different wavelengths using one laser with harmonic generators and optical parametric oscillators. The main aim of this work was evaluation of the influence of the laser beam diametre on the TIS measurement accuracy and roughness estimation of the polished substrates.

Measurement of TIS was based on 1 kHz repetition rate Q-switched laser and capable to perform measurements at 532 nm and 355 nm wavelengths. ISO 13696:2001 requires that laser beam diameter on the measurement surface would be larger than 0.4 mm for correct surface roughness estimation. Measurements in this work were taken using four different diameters – some of them bigger (up to 1,12 mm) and some smaller (0.2 mm) than required by the standard. Scattering losses of the entire mirror surface measured using different beam diameters are presented in the Figure 1. From the experiments conclusions was made, that decreasing of the beam diameter increases resolution of the scattering centers, a little bit increases the surface roughness values for local places and increases the duration of the measurements. When the average surface roughness must be evaluated all used in the experiments beam diameters could be used as it changes the roughness values in the range ±10 %.

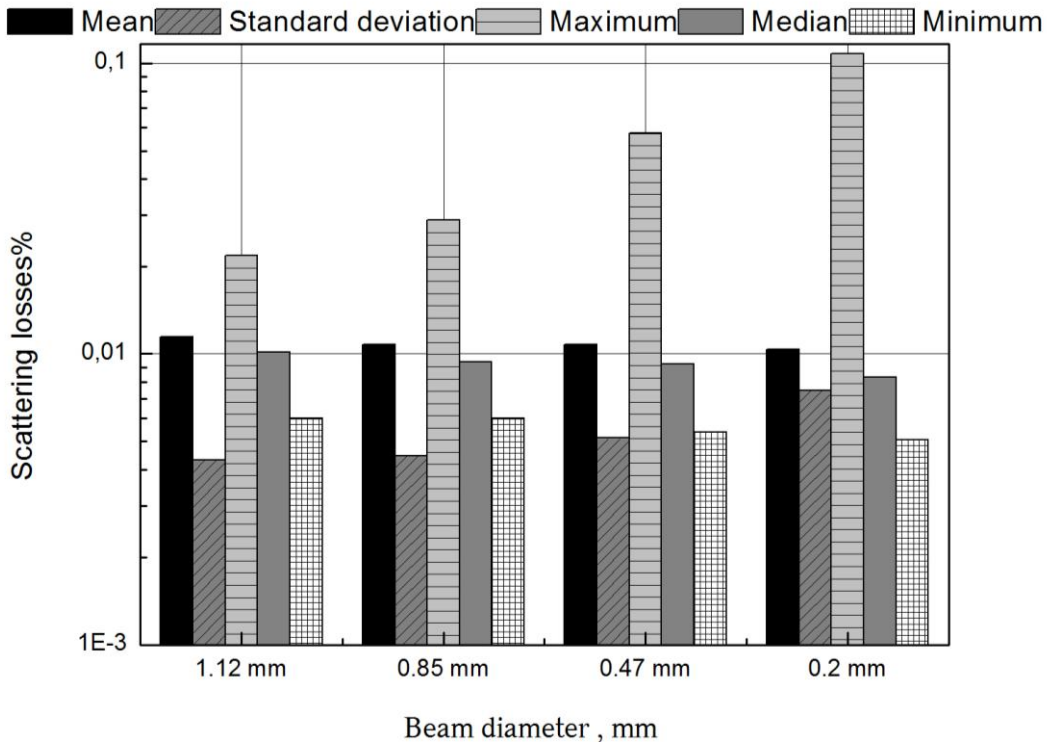

Fig. 1 Scattering losses of the entire mirror surface measured using different beam diameters.

[1] J.C. Stover, Optical Scattering: Measurement and Analysis, S P I E-International Society for Optical Engineering, Bellingham, Washington, USA, 1995.

[2] M. Maciulevičius, Optinių dangų ir lazerinių elementų švesos sklaidos tyrimai plačiame spektro ruože, Daktaro disertacija, Vilniaus universitetas, Vilnius, 2009.

[3] I.O.f. Standardization, International Standard ISO 13696, Optics and optical instruments - Test methods for radiation scattered by optical components, Geneva, Switzerland, 2002.

LASER BEAM PROFILE FORMATION AND MICROFABRICATION OF THIN-FILM SOLAR CELLS

E. Markauskas[1], P. Gečys[2]

[1] *Faculty of Physics, Vilnius University, Saulėtekio Ave. 9-III, LT-10222 Vilnius, Lithuania*
[2] *Center for Physical Sciences and Technology, Savanoriu ave. 231, LT-02300, Vilnius, Lithuania*
Edgaras.markauskas@ff.stud.vu.lt

Efficiency of thin-film $CuIn_xGa_{(1-x)}Se_2$ (CIGS) solar cells with large active area might be maintained if small segments are interconnected in series in order to reduce photocurrent and resistance losses [1]. Theoretical CIGS element efficiency limit reaches 27% [2] with a record value of 20.3% [3] which was demonstrated in laboratory conditions. Cell interconnect formation requires high quality scribing with precise depth control. Laser ablation has been established as one of the most effective method of solar cell element microfabrication method [4]. Scribing the thin-film solar cells with Gaussian beam profile causes damage in the center of laser machined trench and excessive melt formation at the trench edges. To avoid damage and melt formation it is necessary to convert it to a more suitable profile beam [1].

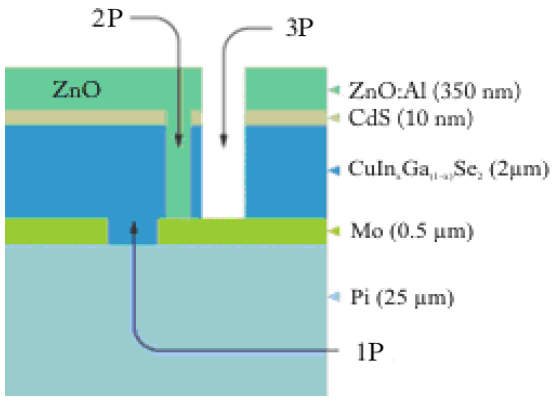

Fig. 1. The structure of CIGS thin-film solar cell element and three scribing processes done at different stages of the production process to form cell interconnect.

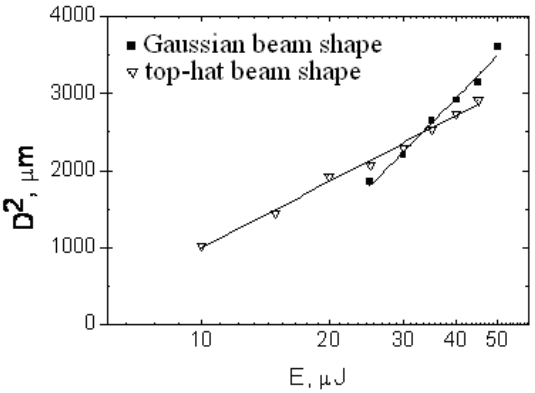

Fig. 2. Relationship between the ablated crater area and laser pulse energy.

The aim of this research was a laser beam profile formation with top-hat laser beam shaper and photovoltaic thin-film processing mode selection in order to maximize the quality and productivity of thin-film laser scribing. The photovoltaic elements used in experiments where complete multilayer thin-film solar cell structures made of ZnO/CdS/CIGS/Mo/Pi layers (Fig. 1). Laser with picosecond pulse duration (10ps), 100 kHz rate and 1064 nm wavelength together with laser beam profile shaper were used in the experiments. In this work, P3 scribing process was studied to expose the Mo back-contact layer. Relationship between the ablated crater area and laser pulse energy is shown in Figure 2. The experiment shows that the laser beam profile has flattened when top-hat laser beam shaper was used.

High quality P3 type scribes in CIGS solar cells using top-hat beam profile were achieved with 500mm/s scanning speed, 5 scans and 0,63 W laser power. Uniform exposure of Mo back-contact was observed with small melted areas at the edges. Using Gaussian beam profile laser scribes were achieved with 500mm/s scanning speed, 3 scans and 0,6 W laser power. In order to maintain damage-free molibdenium back contact less scans were performed, however, wider melt formation areas were observed at the edges.

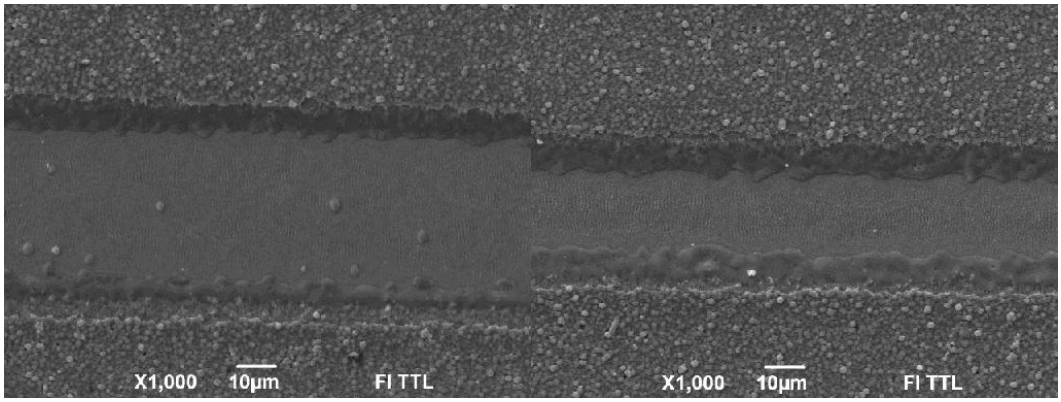

Fig. 3. SEM images of the P3 scribe in CIGS solar element with a) top-hat b) Gaussian beam shapes.

Top-hat laser beam profile increased productivity of thin-film solar cells scribing and has led to greater ablation quality, therefore it has great potential in the roll-to-roll production applications.

[1] P. Gečys, G. Račiukaitis, M. Ehrhardt, K. Zimmer, M. Gedvilas, Applied Physics A: Materials Science & Processing, 2009,101, 373-378.
[2] Cheyney, T. Photovolt. Int. 2008, 1, 8.
[3] Kho, J. Photovoltaics World. 2010, 6, 24-27.
[4] P. Gečys, G. Račiukaitis, M. Gedvilas, A. Selskis, The European Physical Journal Applied Physics, 46, 12508.

SIMULATIONS OF OPTICAL MODES IN InGaN BASED LASER DIODES OPERATING AT 460 NM

G. Muziol[1], C. Skierbiszewski[2]

[1] *Faculty of Applied Physics and Mathematics, Gdansk University of Technology, Gabriela Narutowicza 11/12, 80-233 Gdansk, Poland*

[2] *Institute of High Pressure Physics, Unipress, Sokolowska 29/37, 01-142 Warsaw, Poland*

gmuziol@o2.pl

Nitride based laser diodes (LDs) which cover the emission wavelengths from ultraviolet to the green region recently become a subject of intensive studies. The emission wavelength can be engineered by changing the indium composition in the quantum wells - one can shift the wavelength from ultra-violet up to green from quantum wells [1]. For a successful operation of LDs not only perfect structural quality of grown layers is crucial but also the reduction of the optical losses in the laser structure is of the great importance.

In this work we study a new design for waveguide (WG) and cladding layers (CL) for nitride based true-blue LDs operating at 450-460 nm to reduce optical losses. We calculate the influence of composition and thickness of WG and CL on the confinement factor and internal losses of a LDs (for LDs details see Fig. 1a). A one-dimensional method developed by M. J. Bergmann and H. C. Casey Jr. [2] is used for numerical determination of the transverse electric field distribution. Parameters for calculations were taken from Ref [3]. In Fig. 1b we demonstrate how the thickness of upper cladding layer affects the internal losses. For too thin claddings the mode reaches the highly absorptive upper gold contact which causes unnecessary losses.

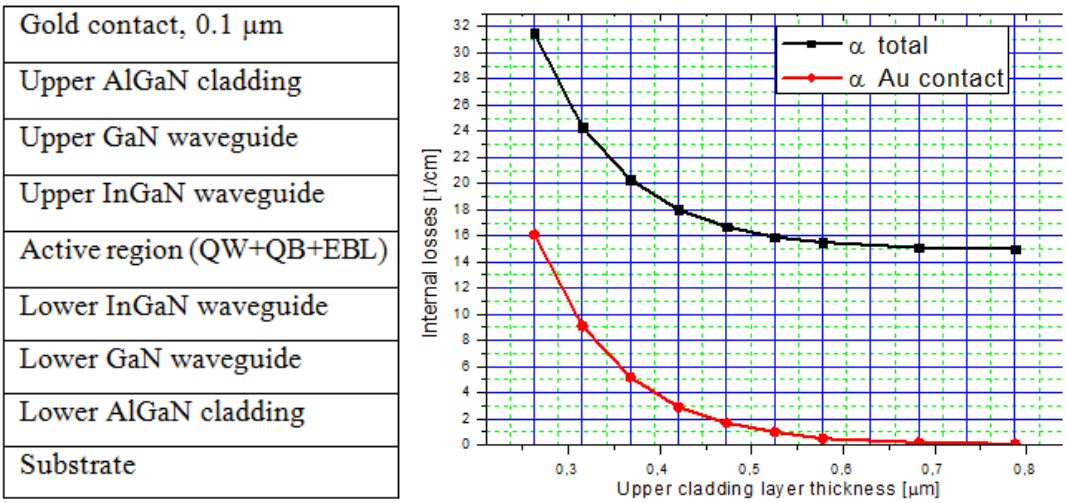

Fig. 1. (a) The simplified LD structure, (b) the influence of upper cladding layer thickness on internal losses for λ=460 nm. Note that cladding thicker than 0.7 µm completely eliminates the absorption in the contact layer.

By changing in the composition of waveguide we can significantly modify the operating parameters of a LD. Fig. 2 shows a comparison between two waveguide designs: a) 180 nm GaN waveguide, b) 180 nm GaN with internal 90 nm InGaN high refractive index waveguide. The second design not only gives a higher confinement factor but also lowers the internal losses

caused by magnesium doped cladding and gold contact. Fig. 3 shows the magnification of optical intensity from Fig. 2. In case of the waveguide without indium the mode leaks to the substrate which negatively affects the far-field pattern [4]. The design with an internal InGaN waveguide eliminates this phenomenon.

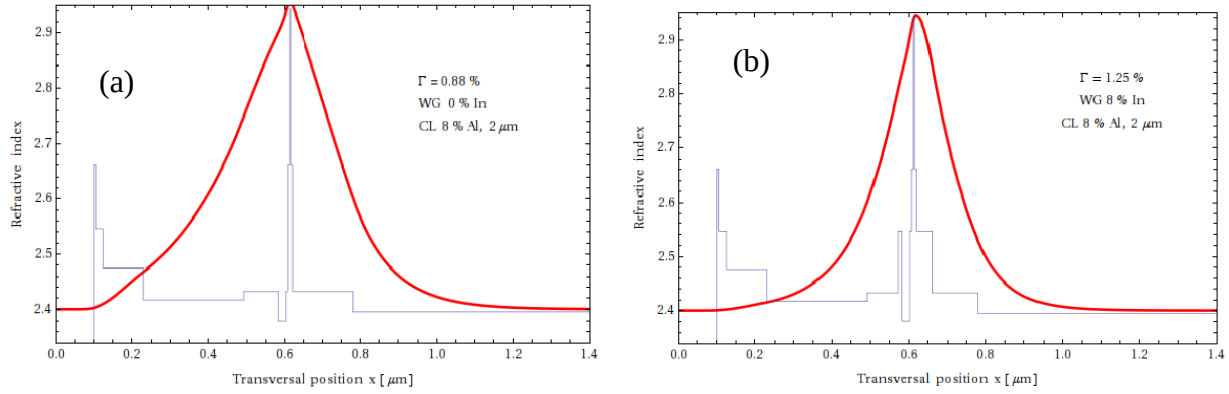

Fig. 2. The cross-section of a LD showing refractive indices (blue) and the optical intensity (red) for λ=455 nm. (a) without indium inside waveguide and (b) with the internal InGaN waveguide.

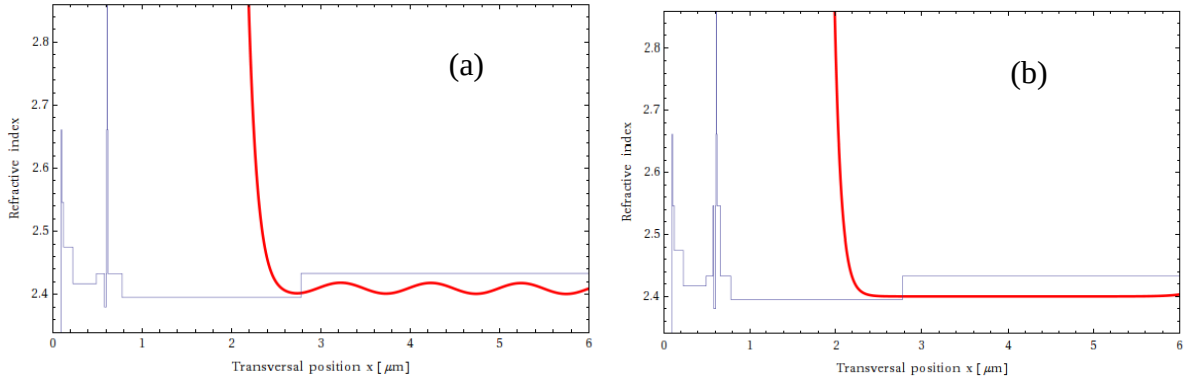

Fig. 3. The magnification showing mode leakage to the substrate for the design without (a) and with (b) the internal InGaN waveguide.

In conclussion, we demonstrated that proper design of the waveguides and claddings reduces the optical losses in the contact layer and the substrate. We will compare one dimensional model prediction with more general two-dimensional method developed by U. Schwarz et al. [5].

[5] J. Wu, W. Walukiewicz, K. M. Yu, J. W. Ager III, E. E. Haller, Hai Lu and William J. Schaff, Appl. Phys. Lett. 80, 4741 (2002).
[6] M. J. Bergmann and H. C. Casey Jr., Journal of Applied Physics, 84(3):1196–1203, 1998.
[7] G. M. Laws, E. C. Larkins, I. Harrison, C. Molloy, and D. Somerford, J. Appl. Phys., 89(2):1108–1115, 2001.
[8] L. A. Coldren and S. W. Corzine. Diode Lasers and Photonic Integrated Circuits. Willey Interscience, 1995.
[9] U. T. Schwarz and B. Witzigmann, “Optical properties of edge-emitting lasers: measurement and simulation”, invited chapter in Nitride Semiconductor Devices, edited by J. Piprek, Wiley-VCH 2007.

OPTICAL PARAMETRIC GENERATION IN 2.7 – 3.1 μm SPECTRAL RANGE IN PERIODICALLY POLED LITHIUM NIOBATE WITH FEMTOSECOND PUMPING

I. Pipinytė, V. Sirutkaitis

Laser Research Center, Department of Quantum Electronics, Vilnius University, Saulėtekio Ave. 10, LT-10223 Vilnius, Lithuania

Ieva.Pipinyte@ff.stud.vu.lt

Optical parametric generation (OPG) is a promising method for development of tunable light sources [1, 2]. These light sources in 2.7 – 3.1 μm spectral range could be useful for analyzing properties of the water rich biological objects, which are characterized by high absorption in this spectral range. It is also important to generate at this wavelength femtosecond pulses with sufficient power for laser micromachining of those biological tissues.

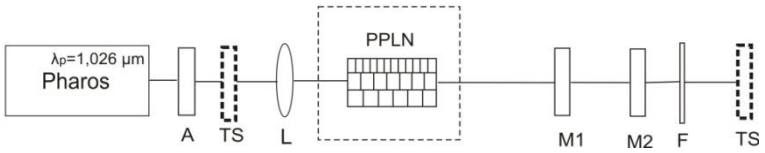

Fig. 1. Experimental setup for measurement of OPG's power characteristics: M1, M2 – mirrors, L –lens, TS –thermal power sensor, f- filter(s), A- attenuator.

The experimental setup (Fig. 1) consist of Pharos laser (Yb:KGW) producing 290 fs pulses at 100 kHz repetition rate at 1026 nm wavelength. We used a 8 mm long and 0.5 mm thick periodically poled lithium niobate (PPLN) structure with 27 gratings, whose periods varied in 0.25 μm step from 25 μm to 31.5 μm. For the generation of the idler wave in 2.7 – 3.1 μm spectral range we used grating with 29.5 μm period. The crystal was heated to 120ºC temperature in the copper oven in order to minimize a photorefractive effect.

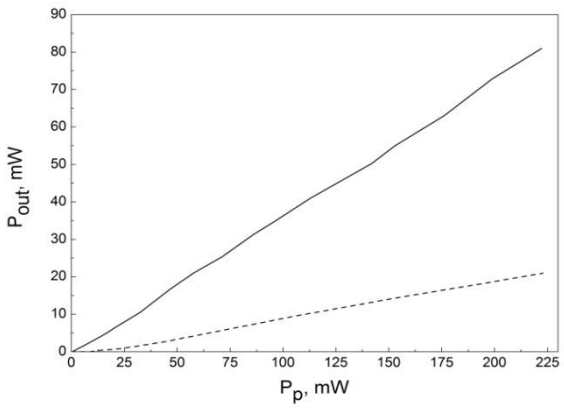

Fig. 2. OPG signal output power (dashed line) and SHG power (solid line) as a function of pumping power.

First of all, the optical damage threshold of the PPLN crystal was found out by taking the measurements of the laser beam diameter on the crystal and energy, which caused surface damage. Measurements showed that damage threshold for S on 1 test with $S=10^6$ pulses with 290 fs duration at repetition rate 100 kHz was 0.02 J/cm^2.

The experimental setup for analysis of the OPG's power characteristics is shown on Fig. 1. Output and pumping power was measured by Ophir Optronics thermal power sensor. Furthermore, two mirrors with high reflection index (~99.6 %) for pumping wavelength (λ= 1.026 μm) were used. Selective filters for required wavelengths were chosen depending which conversion efficiency was measured. Selective filter IKS-5 was used in conversion efficiency to signal power measurements and the filters SZS – 21 and SZS – 25 were used for conversion efficiency to the second harmonic (SHG) (513 nm) measurements. Results are shown in Fig. 2.

Measured threshold pump intensity for parametric generation was equal to 2.77 GW/cm^2 using the 8 mm long PPLN structure. The conversion efficiency from pumping (1026 nm) to signal (1535 nm) was 11 % when 23 GW/cm^2 pumping intensity was reached. Conversion efficiency into SHG was measured 36% when 12.5 GW/cm^2 pumping intensity was reached. Measured data shows, that quite low optical parametric generation efficiency was caused by a competitive process of SHG, which brought away large part of pumping energy.

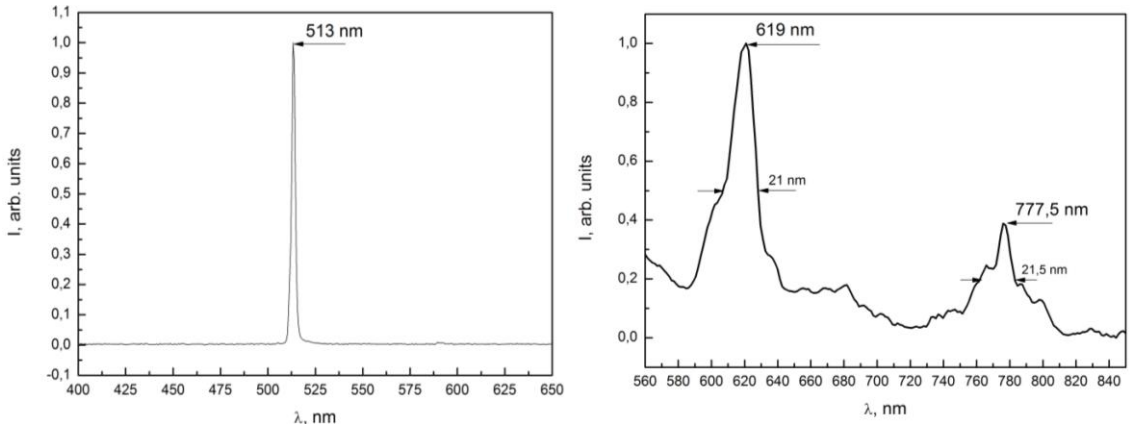

Fig. 3. Registrated spectra of the second harmonics of the pump and signal pulses and spectrum of the sum frequency.

Output parameters of the OPG radiation were measured using Avantes spectograph, with registration range from 200 nm to 1100 nm, i.e. that was too narrow to observe radiation of OPG directly. Recorded spectral distribution is shown in Fig. 3, where spectral line at 619 nm corresponds to the sum frequency generation of signal and pumping pulses, 777,5 nm corresponds to the signal wave's second harmonic and 513 nm corresponds to the SHG of pumping wave.

[1] M. H. Dunn, M. Ebrahimzadeh, Parametric generation of tunable light from continuous-wave to femtosecond pulses, Science, **286**, 1513-1517 (1999).

[2] U. Bader, T. Mattern, T. Bauer et al., Pulsed nanosecond optical parametric generator based on periodically poled lithium niobate, Optics Communication, **217**, 375–380 (2003).

HIGH EFFICIENCY PASSIVE PULSE SHAPER FOR UV PUMPED NOPA

T. Stanislauskas[1,2], G. Veitas[2], R. Danielius[2], R. Grigonis[1,2]

[1] *Faculty of Physics, Vilnius University, Saulėtekio Ave. 9-III, LT-10222 Vilnius, Lithuania*
[2] *Light Convertion Ltd, Saulėtekio Ave. 10, LT-10223 Vilnius, Lithuania*
Tomas.Stanislauskas@ff.stud.vu.lt

Tunable wavelength light pulses with less than 20 fs duration are required for ultrafast molecular dynamics experiment, for example coherent 2D spectroscopy [1]. Such octave wide tunable pulses can be generated at up to 1 MHz repetition rates by a noncollinear optical parametric amplifier (NOPA) pumped by the third harmonic of an Ytterbium laser system [2].

Typical NOPA design employs: white light generator (WLG), an optical parametric amplifier and a pulse compressor. Classical pulse compressor based on a pair of prisms is insufficient in <20 fs regime due to residual third-order dispersion. Other methods are necessary for high-order dispersion compensation of NOPA optical components. Computer programmable pulse shapers based on acousto-optic modulator or liquid crystal mask, which is placed in the Fourier plane of 4f optical systems, allow one to manipulate the phase of the individual frequency components, which permits to compensate complex phase distortions. A simpler alternative of adaptive pulse shapers is 4f optical line with passive phase mask. Such system was developed in commercial NOPA for Ti:Sapphire laser systems – *TOPAS-white* [3] and allows generation of tunable wavelength pulses with duration down to 10 fs. The majority of losses in a pulse shaping apparatus are due to the dispersive element, typically a grating. Energy losses have to be reduced in order to use pulse shaper in the high repetition rate NOPA.

In this contribution we present results on numerical modeling of negative dispersion 4f pulse phase shaper consisting of a prism (near Brewster) as the dispersive element and passive phase mask, which is placed in the Fourier plane. A simplified setup of the pulse shaper model is shown in Fig. 1. A phase mask, which we use in our model, is thin, transparent glass plate with a curvature as a function of the spatial coordinate. Group delay of each frequency component is predefined by a refraction angle in the Fourier plane and the path length in the second prism. Spatial dispersion after the second prism is compensated by double pass through the optical system.

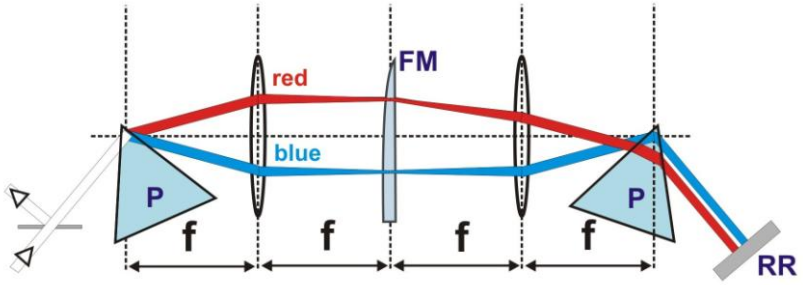

Fig. 1. 4-f pulse shaper configuration (P – prism, FM – phase mask, RR - retroreflector).

The phase mask surface curvature has been estimated using ray tracing technique. We have calculated optical path length and group delay for each frequency component, which is passes all optical system of NOPA, which consists of a WLG crystal plate, pulse shaper, crystals in amplifier and compressor based on material dispersion. Result of the group delay calculation is shown in Fig. 2. Our 3D model of pulse shaper is folded in to a compact 4f configuration with single SF10 prism, spherical mirror instead of the lens and a flat folding mirror in the Fourier plane. The phase mask is positioned in front of the folding mirror.

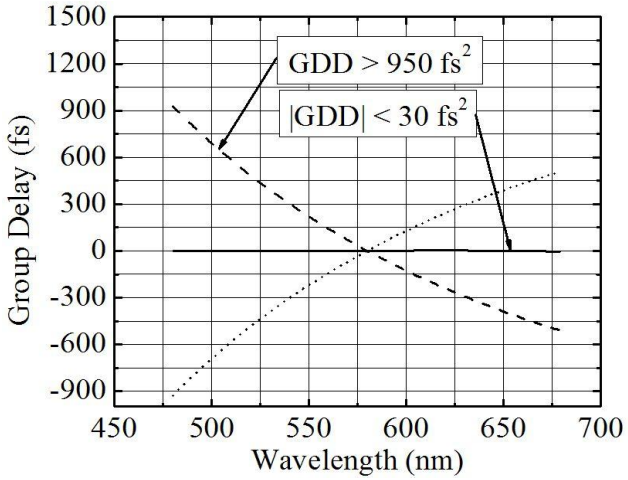

Fig. 2. Dispersion property of the NOPA components. The GDs of materials in WLG, amplification and compression stages (dashed curve), the pulse shaper (dotted curve) and the total NOPA (solid curve) are shown. Also shown is calculated coefficient of group delay dispersion.

The upcoming work is to check newly designed pulse shaper experimentally with a NOPA pumped by the third harmonic of an Yb:KGW femtosecond laser (PHAROS, Light conversion Ltd.).

[1] Two-dimensional electronic spectroscopy of the B800–B820 light-harvesting complex, D. Zigmantas, E. Read, T. Mancal, T. Brixner, A. Gardiner, R. Cogdell, G. Fleming, PNAS **103**, 12672-12677 (2006)
[2] C. Homann, C. Schriever, P. Baum, E. Riedle, Octave wide tunable UV-pumped NOPA: pulses down to 20 fs at 0,5 MHz repetition rate, Opt. Express **16**, 5746-5756 (2008)
[3] www.lightcon.com

FABRICATION OF MICROLENS ARRAYS BY DIRECT LASER WRITING

K. K. Tikuišis[1], K. Belazaras[1], E. Stankevičius[2], and M. Malinauskas[1]

[1] *Laser Research Center, Physics Faculty, Vilnius University, Saulėtekio ave. 10, LT-10223 Vilnius*
[2] *Laboratory for Applied Research, Center for Physical Sciences & Technology, Physics Institute, Savanorių str. 231, LT-02300 Vilnius*

nanopolimerizacija@gmail.com

Various microoptical devices allowing to guide and direct light are used nowadays. Those devices range from microlens, diffraction gratings to photonic crystals. Microlens are now fairly widely used in scientific research and industrial applications, although one can miss a detailed examination of their focusing properties, especially when nearing the nanoscale.

Here we present aspherical microlens arrays of various parameters (Fig. 1) fabricated by means of multi-photon polymerization technique, granting unrelevant flexibility of microsystems design. The arrays are made of hybrid organic-inorganic photoresist ORMOSIL (SZ2080, FORTH), chosen because of its high mechanical resistance and good optical properties.

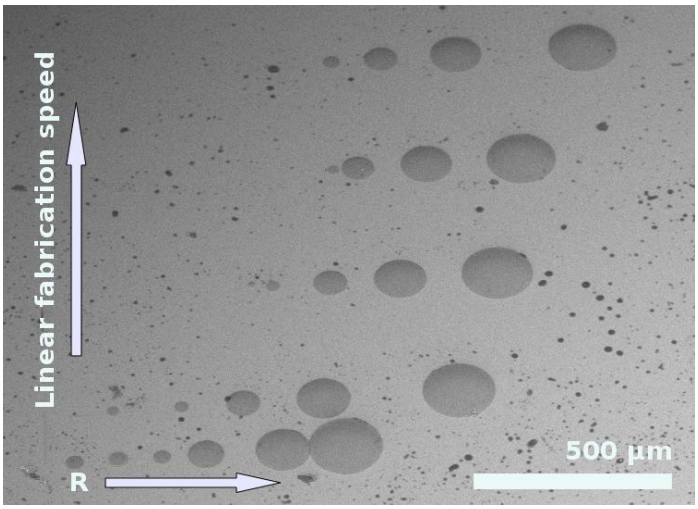

Fig. 1. SEM micrograph of aspherical microlenses with various parameters fabricated by means of multi-photon polymerization.

Microlenses with radii varying from 25 µm to 100 µm and linear translation speed ranging from 1000 µm /s to 1800 µm /s were successfully fabricated. Their focusing properties - specifically focal distance and beam waist radius - were examined (Fig. 2).

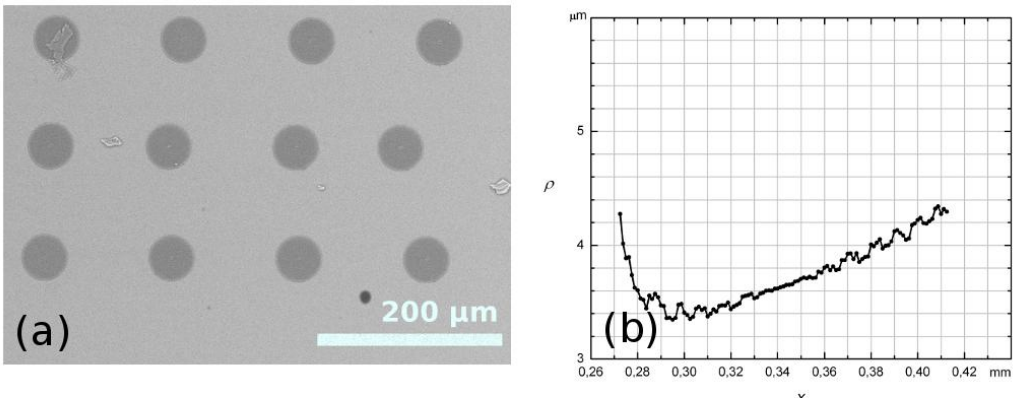

Fig. 2. (a) SEM micrograph of 25 µm radius aspherical microlens array. (b) Beam waist radius (ρ) vs distance from lens surface (x) of one selected microlens.

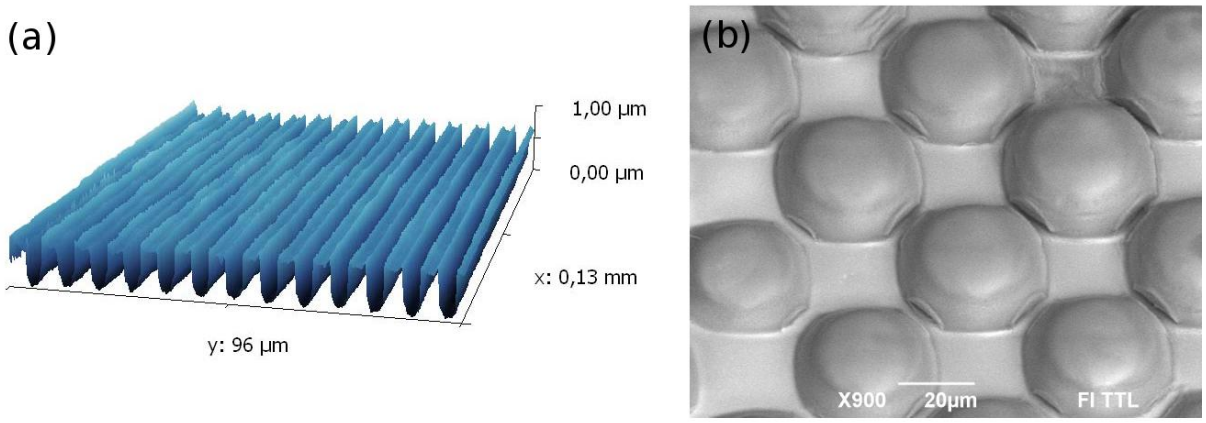

Fig. 3. (a) Surface topography of a diffractive optical element. (b) SEM micrograph of microlens array made by interference polymerization.

One of many possible applications of microlens arrays is their use for multibeam two-photon polymerization processing [2, 3], allowing to noticeably reduce fabrication time of repetitive structures and still employ an unprecedented flexibility of the technology. Here diffractive optical elements and microlens arrays made by interference polymerization technique (Fig. 3) are presented.

[1] M. Malinauskas, A. Zukauskas, V. Purlys, K. Belazaras, A. Momot, D. Paipulas, R. Gadonas, A.Piskarskas, H. Gilbergs, A. Gaidukevičiūtė, I. Sakellari, M. Farsari, S. Juodkazis, Femtosecond laser polymerization of hybrid/integrated microoptical elements and their characterization, J. Opt. **12**, 124010 (2010) .

[2] C. S. Lim, M. H. Hong, Y. Lin, Q. Xie, B. S. Luk'yanchuk , A. S. Kumar, M. Rahman , Microlens array fabrication by laser interference lithography for super-resolution surface nanopatterning , Appl. Phys. Lett. **89**, 191125 (2006).

[3] R. Guo, D. Yuan, S. Das , Large-area microlens arrays fabricated on flexible polycarbonate sheets via single-step laser interference ablation, J. Micromech. Microeng. **21**, 015010 (2010).

MODELING OF ULTRASHORT PULSE GRATING AND PRISM PAIR COMPRESSOR FOR OPTICAL PARAMETRIC CHIRPED PULSE AMPLIFICATION SYSTEM

D. Urbonas

Laser Research Center, Department of Quantum Electronics, Vilnius University, Saulėtekio Ave. 10, LT-10223 Vilnius, Lithuania

darius.urbonas@ff.stud.vu.lt

Every modern high-power ultrashort laser system involves pulse stretcher and compressor. Ultrashort pulses are initially stretched in time and after amplification, they are re-compressed with the help of the reversed dispersion compressor.

The aim of this work was to develop the compressor for ultrashort pulses derived from femtosecond oscillator and further amplified in an optical parametric amplifier. In order to obtain high stretch factor, it is necessary to use highly-dispersive SF 10 bulk glass stretcher. The compressor must compensate not only group velocity dispersion or GVD (that is introduced by dispersive material) but also the third order dispersion or TOD. If left uncompensated, leftover TOD will prevent the pulse from being compressed to its transform-limited duration.

A compressor consisting of grating and prism pairs has been modeled. For any configuration of a grating compressor, the GVD is always negative and the TOD is always positive. However, a prism pair produces negative GVD and negative TOD and can be used complementary with a pair of gratings. The results of output pulse group delay or GD modeling are depicted in fig. 1.

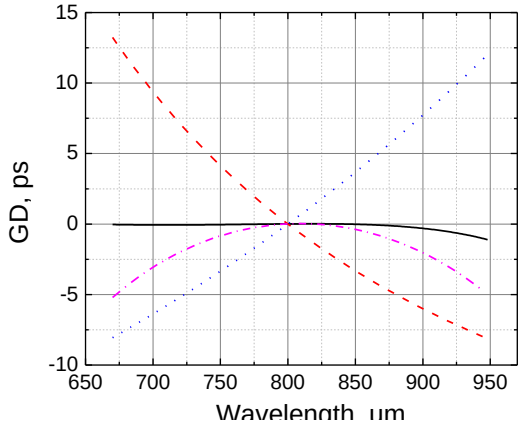

Fig. 1. Compensated GD (solid line), GD induced by glass (dash), grating pair GD (dots), prism pair GD (dash and dot)

[1] C. Wang , Y. Leng, C. Li, B. Zhao, Z. Xu, Parameters optimization and phase analysis of decentered grating stretchers, Optics & Laser Technology 42, 657-661 (2010).

[2] L. P. Kuznetsova, HIGH ENERGY ULTRASHORT-PULSE FIBER AMPLIFIERS (A Dissertation Presented to the Faculty of the Graduate School of Cornell University, 2008).

[3] J. C. Diels, W. Rudolph, Ultrashort Laser Pulse Phenomena (Elsevier Inc, 2006).

STUDIES OF OPTICAL POLING SPATIAL LOCALIZATION

D. Urbonas[1], R. Petruškevičius[2]

[1] *Laser Research Center, Department of Quantum Electronics, Vilnius University, Saulėtekio Ave. 10, LT-10223 Vilnius, Lithuania*

[2] *Center for Physical Sciences and Technology, Savanoriu ave. 231, LT-02300, Vilnius, Lithuania*

darius.urbonas@ff.stud.vu.lt

The beam propagation method (BPM) is an approximation technique for simulating the propagation of light in slowly varying optical waveguides. BPM has several key advantages. First, BPM is an effective method of modeling. Second, BPM is a quick and easy method of solving for fields in integrated optical devices. Third, BPM has also been extended to be applicable to analyze: polarization, nonlinearity, nonparaxiality, reflections and other physical phenomena.

Two coupled Fresnel equations in partial derivatives (3D geometry system) are used to describe first and second harmonic waves in 3D polymer layer with $\chi^2(x,y,z)$ micro-grating pattern:

$$2jk_0 n_{\omega 0}\frac{\partial E_\omega}{\partial z}=\frac{\partial^2 E_\omega}{\partial x^2}+\frac{\partial^2 E_\omega}{\partial y^2}+k_0^2\left(n_\omega^2(x,y,z)-n_{\omega 0}^2\right)E_\omega+k_0^2\chi^{(2)*}(x,y,z)E_{2\omega}E_\omega^* e^{-j\Delta\beta z} \tag{1}$$

$$4jk_0 n_{2\omega 0}\frac{\partial E_{2\omega}}{\partial z}=\frac{\partial^2 E_{2\omega}}{\partial x^2}+\frac{\partial^2 E_{2\omega}}{\partial y^2}+4k_0^2\left(n_{2\omega}^2(x,y,z)-n_{2\omega 0}^2\right)E_{2\omega}+k_0^2\chi^{(2)}(x,y,z)E_\omega E_\omega e^{j\Delta\beta z} \tag{2}$$

where $k_0=k_\omega=\frac{\omega}{c}$, $j=\sqrt{-1}$, $\Delta\beta=2k_0\left(n_{2\omega 0}-n_{\omega 0}\right)$ - phase matching mismatch (determines QPM grating period), $n_{\omega 0}$ and $n_{2\omega 0}$ are refractive indices of the first and second harmonic waves. Induced second-order nonlinear susceptibility is described as follows:

$$\chi^{(2)}(x,y,z)=\chi_{eff}^{(2)}(x,y,z)\cos(\Delta\phi+\Delta kz)\exp\left(-\frac{\alpha_{2\omega}(x,y,z)}{2}z\right) \tag{3}$$

where $\Delta\phi=\phi_{2\omega}-2\phi_\omega$ - phase mismatch, $\alpha_{2\omega}$ second harmonic absorption coefficient and induced effective nonlinear susceptibility:

$$\chi_{eff}^{(2)}(x,y,z)=\chi_{eff}^{(3)}(x,y,z)\,\mathrm{Re}(E_\omega^2 E_{2\omega}^*) \tag{4}$$

Eq. (4) means that we have a generation of static electric field [1].

The above Eq. (1) and Eq. (2) system is so called BPM model of electromagnetic optical poling. Equations are solved by finite difference BPM [2, 3], using the Crank-Nicholson difference schemes with ADI (alternating direction implicit) algorithm. A transparent boundary condition (TBC) capable of handling wave propagation in the infinite space is incorporated in the finite difference algorithm.

3D optical poling results (first and second harmonic intensity distributions and induced $\chi^{(2)}$ distribution) are shown in Fig. 1, where $\chi^{(3)} = 1.8 * 10^{-23} m^2 / V^2$. As shown in Fig. 1, we get depletion of first harmonic and localization effect of second harmonic and induced $\chi^{(2)}$.

During this work 3D optical poling BPM model for focused polychromatic beams has been presented. This model also takes into account optical poling specifics related to the orientational hole burning mechanisms. Furthermore, it was shown that it is possible to achieve spatial localization of induced $\chi^{(2)}$ and depletion of first harmonic.

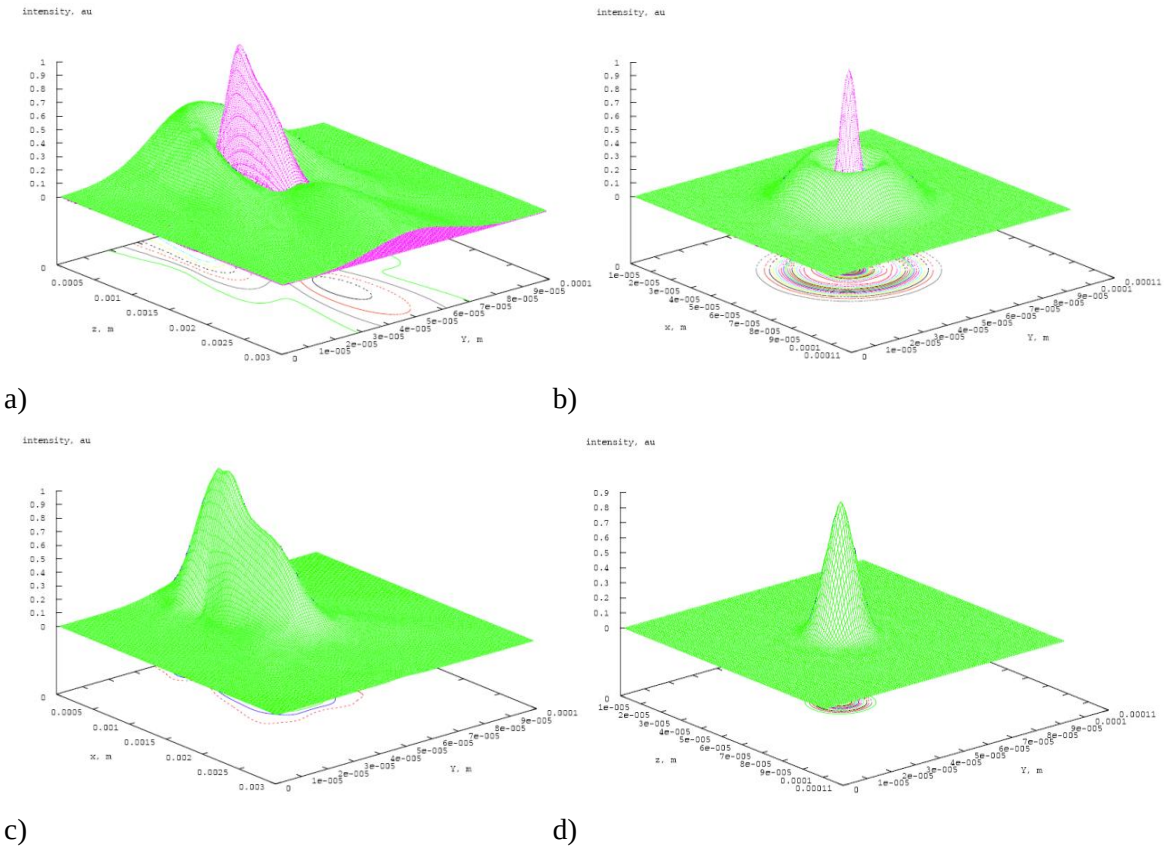

Fig. 1. First (green color) and second (pink color) harmonic distributions (a) - (ZY plane), (b) -(XY plane), where z = 0.7mm, (c) - shows the induced $\chi^{(2)}$ (ZY plane), (d) - induced $\chi^{(2)}$ (XY plane), where z = 0.7mm. In all figures $\chi^{(3)} = 1.8 * 10^{-23} m^2 / V^2$.

[1] P.S. Weitzman, U. Österberg, A modified beam propagation method to model second harmonic generation it optical fibers, Journal of quantum electronics 29, 1437-1443 (1993).
[2] R. Petruškevičius, BPM modeling of three-wave interaction in periodically poled second-order nonlinear materials, Lietuvos fizikos žurnalas 38. 168-175 (1998).
[3] R. Petruškevičius, Artimo lauko ir plačiakampė optika (TEV, Vilnius. 2008).

SPATIAL CHIRP AND ANGULAR DISPERSION DYNAMICS IN FEMTOSECOND NONCOLLINEAR OPCPA

A. Zaukevičius, V. Jukna, R. Antipenkov, V. Martinėnaitė, A. Varanavičius, A. Piskarskas, and G. Valiulis

Department of Quantum Electronics, Faculty of Physics, Vilnius University, Saulėtekio Ave. 9-III, LT-10222 Vilnius, Lithuania

audrius.zaukevicius@ff.stud.vu.lt

Nowadays the noncollinear optical parametric chirped pulse amplification (NOPCPA) [1] is a well established technique for generation of ultra-high-power, few cycle optical pulses. A number of published analytical treatments and numerical simulations on NOPCPA performance optimization focus mainly on achievable gain bandwidths and conversion efficiencies. However in case when pulse length in space is shorter than its transverse dimension it is necessary to consider also the possible spatio-temporal pulse distortions, such as pulse front tilt, angular dispersion, spatial chirp arising as a consequence of noncollinear parametric interaction geometry of NOPCPA.

In this contribution we present the results of theoretical and experimental study on transformation of chirped pulse spatio-temporal characteristics during the amplification in femtosecond noncollinear parametric amplifier.

As it was demonstrated by Akturk et al. [2], pulse front tilt and angular dispersion are not equivalent, thus from pulse front tilt one cannot conclude that pulse has angular dispersion. Alternatively, pulse front tilt can originate from the presence of simultaneous spatial and temporal chirps. The origin of spatial chirp and signal pulse tilt during amplification in NOPCPA can be explained with the help of Fig. 1.

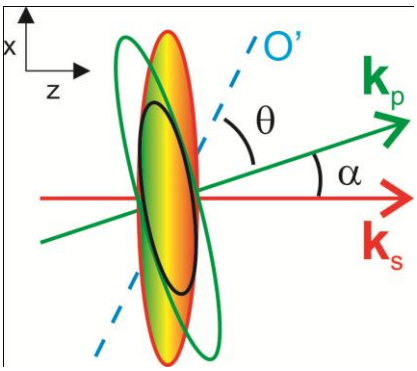

Fig. 1. Noncollinear interaction scheme when pump and signal fronts are mismatched. $\mathbf{k}_s$ and $\mathbf{k}_p$ denote propagation directions of signal and pump pulses, respectively; O' denotes the optical axis; θ – phase matching angle, α – noncollinearity angle.

As one can see the gain contour (defined as overlap area and depicted with the black line) is tilted, i.e. at different time slices different part of signal beam (red line) is amplified. Therefore, during parametric amplification powerful pump (green line) makes signal pulse tilted.

Moreover, if input signal pulse is temporally chirped then different wavelengths are amplified at different transverse positions (Fig. 1), thus amplified signal pulse acquires spatial chirp as well.

These considerations were approved by (2D+1) numerical simulations of BBO-based femtosecond NOPCPA. Signal pulse spatio-temporal characteristics after amplification obtained by numerical modeling are depicted in Figs. 2a-2c. As we can see amplified signal pulse is tilted (Fig. 2a), has spatial chirp (Fig. 2b) and has negligible angular dispersion (Fig. 2c).

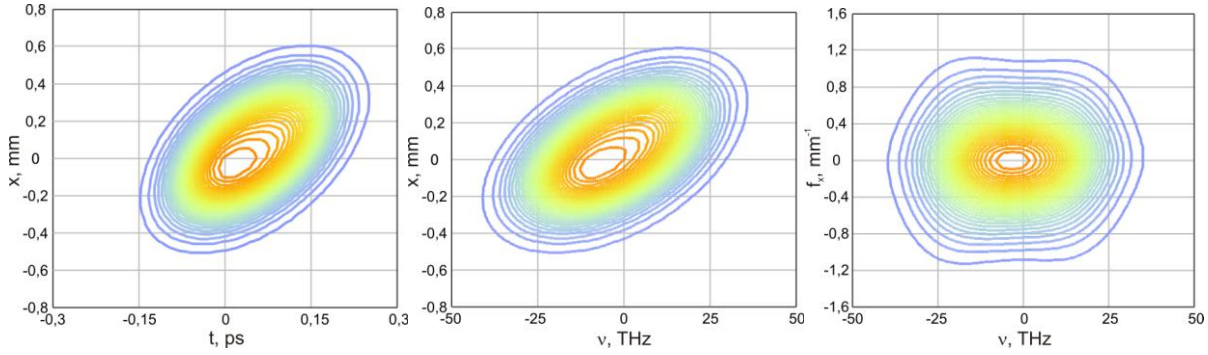

(a) (b) (c)

Fig. 2. Amplified signal pulse intensity profiles in three different domains: (a) space-time domain (x-t); (b) spatio-spectral domain (x-ν); (c) spatio-temporal spectrum domain (f_x-ν).

Also, analytical treatment of this phenomenon have been performed and two important expressions were obtained from which we can conclude that after amplification signal pulse may have angular dispersion or spatial chirp or both at the same time. It depends on the amount of temporal chirp of the signal pulse before amplification: angular dispersion is always decreasing by the rate proportional to γ^{-2} when increasing signal temporal chirp γ, whereas spatial chirp is increasing by the rate proportional to γ.

The theoretical considerations were verified experimentally as well. Obtained results show, that chirped pulses acquired spatial chirp during parametric amplification in case of not matched pulse fronts. This spatial distortion of amplified pulse corresponded to spatial dispersion parameter of ~1 μm/nm, while the angular dispersion was negligible.

[1] Dubietis, G. Jonusauskas, and A. Piskarskas, „Powerful femtosecond pulse generation by chirped and stretched pulse parametric amplification in BBO crystal“, Opt. Commun. 88, 437 (1992).
[2] S. Akturk, X. Gu, E. Zeek, and R. Trebino, „Pulse-front tilt caused by spatial and temporal chirp“, Opt. Express 12, 4399 (2004).

SECOND HARMONIC GENERATION USING BROADBAND FIBER AMPLIFIER OUTPUT

J. Želudevičius, K. Regelskis

Laboratory for Applied Research, Center for Physical Sciences and Technology, Savanoriu ave. 231, LT-02300, Vilnius, Lithuania

ckjulek@gmail.com

Modern pulsed fiber amplifiers and lasers are capable of providing high peak power output with excellent beam quality [1], what makes them attractive for variety of applications. Silica based rare-earth-doped fiber lasers and amplifiers usually work in infrared wavelength region but for some applications shorter wavelength light is more suitable. Frequency conversion can be accomplished using nonlinear crystals [2], however, when high peak power light pulses travel through fiber their spectrum is inevitably broadened due to phase self-modulation. This limits frequency conversion efficiency because nonlinear crystals have limited phase-matching (acceptance) bandwidths. In order to overcome this problem, in this work we investigate experimentally two methods for improving efficiency of second harmonic generation (SHG) using broadband fiber amplifier output.

Our experimental setup consisted of Yb-doped, double-clad LMA fiber amplifier with core diameter of 30 μm seeded by pulsed solid state laser working at 1064 nm wavelength. Two different solid state lasers where used for experiment: one of them generated 15 ps pulses at 4 MHz repetition rate and the other - 8 ps pulses at 100 kHz repetition rate. Fiber amplifier output was directed and focused to LBO crystal (14x3x3 mm), where frequency conversion took place in form of second harmonic generation (critical phase matching setup).

When amplifying 15 ps pulses up to 2 μJ energy in fiber amplifier, light spectrum was broadened up to 1.7 nm because of phase self-modulation. Second harmonic generation energetic efficiency of 50% was easily achieved using this radiation, as crystal phase-matching bandwidth was not exceeded. Theoretical estimation of crystal phase phase-matching bandwidth provides value of 2.2 nm, what is more than the bandwidth of radiation used for second harmonic generation. In contrast, when 8 ps pulses were amplified up to ~3.3 μJ energy, pulse spectrum was expanded much more - to about 24 nm and second harmonic generation efficiency dramatically decreased to less than 10 %. At this point, two different methods for increasing SHG efficiency were implemented and investigated.

First method was based on double pass of first harmonic light through the crystal. Second pass was at some other angle in respect to crystal axes than the first one so phase matching occurred for some different wavelengths than during the first pass. This method increased second harmonic generation efficiency to about 16 % for 24 nm broad spectrum (at 3.4 μJ pulse energy).

Second method was based on spectral splitting (using dichroic mirror) first harmonic beam into two separate beams, so as half of initial beam spectrum goes to one resulting beam and half to another. Next, noncollinear sum-frequency generation was performed in LBO crystal. In this configuration second harmonic generation efficiency of 22 % was achieved (for 24 nm broad spectrum and 3.3 μJ pulse energy).

Experimental results are summarized in Fig. 1, which shows second harmonic average power and first harmonic (pump) spectrum width as function of first harmonic (pump) average power. From presented graph it can be concluded, that second method (based on spectral splitting) allows achieving highest power of SH in comparison with other two methods at highest pump power (and broadest spectrum). Frequency conversion efficiency using this method can be increased twice in comparison with conventional SHG. However, it shows not very good results at lower pump. This decrease at lower pump (in comparison with other methods) can be explained by shorter interaction length as beams travel noncollineary and the distance they overlap in nonlinear crystal is shorter.

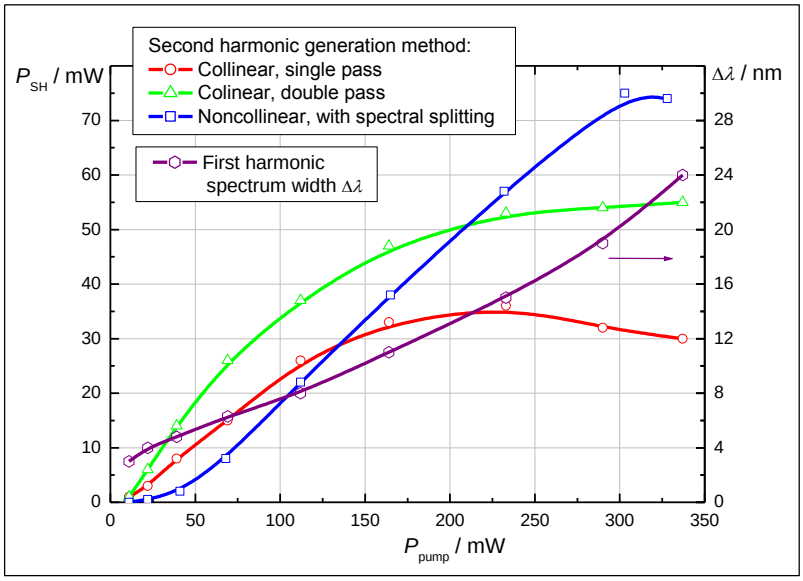

Fig. 4. Second harmonic average power and first harmonic spectrum width as function of first harmonic average power

[1] [1] Roger L. Farrow, Dahv A. V. Kliner, Paul E. Schrader, et al., *High-peak-power (>1.2 MW) pulsed fiber amplifier*, Proc. of SPIE Vol. 6102 (2006)

[2] [2] Dahv A.V. Kliner, Fabio Di Teodorob, Jeffrey P. Koplowb, et al., *Efficient visible and UV generation by frequency conversion of a mode-filtered fiber amplifier*, Proc. of SPIE Vol. 4974 (2003)

FLUENCE DEPENDENT VARIATIONS OF CURRENT AND CAPACITANCE CHARACTERISTICS IN Si PARTICLE DETECTORS

D. Bajarūnas, T. Čeponis, and E. Gaubas

Institute of Applied Research, Vilnius University, Saulėtekio Ave. 9-III, LT-10222 Vilnius, Lithuania

darius.bajarunas@gmail.com

In high energy particle experiments it is very important to register ionising radiation rapidly, reliably and effectively. Therefore, Si pin particle detectors, operating at full depletion regime are commonly employed. However, radiation induced defects affect the detectors functional parameters by the increase of leakage current, of full depletion voltage, and by a reduction of charge collection efficiency, etc [1]. So it is important to investigate the variations of these parameters in radiation damaged diodes. Commonly, these parameters are examined by employing current-voltage (I-V) and capacitance-voltage (C-V) techniques [2].

In this work Float Zone (FZ) and Magnetic Czochralski (MCZ) Si pin diodes irradiated by reactor neutrons at fluences in the range of 10^{12}-10^{16} cm^{-2} have been examined by combined analysis of I-V and C-V characteristics measured at various temperatures. Measurements of I-V and C-V characteristics have been performed by employing Sub-Femtoamp Keithley 6430 electrometer and high precision QuadTech 7600 LRC meter, respectively. Temperature dependent measurements have been carried out by placing the samples in the cryostat.

It has been found that leakage current increases proportionally to a fluence increment of reactor neutrons irradiation at room temperature in FZ and MCZ Si diodes due to the radiation induced defects acting as generation centres. The capacitance obtained at low temperatures (<120 K) in irradiated detectors is invariable with voltage and equal to a value of a diode geometrical capacitance. This indicates a complete compensation of the shallow dopants by radiation traps within a range of low temperatures. It was also shown that different kind defects are produced in FZ and MCZ Si diodes during irradiation by close values of neutron fluence.

[1] B. J. Baliga, Fundamentals of Power Semiconductor Devices. (Springer Science Business Media, LLC, New York, 2008).

[2] P.Blood and J.W. Orton, The Electrical Characterization of Semiconductors: Majority Carriers and Electron States (Academic Press Inc., San Diego, 1992).

INVESTIGATION OF THE AUGER RECOMBINATION PARAMETERS IN Ge BY FREE CARRIER ABSORPTION TRANSIENT SPECTROSCOPY TECHNIQUES

A. Balčytis, A. Uleckas, and E. Gaubas

Institute of Applied Research, Vilnius University, Saulėtekio Ave. 9-III, LT-10222 Vilnius, Lithuania
armandas.balcytis@ff.stud.vu.lt

Due to its high carrier mobility, excellent lattice match GaAs (0.08% lattice mismatch), as well as superior properties at cryogenic temperatures compared to Si, germanium is ideally suited for special applications, such as in multijunction solar cells, strained channel FET's and cryogenic power electronic devices. Precise knowledge of the characteristic parameters for Auger recombination is necessary when developing various power devices, as this process is the limiting factor for carrier lifetime in the indirect-band semiconductors [1]. However, Auger recombination parameters in Ge have been determined with limited precision.

In this work, a linear and the Auger recombination processes in crystalline Ge have been studied in a broad range of excitation conditions using a contact-less pump-probe measurement setup, using free carrier absorption techniques. In order to achieve homogenous excess carrier generation a 100 fs laser of variable wavelength ($\lambda \sim 1/E_g > 2$ μm) was used. Nonlinear carrier density decay transients have been examined by probing the pulsed excited sample by continuous infrared (2.4 μm) radiation. In order to reliably single out the Auger recombination processes in Ge, additional doping and injection level dependant carrier decay transients have been measured at low excitation regime using a continuous wave microwave (ν = 22 GHz) probe [2].

Both, Auger and Shockley-Read-Hall type recombination processes have been observed in Ge wafers. In low injection regime, the characteristic dependence of linear recombination lifetimes on doping level has been determined. At high injection levels, carrier decay processes are determined by the Auger mechanism, for which the inherent parameters have been determined. The results indicate, that the values published by other authors [3], and measured at inhomogeneous excitation conditions, have been overestimated.

[1] P.T. Landsberg, Recombination in Semiconductors (Cambridge University Press, Great Britain, 1991).
[2] K.G. Svantesson, N. G. Nilsson, Measurement of Auger recombination in silicon by laser excitation, Solid-State Electronics **21**, 1603-1608 (1978).
[3] D. Poelman, P. Claws, B. Depuydt, Chemical surface passivation of low resistivity p-type Ge wafers for solar cell applications, Solar Energy Materials and Solar Cells **76**, 167-173 (2003).

INVESTIGATION OF ADSORPTION OF EVAPORATED FROM METAL DISPENSED EMITTERS ELEMENTS ON SCANDIUM OXIDE

A.O. Dudko, O.E. Lushkin

Taras Shevchenko Kiev University, Volodymyrska str., 64, 01033, Kiev, Ukraine.
dudkone@gmail.com

The researches of thermoemitters are relevant because nowadays they are the main element in the microwave devices. The best parameters of these devices are achieved when using Sc metal dispensed emitters (MDE). However, to date there is no clear theory for explanation of the mechanism of the emission for such emitters. Despite the fact that already received a lot of experimental results there is a series of questions, which need to find the answer. One of them is the possible dependence of the emission possibility of the emitters from its structure (needle-shaped formation of the active substance or thick layers of this substance on tungsten matrix) and the composition of the emitting surfaces. So investigation of formation of nanostructures of alkaline earth metals oxides on scandium oxide and development of the model of crystal grow on its surface is relevant.

The researches were carried out in ultra high vacuum chamber at the pressure that does not exceed $6.8 \cdot 10^{-7}$ Pa. There was an Auger analyzer type cylindrical mirror to analyze the composition of the surface. As a substrate compressed mixture of tungsten powder with submicron grains of Sc_2O_3 powder was selected. Activated $2.4BaO \times 0{,}6CaO \times Al_2O_3$ MDE was used as a source of Ba, BaO and Ca components.

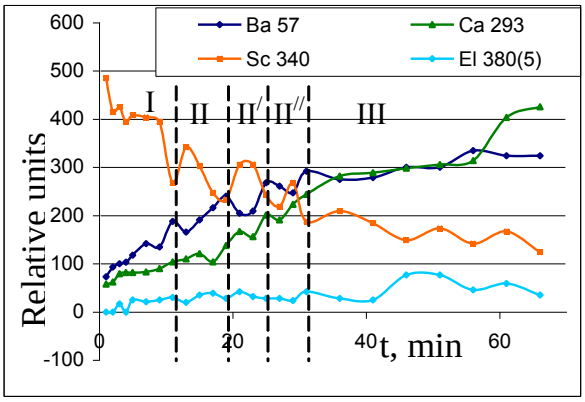

Fig. 1. Time dependence of Auger peak amplitudes of the active substance during MDE sputtering the surface Sc_2O_3.

The experiment showed that scandium oxide surface loosening by barium atoms take place in first minutes of adsorbate sputtering. Our studies also confirmed the main role of calcium oxide molecules for the formation of crystallites on the basis of oxides of alkaline earth metals.

Binding energy of scandium oxide with Ba- and Ca- components differs: Ba- component has bigger thermal stability than Ca- component.

It helps to build a model of complicated structure grow on the scandium oxide surface in which Ba- component adsorbs with a Stranski-Krastanov mechanism and Ca- component adsorbs with a Volmer-Weber mechanism. Grow of Ba- islands and increase of Ca- cone volume depends on a ratio between their volume and surface diffusion coefficients.

FLUENCE DEPENDENT CAPACITANCE-VOLTAGE AND CURRENT-VOLTAGE CHARACTERISTICS IN NEUTRON IRRADIATED Si PARTICLE DETECTORS

R. Dvaranauskas, T. Čeponis, and E. Gaubas

Institute of Applied Research, Vilnius University, Sauletekio Ave. 9-III, LT-10222 Vilnius, Lithuania
Remigijus.Dvaranauskas@ff.stud.vu.lt

Future high energy physics experiments such as experiments at CERN will use silicon detectors for fast and high precision tracking of particles. The high hadron fluences in these experiments cause a crucial damage of the material of detectors. The radiation defect attributed energy levels are introduced in the bandgap of Si thus changing the electrical properties such as leakage current, full depletion voltage (V_{fd}) and charge collection efficiency (CCE). Enhanced leakage currents are observed after irradiation, and this leads to the higher electronic noise and reduction of spatial resolution of particle detectors. V_{fd} increases after irradiation and eventually reaches values beyond the stable range of diode operation. I-V and C-V measurement is a standard tool to characterize the steady-state properties of silicon detectors which provides information on the quality of diode, on amount of leakage current and on depletion voltage, stability and breakdown characteristics.

In this work, the combined analysis of the capacitance-voltage and current-voltage characteristics has been performed on CERN standard Si pad-detectors irradiated by reactor neutrons. The rectification properties of diodes are clearly observed for detectors irradiated with small fluences, while symmetrization of I-V characteristics occurs in heavily neutron irradiated detectors. These observations correlate rather well with C-V characteristics measured on the same detectors, when crucial deviations between conductance and impedance C-V characteristics give rise with enhancement of neutron irradiation fluence. The unveiled effects are explained by the increased role of the carrier capture/generation processes within depleted base regions of a diode. It has been confirmed that the impact of carrier generation/capture currents can be reduced by shifting the measurement regimes towards the high frequency range.

STUDY OF STRESS LOCALIZATION IN POLYCRYSTALLINE GRAINS USING SELF-CONSISTENT MODEL AND NEUTRON DIFFRACTION

A. Baczmański [1], A. Gaj [1], L. Le Joncour [2], S. Wroński [1], M. François [2], B. Panicaud [2], C. Braham [3], and A. Paradowska [4]

[1] *Faculty of Physics and Applied Computer Science, AGH- University of Science and Technology, Al. Mickiewicza 30, 30-059 Kraków, Poland*

[2] *Université de Technologie de Troyes (UTT), LASMIS-ICD, FRE CNRS 2848, 12 rue Marie Curie, 10010 Troyes, France*

[3] *PIMM, CNRS UMR 8006, Ecole Nationale Supérieure d'Arts et Métiers, 151 Bd de l'Hôpital 75013 Paris, France*

[4] *Rutherford Appleton Laboratory (ISIS), Chilton Didcot, Oxfordshire OX11 0QX, UK*

gaj.anita@gmail.com

The time of flight neutron diffraction technique and the elastoplastic self-consistent modelling were used to study behaviour of single and multi-phase materials. Critical resolved shear stresses and hardening parameters in austenitic and austeno-ferritic steels were found. The special attention was paid on transition between elastic and plastic range during deformation. Moreover, the evolution of stress localization tensor in function of macrostress was estimated from self-consistent model by fitting theoretical lattice strains to experimental values. Model predictions were successfully compared with experimental results for both phases of the duplex steel and also for austenitic steel.

[1] Clausen B, Lorentzen T, Bourke MAM, Daymond MR. Mater Sci Eng A 1999; 259: 17–24.
[2] Baczmanski A, Braham C. Acta Mater 2004;52:1133-1142.
[3] Dakhlaoui R, Baczmański A, Braham C, Wronski S, Wierzbanowski K, Oliver EC. Acta Mater 2006;54:5027 -5039.
[4] Cai S, Daymond MR, Holt RA. Acta Mater 2009; 57: 407–419.

LASER ABLATION MODELING OF CIGS SOLAR CELLS

S. Grubinskas

Center for Physical Sciences and Technology, Savanoriu ave. 231, LT-02300, Vilnius, Lithuania
simonas.grubinskas@ff.stud.vu.lt

A permanent growth of the thin-film electronics market stimulates the development of versatile technologies of patterning thin-film materials on flexible substrates. Selective ablation is one of the most important parts of these processes therefore deeper understanding of underlying physical phenomena is required for further development of the technology.

Structure under consideration is layered medium consisting of thick polymer substrate at the bottom, 1um molybdene layer 2um CIGS layer, 50nm CdS and 50nm ZnO and a 500nm layer of ITO on top of the solar cell. Material is irradiated by laser from ITO side. Modeling consists of three parts: energy coupling calculation taking into account interference effects, two-temperature model for heat calculation and phase transition considerations.

Energy coupling modeling is carried out in the following way. We consider 2D geometry of solar cell layers in which harmonic TE waves propagate according to wave equation:

$$\nabla \times (\nabla \times \mathbf{E}) - n^2 k_0^2 \boldsymbol{E} = 0 \tag{1}$$

Where $n = n_0 + jk$ is a complex refractive index. Due to boundary conditions between two adjacent layers multiple reflections occur. In some cases energy coupling profile in the material deviates from its' usual exponential decay form significantly. Floquet boundary conditions must be set on exterior boundaries of 2D domain to simulate plane wave propagation.

Diffusion equation is required in this model. Due to apparent extremely high temperatures and fast absorption when imaginary refractive index part is significant, two-temperature model must be used:

$$C_e \frac{\partial T_e}{\partial t} = \nabla \cdot (K_e \nabla T_e) - G(T_e - T_l) + S(\boldsymbol{r}, t) \tag{2}$$

$$C_l \frac{\partial T_l}{\partial t} = \nabla \cdot (K_l \nabla T_l) + G(T_e - T_l) \tag{3}$$

These equations physically mean that electrons and lattice are separate physical systems and for each a separate diffusion equation is in operation. Electrons are first to absorb laser energy, only then with the help of electron-lattice coupling term $G(T_e - T_l)$ electron system transfers energy to lattice. $S(\boldsymbol{r}, t)$ term corresponds to energy coupling from the first part of the modeling.

Since achieved lattice temperatures surpass those required to heat it up to a melting point, a phase transition had to be included in the model. Advantage was taken of Gaussian function which was added to specific heat expression:

$$C_l^{ph} = C_l + \frac{L}{\sqrt{2\pi}\sigma} e^{-\frac{(T_l - T_0)^2}{\sigma^2}} \tag{4}$$

Where L corresponds to latent heat, T_0 - melting temperature and σ is a numerical stability parameter, which was chosen to be approximately 1-2% of the maximum lattice temperature. Analogous term was added for evaporation processes if necessary.

A typical modeling result (the picture is deprived of phase transition effects) is represented in Figure 1.

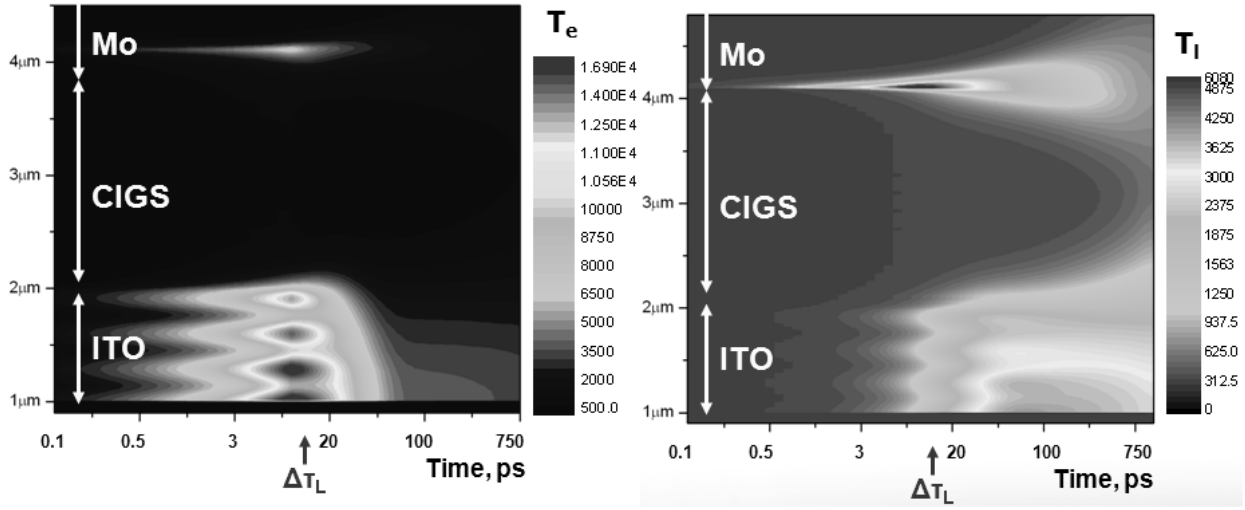

Fig. 3. Temperature profile at various points in the sample at various times. Although electron temperature is low in the molybdenum but fast transfer of energy results in fast heating of molybdenum and subsequent ablation of cold CIGS and ITO layers.

[1] N. Bianco, O. Manca, B. Morrone, Instationary conjugate optical-thermal fields in thin films, Heat and Mass Transfer, 34, 255-261 (1998)

[2] MV Shugaev, NM Bulgakova, Thermodynamic and stress analysis of laser-induced forward transfer of metals Appl Phys A, 101, 103-107 (2010)

INFLUENCE OF RADIATION DEFECTS ON THE FORMATION OF H-DONORS IN SILICON

A. Hiro, Yu. Pokotilo

Belarusian State University, Faculty of Physics, Department of Physical Informatics and Atomic-molecular Physics, Nezavisimosti ave. 4, 220030, Minsk, Belarus

hiro@me.by

Proton-beam irradiation is a prospective technique for modifying the electrical properties of silicon crystals [1]. One of the most interesting properties of implanted hydrogen is that its interaction with radiation induced and native defects during heat treatment leads to the formation of shallow hydrogen-related donors (H-donors) [2].

In our studies we used commercial Pd-Si Schottky diodes. The diodes were implanted with 300-keV H^+ -ions at room temperature. The dose varied in the range F = ($1x10^{13}$ – $1x10^{15}$) cm^{-2}. The electron concentration profiles were obtained by C–V (voltage-capacitance) measurements at a bridge frequency of 1.2 MHz. The parameters of radiation-induced defects were determined by deep level transient spectroscopy (DLTS) at 1 MHz and a gating time ratio t_2/t_1= 5.

Changes of the depletion region width (reverse bias U=-5 V, temperature T=86 K) and dependence of radiation-induced defects concentration from isochronal (20 min) annealing temperature are presented in Fig. 1. DLTS spectra are shown in Fig. 2. Values of parameters of post-implantation radiation defects (a curve 1) are found using Arrhenius plots. These parameters are used for identification of defects (according to data [1])

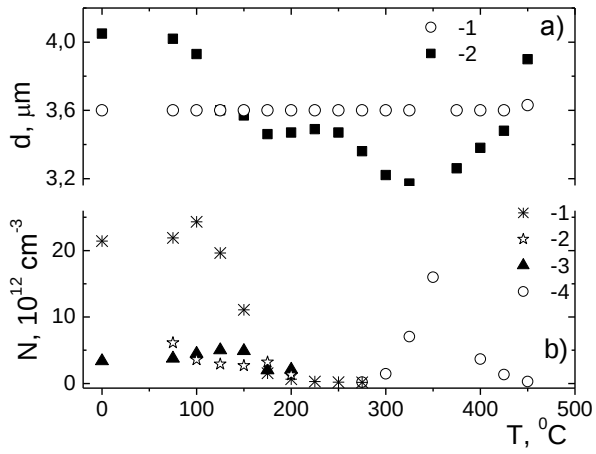

Fig.1. Depletion region width (a) and radiation defects concentration (b) changing with rising of annealing temperature; a) 1- control, 2- after irradiation; b) 1- E-center, 2- A-center, 3- VOH, 4- E_c-0.21 eV.

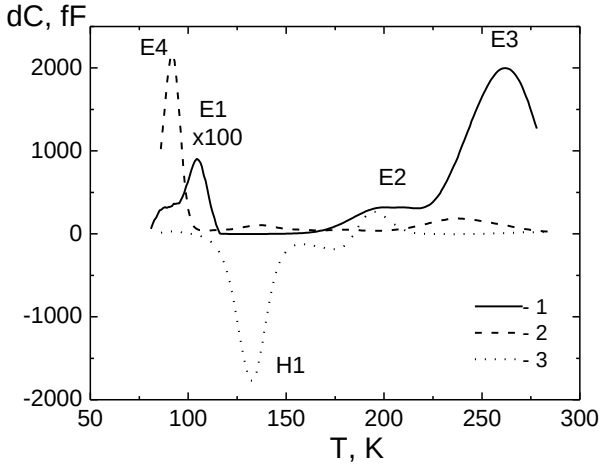

Fig. 2. DLTS spectra of Schottky diodes implanted with H^+-ions at the different thermal treatment: 1- after implantation; 2- 350 ^{0}C; 3- 450 ^{0}C.

The depletion region width before implantation was *d*=3.6 μm. According to the comparative analysis of the obtained data (fig. 1), increasing of *d* up to 4 μm is generally caused by formation E-center (curve 1), because concentration of A-center and VOH defect (curves 2,

3) are negligible (E-center – defect donor-vacancy, A-center – defect oxygen-vacancy, VOH – defect vacancy-oxygen-hydrogen). After E-center annealing at T=200 ^{0}C d restores to initial value. At the further rising of annealing temperature quantity d becomes below initial value. This fact indicates of donors' formation. Their maximum concentration is reached at T=350 ^{0}C and it coincides with concentration of undefined defect E4 (energy level E_c-0.21 eV and electron capture cross-section $\sigma=2x10^{-11}$ cm^2) in fig. 2 (curve 2). At the temperature T=450 ^{0}C the depletion region width exceeds the initial value, and anomalous peak (a minority carriers trap in the absence of hole injection) appears in DLTS spectrum (curve 3). This peak corresponds to acceptor center H1 (energy level E_v+0.31 eV), and their concentration is approximately equal to concentration of E4 defect.

Thus we can see relationship between radiation defects and donors in silicon. After annealing of radiation defects (such as E-center, A-center, VOH defect) we observe formation of H-donors. After annealing at 350 ^{0}C we observe maximum concentration of donors, and it corresponds to maximum concentration of E4 defect. Subsequent annealing leads to the disappearance of E4 defect and reduce the concentration of donors.

[1] V.V. Kozlovskii, *Proton Beam Modification of Semiconductors* (Nauka, St. Petersburg, 2003).
[2] B.N. Mukashev, M.F. Tamendarov, S.Zh. Tokmoldin, V.V. Frolov, Phys. Status Solidi A **91**, 509-522 (1985).

DEVELOPMENT OF TITANIUM DIOXIDE LAYERS FOR SOLAR CELLS APPLICATIONS

K. Krivas, K. Genevičius

Department of Solid State Electronics, Faculty of Physics, Vilnius University, Saulėtekio Ave. 9-III, LT-10222 Vilnius, Lithuania

kasparas.krivas@gmail.com

In our days, demand for energy saving technologies is constantly growing. European Union, due to greenhouse effect, is planning to produce about 25% of all electricity from alternative energy sources until 2030. One of possible ways to reach this target is further development of solar energy production, by replacing expensive crystalline solar cells with cheaper cells made of amorphous materials. Grätzel cell, also known as dye-sensitized solar cell, has a big potential due to the simple production technology and high efficiency. One of main component, used in Grätzel cell, is a porous layer of titanium dioxide, covered with thin layer of the organic dye.

The aim of this research was the development of various compositions of titanium dioxide pastes and finding the best technological conditions for porous titanium dioxide layers to form.

Pastes of titanium dioxide were made from titanium dioxide powder (*AEROXIDE® TIO2 P 25*) by adding acetic acid (CH_3COOH), water, methanol, terpineol [1].

Titanium dioxide pastes, made in laboratory, were compared with industrial d titanium dioxide paste. Morphology of the layers was examined by the means of the atomic force microscope (AFM). Electrical features were examined by photogenerated charge carriers extraction with linearly increasing voltage technique (photo-CELIV).

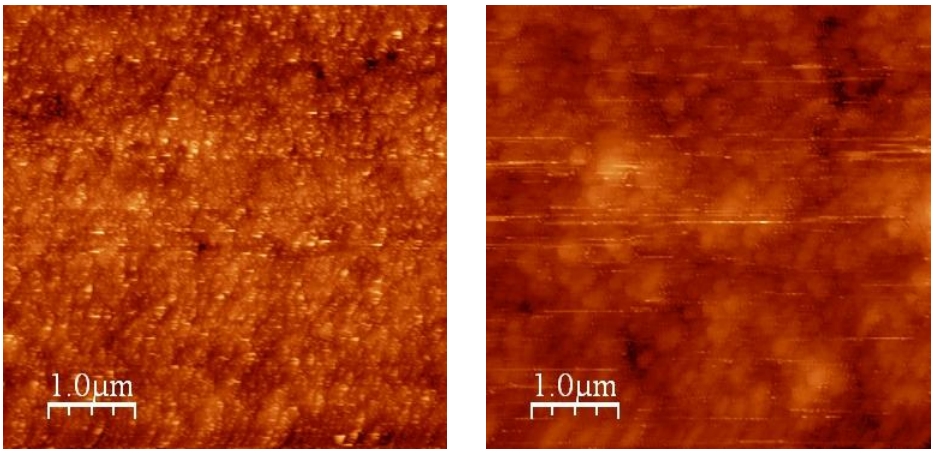

Fig. 1. ATF photographs of porous TiO2 layers showing the surface morphology of industrial manufactured (left) and homemade TiO2 (right).

[1] Ito S., Chen P., Comte P., Nazeeruddin M.K, Liska P., Péchy P., Grätzel M., Progress in Photovoltaics: Research and Application. **15**, 603-612 (2007)

INVESTIGATION OF AMPLIFIED SPONTANEOUS EMISSION IN FLUORENE-CARBAZOLE DERIVATIVES

S. Krotkus, K. Kazlauskas, S.Juršėnas

Institute of Applied Research, Vilnius University, Saulėtekio Ave. 9-III, LT-10222 Vilnius, Lithuania
simonas.krotkus@ff.stud.vu.lt

Organic semiconductors are promising materials for optoelectronics due to their properties resembling conventional semiconductors combined with easy processing and a variety of organic materials. Considerable Stokes shift, large optical gain and possibility to avoid concentration quenching in the solid state by controlling intermolecular interactions make organic semiconductors attractive as a novel laser gain media [1-3]. Organic semiconductor lasers (OSL) promise easy tunability of lasing wavelength over the entire visible spectrum [3, 4] due to the broad fluorescence band of organic molecules and possibility to control materials photophysical properties via chemical engineering. However, to date, there were no reports on electrically driven OSL which is a consequence of problems associated with poor charge transfer in the organic media. One approach to the issue is the search and study of the new multifunctional molecules composed of several fragments carrying different functionalities [5].

In this work we present study of photophysical properties of multifunctional fluorene/carbazole compounds [6] and their perspectives to be used as OSL gain media. Suitability of material for OSL operation is characterized by its short transient fluorescence lifetime τ_f and high photoluminescence efficiency Φ_{PL}, since radiative decay rate $k_r=\Phi_{PL}/\tau_f$ is directly proportional to Einstein's B coefficient, Eq. (1):

$$B \propto \frac{c^3}{8\pi h \nu_0^{\,3}} k_r , \qquad (1)$$

where h is Planck's constant, ν_0 is the frequency of light and c is the velocity of light. One of the straightforward methods for experimentally determining materials ability for lasing is by measurement of amplified spontaneous emission (ASE). 3rd harmonic of Nd^{3+}:YAG laser (355nm, pump pulse 10 ns) was employed to excite samples. To determine the threshold of ASE I_{thr} (Fig. 1 (a)) excitation power density was varied by several orders of magnitude. Fluorene-carbazole derivatives were embeded in a solid polystyrene (PS) matrix. Films were casted from THF solution.

CFC compound (Fig. 1(b) inset) showed best results with Φ_{PL}=100±5% and τ_f=1ns in a solution, which resulted in a distinctly low I_{thr}=0.6 kW/cm^2. However, Φ_{PL} dropped significantly in a neat film to 18% (I_{thr}=160 kW/cm^2), which can be explained by fluorescence quenching via exciton migration. In a solid PS matrix at low concentrations such quenching mechanism is negligible which resulted in Φ_{PL} values of up to 48% (I_{thr}=22kW/cm^2, Fig. 1(b)) in optimal

concentration of 1wt%. Lower values of fluorescence quantum yield compared to Φ_{PL} in a solution were showed to be a consequence of twisted conformers present in a rigid matrix of PS.

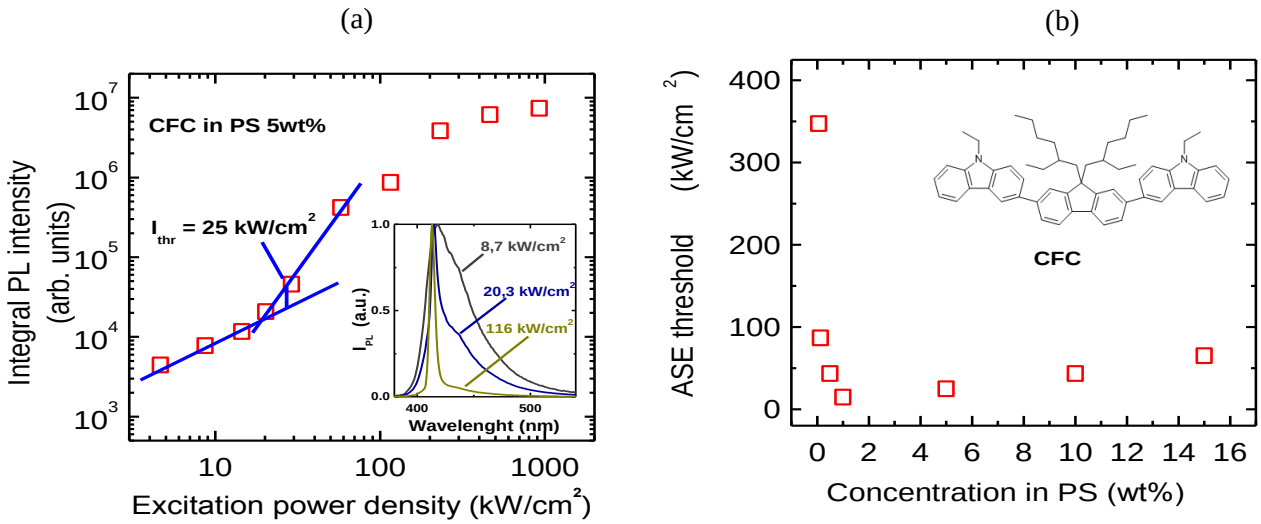

Fig. 1. (a) Integral PL intensity and normalized fluorescence spectra (inset) of CFC in PS (5wt%) at various excitations. I_{thr} indicates where intensity of ASE band exceeds twice the intensity of spontaneous emission band; (b) I_{thr} dependence of the CFC concentration in PS matrix. Chemical structure of CFC is also depicted (inset).

[1] N. Tessler, Lasers based on semiconducting organic materials, Adv. Mater., **11**, 363-369 (1999).

[2] M.D. McGehee, S.J. Heeger, Semiconducting (conjugated) polymers as materials for solid-state lasers, Adv. Mater., **12**, 1655-1668 (2000).

[3] I.D.W Samuel, G.A. Turnbull, Organic semiconductor lasers, Chem. Rev., **107**, 1272-1295 (2007).

[4] J.M. Lupton, Over the rainbow, Nature **453,** 459-460 (2008).

[5] B.C. Thompson, Y.-G. Kim et al., Soluble narrow band gap and blue propylenedioxythiophene-cyanovinylene polymers as multifunctional materials for photovoltaic and electrochromic applications, J. Am. Chem. Soc. **128**, 12714-12725 (2006).

[6] S. Grigalevicius, L. Ma et al., Synthesis and characterization of new carbazole/fluorene-based derivatives for blue-light-emitting devices, J. Polym. Sci. Pol. Chem. **44**, 5987-5994 (2006).

DEEP LEVEL DEPENDENT VARIATIONS IN CAPACITANCE TRANSIENTS

J. Kusakovskij, E. Gaubas

Institute of Applied Research, Vilnius University, Saulėtekio Ave. 9-III, LT-10222 Vilnius, Lithuania
jevgenij.kusakovskij@tmi.vu.lt

Semiconductor device characteristics are determined, to a large extent, by intrinsic and extrinsic defects. Consequently deep level induced variations in static and dynamic device characteristics are subjected to intensive research. Moreover, results of these studies are essential for further developments in semiconductor device fabrication technologies and deeper understanding of defect caused phenomena.

Built-in potential and its stability under intense irradiation are considered to be an essential characteristic of solid state particle detectors. Dependencies of these parameters are traditionally studied by analysis of steady state current-voltage and ac small signal capacitance-voltage characteristics. However, possible implementations of the mentioned methods are limited by noise levels in measurement circuits and the linear range of response amplitudes, i.e. commonly used LRC meters are developed to measure parameters in linear elements.

In this work, a technique based on measurements of barrier charging and charge extraction current transients caused by linearly increasing voltage (BELIV) is proposed as an alternative to traditional methods. The principle of the BELIV method is discussed. Characteristics measured in Si pin diodes under various experimental conditions, such as reverse and forward biasing at various temperatures and steady-state illumination, are presented. Simulated and measured characteristics of the BELIV signal dependent on density of deep-level traps are compared.

DETERMINATION OF THREADING DISLOCATION DENSITY IN GaN FILMS

S. Lapinskas

Institute of Applied Research, Vilnius University, Saulėtekio Ave. 9-III, LT-10222 Vilnius, Lithuania
skirmantas.lapinskas@gmail.com

Gallium nitride (GaN) and related alloys have been the subject of extensive research because of their application in blue laser, LED's, high power and high frequency electronics [1]. Usually GaN epitaxial layers are grown on a sapphire substrate which results in a poor matching of lattice parameters and gives a high density of threading dislocations (10^8-10^{10} cm^{-2}) which is usually not acceptable for applications mentioned before [2].

This work is devoted for determination of threading dislocation density in GaN films using wet etching and scanning electron microscopy (SEM) and atomic force microscopy (AFM) microscopy. Usually you cannot detect dislocations on a raw sample therefore etching technique is used to etch pits around dislocation making them more visible for microscopy analysis.

2-3 μm-thick GaN epitaxial layers were grown on sapphire substrate using metal-organic chemical vapor deposition (MOCVD) reactor at the Institute of Applied Research, Vilnius University. For etching experiments a hot phosphoric acid (H_3PO_4) (85%) was used together with a digital hot plate to maintain acid's temperature which was varied in this range 160 – 200 ºC. The etching duration was changed from 8 min. to 20 min.

Etched films will be analyzed using SEM and AFM microscopy to determine threading dislocation density, and to identify the best etching conditions for revealing the dislocations. Later determination of dislocation density in GaN will be used to optimize conditions of MOCVD growth.

[1] Xuenping Xu, R.P. Vaudo, J. Flynn, and G.R. Brandes, *Journal of Electronic Materials* 31, 5 (2002)
[2] T. Hino, S. Tomiya, T. Miyajima, K. Yanashima, S. Hashimoto, and M. Ikeda, *Appl. Phys. Lett.* 76, 3421 (2000)

INVESTIGATION OF PHOTOELECTRIC FEATURES OF VACUUM DEPOSITED ORGANIC MATERIAL MULTILAYER STRUCTURES AND BULK HETEROSTRUCTURE LAYERS

B. Lenkevičiūtė

Department of Solid State Electronics, Faculty of Physics, Vilnius University, Saulėtekio Ave. 9-III, LT-10222 Vilnius, Lithuania

Brone.Lenkeviciute@ff.stud.vu.lt

The single, double, triple and bulk heterostructure organic material layers were vacuum deposited or spin coated onto by ITO covered glass and their electrical, photoelectrical and electroluminescence (EL) features were investigated.

Mobility of charge carriers of materials V-417 and C_{60} were measured using photo generated charge extraction by linearly increasing voltage method (photo-CELIV). The mobility of electrons in C_{60} layer was of the order of $5 \cdot 10^{-6}$ $cm^2/V \cdot s$, while the mobility of holes of V-417 layer was approximately $5 \cdot 10^{-7} cm^2/V \cdot s$. Obtained results demonstrated that C_{60} is suitable electron transport material, and V-417 may be used as emission as well as hole transport material while depositing organic light emitting diode of bulk heterostructure.

The family of Volt-Ampere Characteristic (VACh) of organic material layers was measured in the dark and in the light. It is demonstrated that PEDOT: PSS sub layer upgrades injection of holes from indium tin oxide (ITO) into V-417 emission layer and into V-417+C_{60} bulk heterostructure.

The EL of single V-417 layer was observed at 30 V threshold voltage while the EL of double PEDOT: PSS/V-417 layer was observed at 20 V threshold voltage. There was no EL of deposited organic light emitting diode of bulk heterostructure, while after annealing for 1 h at 120^{o}C in nitrogen atmosphere EL was observed at 22 V threshold voltage.

DIELECTRIC PROPERTIES OF $Pb(Fe_{1/2}Nb_{1/2})O_3$ CRYSTAL

R. Mackevičiūtė[1], S. Greičius[1], J. Banys[1], and A. Kania[2]

[1] *Department of Radiophysics, Faculty of Physics, Vilnius University, Saulėtekio Ave. 9-III, LT-10222 Vilnius, Lithuania*

[2] *A. Chelkowski Institute of Physics, University of Silesia, ul. Uniwersytecka 4, PL 40-007 Katowice, Poland*

Rūta.Mackevičiūtė@ff.stud.vu.lt

Recently, there is a great interest in multiferroics – materials which in the certain temperature range are ferroelectrics and ferromagnetics. The most popular multiferroics are lead – iron niobium $Pb(Fe_{1/2}Nb_{1/2})O_3$ and bismuth ferrite $BiFeO_3$. These multiferroics could be used in microelectronics for example, producing MERAM memories.

PFN crystal dynamic dielectric properties have not been published anywhere, so the aim is to investigate these properties.

In the present study, the $Pb(Fe_{1/2}Nb_{1/2})O_3$ single crystals were grown using the flux method [1]. Dielectric measurements were performed at temperature range (300 – 500) K and in the frequency range (20 – 1000) kHz and (300 MHz – 3GHz). In the low frequency range (20 kHz – 1000 kHz), investigation was performed by measuring samples' capacity and the tangent of loss angle using LCR-meter HP4284A. In the high frequency range (300 MHz – 3GHz) investigation was performed by using network analyzer Agilent 8714ET. Measurements were performed by reducing the temperature of the sample and the temperature variation rate was about 0,5 K/min.

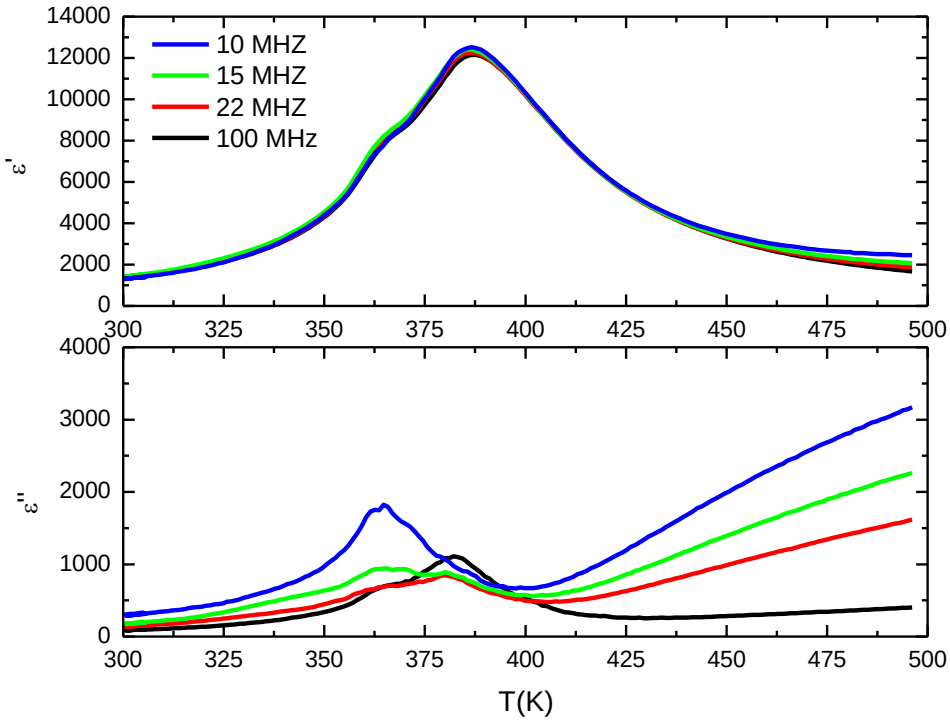

Fig. 1. Temperature dependence of the real and imaginary parts of dielectric permittivity of PFN crystal.

Figure 1 shows the temperature dependence of the real and imaginary parts of dielectric permittivity of PFN crystal. This investigation shows that PFN crystal has two structural phase transitions. First structural phase transition is from the monoclinic ferroelectric phase to the tetragonal ferroelectric phase at 365 K and the second is from the tetragonal to the cubic paraelectric phase at 385 K [2].

[1] A. Kania, E. Talkin and M. Kruczek, Ferroelectrics, 391: 114-121 (2009)
[2] V. Bonny, M. Bonin, P. Sciau, K. J. Schenk and G. Chapuis, Solid State Commun. 102, 347-352 (1997)

PHOTO-HALL EFFECT AND TIME RESOLVED PHOTOCONDUCTIVITY IN 3C-SiC

P. Malinovskis[1,2], A. Mekys[1,2], J. Storasta[1,2], and R. Vasiliauskas[3]
[1] *Institute of Applied Research, Vilnius University, Saulėtekio Ave. 9-III, LT-10222 Vilnius, Lithuania*
[2] *Department of Semiconductor Physics, Faculty of Physics, Vilnius University, Saulėtekio Ave. 9-III, LT-10222 Vilnius, Lithuania*
[3] *Linköping University, Department of Physics, Chemistry and Biology (IFM), Semiconductor Materials, Linköpings Universitet SE-581 83, Sweden*
paulius.malinovskis@ff.vu.lt

Cubic silicon carbide (3C-SiC) is one of the most promising materials for new generation extreme conditions electronics. The main property of this polytype is the biggest mobility value of the charge carriers (~1000 cm^2/Vs) and the forbidden energies gap (~2.2 eV) corresponding to visible light spectrum.

In this work using the temperature dependence of the Hall voltage and photoconductivity we have tested 3C-SiC specimens grown by sublimation epitaxy method in Linköping University (Sweden). Samples were cleaned with KOH and oxides were etched with HF [1] water solutions respectively, and Ni-Au Ohmic contacts were fabricated at 400ºC temperature using Physical Vapour Deposition technique in Vilnius University laboratory.

In the next stage we measured the samples conductivity, photoconductivity, Hall voltage and magnetoresistivity temperature dependencies (in range 100-400 K), from this experimental data we calculated the carriers mobility, concentration and lifetime temperature dependencies, which revealed the scattering mechanisms and the forbidden energies gap perturbation effects. We estimated the corresponding energy values, which correlate with those given by other authors for nitrogen (N) [2] and oxygen (O) [3] residual impurities (unintentionally doped crystals). Some experimental data of our complex researches can be explained by the existence of the extended defects and the forbidden energies gap perturbations.

[1] Gwiy-Sang Chung, Kyu-Hyung Yoon. Ohmic contacts to single-crystalline 3C-SiC films for extreme-environment MEMS applications. Microelectronics Journal 39. 2008. Pp. 1408-1412.
[2] Internet database: http://www.ioffe.ru/SVA/NSM/Semicond/SiC/impurities.html (looked: 2011-02-20).
[3] J. Han, S. Dimitrijev, F. Kong, P. Tanner, A. Atanacio. SIMS Investigation of Oxygen in 3C-SiC on Si. Proceedings of the 2008 conference on optoelectronic and microelectronic materials and devices. Book of Abstracts (2008). Sydney, Australia. Published by IEEE. p. 3.

PHOTOELECTRIC FEATURE INVESTIGATION OF VACUUM DEPOSITED CuPc/C_{60} SOLAR CELLS

A. Melianas

Department of Solid State Electronics, Vilnius University

armantas.melianas@gmail.com

Organic layers of CuPc and C_{60} followed by solar cells of different structures (Fig. 1) were formed by vacuum deposition onto by ITO covered glass substrates: two layer CuPc/C_{60} (Fig. 1a), two layer with mixture CuPc/CuPc+C_{60} (Fig. 1b), gradient mixture CuPc:C_{60} (Fig. 1c) solar cells. Their absorption spectra and photoelectric feauture dependence on annealing and various C_{60} and CuPc ratios in mixtures was investigated.

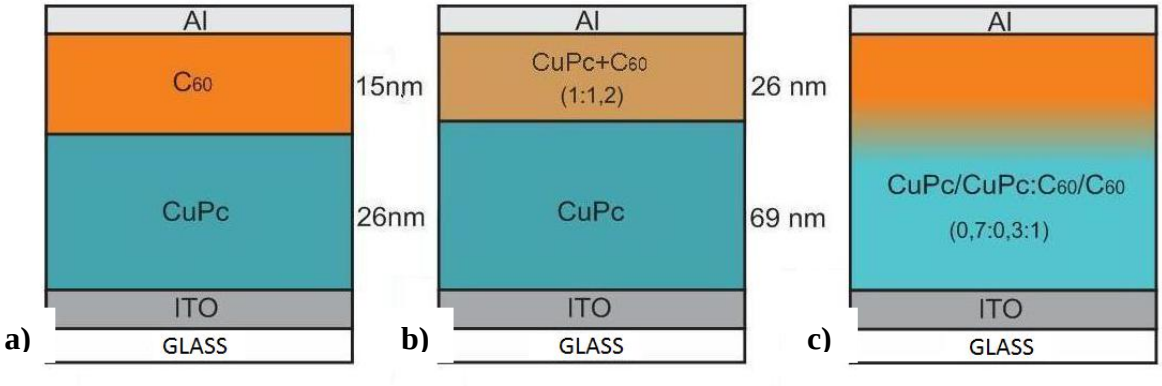

Fig. 1. Structure of some of the fabricated solar cells: a) CuPc/C60 b) CuPc/ CuPc+C60 c) Gradient CuPc:C60

Carrier mobility μ dependences on electric field E and carrier lifetimes $\tau_{1/2}$ were measured by photo-CELIV (charge extraction by linearly increasing voltage) technique [2].

Estimated CuPc hole drift mobility and carrier lifetime $\mu = 3 \cdot 10^{-8}$ cm^2/Vs, $\tau_{1/2} = 48$ ms; C_{60} electron drift mobility and carrier lifetime $\mu = 2 \cdot 10^{-5}$ cm^2/Vs, $\tau_{1/2} = 200$ μs. 60 min 100^{o}C annealing of CuPc had no effect on hole transport but C_{60} electron transport was enhanced: $\tau_{1/2} = 430$ μs and μ having weaker dependence on t_d (t_d is the delay between the light pulse and the linearly increasing voltage pulse), which may be explained by formation of a more favorable C_{60} molecule arrangement after annealing that is confirmed by the absorption spectra.

Estimated hole drift mobility $\mu = (3{,}5 - 7{,}5) \cdot 10^{-8}$ cm^2/Vs of CuPc/C_{60} sample exhibits a weak dependence on the applied electric field which may attributed to the formation of CuPc and C_{60} heterojunction that affects the electric field distribution inside the sample. Two layer solar cell was fabricated, which demonstrated $\eta_{eff} = (0.36 - 1.05)$ % efficiency (compared to CuPc (20 nm)/C_{60} (40nm)/ BCP (2 nm) $\eta_{eff} = 0{,}75$ % [1]).

Samples of CuPc/CuPc+C_{60} structure demonstrated electron drift mobilities $\mu = (1 - 5) \cdot 10^{-6}$ cm^2/Vs which were mildly enhanced by 60 min 100^{o}C annealing $\mu = (2{,}5 - 6) \cdot 10^{-6}$ cm^2/Vs. The latter can be attributed to a formation of a more energetically

favorable CuPc and C_{60} mixture which is confirmed by the increase of absorption in 400 - 600 nm range.

In samples of gradient mixture CuPc:C_{60} solar cells estimated electron drift mobility was $\mu = (9 \cdot 10^{-6} - 1 \cdot 10^{-5})$ cm^2/Vs, which is close to pure C_{60} electron drift mobility. After 60 min 40^{o}C + 60 min 80^{o}C annealing the electron drift mobility dependence on t_d was sufficiently increased, which may be explained by a formation of bulk heterojunction. The latter is confirmed by the increase of current in current voltage characteristics and electron lifetime decrease: $\tau_{1/2} = 280$ μs, after annealing $\tau_{1/2} = 100$ μs.

[1] P. Sullivan, S. Heutz, B. Sanderson, S. Schultes, T.S. Jones. The influence of co-deposition on the performance of CuPc/C_{60} heterojunction photovoltaic cells. Centre for Electronic Materials and Devices, Chemistry Department, Imperial College, SW7 2AZ London, UK (2008).

[2] G.Juška, K.Genevičius, K.Arlauskas, R.Osterbacka, H.Stubb. Features of charge carrier concentration and mobility in π-conjugated polymers. Macromolecular Symposia 212, 209-217 (2004).

LUMINESCENCE OF NOVEL CERIUM – DOPED PHOSPHORS FOR WHITE LEDS

K. Nalivaika, G. Tamulaitis

Semiconductor Physics Department and Institute of Applied Research, Vilnius University, Saulėtekio ave. 9 – III, LT – 10222 Vilnius, Lithuania

Kristijonas.Nalivaika@ff.stud.vu.lt

Solid-state lighting technology is emerging as a cost-competitive, energy-efficient alternative to conventional electrical lighting [1]. Currently, much effort is being put into improving efficiency and color rendering of the solid-state lamps designed for general lighting. One of the most important issues in phosphor conversion light emitting diodes (LEDs) is search for new efficient phosphors ensuring better color rendering than the currently most popular phosphor YAG:Ce.

In this work, new sol-gel derived $Y_{3-x}Lu_xAl_3MgSiO_{12}:Ce^{3+}$ phosphors are being investigated. A set of phosphors consisting of 16 samples with different relative numbers of Y and Lu atoms and different cerium content (0.25%, 0.5%, 0.5% and 1%) was under study. All the samples were annealed at 1600°C. Quantum yield (QY) was measured and luminescence spectra were investigated using an Integrating Sphere (*SphereOptics*) and spectrophotometer (*Hamamatsu PMA-12*). A blue 440 nm InGaN light emmiting diode was used for the excitation of the samples.

A descrease in luminescence intensity at increasing Ce concentration from 0.5% to 1% due to concentration quenching effect [2] was observed. Spectra of $Y_{3-x}Lu_xAl_3MgSiO_{12}:Ce^{3+}$ phosphors are red-shifted from 3 to 15 nm if compared to most widely used YAG:Ce phosphor what is very beneficial considering better color rendering of white LEDs. High values of QY were observed (the highest QY (89%) was exhibited by $Lu_3Al_3MgSiO_{12}$:0,25% Ce^{3+} sample). However the QY decreased rapidly with the increase of cerium content.

[1] Shur MS, Zukauskas A, Solid-state lighting: Toward superior illumination, Proceedings of the IEEE **93,** 1691–1703 (2005).

[2] Haranath, Chander, Sharma, Singh, Enhanced luminescence of Y3Al5O12:Ce3+ nanophosphor for white light emitting diodes, Appl. Phys. Lett., **89**, 173118 (2006).

STUDY OF ELECTRON IRRADIATION INDUCED DEEP LEVELS IN Ge DOPED Si DIODES

J. Pavlov, A. Uleckas, and E. Gaubas

Institute of Applied Research, Vilnius University, Saulėtekio Ave. 9-III, LT-10222 Vilnius, Lithuania
Jegenij.Pavlov@ff.stud.vu.lt

Defects engineering by specific doping and irradiation technologies is one of the trends in improving and modifying of specific parameters of semiconductors devices. It is known that Ge doping of Si during the Czochralski (CZ) growth process has a beneficial effect on strength of Si wafers and thus on reduction of dislocation nucleation [1]. Also, introduction of Ge into Si has additional advantages because it is isovalent impurity and do not introduce electrically active deep centres. Therefore, it is a promising dopant for the expedient manipulation of the internal gettering capacity [1]. Ge doping above 10^{20} cm^{-3} leads to the formation of germanium clusters acting as gettering centres for the intrinsic point defects. The effect of germanium doping has the important consequences for radiation-induced defect formation and population dynamics. [1-2]. It is also known that Ge doping suppresses formation of thermal donors [2].

In this work two sets of n-type CZ grown Si diodes have been investigated, one of them with Ge doping concentration of 10^{19} cm^{-3} (GCZ) and the second one without Ge doping (CZ). P-on-n diodes were irradiated with 2 MeV electrons with fluence in the range of 10^{15} and 10^{16} e/cm^2. Deep Level Transient Spectroscopy (DLTS) has been employed to identify specific defects and to evaluate density of these deep centres, of carrier capture cross-section and activation energy in order to reveal an impact of Ge doping on parameters of radiation defects. Three peaks have been observed in both sets of samples after irradiation. Electron traps corresponding to the V-O complex (the so-called A-centre), to di-vacancy and to P-V complex (E-centre) have been identified after irradiation by 10^{15} e/cm^2 fluence of 2 MeV electrons. An amplitude of the DLTS peak attributed to V-O centre slightly increases in GCZ sample, while concentration of other defects does not depend on Ge doping. Peaks corresponding to di-vacancy and phosphorous-vacancy (P-V) complex strongly increase with electron irradiation fluence.

[1] I.Yonenaga, J. Cryst. Growth 275 (2005) 91.
[2] J.Vanhellemont, et al., J. Cryst. Growth (2010)

THERMAL CHARACTERIZATION OF LEDs MULTICOLOUR CLUSTERS

A. Petrulis

Institute of Applied Research, Vilnius University, Saulėtekio Ave. 9-III, LT-10222 Vilnius, Lithuania
andrius.petrulis@ff.stud.vu.lt

LEDs clusters based on red, green and blue (RGB) LEDs are widely using in full-colour video displays and general lighting. Adding phosphor conversion amber LED to RGB cluster makes trading off between colour rendition characteristics possible [1]. LED operation based on injection electroluminescence which defines unbalanced carrier radiative recombination [2]. Density of states and carrier distribution are depended on temperature so LED spectral power distribution (SPD) varies. Respectively, cluster output characteristics depend on temperature.

In this work, separate LEDs spectral and thermal characteristics were investigated before modelling white light clusters at 3500 K, 4500 K and 6500 K colour temperatures. AlGaInP red, phosphor conversion InGaN amber, InGaN green and blue LEDs were used. All measurements were performed within cryostat/oven in order to stabilize the temperature of the LED mounting pad. Temperature range was set between 273 K and 333K with 10 K step. SPD were measured using integration sphere and multichannel spectrometer. There types of LEDs clusters were modelled: RGB, RAGB and AGB, which characterized by the highest colour saturation, fidelity and dulling index respectively. RAGB cluster is linear combination of RGB and AGB clusters with 0.24 weigh coefficient.

Results shows that AGB cluster chromaticity coordinates in the widest LEDs mounting pad temperatures are in three-step MacAdam ellipse area which limits unnoticed distortion of the colour by over 99% of individuals with normal vision. RGB cluster at high mounting pad temperatures (323 K and 333 K) can not be defined as white light source considering American National Standard for electric lamps (ANSI_ANSLG C78.733 - 2008). RGB cluster at low pad temperatures (273 K) can be described as lower colour temperature white light source. RAGB cluster only at 333 K pad temperature are not described as white light source. The highest chromaticity shift for RGB cluster can be explained by AlGaInP red LED radiant flux the highest decrease. AGB cluster are the most stable at all pad temperatures independent of colour temperatures. This is influenced by the same radiant flux decrease of amber, green and blue LEDs.

[1] Žukauskas, R. Vaicekauskas, M.S. Shur, Colour-rendition properties of solid-state lamps, IEEE Journal Of Selected Topics In Quantum Electronics, 15-6, p. 1753-1762 (2009).
[2] E. F. Schubert, Light-Emitting Diodes (Cambridge University press, Cambridge, 2006).

PHOTOPHYSICAL PROPERTIES OF TRIPHENYLAMINE BASED DERIVATIVES WITH METHOXY AND 2,2–DIPHENYLETHENYL SUBSTITUENTS

S. Raišys

Institute of Applied Research, Vilnius University, Saulėtekio Ave. 9-III, LT-10222 Vilnius, Lithuania
steponas.raisys@ff.stud.vu.lt

Triphenylamine (TPA) derivatives are recognized for their excellent hole transport properties with mobility reaching up to $1.5 \cdot 10^{-2}$ $cm^2/V \cdot s$ [1]. In addition to superior transport properties, TPA compounds also feature high fluorescence efficiency in the UV-blue region. These properties including high stability of TPA derivatives make them viable in the field of information storage devices, field-effect transistors, photovoltaic cells, and organic light emitting diodes (OLEDs). Starburst TPA derivatives exhibiting efficient emission in the solid state can be highly suitable as bifunctional materials in OLEDs, i.e. as hole-transporting and emitting layer simultaneously [2].

Here, the optical properties of new triphenylamine-based derivatives with 2,2-diphenyletenyl and methoxy substituents are reported. Optical properties of the TPA compounds in solution and solid state were assessed by measuring absorption and fluorescence spectra, fluorescence quantum yield and exited state lifetime.

Experimental results indicate that maximum of the absorption spectrum varies in the range of 300 – 400 nm then diphenylethenyl and methoxy substituents are attached. Generally, quantum yields of TPA derivatives were found to be much higher in the solid state than in solution. Up to 16–fold enhancement of the fluorescence quantum yield in solution of the TPA derivative with restricted TPA core by diphenylethenyl groups as compared to the non-restricted derivative was observed. The highest quantum yield in both solution and thin film was estimated for the TPA derivative possessing symmetrical structure. Fluorescence concentration quenching of the TPA compounds in transparent polymer matrix was also investigated and discussed.

The quantum yield data was supported by fluorescence lifetime measurements. Significantly lower quantum yields and shorter decay times obtained in solutions as compared to those in thin films indicated intramolecular torsions of the phenyl groups, which caused dramatic fluorescence quenching.

[1] Y. Song, C. Di, X. Yang, S. Li, W. Xu, Y. Liu, L. Yang, Z. Shuai, D. Zhang, D. Zhu, A cyclic triphenylamine dimer for organic field-effect transistors with high performance, J. Am. Chem. Soc. 128, 15940 – 15941 (2006);

[2] S. Tao, Y. Jiang, S.-L. Lai, M.-K. Fung, Y. Zhou, X. Zhang, W. Zhao, C.-S. Lee, Efficient blue organic light-emitting device with a new bipolar emitter, Organic Electronics 12, 358-363 (2011).

DYNAMICS OF YELLOW LUMINESCENCE IN GaN EPILAYERS

I. Reklaitis

Institute of Applied Research, Vilnius University, Saulėtekio Ave. 9-III, LT-10222 Vilnius, Lithuania
ignas.reklaitis@gmail.com

Nonequilibrium carrier lifetime of GaN epilayers is one of the most important parameters indicating materials quality and influencing the performance of AlN/GaN/InN optoelectronic devices. Dynamics of the nonequilibrium carrier density in GaN and related alloys is strongly affected by recombination through donor and acceptor levels and by carrier trapping [1]. However, transient recombination processes in GaN are complex and not well understood so far. In particular, data on photoluminescence response time for the yellow luminescence, which is due to impurity related recombination, is ambiguous [2,3].

In this work carrier dynamics in GaN was investigated using luminescence lifetime measurements in the frequency domain under low-power-density excitation provided by an ultraviolet light emitting diode. The decay time was measured within a temperature range from 80 to 280 K. The GaN samples were grown over sapphire substrates in MOCVD (*Aixtron CCS*). With increasing temperature, yellow luminescence intensity increased and response became slower. The results are used in for revealing carrier recombination routes in GaN

[1] G. Tamulaitis, J. Mickevičius, P. Vitta, A. Žukauskas, M. S. Shur, Q. Fareed, R. Gaška, Time- and frequency-domain measurements of carrier lifetimes in GaN epilayers, Superlattices and Microstructures **40**, 274-278 (2006).

[2] Y. H. Kwon, S. K. Shee, G. H. Gainer, G. H. Park, S. J. Hwang, J. J. Song, Time-resolved study of yellow and blue luminescence in Si- and Mg-doped GaN, Applied Physics Letters **76**, 840-842 (2000).

[3] M. A. Reshchikov, H. Morkoc, Luminescence properties of defects in GaN, Journal of Applied Physics **97**, 061301-061396 (2005).

ELECTROCHEMICALLY DEPOSITED ZnO LAYERS FOR FORMATION OF GRAZEL TYPE SOLAR CELLS

R. Songaila

Department of Solid State Electronics, Faculty of Physics, Vilnius University, Saulėtekio Ave. 9-III, LT-10222 Vilnius, Lithuania

e4romens@gmail.com

Graetzel type solar cell was formed on electrochemically deposited ZnO layer. Spectrum of light absorbance, conductivity, thickness and irregularity of surface of the electrochemically deposited ZnO layers were investigated. Vacuum deposition was used to form thin layers of photoactive and electron transportation materials. It was used CuPc (copper phthalocyanine) as a photoactive material and V-609 (organic polymer) as electron transport material. The thickness of deposited layers was evaluated using CELIV method [1].

So formed solar cell structure was photoactive, however the built in voltage was absent. The phenomenon of switching was observed while measuring I-V characteristic.

[1] G. Juška, K. Arlauskas, M. Viliūnas, J. Kočka. Extraction current transients: new method of study of charge transport in microcrystalline silicon, Phys.Rev.Letters 84, 4946-4949(2000).

BROADBAND DIELECTRIC SPECTROSCOPY OF $0.4Na_{1/2}Bi_{1/2}TiO_3$ - $(0.6\text{-}x)SrTiO_3$ - $xPbTiO_3$ SOLID SOLUTIONS

Š. Svirskas[1], M. Ivanov[1], Š. Bagdzevičius[1], J. Banys[1], M. Dunce[2], M. Antonova[2], E. Birks[2], and A. Sternberg[2]

[1] *Department of Radiophysics, Faculty of Physics, Vilnius University, Saulėtekio Ave. 9-III, LT-10222 Vilnius, Lithuania*

[2] *Institute of Solid State Physics, University of Latvia, Kengaraga street 8, LV-1063 Riga, Latvia*

sarunas.svirskas@ff.stud.vu.lt

Various solid solutions containing perovskite $Na_{1/2}Bi_{1/2}TiO_3$ (NBT) were investigated in order to find materials suitable for practical use. $SrTiO_3$ (ST) and $PbTiO_3$ (PT) were used as secondary material for $Na_{1/2}Bi_{1/2}TiO_3$. It is known that these materials influence phase transition of NBT in a different manner. ST increases relaxor properties while PT increases first order characteristics of the phase transition [1]. There have not been any thorough studies (except [2]) of such solid solutions as NBT-ST-PT.

Measurements were made for concentrations x = 0; 0.1; 0.15 at temperature interval 110-500 K on cooling with a rate of 1K/min except around phase transition where cooling speed was lowered to 0.4 K/min. Frequency range was from 20 Hz to 40 GHz. Silver paste was used for contacts.

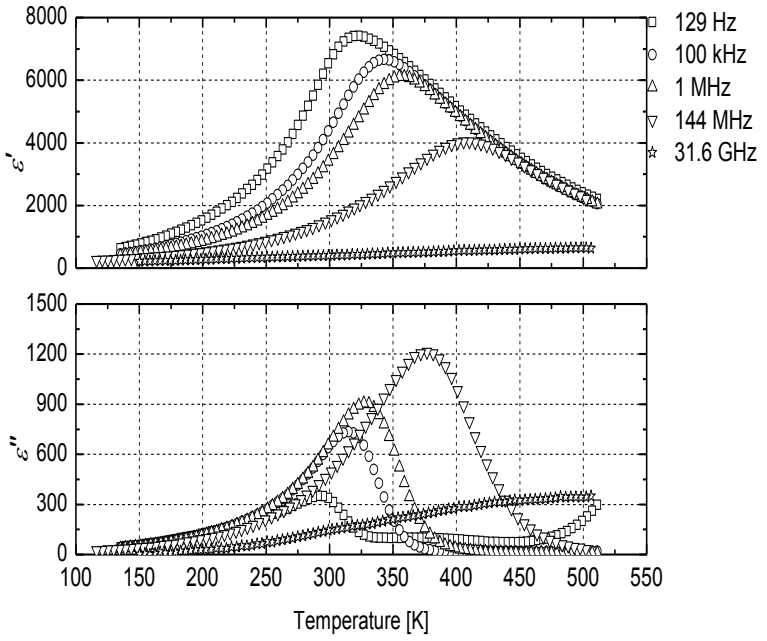

Fig. 4 Temperature dependence of complex dielectric permittivity of 0.4NBT-0.5ST-0.1PT

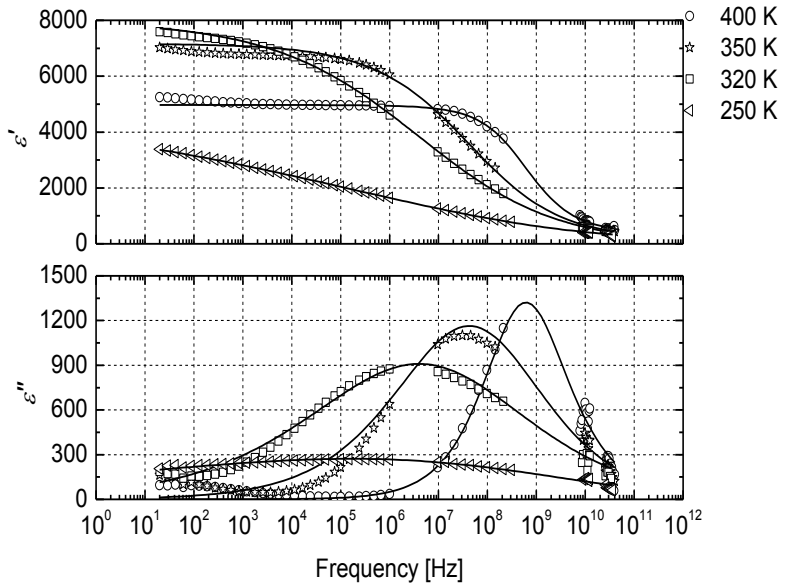

Fig. 2 Frequency dependence of complex dielectric permittivity at different temperatures for 0.4NBT-0.5ST-0.1PT, solid lines represent fits with Havriliak-Negami equation

Fig. 1 shows temperature dependence of complex dielectric permittivity for x = 0.1. The maximum of real part of dielectric permittivity shifts towards higher temperatures when frequency increases. It is typical behavior of relaxor ferroelectrics. Fig. 2 shows frequency dependence of complex dielectric permittivity. Solid lines are fits with empirical Havriliak-Negami formula (1).

$$\varepsilon^*(\omega)-\varepsilon(\infty)=\frac{\varepsilon(0)-\varepsilon(\infty)}{\left(1+(\mathrm{i}\omega\tau)^{1-\alpha}\right)^{\beta}} \tag{1}$$

The purpose of the report is to represent Havriliak-Negami fitting parameters and discuss temperature dependencies.

[1] Lee, J.K.; Hong, K.S.; Kim, Ch.K.; Park, S.E.; Phase transitions and dielectric properties in A-site ion substituted $(Na_{1/2}Bi_{1/2})TiO_3$ ceramics (A=Pb and Sr), *Journal of Applied Physics*, vol. 91, No.7 (2002)

[2] Birks, E., Dunce, M., Antonova, M. and Sternberg, A., Phase transitions in modified $Na_{1/2}Bi_{1/2}TiO_3$-$SrTiO_3$ solid solutions, *Physica Status Solidi C*, vol.6, No.12 (2009)

[3] Gomah-Pettry, J.R.; Said, S.; Marchet, P.; Mercurio, J.P.; Sodium-bismuth titanate based lead-free ferroelectric materials, *Journal of the European Ceramic Society*, vol. 24, Issue 6, Electroceramics VIII (2004)

INFLUENCE OF LASER ANNEALING ON PHOTOLUMINESCENCE OF InGaN EPITAXIAL LAYERS

V. Šukauskas, D. Dobrovolskas

Department of Semiconductor Physics, Faculty of Physics, Vilnius University, Saulėtekio Ave. 9-III, LT-10222 Vilnius, Lithuania

vil.sukauskas@gmail.com

InGaN is a defect-rich material with typical dislocation densities of more than 10^8 cm^{-2} [1]. Despite this fact InGaN materials are efficient light emitters and currently are used in fabrication of various optoelectronic devices, such as green, blue and white light-emitting diodes and lasers. Some of InGaN luminescence peculiarities are described by carrier localization model. During the growth of InGaN epitaxial layers indium tends to form higher concentration areas, which act like quantum wells [2]. Free carriers prefer to localize in those areas and more likely recombine radiatively. Since most of the photoluminescence (PL) comes from indium-rich areas, spatial distribution of the PL in an InGaN are non uniform and PL from high intensity region tends to have longer wavelength of the spectrum peak than from the low intensity region. Besides the band edge PL, InGaN emits longer wavelength radiation caused by the energetic levels of defects. The defect-related emission broadens the PL spectrum and lowers the band edge luminescence causing the reduction in the efficiency of InGaN-based devices.

In this work, investigation of influence of laser annealing on InGaN epitaxial layers was performed. InGaN epitaxial layer grown by MOCVD technique over sapphire substrate was annealed with various laser intensities (ranges from 4.2 MW/cm^2 to 25 MW/cm^2) in 6 different locations. High intensity laser annealing effect to the surface was visible even to the naked eye. The surface relief was investigated using atomic force microscopy technique. Laser annealing causes the formation of bumps with bigger radius, but smaller height.

The PL spatial distribution was obtained from all the annealed areas and the initial area for comparison using laser scanning confocal microscopy technique. Spatial distribution of the PL intensity from all areas was strongly inhomogeneous. Spatially integrated spectra illustrated in Fig. 1. The PL spectrum from the initial area has both band edge and defect-related band with equal intensity. Laser annealing has considerable influence on the shape of the PL spectrum at higher intensities than 12 MW/cm^2. At $\geq$20 MW/cm^2 annealing intensities, the defect-related band disappears, but the intensity of the band edge PL decreases.

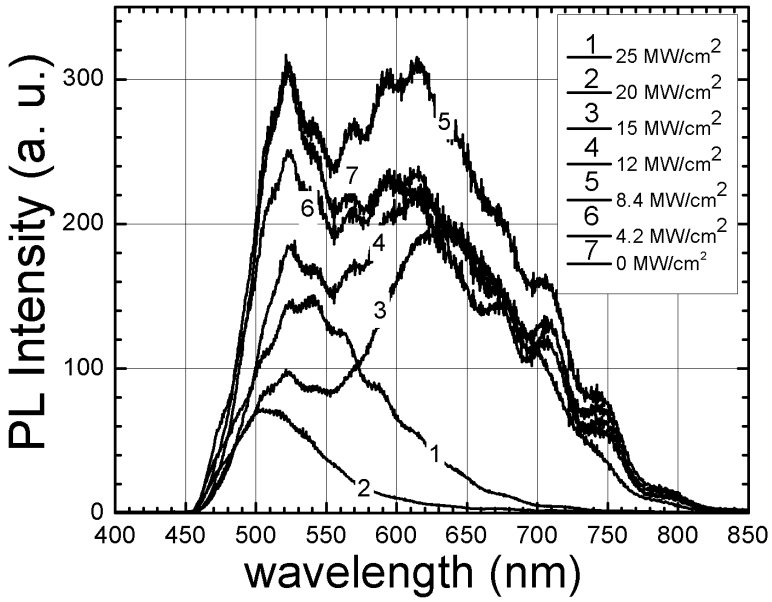

Fig. 1. Spatially integrated spectra from annealed and initial areas. Legend shows intensities of the annealing laser.

[1] S. Nakamura, The Roles of Structural Imperfections in InGaN-Based Blue Light-Emitting Diodes and Laser Diodes, *Science* 281, 956-961 (1998).

[2] K. Okamoto, A. Kaneta, Y. Kawakami, S. Fujita, J. Choi, M. Terazima, T. Mukai, Confocal microphotoluminescence of InGaN-based light-emitting diodes, *Journal of Applied Physics* 98, 064503 (2005).

HETEROJUNCTION BARRIER HEIGHT DEPENDENCE OF SnO2(Pt) – p-Si ON DIOXIDE FILM THICKNESS

V. Il'chenko, O. Kravchenko, and S. Teslenko

Taras Shevchenko Kiev University, Volodymyrska str., 64, 01033, Kiev, Ukraine

teslen@gmail.com

Heterojunction based on tin dioxide films and silicon, are interesting structures for building gas sensors, that's why the investigation of its electro-physical characteristics took place.

The investigated experimental structures were made by spray pyrolysis from solution on p-type silicon plate. Were received samples with tin dioxide film thickness 4, 7, 10, 15, 20 and 30 nm. Current - voltage characteristics (C-V) were measured in voltage range -1,5÷1,5 V (Fig.1).

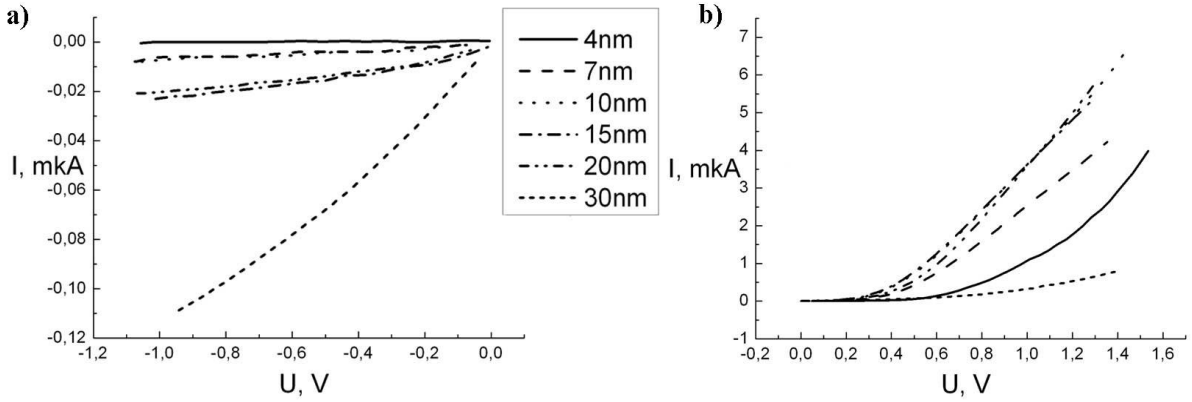

Fig.1. Reverse (a) and direct (b) branches C-V of investigated structures for different thickness of metal dioxide film

C-V analysis carried out in the approximation of over-barrier current transport mechanism. For semiconductors charge transfer can be described by thermionic over-barrier emission for majority carriers.

Barrier height dependence on SnO2 film thickness is shown on Fig.2. The barrier height decreases with increases of a thickness of a film from 4 to 15 nm. After that it gets out on saturation and does not change at the subsequent increase of a film thickness to 30 nm.

As atomic-force microscopy studies have shown tin dioxide films have discontinuous structure. When they are nanoscale they may grow with mechanism of Stranskoho - Krastanova. The number and size of islands varies with the film thickness by qualitatively law. With increasing of film thickness islets dimensions increases, until they begin to merge with each other. The mean surface roughness (as follows from the results of atomic force microscopy) decreases until becoming constant value on film thickness at about 20 nm.

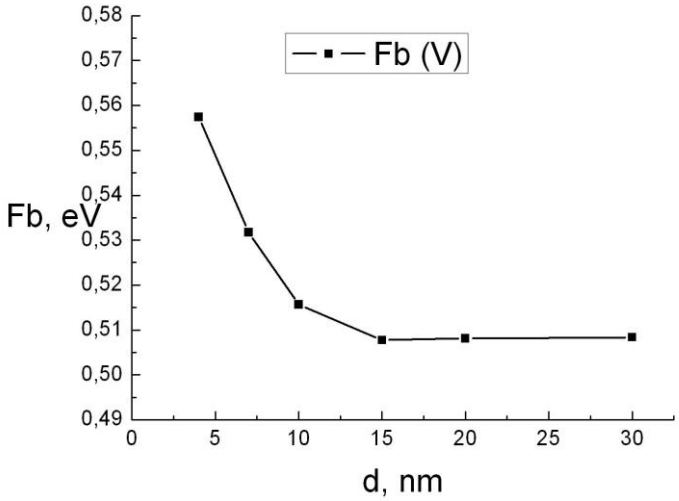

Fig.2. Dependence of barrier height on the thickness of metal dioxide film.

Accordingly to the reduction of mean surface roughness, adsorption-active surface area of metal dioxide film decreases. This reduces the number of traps on the surface of SnO2, which arise as a result of oxygen adsorption on oxygen vacancies. Presumably, this dependence of film morphology explains the dependence of heterojunction barrier height on the thickness of metal dioxide film.

DEPOSITION AND INVESTIGATION OF ORGANIC BULK HETEROSTRUCTURED SOLAR CELLS

I. Vaičiulis

Department of Solid State Electronics, Faculty of Physics, Vilnius University, Saulėtekio Ave. 9-III, LT-10222 Vilnius, Lithuania

Ignas.Vaiciulis@ff.stud.vu.lt

Vacuum deposition method was used to produce bulk heterostructured organic solar cells. The active layer structure and electric features changes were investigated before and after heating solar cells.

The surface structure of organic materials N,N-Bis[4-(2,2-diphenylethenyl)phenyl]-4-methylaniline and fullerene blend was investigated by AFM (atomic force microscope). After heating (30 min. 60 Cº) solar cells active layer surface became flatter. Mobility of charge carriers were measured using TOF (time of flight) method. Measurements showed high mobility of charge carriers of material N,N-Bis[4-(2,2-diphenylethenyl)phenyl]-4-methylaniline and decrease of charge carriers mobility after heating from approximately $8 \cdot 10^{-4}$ $cm^2/V \cdot s$ to $4{,}5 \cdot 10^{-4} cm^2/V \cdot s$.

INVESTIGATION OF DEEP LEVELS IN Si AND IONIZING RADIATION DETECTORS USING PHOTOIONISATION SPECTROSCOPY

N. Vainorius, J. Vaitkus, and V. Kažukauskas

Department of Semiconductor Physics, Faculty of Physics, Vilnius University, Saulėtekio Ave. 9-III, LT-10222 Vilnius, Lithuania

neimantasv@gmail.com

Ionizing radiation detectors are in harsh environment during experiments in Large Hadron Collider (LHC). So they degrade because of it. To develop semiconductor material and create detectors with improved properties, such as high speed and high radiation hardness, the collaboration program RD50 was started by CERN. Silicon is still the best choice for that purpose. It is believed, that new detectors with better properties, achieved by modification of silicon, will replace the old ones in LHC after 5 years of experiments.

One of the aims of our work was to upgrade the photoelectrical spectroscopy equipment, in order to investigate defect properties and their variation upon irradiation by different fluencies of ionizing radiation. Moreover, to observe photoconductivity quenching effect, two-monochromator system was implemented with automatic wavelength and light intensity control.

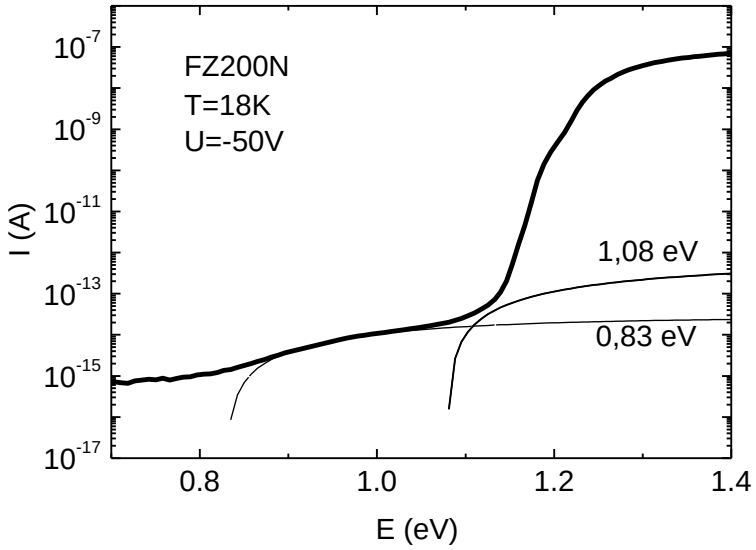

Fig 1. Photoconductivity spectrum of n type Si (thick curve) and its approximation (thin curves)

The main purpose of our research was evaluation of activation energies of local levels in the nonirradiated silicon detectors. The obtained photoconductivity spectra were modeled numerically by Lucovsky model [1] (Fig.1). The following values of optical activation energies of deep centers were determined: 0,83 eV and 1,08 eV.

In order to identify shallower levels which could not be observed using photoionisation spectroscopy, the thermal stimulated currents method was applied. Activation energies of these levels are as folows: n type sample – 0,225 eV, p – type sample 0,15 eV.

[1] G. Lucovsky, Solid State Communications, 299-302 (1965).

NUMERICAL COMPUTATION OF PHOTOGENERATED CHARGE CARRIER EXTRACTION BY LINEARLY INCREASING VOLTAGE (PHOTO-CELIV)

V. Valentinavičius, N. Nekrašas, and G. Juška
Faculty of Physics, Vilnius University, Saulėtekio Ave. 9-III, LT-10222 Vilnius, Lithuania
vytis.valentinavicius@gmail.com

Charge Extraction by Linearly Increasing Voltage (CELIV) is a widely used technique for studying charge carrier transport in semiconductors. Due to certain limitations of the latter technique photogenerated charge extraction (photo-CELIV) is preferred in new material studies. In this work we show that photo-CELIV transients are strongly dependent on experimental conditions such as the light intensity and absorption profile. With this in mind we introduce a correction factor, which extends previously derived CELIV equations [1] to allow carrier mobility to be estimated at various light intensities and photogeneration profiles. In addition, we demonstrated current saturation dependence on recombination. Light absorption is accounted using Beer-Lambert law.

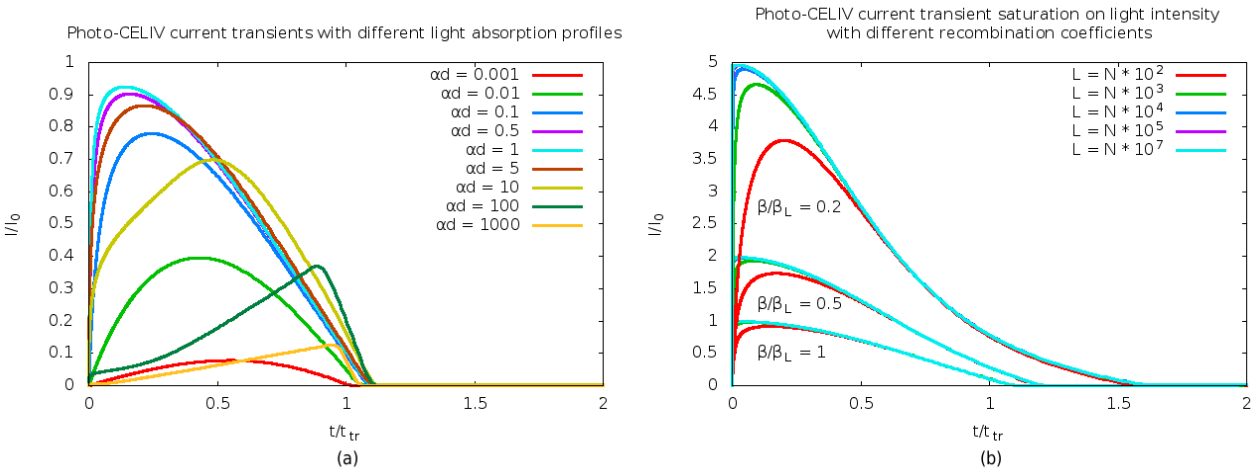

Fig. 1: Photo-CELIV current transient dependency on absorption profile is illustrated (a). Profile ranges from surface (αd = 1000) to bulk (αd = 0.001) absorption. Transient saturation on light intensity is shown (b). Bimolecular recombination coefficient is normalized to Langevin recombination coefficient.

The results are shown in the following figures.

Results shown in figure 1.(b) are yet to be empirically proven. Clearly visible that extraction current saturates at certain value which corresponds to β_L/β. We expect that these results will help to experimentally determine bimolecular recombination coefficient.

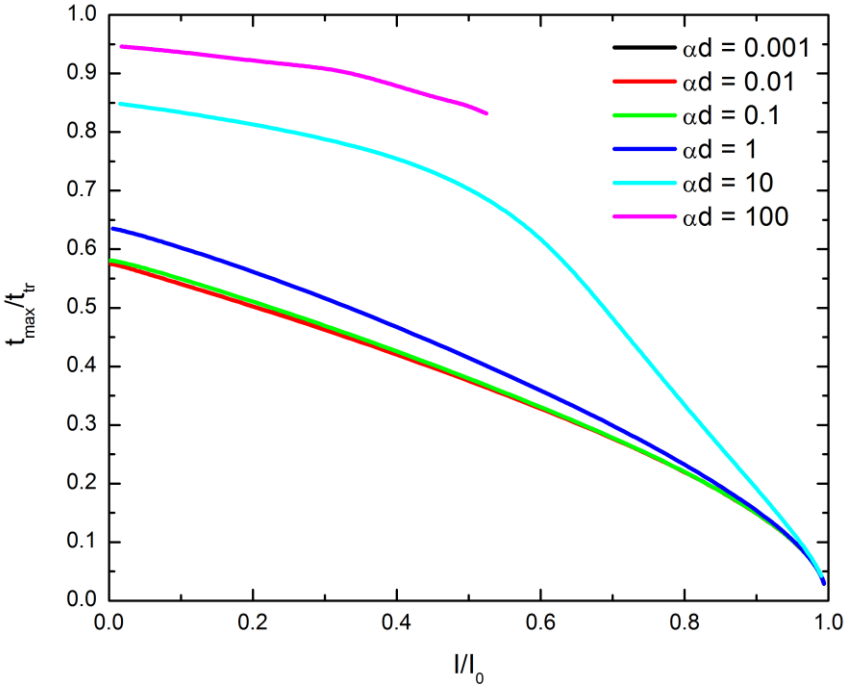

Fig. 2: Numerically calculated correction factor K=tmax $K = t_{max}/t_{tr}$ shown as a function of current ratio. I_0 – displacement current and I_{max} – current transient maximum. Different curves represent various light absorption profiles (αd).

In figure 1.(a) current transient maximum time t_{max}varies when absorption profile changes. Therefore the correction factor $K = t_{max}/t_{tr}$(fig. 2) is used to calculate the charge carrier mobility using equation $\mu = K^2 \frac{2d^2}{At_{max}^2}$at given experimental conditions. These results will be used in application of photo-CELIV.

[1] Juška G. et al Phys. Rev. B. 2000, B62, R16 235 – R16 238.

DEPOSITION OF POLYCRISTALLINE AND ORGANIC LAYERS BY SPRAY TECHNOLOGY AND INVESTIGATION OF THEIR PHOTOELECTRIC FEATURES

J. Varpučianskis, R. Dobužinskas

Department of Solid State Electronics, Faculty of Physics, Vilnius University, Sauletekio Ave. 9-III, LT-10222 Vilnius, Lithuania

justas@fidi.lt, rokas@sweetsalt.lt

Different organic, polycrystalline materials and their mixtures were spray deposited onto glass substrates with ITO and the uniformity of thickness and homogeneity of formed layers were investigated as well as their photoelectric features.

The samples were made using V-606+H_2Pc, TiPc, V-606+ZnCdS, V-606 materials. The materials were dissolved in THF (tetra-hydro-furan) and the solutions were sprayed using nitrogen as carrying gas. The surfaces of formed structures were investigated. The thickness of the layers were measured using charge extraction by linearly increasing voltage (CELIV) method and was estimated 10-490 nm, depending on solution concentration and spraying rate [1]. VoLT-ampere characteristics of the samples were measured in the dark and under illumination by AM1.5 source of light to observe their photosensitivity. The layers of TiPc and V-606+ZnCdS demonstrated a slight photosensitivity, while the samples of other materials were insensitive to light.

The research showed that the spraying method allows produce a thin and photosensitive organic layer, however, in order to form a more uniform structure it is necessary to improve the technology of spraying.

[1] G.Juška, K.Arlauskas, M.Viliūnas, K.Genevičius, R.Osterbacka, H.Stubb. Charge transport in π-conjugated polymers from extraction current transients. Physical Review B **62,** 16235-16238 (2000).

CHARACTERISATION OF THE Si THYRISTOR STRUCTURES BY CAPACITANCE TECHNIQUES

A. Velička, T. Čeponis, and E. Gaubas

Institute of Applied Research, Vilnius University, Saulėtekio Ave. 9-III, LT-10222 Vilnius, Lithuania
Arunas.Velicka@ff.stud.vu.lt

Capacitance techniques are powerful tools for detection and identification of deep level centers in layered structures of the semiconductor devices. Deep centers of considerable densities are as usually introduced during high temperature technological procedures. These defects affect the device operational characteristics. Therefore, combined investigations of the material and of functional characteristics of the devices are necessary to resolve and suppress these technological defects.

In this research, the diffusion doping introduced defects have been investigated in three layer (p-n-p) and four layer (n^+-p-n-p) thyristor structures fabricated by "Vilniaus Ventos Puslaidininkiai", by combining several techniques based on the capacitance control. Two sets of samples as A and B have been examined, - those meet the technical requirements (A) and those are inconsistent with operational limits (B), respectively.

Research has been implemented by combining the Capacitance – Voltage (C-V) and Deep Level Transient Spectroscopy (DLTS) methods. Measurements of the temperature dependent C-V characteristics have been performed using small ac signal technique implemented by QuadTech 7600 LRC meter, cryostat and external galvanic voltage source instrumentation which enabled us to reach high measurement precision. A commercial spectrometer DLS-82E has been used for DLTS spectroscopy of traps employing the temperature scan mode.

Manifestation of deep level centers in both batches of "A" and "B" samples have been revealed by C-V measurements in three-layered structures. The elevated densities of the dominant deep centers, ascribed to sulphur (S) impurities, have been resolved as S duplet peaks within DLTS spectra measured on samples "B" relatively to that of "A" ones. Moreover, it has been unveiled that samples "A" contain the compensating minority carrier traps attributed to copper (Cu3+) impurities. These deep centers appeared to be a reason for the increased leakage current and of the reduced breakdown voltage, inherent for samples "B" relatively to that in samples "A".

INVESTIGATION OF TlBr PHOTOELECTRICAL PROPERTIES

A. Ziminskij, V. Kažukauskas

Institute of Applied Research, Vilnius University, Saulėtekio Ave. 9-III, LT-10222 Vilnius, Lithuania
andzej.ziminskij@ff.stud.vu.lt

Thallium bromide (TlBr) is an attractive and promising material for X- and γ-ray spectroscopy because of its wide bandgap (2.68 eV), high density (7.56 g/cm3) and high atomic numbers (Tl:81 and Br:35). Such properties ensure a high photon stopping efficiency. Nevertheless one of the main problems still hindering practical applications of TlBr is presence of the ionic conductivity, which sensitively depends on the temperature and makes device characteristic unstable in time.

We had investigated two samples of TlBr. The first sample was grown by the Bridgman–Stockbarger method. The sample size was 3:2:1 mm. The second sample was grown by the hydrothermal recrystallisation method and was purified using traveling molten zone method (7 times). Its size was 5:3:2 mm.

We had investigated photoelectrical and current transient properties of TlBr from 100 K up to 300 K, where the effect of the ionic conductivity changes notably. After measuring the spectral dependencies several defect related bands were identified. The curves were approximated using Lukovsky model. Positions of the defect levels were identified being as follows: 0.8 eV, 1.1 eV, 1.6 eV and 1.9 eV. The defects could be related with the impurities in TlBr crystal such as: Fe, Cu, Ba, Cr, Li. The light induced enhanced photoconductivity phenomenon was identified at low temperatures after the photoexcitation of the samples by the intrinsic light.

Non-monotonous conductivity variation with temperature was identified, demonstrating mobility-related maximum that was superimposed on an intrinsic conductivity growth (Fig.1).

After measuring the thermally stimulated currents several defect traps were identified. The curves were approximated using TSC model. Their thermal activation energy values were 0,2 – 0,35 eV, and 0,74 – 0,79 eV.

The slow degradation of the samples was observed, which is related with the change of the potential barrier heights, and variation of the effective activation energy values of the defect bands. Moreover, photoconductivity of the samples decreases too. This could be explained by the creation of new recombination channels in the crystals due to the diffusion of Tl ions.

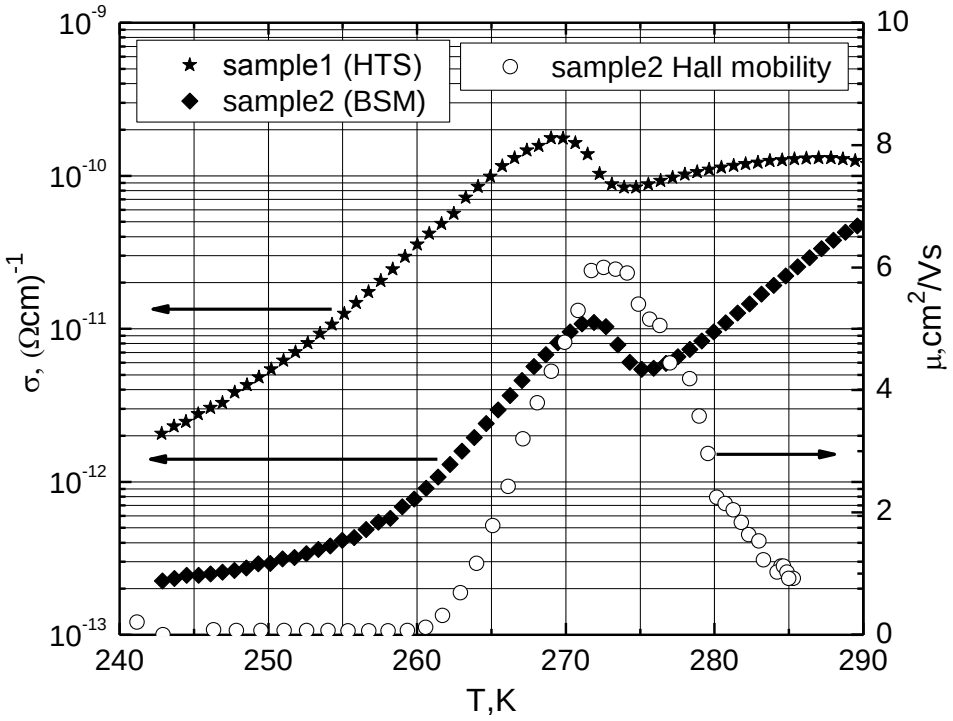

Fig. 1. Temperature dependences of the samples current and Hall mobility.

Acknowledgements. This work was supported by the Lithuanian and Ukrainian Ministries of Education and Science and the Research Council of Lithuania (projects No TAP-21 and TAP-63). A. Ziminskij acknowledges Student Research Fellowship Award from the Lithuanian Science Council.

SETTING GUPTA AND SCHOTTKYS' FORMULAS VALIDITY BOUNDARIES BY EXAMINING SEMICONDUCTOR DIODES ELECTRICAL NOISE

T. Ždanovičius, J. Matukas

Faculty of Physics, Vilnius University, Saulėtekio Ave. 9-III, LT-10222 Vilnius, Lithuania
laiskaitomui@gmail.com

Recently interests in electrical fluctuations of electrical signals were expeditiously growing due to growth of nanotechnologies production perfection, as the smaller electrical devices gets, the greater electrical fluctuations can be detected in transmitted signal. Electrical noise is usually named as accidental microscopic particles deviation from average value.

Semiconductor diodes could be examined as nonlinear resistive devices, but what is in common between nonlinear element thermal and shot electrical noises? The answer was partly found when Gupta's theorem appeared in 1978, but since nowadays there are no experimental results published which could prove that theorem is absolutely correct. Usually shot noise is described with Schttky's formula $S_I = 2eI$, but this formula validates only when semiconductor diode's voltamperic characteristic's perfection coefficient n is equal 1 [1-2].

To estimate these problems, Si and GaAs Schottky diodes were chosen, to examine their voltamperic characteristics (Fig. 1) and electrical noise (voltage fluctuations) (Fig. 2 *a*) in wide temperature and current range. Noise measurement was made in highly shielded Noise laboratory, even measurement system was placed in metal case to maximum protects it from external electromagnetic field impact.

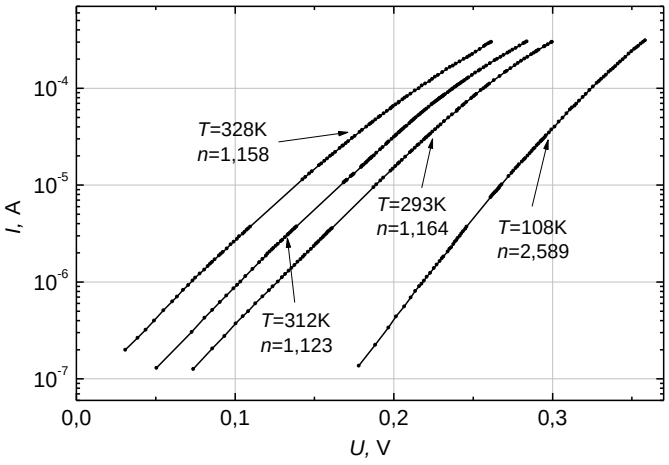

Fig.1. Schottky diode voltamperic characteristics measured in different temperatures.

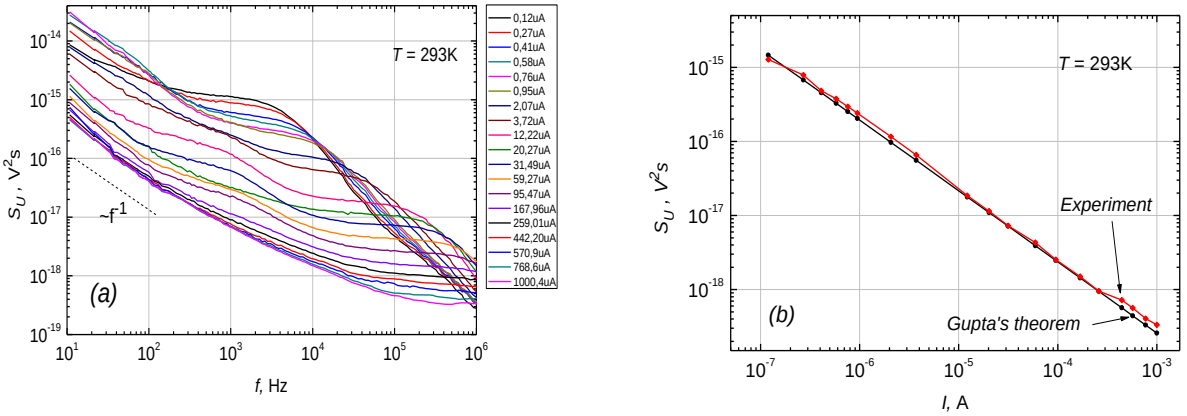

Fig. 2. a) Electrical noise spectral density dependence on frequency; b) Experiment and theoretic results comparison.

In measurements is visible that in low frequencies there is 1/*f* noise, which, rising frequency, merges to shot noise (Fig. 2 *a*). Si and GaAs Schottky diode's voltage fluctuation spectral density theoretic results, calculated from Gupta and Schottky, coincides with experiment result in low current range, however, when current gets higher, there is trivial error (Fig. 2. *b*).

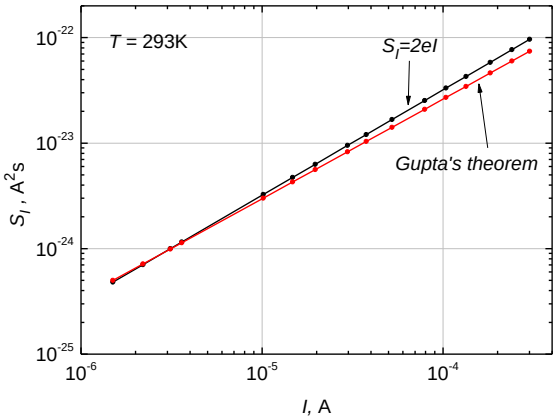

Fig. 3. Schottky diode electrical noise dependence on current (comparison of theoretic results).

During noise investigation, were established that experiment results in Schottky diodes coincide with Gupta's theorem, while Schottky formula validates only when perfection coefficient *n* is 1.

[1] V. Palenskis. Fliuktuacijos elektroninėse sistemose. Vilnius: VU FF Radiofizikos katedra, p.127-129, (1998).

[2] M. S. Gupta. Thermal fluctuations in driven nolinear resistive system. Phys.Rev.A. No 6, p.2725-2731, (1978).

INSTRUMENTATION AND TECHNOLOGY FOR THE *IN SITU* CARRIER LIFETIME CONTACTLESS CONTROL UNDER VARIOUS IRRADIATION CONDITIONS

K. Žilinskas, T. Čeponis, A. Uleckas, and E. Gaubas

Institute of Applied Research, Vilnius University, Saulėtekio Ave. 9-III, LT-10222 Vilnius, Lithuania
kestutis.zilinskas@ff.stud.vu.lt

Ion implantation is a technological procedure widely used in semiconductor device fabrication. Carrier lifetime is one of the most sensitive parameters to defects in semiconductor materials. Therefore defect introduction by high energy particle irradiation is an effective technological tool for manipulation of semiconductor device characteristics. Consequently, in situ control of defect introduction and their evolution during implantation of different ions is important for development of the radiation technologies in micro- and nano-electronics [1]. Contactless transient technique, based on analysis of the microwave probed photoconductivity dynamics, has been employed to monitor the evolution of defects in silicon during proton irradiation. A sketch of the measurement setup, containing an irradiation chamber installed within particle accelerator Tandetron 4110A and an instrument for carrier lifetime in situ control, is illustrated in Figure 1.

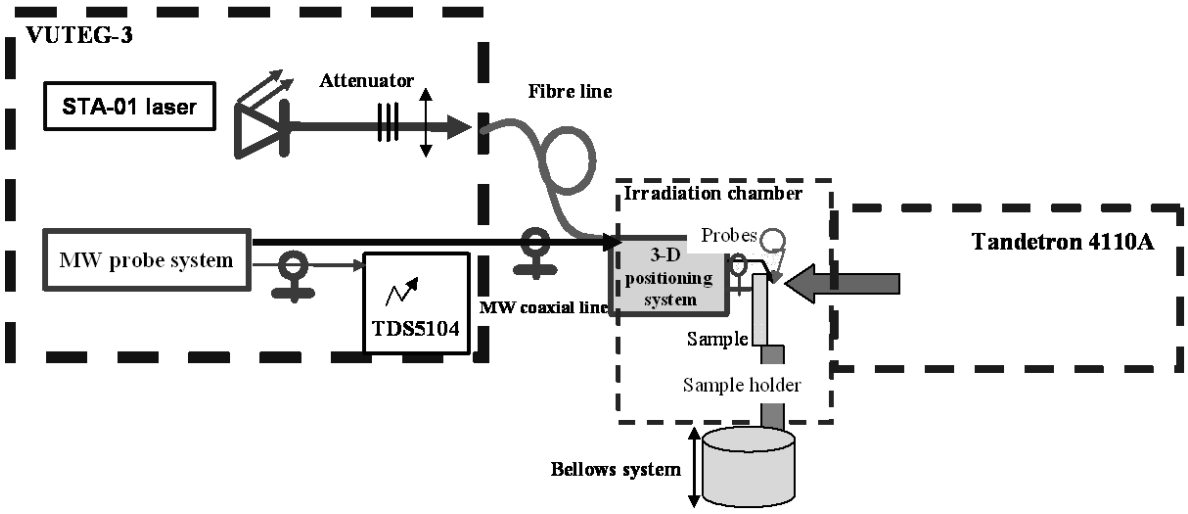

Fig. 1. Sketch of the experimental setup.

In this work, carrier lifetime variations ascribed to 1.5 MeV proton implantation induced radiation defects, acting as fast carrier traps, are analyzed. Changes of the surface and bulk recombination components revealed within photoconductivity transients recorded in 300 μm thick SiO_2 passivated Si wafers under various particle fluences and exposure times will be discussed.

[1] E. Gaubas, T. Čeponis, A.Uleckas, J.Vaitkus, K.Žilinskas, V.Kovalevskij, M.Gaspariunas, V.Remeikis. *In situ analysis of the carrier lifetime in silicon during implantation of 1.5 MeV protons.* Lithuanian Journal of Physics, Vol. 50, No. 4, (2010)

NUMERICAL MODELING OF POLARIZATION IN InGaN SOLAR CELLS

A. Časas

Institute of Applied Research, Vilnius University, Saulėtekio Ave. 9-III, LT-10222 Vilnius, Lithuania
algimantas.casas@ff.stud.vu.lt

Growing global energy demand, shortage of oil, gas and coil and concerns about ecology lead the world to search for a new way to generate energy. One of the solutions for these problems is to use the energy of the Sun with photovoltaic devices. The most efficient solar cell design is found to be tandem solar cell with theoretical efficiency of up to 87 % on concentrated light. The most important issue is finding appropriate materials for production of solar cells that could exhibit previously mentioned efficiencies. The InGaN material system which band gap covers entire solar spectrum is a promising candidate. Also this material system show extreme radiation, thermal, mechanical robustness, therefore InGaN tandem solar cells could be very suitable for space and concentrated photovoltaic applications. The computation modeling is cost and time effective way to develop new design of solar cells structures.

First goal of this work was to study several computation programs and to find one which is best suited for modeling of devices made of III-group nitrides. After trying several programs later we have chosen PC1D – one dimension carrier drift-diffusion solver for solar cells with implemented polarization effects. The second task was to understand fundamentals of solar cell by modeling classical solar cells with one p-n junction. For the test modeling we calculated how efficiency of solar cell made of one p-n junction depends on the band gap of material. The obtained results was consisted with Shockley-Queisser [1] detailed balanced limit and showed maximum possible efficiency of 30 % at E_g = 1.1 eV. Second modeling was to investigate influence of surface recombination to the quantum efficiency of the solar cell.

Working with III group nitrides, such as InGaN, GaN materials strong effect that changes energy band structure, electrical characteristics of the device – polarization was discovered. Trying to get the best results out of modeling III group nitrides, the program has to be able to apply piezoelectric and spontaneous polarizations to structure of the device [2]. The effect of polarization was examined and the solution how to overcome that problem with changing the device structure was made [3]. In the upcoming part of the research the new modeling program Nextnano3 which allows calculation of quantum effects and graded InGaN structures will be used.

[1] W. Shockley, H. J. Queisser J. Appl. Phys. 32, 510 (1960).
[2] Omkar K. Jani, “Development of wide-band gap InGaN solar cells for high efficiency photovoltaics“ PhD thesis, Georgia Institute of Technology (2008).
[3] J. J. Wierer, A. J. Fischer, and D. D. Koleske Appl. Phys. Lett. 96, 051107 (2010).

STRUCTURE OF 1-CHLORO-1-METHYL-SILACYCLOHEXANE: TEMPERATURE-DEPENDING RAMAN AND IR SPECTROSCOPY

R. Belovas, V. Aleksa

Department of General Physics and Spectroscopy, Faculty of Physics, Vilnius University, Saulėtekio Ave. 9-III, LT-10222 Vilnius, Lithuania

rimantas.belovas@ff.stud.vu.lt

It is important fully characterize silacyclohexanes. There are different methods of physical characterizations of the molecules, but one of the most effective methods is vibrational spectroscopy: Raman light scattering and FT-infrared absorption techniques [1-3]. Temperature-depending Raman spectra of light scattering allow studying equilibrium evolution of *axial* and *equatorial* molecular conformers.

An important step towards more accurately distinguishing between the vibrational contours and assigning them was done. Raman light scattering spectra at various temperatures were recorded from 293K to 133K and analyzed with 2DCoS, AXI$^-$ and AXI$^+$routines.

From the experimental Raman light scattering spectra calculated enthalpy difference between conformers ΔH = (1,7±0,6) kJ·mol^{-1}, which does quite well corespond to the results of theoretical calculations (2,5 kJ·mol^{-1}).

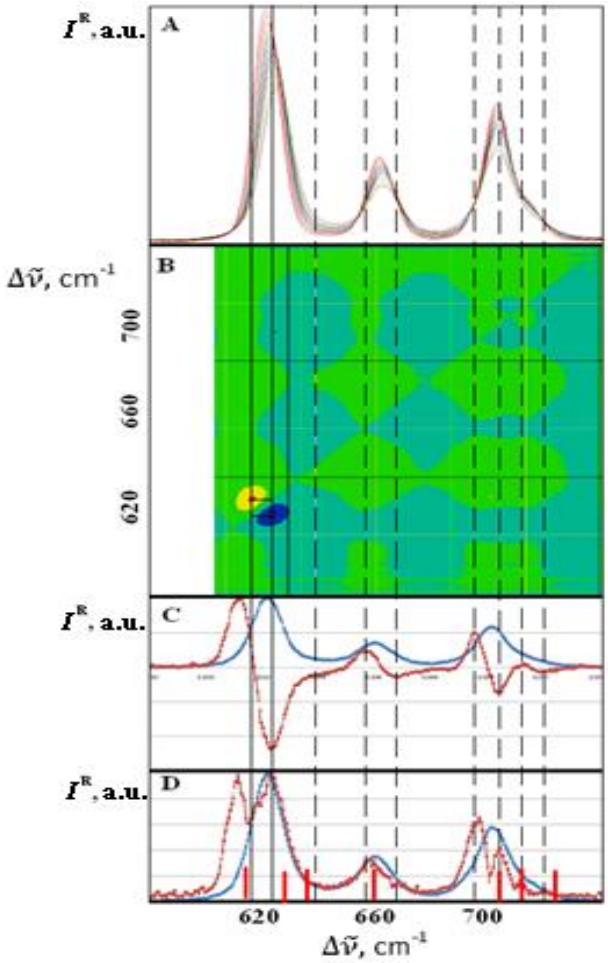

Fig. 1. A – temperature-depending Raman spectra of 1-Chloro-1-methyl-silacyclohexane; B – 2DCoS spectrum; C – AXI- spectrum; D – AXI+ spectrum and theoretical (B3LYP/cc-pVTZ) frequencies (red bars).

[1] Sunna Ó. Wallevik, Ragnar Bjornsson, Ágúst Kvaran, Nina I. Giricheva, Karl Hassler, Ingvar Arnason, Conformational properties of 1-fluoro-1-methyl-silacyclohexane and 1-methyl-1-trifluoromethyl-1-silacyclohexane: Gas electron diffraction, low-temperature NMR, temperature-dependent Raman spectroscopy, and quantum chemical calculations, Journal of Molecular Structure 978 (2010) 209–219.

[2] Ingvar Arnason, Agust Kvaran, Sigridur Jonsdottir, Palmar I. Gudnason, and Heinz Oberhammer, Conformations of Silicon-Containing Rings. 5. Conformational Properties of 1-Methyl-1-silacyclohexane: Gas Electron Diffraction, Low-Temperature NMR, and Quantum Chemical Calculations, J. Org. Chem. (2002), 67, 3827 3831.

[3] M. Dakkouri, V.P. Novikov, L.V. Vilkov, A gas-phase electron diffraction and quantum chemical investigation of the molecular structure of 1-bromosilacyclobutane, Journal of Molecular Structure 978 (2010) 234–245.

NOISE CHARACTERISTICS AND RADIATION SPECTRA OF MULTIMODE LASER DIODES DURING MODE-HOPPING EFFECT

V. Kornijčuk, S. Pralgauskaitė

Department of Radiophysics, Faculty of Physics, Vilnius University, Saulėtekio Ave. 9-III, LT-10222 Vilnius, Lithuania

Vladimir.Kornijcuk@ff.stud.vu.lt

Infrared laser diodes (LDs) generally are used in optical communication systems as their narrow and stable radiation spectrum meets highly strict requirements for suppressing dispersion in fiber. However temperature changes lead to the LD radiation spectrum movement along wavelength scale and mode-hopping effect occurs [1]. During such phenomenon radiation spectrum of Febry-Perot (FP) LD is unstable – highly correlated intense optical and electrical fluctuations are observed [2]. It is known, that low frequency noise characteristics are very sensitive to physical processes which take place in semiconductor materials [3], so in this project noise research was invoked in order to clarify the origin of intense fluctuations during mode-hopping phenomenon in FP LDs.

InGaAsP/InP Febry-Perot lasers radiating at 1,3 μm were used for the investigation. LD radiation spectrum and low frequency (20 Hz – 200 kHz) noise characteristics (optical, electrical noise and cross-correlation factor between them dependency on frequency, current and temperature) have been measured simultaneously (Fig. 1.).

Typical electrical and optical fluctuations of FP LD at stable operation region are characterized by $1/f^{\alpha}$ – type noise spectra and small (from -10 % to +10 %), almost non-dependent on frequency cross-correlation factor between them. Origin of such noise in semiconductor devices usually is related to generation-recombination (GR) processes through generation-recombination and capture centers with widely distributed relaxation time. Those centers are formed by defects and impurities in the device structure.

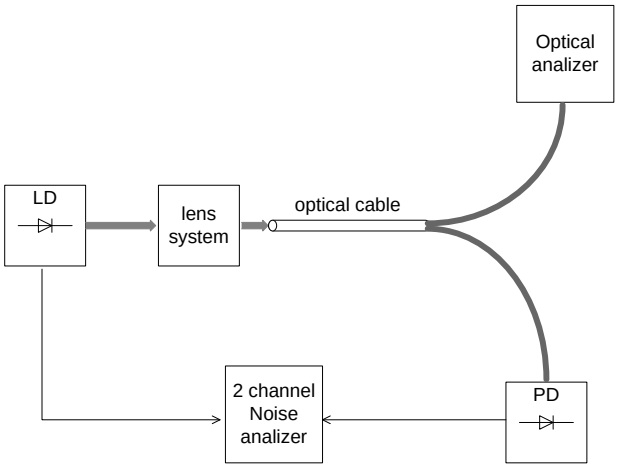

Fig. 1. LD radiation spectrum and noise characteristics measurement scheme.

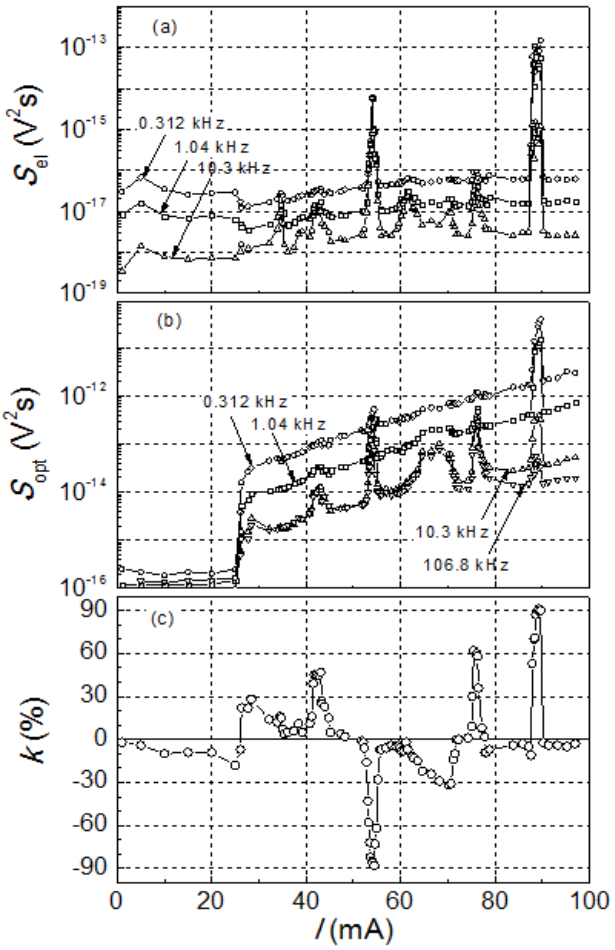

Fig. 2. Electrical (a) and optical (b) noise spectral density and cross-correlation factor over 10 Hz – 20 kHz frequency range (c) dependency on current at 293,25 K temperature.

However when mode-hopping effect occurs, electrical and optical noise intensity, as well as the cross-correlation factor between them, strongly increase (Fig 2). Intense fluctuations observed at this point are characterised by Lorentzian spectrum (it is caused by generation-recombination ant carrier capture processes in centers formed by defects in the barrier layer) and highest correlation is found at frequencies, close to the spectrum cut-off frequency, which ranges 1 kHz to 1 MHz. Therefore characteristic times of processes that take place at device during mode-hopping effect ranges from 0,2 μs to 0,2 ms.

High cross-correlation factor between electrical and optical noise during mode-hopping effect shows that processes which determine it at this operation point take place in the active region of LD. Moreover different cross-correlation factor value and sign, different cut-off frequencies at different LD operation conditions indicate that there are several physical processes that take place in the device structure during mode-hopping. Therefore there are several GR centers in the sample and they are activated at different operation conditions.

[1] M. Yamada, IEEE J. Quantum Electron., QE-22, 1052-1059 (1986).
[2] V. Palenskis, S. Pralgauskaitė, J. Matukas, J.G. Simmons, S. Smetona, R. Sobiestianskas, IEEE Trans. Electron Dev., 50, 366-371 (2003)
[3] B.K. Jones, IEEE Trans. Electron Dev., 41, 2188-2197 (1994)

TWO DIMENSIONAL CORRELATION SPECTROSCOPY AND PRINCIPAL COMPONENT ANALYSIS APPLICATION FOR MOLECULAR COMPOUNDS RAMAN AND IR SPECTRA PROCESSING

M. Pareigis, J. Kausteklis, and V. Aleksa

Department of General Physics and Spectroscopy, Faculty of Physics, Vilnius University, Saulėtekio Ave. 9-III, LT-10222 Vilnius, Lithuania

martynas.pareigis@gmail.com; jonas.kausteklis@gmail.com

The research analysis of spectra of various molecular compounds like ionic liquids due to many together overlapping peaks bands is difficult often [1]. The difficulties related to highly overlapping peaks of vibrational bands in one dimensional spectrum were solved using the two powerful spectroscopy methods. We represent two mathematical methods which could be used for all kind of spectra if it has overlapped spectral components. Two dimensional correlation spectroscopy (2DCoS) and Principal Component analysis (PCA) have been used to investigate Raman and FTIR spectra of acetonitrile and water mixture Advantages and disadvantages of both mathematical methods have been discussed [2,3]. Analysis of the data using both methods suggested that the bands could be separated and explained more precisely (Fig. 1.).

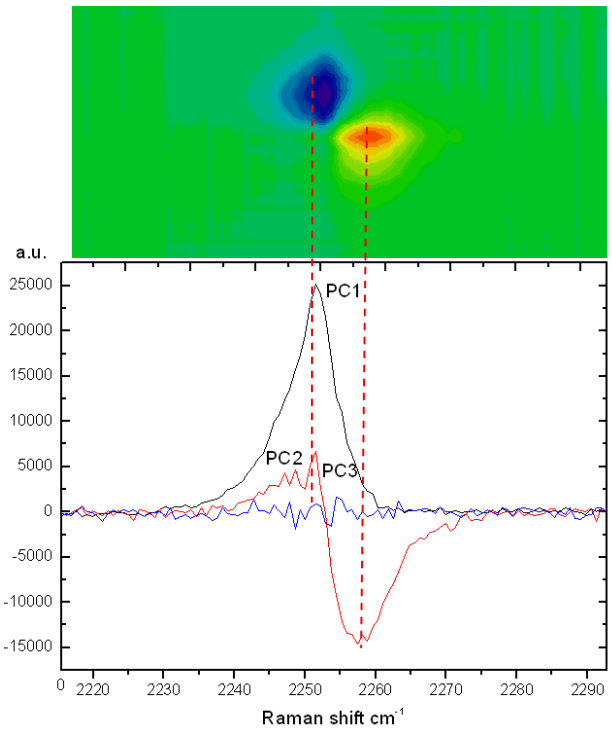

Fig. 1. Asynchronous correlation map (upper) obtained from 2D Raman spectra and PCA analysis (lower) of acetonitrile and water mixtures.

[1] V. Aleksa, J. Kausteklis, V. Klimavicius, Z. Gdaniec, V. Balevicius. Raman and NMR spectroscopy study of liquid crystalline ionogel phase in ionic liquid/H2O mixtures: The states of water. Journal of Molecular Structure (2011, accepted)

[2] Noda. Determination of Two-Dimensional Correlation Spectra Using the Hilbert Transform. Applied spectroscopy. 54(7), 994-999 (2000).

[3] F.H. Tukhvatilin, A. Jumabaev, G. Muradov, H.A. Hushvaktov and A.A. Absanov. Raman Spectra of CN Vibrations of Acetonitrile in Aqueous and Other Solutions. Experimental results and ab initio Calculations. Journal Of Raman Spectroscopy. 36, 932-937 (2005).

INFRARED SPECTROSCOPY STUDY OF THE MOLECULES WITH INTERNAL HYDROGEN BONDS ISOLATED IN THE LOW TEMPERATURE MATRICES

M. Pučetaitė, J. Čeponkus

Department of General Physics and Spectroscopy, Faculty of Physics, Vilnius University, Saulėtekio Ave. 9-III, LT-10222 Vilnius, Lithuania

milda.pucetaite@ff.stud.vu.lt

The formation of hydrogen bond is very important in many aspects of physics, chemistry and biology. It can alter properties of the matter and influence processes occurring in chemical and biological systems. For these reasons, hydrogen bonded systems are subjects of numerous experimental and theoretical studies. Carboxylic acids, which form a variety of different complexes via hydrogen bond, are an example of such systems. Formic and acetic acids form three types of dimers. Their structure and the strength of hydrogen bond depend on the length of the aliphatic radical [1, 2]. However, the alterations of the strength of the hydrogen bond, when the aliphatic radical is prolonged, are not linear. In this work we present a study of heavier carboxylic acids hydrogen bonded associates. The aim of this study is to determine the links between the length of the aliphatic chain and the self association of the carboxylic acids.

The experiments were performed using low temperature infrared spectroscopy method. The samples were prepared using matrix isolation technique: the molecules of the acid and inert gases (in this study we used argon (Ar)) were mixed in the vacuum line and deposited on cold (9 – 10 K) CsI window in the close cycle helium cryostat. Gas flow into the cryostat was regulated using the needle valve. The acid to argon ratio was 1:200. Infrared absorption spectra were recorded using *IFS 113v* spectrometer from *Bruker* with infrared radiation source “glowbar” and liquid nitrogen cooled MCT (mercury-cadmium-telluride) detector. Spectra were obtained using 0.1 and 1 cm^{-1} spectral resolution. The spectral region corresponding to C=O stretch vibration of carboxylic acids is presented in figure 1.

It has been shown that binding energy of the associates of small carboxylic acids (formic, acetic, propanoic) is decreasing as the length of the radical chain is increase. The decrease is not linear and alternates for even and odd number of carbon atoms in the radical chain. The alternation depends on how the CH_3 group is situated in respect to C=O bond. The strength of the hydrogen bond is indicated by the red shift of the C=O vibration band of carboxylic acid complex in respect to the corresponding monomer band. The stronger the bond, the larger the red shift. [3].

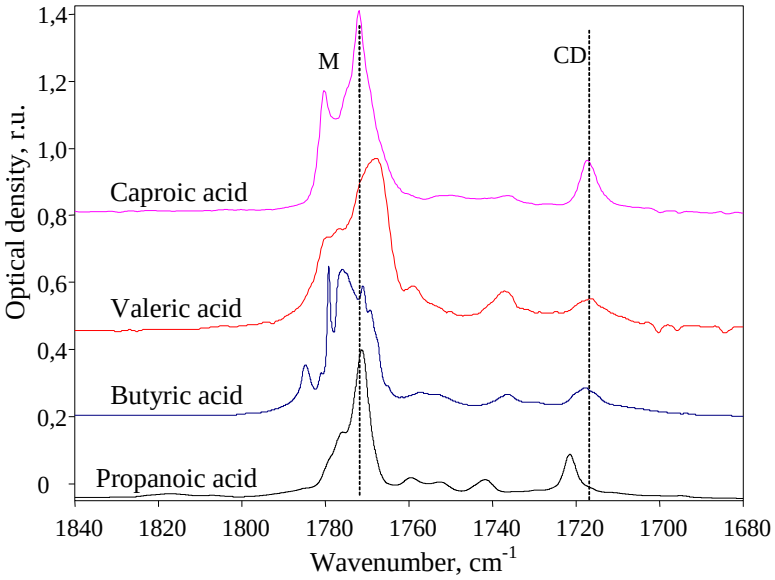

Fig. 1. The infrared absorption bands of C=O vibration of carboxylic acids isolated in argon matrices (M – monomer, CD – cyclic dimer)

In this work, the self association of heavier carboxylic acids (butyric, valeric, caproic) was analysed. Their infrared absorption spectra are very similar (Fig. 1). According to the spectra obtained, it was determined that in low temperature matrices two types of self associates form: stabile cyclic and less stabile, corresponding to intermediate state, open dimers. As mentioned above, the strength of the hydrogen bond, or the magnitude of binding energy, can be evaluated observing the red shift of the C=O vibration band of the dimer in respect to the corresponding monomer band. It is shown in figure 1 that in case of the heavier carboxylic acids (the ones that have more than three carbon atoms in their radical chain) the red shift is the same. These results allow us to assume that the binding energy of the self associates is very similar and the length of the C-C chain has no further influence on its magnitude.

[1] Sander W., Gantenberg M., *Spectrochimica Acta Part A.* 2005, 62, 902–909.
[2] Sablinskas V., Pucetaite M., Ceponkus J., Kimtys L., *Journal of Molecular Structure*. 2010, 976, 263-269.
[3] Ceponkus J., Lesciute D., Cepulinskaite D., Pucetaite M., Sablinskas V., *Lithuanian Journal of Physics*. 2009, 49.

DIELECTRIC PROPERTIES OF RUBITHERM PX 21 LATENT HEAT POWDER

A. Sakanas, R. Sobiestijanskas, and J. Banys

Department of Radiophysics, Faculty of Physics, Vilnius University, Saulėtekio Ave. 9-III, LT-10222 Vilnius, Lithuania

aurimas.sakanas@ff.stud.vu.lt

RUBITHERM PX [1] is an innovational material mainly used in thermal energy storage applications due to its heat storage properties. RUBITHERM PX powder has a mechanically stable structure – a hydrophilic silica powder as matrix material. It contains up to 60% paraffin as phase change material (PCM) in a polymer structure [2]. The melting point of the investigated material is approximately 21 °C.

The purpose of the study is to investigate if there is any kind of anomaly in the dielectric permittivity and capacity, as these parameters usually show fundamental changes in the material's structure.

In the present study samples were made in shape of 7,84 mm diameter brass cylinders using a Teflon tube as part of powder sample holder. The powder was placed between the cylindrical metal contacts, forming the capacitor for material investigation. Dielectric measurements were performed at temperatures 250 – 310 K and in the frequency range 100 Hz – 1 MHz. The capacity of samples was measured using LCR-meter HP4284 at a rate of 1 K/min during cooling and heating. Temperature was measured using Type-T thermocouple and Keithley Integra 2700 multimeter.

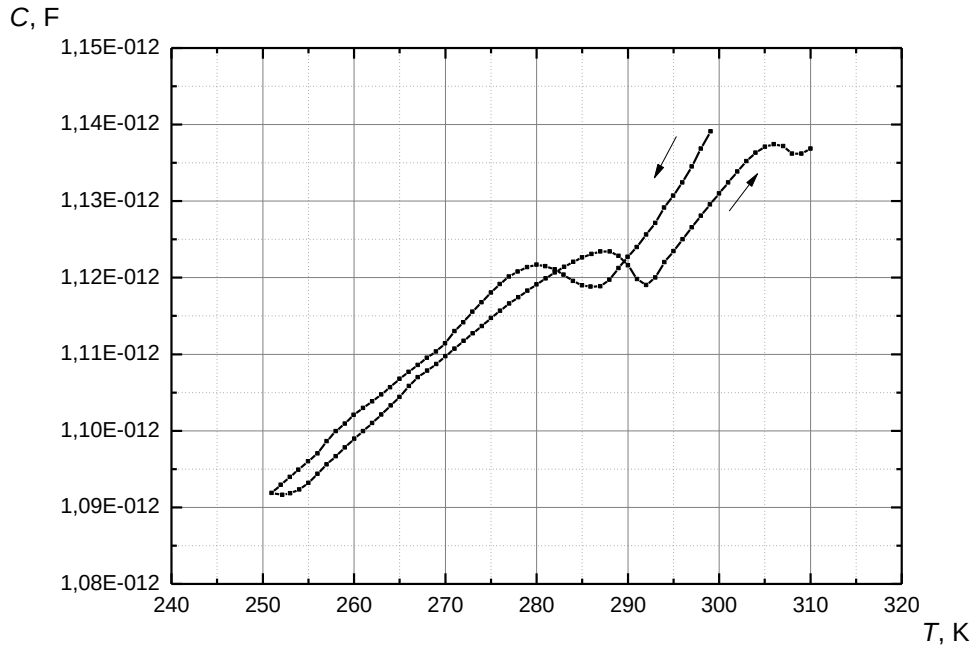

Fig. 1. Measured material's capacitance changes during cooling and heating

Figure 1 shows capacitance changes when cooled and heated. Two curves for the cooling – heating cycle clearly indicate presence of the hysteresis of approximately 7 K near the RUBITHERM PX 21 melting point. However, the depth of dielectric anomaly is only about 3%, thus no parameters related to the phase transition and related dielectric dispersion can be determined. Variations in wider temperature region revealed upper temperature stability limit of the material to be 370 K.

[1] Rubitherm GmbH. (2011). Product sheets (http://www.rubitherm.com/english/index.htm ; last visit 2011/02/25).

[2] H. Mehling, L.F. Cabeza. Heat and cold storage with PCM, pp. 44 (Springer-Verlag Berlin Heidelberg, Germany, 2008).

ELECTRICAL PROPERTIES OF MICRODISCHARGE IN AIR

Ok. Solomenko, I. Prysiazhnevych, V. Chernyak, V. Zrazhevskij

Taras Shevchenko National University of Kyiv, Kyiv, Ukraine
oksana_solomenko@ukr.net

The last two decades there is a continuous growing interest to microdischarges, which are characterized by small geometric dimensions. Today already accomplished a lot of small size configurations of electrical discharges as an open metal electrodes and dielectric shield electrodes, which are referred to as microdischarges [1].

Ascertained for microdischarges are the conditions: $pd \leq 10$ torr*cm at geometry discharge less than 1 mm [2], where p - gas pressure and d - the distance between the electrodes. Discharge of a large geometry ($d > 1$ cm) $pd \leq 10$ torr*cm identifies as a glow discharge, in which diffusion suppresses the development of ionization instability and high level of nonequilibrium plasma glow discharge (excess electron temperature - T_e above the temperature of gas - T).

Especially for the generation of nonequilibrium plasma at atmospheric pressure with low temperature gas was created first microdischarge (microdischarge with hollow cathode) [3]. High level of nonequilibrium plasma microdischarge defines broad range of its applications today.

Another characteristic of microdischarges is positivity differential resistance, which is crucial in technology, because it gives the opportunity to supply a large number of microdischarges from other sources without ballast resistance [2].

The system with hollow cathode and anode was studied. Discharges at different pressures (pd range 0.76-7.6 torr*cm) were investigated. When system realized with hollow cathode differential resistance decreases and doesn't depend of pressure. In case hollow anode, with pressure increasing, differential resistance changes sign to negative.

[1] А. Энгель, Ионизованные газы, (Москва: ФМЛ, 1959).
[2] K.H. Becker, U. Kogelschatz, K.H. Schoenbach, R.J. Barker, Non-Equilibrium Air Plasmas at Atmospheric Pressure, (Bristol and Philadelphia: IOP Publishing Ltd., 2005).
[3] K.H. Schoenbach, R. Verhappen, T. Tessnow, F.E. Peterkin, W.W. Byszewski, Microhollow cathode discharges, Appl. Phys. Lett. **68**, 13-15 (1996).

TERAHERTZ IMAGING OF THE OBJECTS CONTAINING SUCROSE AND TARTARIC ACID

R. Venckevičius[1], I. Kašalynas[2]

[1] *Faculty of Physics, Vilnius University, Saulėtekio Ave. 9-III, LT-10222 Vilnius, Lithuania*
[2] *Center for Physical Sciences and Technology, A. Goštauto 11, LT-02300 Vilnius, Lithuania*
r.venckevicius@gmail.com

Terahertz (THz) radiation (10^{12} Hz) is electromagnetic waves lying in frequency range between microwaves and far infrared. THz radiation can be used for material composition and/or quality inspection. Recent work [1] shows that THz radiation could be used for explosive and drug detection as well as an efficient various packages screening. In this work THz transmittance of the sucrose and tartaric acid was investigated, THz imaging at selected frequencies was performed.

The investigated materials were sucrose (SC) and tartaric acid (TA) exhibiting partial transmittance in THz frequency range. The samples were prepared by mixing materials with polytetrafluoroethene (PTFE) powder and subsequently forming pellets of 1.4 mm thickness and 13 mm diameter under application of pressure. In this way it was fabricated three pellets consisting of 10% SC, 10% TA, and mixture of 5% SC and 5% TA, and one pellet - of pure PTFE. To determine possible frequencies for THz imaging, the pallets with SC and TA spectra were measured with a resolution of 1 cm^{-1} by means of vacuum Fourier spectrometer operating as ordinary Michelson interferometer. The transmittance spectra from 0.6 to 5.7 THz are shown in Fig. 1a. The PTFE itself has no absorption features but SC and TA demonstrate several absorption lines. The strongest lines for the SC are at frequencies of 61.0, 87.9, 114.7, 141.8 cm^{-1}, while for the TA – at 36.5, 87.9, 100.1, 121.8, 136.6 cm^{-1}. Available THz laser lines (46.6 cm^{-1} and 61.3 cm^{-1}) are also indicated in the spectrum by arrows. For THz imaging one can use them due to distinctive SC peak at 49 cm^{-1} and peak at 61 cm^{-1} in which TA has stronger absorption.

The spatial pattern of material in each sample was investigated via active THz imaging technique. Experiment setup is shown in Fig. 1b. THz image of the object was recorded by moving sample with a constant speed in focal plane (XY) of parabolic mirror M2 and at the same time measuring sample's transmittance. Fast raster scanning technique with position synchronized measurement was developed to reduce imaging time. Using this method image recording time depends on imaging area, sample translation velocity and desirable resolution. For example, it takes about 5 minutes to record an image of size 6x3.5 cm^2 with 0.03 cm resolution, when object's translation velocity and measurement period is of 6 cm/s and 5 ms, respectively.

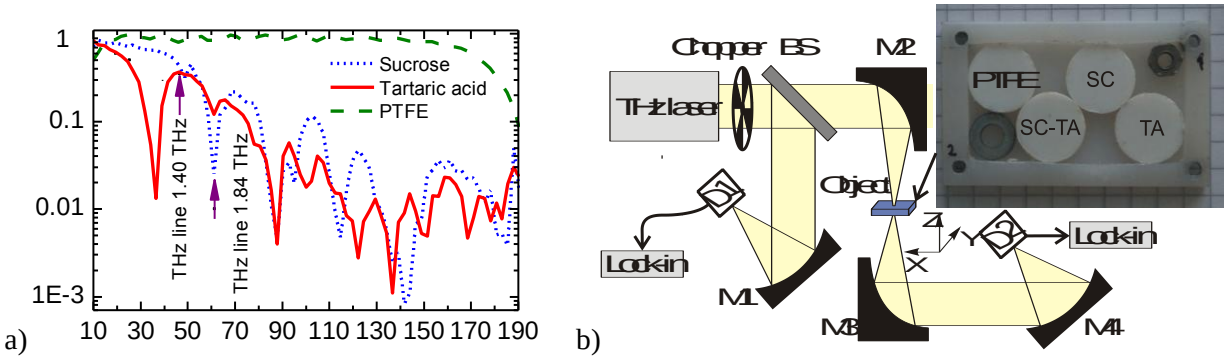

Fig. 1. (a). Transmittance spectra of SC and TA placed in PTFE matrix. Arrows indicate the place of the THz laser lines. (b) The THz imaging setup and investigated objects all packed in a plastic box.

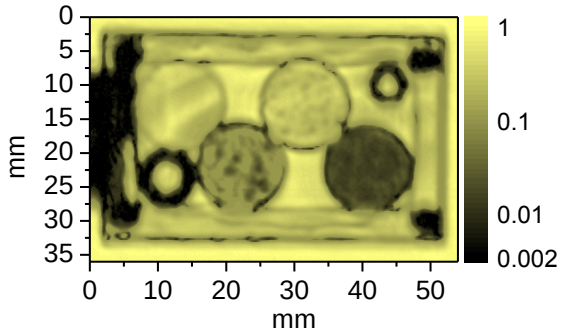

Fig. 2. THz image of inspected sample obtained using 1.40 THz radiation. Vertical axis shows object's transmittance in logarithmic scale.

Prepared four sample pellets together with two metal washers were enclosed in a plastic box made of HDPE, which is opaque for visible light but not for THz. The THz images of the box at 1.40 THz and 1.84 THz are shown in Fig. 2. In THz light the box content is screened. At both frequencies the pellet of PTFE exhibits highest transmittance in comparison to others. However, the pallets with SC and TA which have different transmittance (see also Fig. 1a) behave differently. In the image taken at 1.40 THz, the pellet with SC is brighter (higher transmittance) as compared to the pellet with TA and conversely in the image recorded at frequency of 1.84 THz. The pellet with mixture of SC and TA is always in between. In such a way THz imaging allows us to distinguish pellets with SC, TA, and mixture of both. Additionally, the material distribution in the pellets can also be inspected which appears as spots of smaller transmission in the pallet area.

To summarize, in this work we measured transmittance spectra of the sucrose and tartaric acid in frequency range from 0.3 to 5.7 THz. The THz imaging of the pellets with different content of sucrose and tartaric acid were performed at properly selected frequencies.

[1] L. Zhang, H. Zhong, C. Deng, C. Zhang, Y. Zhao, Terahertz wave reference-free phase imaging for identification of explosives, Applied Physics Letters **92**, 091117 (2008).

MORPHOLOGICAL ANALYSIS OF MULTICOMPONENT KIDNEY STONES BY MEANS OF INFRARED MICROSCOPY

T. Žalys, M. Pučetaitė, and V. Šablinskas

Department of General Physics and Spectroscopy, Faculty of Physics, Vilnius University, Saulėtekio Ave. 9-III, LT-10222 Vilnius, Lithuania

Tomas.Zalys@ff.stud.vu.lt

Kidney disease is a growing problem. In some countries up to 12 percent of total population suffer from kidney stones and it is still unknown how and why these stones are being formed. It is very important that the causes of stone formation must be understood in order to enable the doctors stopping the disease and preventing its recurrence. Therefore the studies of chemical composition and domain structure of the stones are of the great importance.

Fourier transform infrared (*FTIR*) microscopy [1, 2] is an effective method for qualitative and quantitative analysis of the spatial distribution of chemical compounds in kidney stones. In this study Bruker "Hyperion 3000" infrared microscope was used, connected to FTIR spectrometer „Vertex 70". The data was registered and processed using „Opus 6.5" software package. The spectra were collected using specular reflectance method. In the analysis of the sample single channel semiconductor mercury-cadmium-telluride (*MCT*) detector and multi-channel focal plane MCT 64x64 array (*FPA*) detector were used. Multi-channel detector enables to achieve higher spatial resolution (up to 20 μm) compared to a single channel detector (100 μm). The results showed that chemical maps, created using FPA detector, were more detailed and smaller domain structures were visible (Fig. 1).

These studies also allow concluding that the stones can be formed in at least two different ways. Formation of the stone can be induced by small deposit of one component on the epithelium of urinary tract and a layer of another component forms on it through time. In this particular case stone had calcium oxalate core with uric acid layer formed around it. Stone can also be formed in the oversaturated urine from various mineral salts.

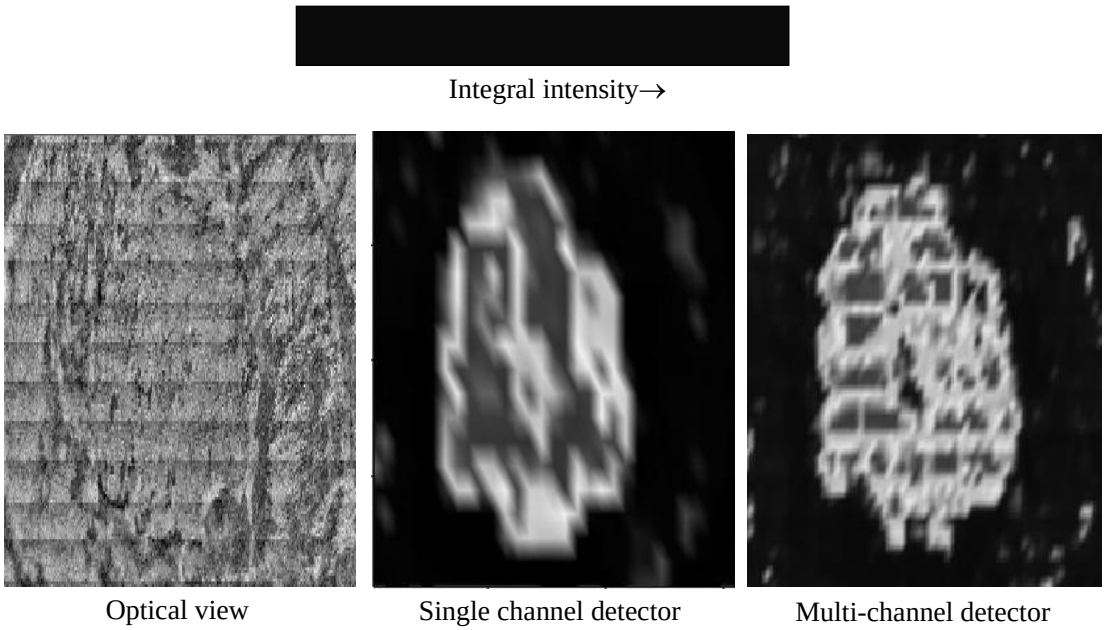

Fig. 1. Visible image of a cross-sectioned renal stone and distribution of calcium oxalate in the sample, registered using single channel and multi-channel detectors.

[1] J. C. Anderson, James C. Williams Jr, Andrew P. Evan, Keith W. Condon, Andre J. Sommer, *Analysis of urinary calculi using infrared microspetroscopic surface reflectance imaging technique*, USA, (2007).
[2] Hollas J. M., *Modern spectroscopy*, John Wiley & Sons, Ltd, Chichester. 2004. 452.

QUANTUM COHERENCE IN SIMULATIONS OF 2D OPTICAL SPECTRA OF EXCITONICALLY-COUPLED MOLECULAR AGGREGATES

V. Butkus[1], D. Abramavicius[1], A. Gelzinis[1], and L. Valkunas[1,2]

[1] *Department of Theoretical Physics, Faculty of Physics, Vilnius University, Saulėtekio Ave. 9-III, LT-10222 Vilnius, Lithuania*

[2] *Center for Physical Sciences and Technology, A. Goštauto 11, LT-02300 Vilnius, Lithuania*

vytautas.butkus@ff.vu.lt

Time-resolved two-dimensional photon-echo (2D PE) spectra of excitonically coupled dimer as well as linear J-aggregates containing four molecules per unit cell is theoretically considered. Analysis of a single unit cell and the full-sized J-aggregate is carried out. Spectral features of a single unit cell are sorted out by assigning them to specific double-sided Feynman diagrams. Two different approaches of disorder are employed, the resulting differences in the spectra are discussed and the conditions for their utilization are described. Special attention is paid to quantum coherence dynamics of a single unit cell and the full-sized J-aggregate. Possibilities of probing quantum coherences as well as performing quantum control by two-colour 2D PE spectroscopy are discussed.

To simulate the third-order polarization for 2D spectra calculations, we use the system response function theory considering the field-matter interaction perturbatively in terms of the time-dependent density operator [1-3]. The third-order polarization, detected at the photon-echo direction, is obtained as a triple convolution of the system response function and the sample-exciting electric field:

$$P_{\mathrm{PE}}^{(3)}(\tau,T,t) = \int_0^\infty \mathrm{d}t_3 \int_0^\infty \mathrm{d}t_2 \int_0^\infty \mathrm{d}t_1 S^{(3)}(t_3,t_2,t_1) \times E(\vec{r},t-t_3)E(\vec{r},t-t_3-t_2) E(\vec{r},t-t_3-t_2-t_1) \quad (1)$$

The total system response is resolved as a number of oscillating patterns corresponding to Liouville space pathways. Using a second-order cumulant expansion technique, the shapes of spectral elements of the oscillating terms in frequency domain are determined by summing up the time-dependent lineshape functions, that are calculated using the classically-defined spectral density function of the bath fluctuations.

Time-resolved two-dimensional photon-echo spectra of linear J-aggregates containing four molecules per unit cell - a model system for a concentrated water solution of the pseudoisocyanine dye - is theoretically considered. The superradiant J-band spectrum is a superposition of a few different pathways. The simulated quantum coherence beats are dependent on the model of disorder.

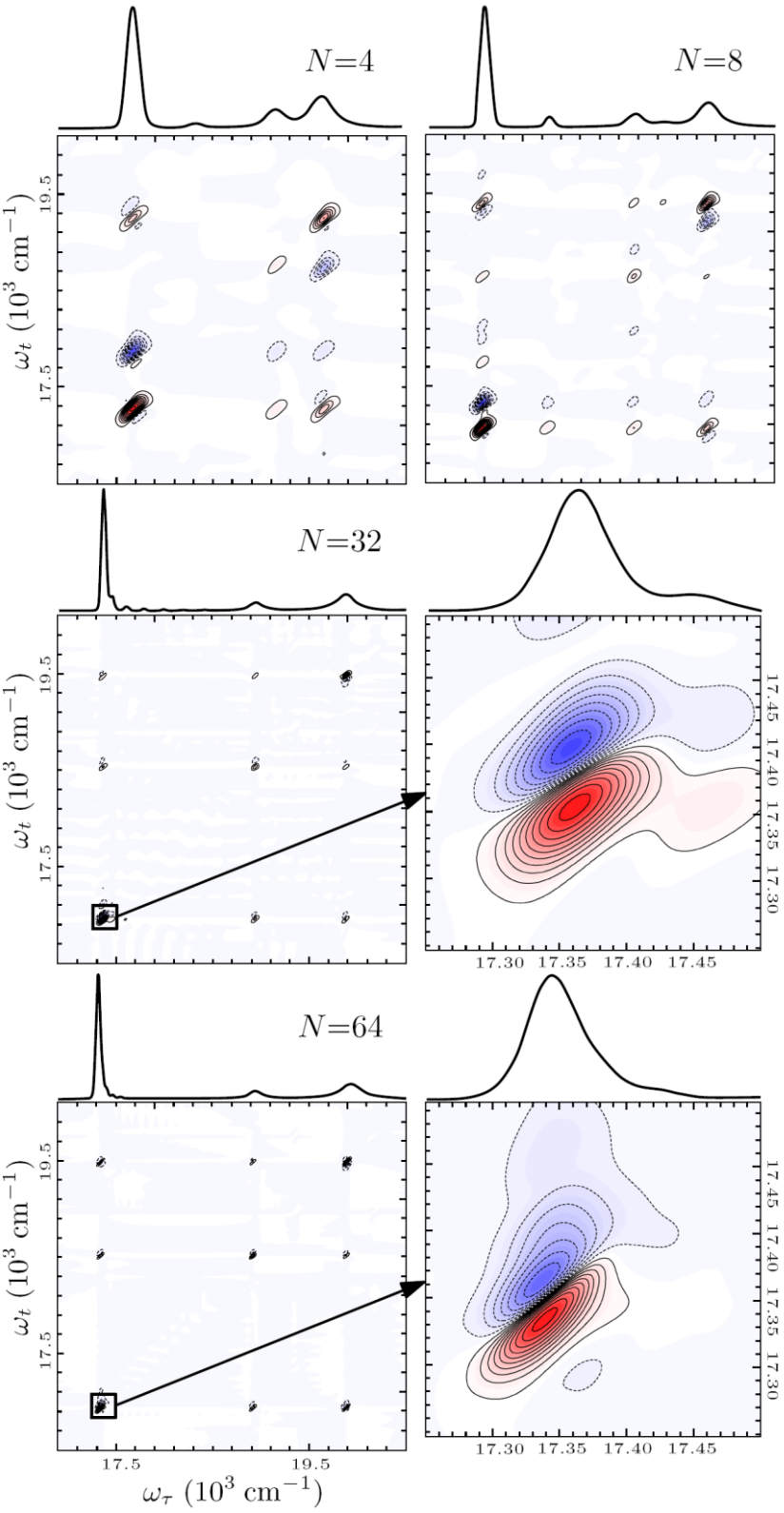

Fig. 1. Absorption spectra and the real part of total 2D spectra of PIC J-aggregate with different number of chromophores N.

[1] S. Mukamel, Principles of Nonlinear Optical Spectroscopy, (Oxford University Press, New York, 1995).
[2] D. Abramavicius et al., Chem. Rev., 109, 2009.
[3] V. Butkus et al., Lith. J. Phys., 50, 2010.

THE RADIATION OF A RELATIVISTIC ACCELERATED CHARGE IN A COMOVING FRAME

P. Drobiński

College of Inter-faculty Individual Studies in Mathematics and Natural Sciences, University of Warsaw, Poland

patryk.drobinski@gmail.com

It is known that an accelerated charge emits electromagnetic radiation. However, a charge which is at rest in a gravitational field does not seem to radiate. I discuss the problem of whether acceleration can be distinguished from a gravitational field by observing the radiation of a charged particle at rest.

I consider a charged particle moving with constant acceleration in a flat spacetime. I establish its comoving frame using the Rindler coordinates.

First, I transform Maxwell's equations to this frame, using the formalism of general relativity and attempt to solve them analytically. However, it proves too complicated. Next, I explicitly find the electromagnetic field in an inertial frame using the Liénard-Wiechert potential and transform it to the comoving frame.

It turns out that the field is independent of the particle's proper time. Thus, no radiation can be seen by an observer staying at rest in the particle's frame. This result agrees with the equivalence principle.

ANALYSIS OF ELECTRONIC EXCITATION DYNAMICS IN A MOLECULAR DIMER VIA HIERARCHICAL EQUATIONS OF MOTION

A. Gelžinis[1], D. Abramavičius[1], V. Balevičius Jr.[1], and L. Valkūnas[1,2]

[1] *Department of Theoretical Physics, Faculty of Physics, Vilnius University, Saulėtekio Ave. 9-III, LT-10222 Vilnius, Lithuania*

[2] *Center for Physical Sciences and Technology, A. Goštauto 11, LT-02300 Vilnius, Lithuania*

Andrius.Gelzinis@ff.stud.vu.lt

Analysis of electronic excitation dynamics is important in order to understand the efficiency of excitation energy transfer (EET) in wide variety of molecular complexes including photosynthetic pigment-protein membrane aggregates [1]. Redfield theory is commonly applied for studying dissipative electronic excitation dynamics. However, because of its perturbational nature and Markovian approximaton, the Redfield theory is limited to weak coupling between the system and the environment. While these limitations pose no problems in most applications, it has been shown that there are cases when the Redfield theory is not suitable [2].

Hierarchical equation of motion (HEOM) theory [3] is a nonperturbational theory and it allows going beyond the Markovian regime. However, the full HEOM theory is very expensive computationally and is usually applied only for small systems: monomers and dimers. In this work, we utilize a simpler version of HEOM, named Hierarchical quantum master equation (HQME), which has an impressive applicability range but much lower computational cost [4].

Here we analyze electronic excitation dynamics in a molecular dimer using HQME, with a set of parameters typical to photosynthetic EET. Time evolution of the population of the lowest energy exciton state (denoted $\rho_{e_1e_1}$) is presented in Fig. 1. Here λ denotes electron-phonon coupling strength whereas J denotes intermolecular coupling strength.

First, it should be noted that, when electron-phonon coupling is not very strong, oscillations in population dynamics can be observed. These oscillations show influence of electronic coherence to population dynamics. The aforementioned oscillations last for relatively long times.

Second, it can be seen that electron-phonon coupling strength strongly influences relaxation rates. The data in Fig. 1 shows that population of the lowest energy exciton state relaxes to equilibrium faster, when $\lambda = J$. The rate of relaxation decreases, however, when electron-phonon coupling strength is relatively weaker or stronger than intermolecular coupling strength.

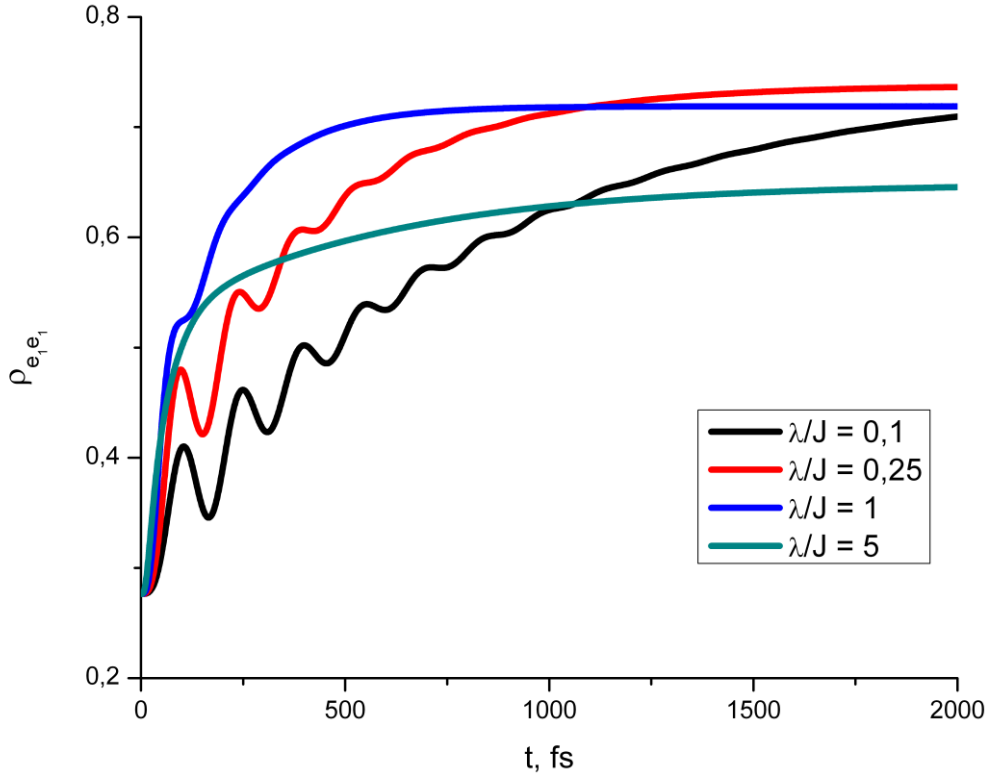

Fig. 1. Time evolution of the population of the lowest energy exciton state in a dimer.

Finally, as can be seen from Fig. 1, the equilibrium distribution in the dimer depends on electron-phonon coupling strength. It can be shown that increasing λ lowers the difference between the energies of the dimer eigenstates. This corresponds to effective decrease of intermolecular coupling strength due to electron-phonon coupling.

[1] G. S. Engel, T. R. Calhoun, E. L. Read, T. K. Ahn, T. Mancal, Y. C. Cheng, R. E. Blankenship, G. R. Fleming. Evidence for wavelike energy transfer through quantum coherence in photosynthetic systems. Nature, **446**, 782 (2007).

[2] Ishizaki, G. R. Fleming. On the adequacy of the Redfield equation and related approaches to the study of quantum dynamics in electronic energy transfer. The Journal of Chemical Physics, **130**, 234110 (2009).

[3] Y. Tanimura, R. Kubo. Time Evolution of a Quantum System in Contact with a Nearly Gaussian-Markoffian Noise Bath. Journal of the Physical Society of Japan, **58**, 101 (1989).

[4] R. X. Xu, B. L. Tian, J. Xu, Q. Shi, Y. J. Yan. Hierarchical quantum master equation with semiclassical Drude dissipation. The Journal of Chemical Physics, **131**, 214111 (2009).

GENERATION OF $1/f^{\beta}$ NOISE USING THE SUPERPOSITION OF PROCESSES WITH TWO RELAXATIONS

R. Kazakevičius, B. Kaulakys

[1] *Institute of Theoretical Physics and Astronomy, Vilnius University, Goštauto 12, LT-01108 Vilnius, Lithuania*

Rytis.Kazakevicius@gmail.com

A random process characterized in some frequency range by the power spectral density proportional to $1/f^{\beta}$ is called "$1/f^{\beta}$ noise", where β is real number between 0 and 2. Such processes have been observed in various areas. For example, $1/f^{\beta}$ noise plays an important role in electronic oscillators noise spectra [1]-[3]. The variability of biological rhythms generated by diverse functions in the human organism has revealed the persistent long-range correlation, or $1/f^{\beta}$ noise [4].

Many methods have been developed for generating process sequences with power spectral densities approximating $1/f^{\beta}$ over the given frequency range, such as wavelet-based methods [5], fractional integration-based methods [6], the fractional Brownian motion method [7], Fourier transform based-methods [8], Point process model [9] and other methods.

We analyzed the model based on signal $I(t)$ that was a superposition of uncorrelated processes with two relaxations,

$$I(t) = \sum_{l=1}^{N} z_l(t). \tag{1}$$

Here N is a number of processes and $z_l(t)$ is a process with two relaxations. It is described by the differential equation

$$\dot{z}_l = -\gamma_z z_l + v_l(t) \tag{2}$$

where γ_z is the relaxation rate of process, $v_l(t)$ is velocity of the Brownian particle and it is described by the Langevin equation

$$\dot{v}_l = -\gamma_l v_l + \sigma_l \xi_l(t) \tag{3}$$

where $\xi_l(t)\xi_l(t)$ is the white noise and σ_l is standard deviation of white noise.

The power spectral density of such signal $I(t)$ is

$$S_I(f) = \frac{2A}{\omega^2(\omega^2+\gamma_z^2)} \frac{\gamma^{2-\beta}}{2-\beta^2} F_1\left(1, \frac{2-\beta}{2}, \frac{4-\beta}{2}, -\frac{\gamma^2}{\omega^2}\right)\Bigg|_{\gamma_{\min}}^{\gamma_{\max}} \tag{4}$$

Model generated power spectral density as a function of frequency is represented Fig. 1. We proved that the model of superposition of processes with two relaxations in specific frequency ranges $\gamma_{min} \ll f \ll \gamma_{max} \ll \gamma_z$ and $\gamma_{min} \ll f \ll \gamma_z \ll \gamma_{max}$ generated power spectral

density proportional to $1/f^{\beta}$. Here γ_{min} and γ_{max} are minimal and maximal values of the Brownian particle relaxation rates.

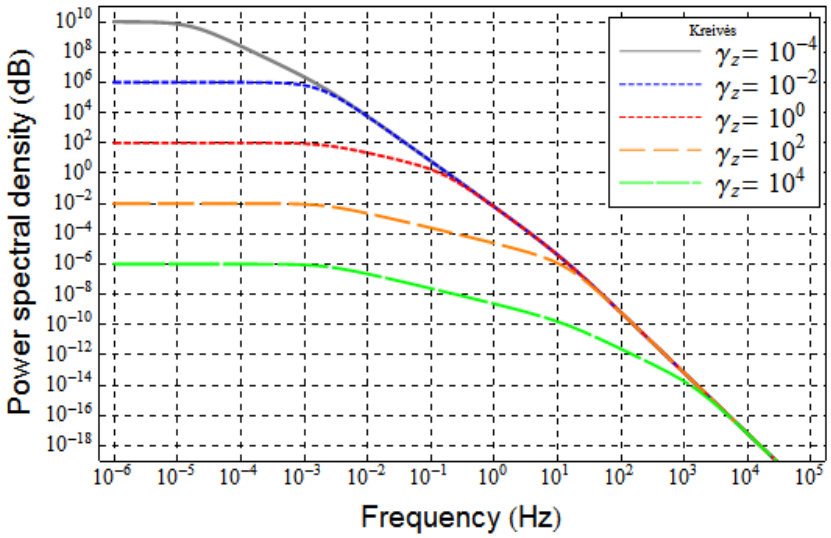

Fig. 1. Power spectral densities generated by Eq. (4), each spectral density are generated with different γ_z other parameters $\gamma_{min} = 0.01, \gamma_{max} = 100, A = 0.5$

[1] J. Mukherjee, P. Robin, and S. Akhtar, An analytic circuit-based model for white and flicker phase noise in LC oscillators, IEEE Trans.Circuits Syst. I, Reg. Papers, 1584–1598 (2007).

[2] P. Maffezzoni, Frequency-shift induced by colored noise in nonlinear oscillators, IEEE Trans. Circuits Syst. II, Exp. Briefs, 887–891, 2007).

[3] P. Andreani, Time-variant analysis of the $1/f^2$ phase noise in CMOS parallel LC-tank quadrature oscillators, IEEE Trans. Circuits Syst. I, Reg. Papers, 1749–1760 (2006).

[4] K. Torre, D. Delignières, Unraveling the finding of $1/f^{\beta}$ noise in self-paced and synchronized tapping: a unifying mechanistic model, Biological Cybernetics, 159–170 (2008).

[5] G. W. Wornell, Wavelet-based representations for $1/f^2$ family offractal processes, Proc. IEEE, 1428–1450 (1993).

[6] J. A. Barnes and D. W. Allan, A statistical model of flicker noise, Proc. IEEE, 176–178 (1966).

[7] B. B. Mandelbrot and H. W. Van Ness, Fractional Brownian motions,fractional noises and applications, SIAM Rev., 422–436, (1968).

[8] A. V. Chechkin and V. Y. Gonchar, Fractional Brownian motion based on fractional integration of a white noise, Chaos, Solitons, Fractals, 391–398 (2001).

[9] B. Kaulakys, V. Gontis, and M. Alaburda, Point process model of 1/f noise vs a sum of Lorentzians, Phys. Rev. E 71 (5) 051105 (2005).

IMPURITIES SUPERDIFFUSION IN Si CRYSTAL LATTICE

K. Petravičius

Faculty of Natural Sciences, Šiauliai University, P. Višinskio 19, 77156 Šiauliai, Lithuania

kostex12@gmail.com

Taking in the care that diffusion must occure with finite velocity the nonlinear diffusion equation with diffusion coefficient directly proportional to the impurities concentration [1]. This equation was applied for consideration the ultrafast impurities diffusion or superdiffusion assisted by vacancies generated by soft X-rays. Also superdiffusion can be realized beams of electrons, protons and electrons. We theoretically consider reasons of impurities superdiffusivity experimentally obtained in crystal silicon irradiated by soft X-ray [2]. The boron and phosphorus introduction in p-type crystal silicon at room temperature [2] was assisted by high concentration $\approx 10^{13} cm^{-3}$ of metastable vacancies generated by Auger effect.

M. E. Glicksman [3] proposed statistical method for diffusion processes assisted by vacancies. We included the anharmonic vibrations of atom-vacancies pairs and got more exast expression for atoms hoping frequencies

$$\Gamma_\nu = \frac{1}{2\pi kT\sqrt{\frac{m}{k_E}} + Anh\sqrt{2m\pi kT}} \cdot e^{-\frac{k_E(X_0 - X^*)^2 + \frac{r}{3}(X_0 - X^*)^3}{2kT} \cdot kT}, \qquad (1)$$

which depends lattice excitation parameter α and period of excited states existence. For excited lattices we have $\alpha < 1$. Diffusion coefficient in the excited crystals lattices can be considered introducing temperature function

$$T(t) = -\frac{1}{b\ln(z)}, \qquad (2)$$

$$b = \frac{k(\alpha - 1)}{E}. \qquad (3)$$

Our theory was used for evaluation of impurities diffusion coefficients in crystals irradiated by soft X-rays.

[1] J. Janavičius. Phys. Lett. A 224, 159 (1997). 12, p. 19 (2005).
[2] J. Janavičius, S. Balakauskas, V. Kazlauskienė, A. Mekys, R. Purlys, J. Storasta. Superdiffusion in Si Crystal Lattice Irradiated by Soft X-Rays. Acta Physica Polonica A, Vol. 114, No. 4, 779 (2008).
[3] M. E. Glicksman. Diffusion in solids, JOHN WILEY & SONS, INC, New York, (2000) p. 472.

CONFIGURATIONAL ENTROPY OF WIGNER CLUSTERS

A. Radzvilavičius, E. Anisimovas

Department of Theoretical Physics, Faculty of Physics, Vilnius University, Saulėtekio Ave. 9-III, LT-10222 Vilnius, Lithuania

arunas.radzvilavicius@ff.stud.vu.lt

Strongly interacting systems of classical charged particles confined in traps are known to form regular structures, known as Wigner clusters. Typical experimental realizations of such systems include electrons on the surface of liquid helium and micro-metric charged dust particles in low-temperature complex plasmas [1]. It turns out that in most cases besides the unique ground-state configuration, corresponding to the global minimum of the potential energy, a number of metastable states corresponding to various local minima are present (Fig. 1). The number of stable states grows very rapidly with the number of particles and reaches hundreds already for moderate systems containing only several tens of particles. Different stable states are typically realized with very different probabilities and often the ground-state configuration is not the most probable one [2].

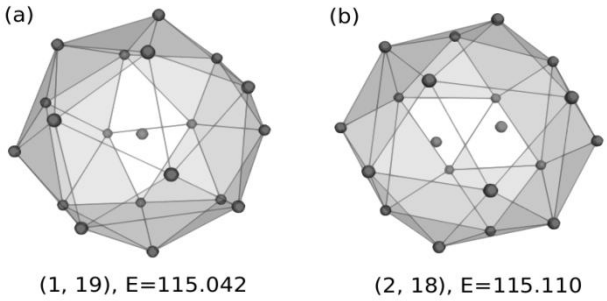

Fig. 1. Ground (a) and metastable (b) states of 20-particle 3D Coulomb cluster.

In the present work we present a theoretical study of classical Wigner clusters in two- and three-dimensional isotropic parabolic traps aiming at understanding and quantifying the configurational uncertainty due to the presence of multiple stable configurations. Employing the computational procedure based on Monte Carlo and downhill minimization techniques, we investigate the cases of both Coulomb and Yukawa inter-particle interactions in the systems of up to N=100 particles. We show, that the total number of metastable configurations is ill-defined and not a representative quantity for large clusters. Instead, following the definitions accepted in information theory [3], we propose to rely on the concept of *configurational entropy* and investigate its dependence on the system size, dimensionality and screening.

Configurational entropy could be understood as the expected value of the logarithm of state probability, or as the logarithm of the *effective number of states* [4]. It is a robust and objective measure of uncertainty, insensitive to the presence of overlooked low-probability states and can be reliably determined even within the limited time of the experiment or a simulation. It

turns out, that the effective number of stable states grows faster than exponentially. That is, on the average, the entropy grows as the logarithm of the factorial of N (Fig. 2). The entropy grows faster in systems with short inter-particle interaction range.

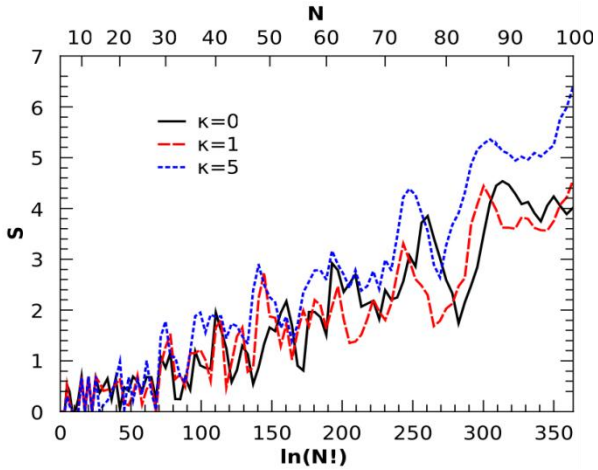

Fig. 2. Configurational entropy of a 2D system with screening parameter κ as a function of the parameter ln(N!). Nonlinear top axis gives the corresponding values of N.

[1] M. Bonitz, C. Henning and D. Block, Complex plasmas: a laboratory for strong correlations, Rep. Prog. Phys 73 066501, 2010.
[2] H. Kählert, P. Ludwig, H. Baumgartner et al., Probability of metastable configurations in spherical three-dimensional Yukawa crystals, Phys. Rev. E 78 036408, 2008.
[3] E. T. Jaynes, Information Theory and Statistical Mechanics, Phys. Rev. 106, 620-630, 1957.
[4] A. Radzvilavičius and E. Anisimovas, Configurational entropy of Wigner clusters, J. Phys.: Condens. Matter 23 075302, 2011.

INVESTIGATION OF DIFFUSION PARAMETERS OF METASTABLE VACANCIES IN CRYSTAL SILICON

V. Rumbauskas

Faculty of Nature Science, Šiauliai University, Višinskio 19, Šiauliai, Lithuania
rumbauskasv@yahoo.com

Work aim: theoretical evaluation of superdiffusion coefficients of metastable vacancies generated by soft X-rays in crystal silicon.

Using dynamical theory of Flynn's model the vacancy atom exchange frequency can be calculated by distribution function in two dimensional phase space [1]

$$E(X_0 - X, p) = const \cdot e^{-\frac{E_{tot}}{kT}} = \zeta e^{-\frac{\left[(1/2)mv^2 + (\kappa_E/2)(X_0 - X)^2\right] + \frac{r}{3}(X_0 - X^*)^3}{kT}}.$$

Using nonharmonic approach after calculations we obtain the following expression for frequencies

$$\Gamma_\nu = \frac{e^{-\frac{\kappa_E (X_0 - X^*)^2 + \frac{r}{3}(X_0 - X^*)^3}{2kT}} kT}{2\pi kT\sqrt{\frac{m}{\kappa_E}} + Anh\sqrt{2m\pi kT}}.$$

We obtained more exact results then [1] including anharmonic part $\frac{r}{3}(X_0 - X^*)^3$ of lattice potential. For evaluation of superdiffusion coefficients of vacancies we used temperature function for crystal excited by X-rays $T(t) = -1/(b \ln z)$ [2]. Parameter $b = k(\alpha - 1)/E$ can be expressed by excitation term α proportional to intensity of irradiation. In this case we obtained diffusion coefficient

$$D = 0.5 a_0^2 \Gamma_\nu \exp(-E_{mig}/(kT)), \quad E_{mig} = 0.5\kappa_E (X_0 - X^*)^2 + r(X_0 - X^*)^3/3.$$

When α=1,001 hops frequency Γ_υ=1,51·10^{13} s^{-1}, diffusion coefficient D = 3,427·10^{-11} cm^2/s. When α=1,5 frequency Γ_υ=5,587·10^{13} s^{-1}, diffusion coefficient D=1,237·10^{-10} cm^2/s. Excitation of crystals by soft X-rays generates Augers transitions which transmit atoms of lattice in to the higher energy levels and increase frequency of atoms hops and diffusion coefficient.

[1] M. E. Glicksman. Diffusion in solids, JOHN WILEY & SONS, INC, New York, (2000) p. 472.
[2] A. J. Janavičius, Ž. Norgėla, R. Purlys. Nonlinear diffusion in excited Si crystals. Eur. Phys. J. Appl. Phys. 29. 127-131, (2005).

APPLICATION OF THE AVERAGE UNIT CELL CONCEPT TO THE 3D APERIODIC AMMAN TILING

R. Strzalka, P. Kuczera, J. Wolny

Faculty of Physics and Computer Science, AGH University of Science and Technology, Krakow, Poland
radek.strzalka@gmail.com

Amman tiling is a 3D generalization of the Penrose tiling. It reveals an icosahedral symmetry, thus it can be used as a quasilattice for building a model of an icosahedral quasicrystal (Fig. 1.). One can generate the set of points of the Amman tiling by projecting a 6D hypercubic lattice via 3D window - the so called atomic surface. In case of the Ammnan tiling the atomic surface has the shape of a rhombic triacontahedron (Fig. 2.).

I present a derivation of the structure factor of the Amman tiling on the basis of the average unit cell concept, which allows a structure factor calculation in 3D physical space only.

Any point of the Amman tiling can be written in the so called reference lattice. The position distribution of Amman tiling points is called an average unit cell. One can show that that there is a linear relation between the shape of the distribution *P* and the shape of the atomic surface. A structure factor can be calculated as a Fourier transform of this distribution.

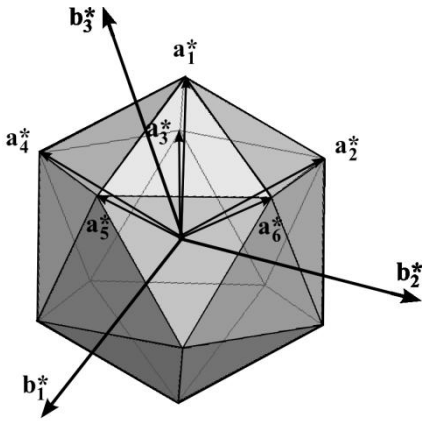

Fig. 1. Icosahedron with 2 complementary vector basis $\mathbf{a}_i$ and $\mathbf{b}_i$.

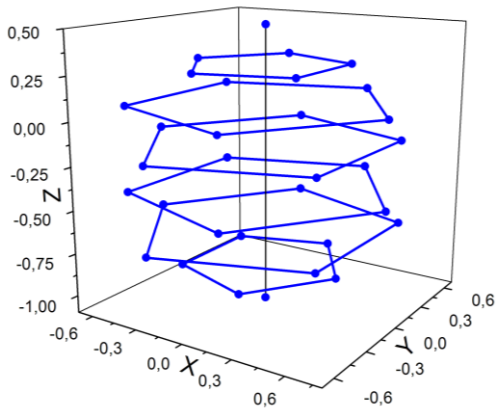

Fig. 2. Atomic surface of Amman tiling in basis $\mathbf{a}_i$

[1] Levine D., Steinhardt P. J., *Phys. Rev. B* **34** (1986) 596-616.
[2] Wolny J., *Phil. Mag.* ***77*** (1998) 395-414.
[3] Wolny J., Kozakowski B., Kuczera P., Takakura H., *Z. Kristallogr.* 223 (2008) 847-850.
[4] Kuczera P., Kozakowski B., Wolny J., Steurer W., *JPCS* **226** (2010) 012001.
[5] Steurer W., Deloudi S., *Crystallography of Qausicrystals*, Springer (2010) Vol. **126**.

THE AIR REFRACTIVE INDEX GRADIENT OVER VILNIUS

E. Valma[1], M. Tamošiūnaitė[1], and S. Tamošiūnas[1,2]

[1]*Vilnius University, Faculty of Physics, Saulėtekio Ave. 9-III, Vilnius, Lithuania*
[2]*Vilnius University, Institute of Applied Research, Saulėtekio Ave. 9-III, Vilnius, Lithuania*
egidijus.valma@ff.stud.vu.lt

In regulation of the radio communication networks, it is necessary to evaluate the variation of the atmospheric radio refractive index, *n*, which is a ratio of the radio wave propagation velocities in free space and air. Changes of the atmospheric radio refractive index influence the path of the radio wave propagation. Therefore, quantitative knowledge of atmospheric refractivity variations is required in order to design reliable and efficient radio communication systems. The *n*-value is very close to the unit. Changes in this value are very small in time and space. On purpose to make those changes more visible, the term of radio refractivity, *N*, is used [1]:

$$N = (n-1)\cdot 10^6 . \tag{1}$$

The atmospheric radio refractive index (and refractivity as well) significantly depends on air temperature, pressure and relative humidity. These parameters vary according to the height from the Earth's ground, locality, season and diurnal time [2]. According to [3], for operating frequencies below 100 GHz, *N* may be written as:

$$N = \frac{A(p + B\cdot p_v / T)}{T}, \tag{2}$$

where p is an atmospheric pressure (hPa), p_v – water vapour partial pressure, T – absolute temperature (K), $A = 77{,}6$ K/hPa, and $B = 4810$ K. Error is less than 0.5 %.

The ratio of *N*-value and height value (km) is called vertical radio refractivity gradient, *G*:

$$G = \frac{N_1 - N_2}{h_1 - h_2}, \tag{3}$$

where N_1 and N_2 are the values of radio refractivity at heights h_1 and h_2, respectively.

It was concluded in [4], that the vertical radio refractivity gradient mostly depends on variations of humidity, and that influence of temperature variations is insignificant. In our previous paper [5], the peculiarities of the radio refractivity variations near the ground in time and location have been analyzed. In this work, using the meteorological data, which was measured in Vilnius, the values of vertical radio refractivity gradient were investigated in different heights from the Earth's surface, up to 1.2 km. The dependency of an average radio refractivity *N* and its vertical gradient *G* values (both *N* and *G* are average values of whole month on selected diurnal time) on the height above Earth's surface has been analyzed.

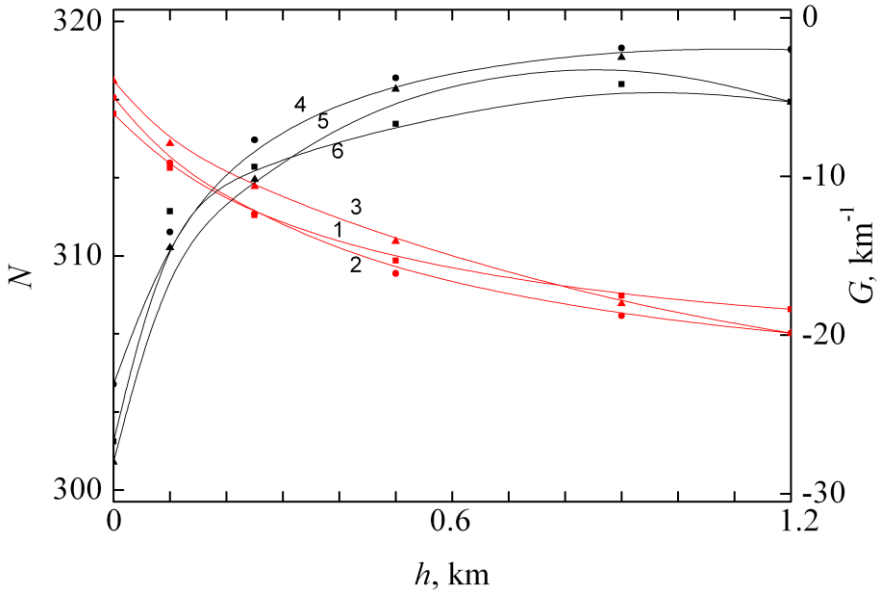

Fig. 1. The dependencies of radio refractivity *N* (curves 1–3) and its gradient *G* (curves 4–6) on height above Earth's surface, in Vilnius, on 19 October 2010.

According to the results, *G*-values in October and November are higher than in December. The saturated vapour pressure varies in very narrow range when the temperature is significantly below 0°C. When temperature is slightly below, equal or above 0°C, the range is wider, and consequently the variations of saturated water vapour pressure are more noticeable. Consequently, the variations of *G*-values are considerable in October and November and quite trivial in December. In Fig. 1, the dependences of *N* and *G* on the height above the Earth's surface (in Vilnius, on 19 October 2010) are presented. The curves 1 and 4 correspond to the meteorological data measured on 6 AM; curves 2 and 5 - to 12 AM, and curves 3 and 6 – to 6 PM. The average daily temperature was about 4°C and the average relative humidity was about 93%.

[1] R. L. Freeman, Radio System Design for Telecommunications, Third Edition (WILEY–INTERSCIENCE, JOHN WILEYand SONS, INC., New York, 2007).
[2] K. C. Igwe, I. A., Adimula, Variations of surface radio refractivity and radio refractive index gradients in the Sub-Sakel, ISSN 0794-4489 Nigerian Journal of Space Research, 6, pp.135-144 (2009).
[3] Recommmendation ITU–R P.453–9 (1970-1986-1990-1992-1994-1995-1997-1999-2001-2003).
[4] J. Gao, K. Brewster, M. Xue, Variation of radio refractivity with respect to moisture and temperature and influence on radar ray path, ISSN: 0256-1530 Advances in Atmospheric Sciences, 25 (6), pp. 1098-1106 (2008).
[5] E. Valma, M. Tamošiūnaitė, S. Tamošiūnas, M. Tamošiūnienė, R. Žilinskas, Determination of radio refractive index using meteorological data, ISSN 1392 – 1215 Electronics and Electrical Engineering, No. 10 (106) pp. 125 - 128 (2010).

TABLE OF CONTENTS

Oral Presentations

Poster Presentations

PP-1 *Artiom Skripka* Förster resonant energy transfer from two-photons excited Quantum dots to chlorin e_6

PP-2 *Eglė Jakubavičiūtė* Perch (Perca Fluviatilis) stock exploitation by great cormorants (Phalacrocorax Carbo Sinensis) and fishery in the Curonian Lagoon

PP-3 *Simonas Kecorius* Aerosol spectrometry: parameterization of sub-micrometer aerosol particle size distribution during nucleation episodes in Preila

PP-4 *Jūris Kiškis* Non-linear multimodal optical microscope based on Cars micro-spectrometer

PP-5 *Marius Lukas* Methods of color correction and object identification in seafloor video mosaic

PP-6 *Giedrius Mikalauskas* Prevalence and biological property of medical plants in the Giruliai forest

PP-7 *Anda Svagere* Mercury concentration measurements in lake sediments and water in western Latvia

PP-8 *Sandra Tamošaitytė* Infrared spectrometry method for the prevention of kidney stone disease

PP-9 *Samanta Trumpytė* The growth of the Eastern Atlantic Harbor seals pup's (*phoca vitulina*) in the Lithuanian Maritime Museum

PP-10 *Neringa Usanova* Estimate of live and dead zooplankton individuals in Curonian spit and Baltic Sea coast

PP-11 *Antanas Vinčiūnas* Measuring Be-7, Cs-137 and Pb-210 activity concentrations in the near-ground level atmosphere

PP-12 *Vytautas Klimavičius* NMR monitoring of nonequilibrium aggregation in ionic solutions

PP-13 *Skomantas Puzinas* Spectroscopic properties of cabazole-fluorene-benzotiadiazole compounds

PP-14 *Karolis Šarka* L-ascorbate and menadione complex: efficiency of intermolecular electron transfer

PP-15 *Karolis Šarka* Simulation of intermolecular electron transfer in Ag...Pyr complex using Dalton package

PP-16 *Inga Brice* Activated oxyfluorides for solid-state lighting

PP-17 *Raitis Grzibovskis* Photoelectrical properties of DMABI derivatives in thin films

PP-18 *Austė Kuprevičiūtė* Broadband dielectric spectroscopy of Fe_3O_4-$BaTiO_3$ ceramics

PP-19 *Vytenis Pranculis* Energy transfer in porous silicon and polymer composites

PP-20 *Kaspars Pudzs* Energy structure of thin film with carbazole derivatives determination in light emitting diode structure

PP-21 *Evaldas Balčiūnas* Replication of micro/nanostructures using polydimethylsiloxane soft lithography

PP-22 *Jaroslavas Belovickis* Acoustooptic interaction of leaky surface acoustic waves in YC-LiTaO3 crystals

PP-23 *Andrius Kojelė* Graptolites from Silurian erratic boulders of Mokrzeszów quarry (Lower Silesia, Poland)

PP-24 *Arūnas Matelis* Designing and manufacturing of the amperator

PP-25 *Giedrius Medzevičius* On the development of ionizing radiation detector – cloud chamber

PP-26 *Martynas Velička, Rokas Skaisgiris* Designing and construction of a "Can-crusher"

PP-27 *Vytautas Sabonis* Influence of laser structuring of TiO2 surface to optoelectric features of organic solar cell

PP-28 *Milda Tamošiūnaitė* Electromagnetic wave attenuation due to rain: evaluation of the "worst month" model

PP-29 *Darius Varanius* Method of cervical smears material autofluorescence spectra filtration for cervical pre-cancer diagnostics

PP-30 *Eglė Gabrytė* Femtosecond solid-state UV laser system for the refractive eye surgery

PP-31 *Ieva Gražulevičiūtė, Aušrinė Jurkevičiūtė* Modelling and characterization of diffraction grating based beam splitters

PP-32 *Eglė Karpavičiūtė* In-core pumped Yb-doped fiber amplifier and its application for the amplification of picoseconds pulses

PP-33 *Aleksander Kubica* The spatial shape of the Spiral Zone Plate foci

PP-34 *Vytautas Kučikas* Modeling of self-organisation in thin metal layers under laser irradiation

PP-35 *Lina Kučinskaitė* Modeling of optical poling of polymers

PP-36 *Lubou Krylova* Optimization of short Er-Yb co-doped diode pumped laser

PP-37 *Simona Liukaitytė* Measurement of scattering losses of laser components by total integrated scattering method using different beam diameters

PP-38 *Edgaras Markauskas* Laser beam profile formation and microfabrication of thin-film solar cells

PP-39 *Grzegorz Muziol* Simulations of optical modes in InGaN based laser diodes operating at 460 nm

PP-40 *Ieva Pipinytė* Optical parametric generation in 2,7 – 3,1 μm spectral range in periodically poled lithium niobate with femtosecond pumping
PP-41 *Tomas Stanislauskas* High efficiency passive pulse shaper for UV pumped NOPA
PP-42 *Kristupas Tikuišis* Fabrication of microlens arrays by direct laser writing
PP-43 *Darius Urbonas* Modeling of ultrashort pulse grating and prism pair compressor for optical parametric chirped pulse amplification system
PP-44 *Darius Urbonas* Studies of optical poling spatial localization
PP-45 *Audrius Zaukevičius* Spatial chirp and angular dispersion dynamics in femtosecond noncollinear OPCPA
PP-46 *Julijanas Želudevičius* Second harmonic generation using broadband fiber amplifier output
PP-47 *Darius Bajarūnas* Fluence dependent variations of current and capacitance characteristics in Si particle detectors
PP-48 *Armandas Balčytis* Investigation of the Auger recombination parameters in Ge by free carrier absorbtion transient spectroscopy techniques
PP-49 *Anastasiya Dudko* Investigation of adsorption of evaporated from metal dispensed emitters elements on scandium oxide
PP-50 *Remigijus Dvaranauskas* Fluence dependent capacitance-voltage and current-voltage characteristics in neutron irradiated Si particle detectors
PP-51 *Anita Gaj* Study of stress localization in polycrystalline grains using self-consistent model and neutron diffraction
PP-52 *Simonas Grubinskas* Laser ablation modeling of CIGS solar cells
PP-53 *Aliaksei Hiro* Influence of radiation defects on the formation of h-donors in silicon
PP-54 *Kasparas Krivas* Development of titanium dioxide layers for solar cells applications
PP-55 *Simonas Krotkus* Investigation of amplified spontaneous emission in fluorine-carbazole derivatives
PP-56 *Jevgenij Kusakovskij* Deep level dependent variations in capacitance transients
PP-57 *Skirmantas Lapinskas* Determination of threading dislocation density in GaN films
PP-58 *Bronė Lenkevičiūtė* Investigation of photoelectric features of vacuum deposited organic material multilayer structures and bulk heterostructure layers
PP-59 *Rūta Mackevičiūtė* Dielectric properties of $Pb(Fe_{1/2}Nb_{1/2})O_3$ crystal
PP-60 *Paulius Malinovskis* Photo-Hall Effect and time resolved photoconductivity in 3C-SiC
PP-61 *Armantas Melianas* Photoelectric feature investigation of vacuum deposited $CuPc/C_{60}$ solar cells
PP-62 *Kristijonas Nalivaika* Luminescence of novel cerium – doped phosphors for white LEDs
PP-63 *Jevgenij Pavlov* Study of electron irradiation induced deep levels in Ge doped Si diodes
PP-64 *Andrius Petrulis* Thermal characterization of LEDs multicolor clusters
PP-65 *Steponas Raišys* Photophysical properties of triphenylamine based derivatives with methoxy and 2,2-diphenylethenyl substituents
PP-66 *Ignas Reklaitis* Dynamics of yellow luminescence in GaN epilayers
PP-67 *Ramūnas Songaila* Electrochemically deposited ZnO layers for formation of Grazel type solar cells
PP-68 *Šarūnas Svirskas* Broadband dielectric spectroscopy of $0.4Na_{1/2}Bi_{1/2}TiO_3$-$(0.6-x)SrTiO_3$-$xPbTiO_3$ solid solutions
PP-69 *Vilmantas Šukauskas* Influence of laser annealing on photoluminescence of InGaN epitaxial layers
PP-70 *Stas Teslenko* Heterojunction barrier height dependence of SnO_2(Pt) – p-Si on dioxide film thickness
PP-71 *Ignas Vaičiulis* Deposition and investigation of organic bulk heterostructured solar cells
PP-72 *Neimantas Vainorius* Investigation of deep levels in Si and ionizing radiation detectors using photoionisation spectroscopy
PP-73 *Vytis Valentinavičius* Numerical computation of computation of photogenerated charge carrier extraction by linearly increasing voltage (photo-CELIV)
PP-74 *Justas Varpučianskis, R. Dobužinskas* Deposition of polycrystalline and organic layers by spray technology and investigation of their photoelectric features
PP-75 *Arūnas Velička* Characterisation of the Si thystor structures by capacitance techniques
PP-76 *Andžej Ziminskij* Investigation of TlBr photoelectrical properties
PP-77 *Tomas Ždanovičius* Setting Gupta and Schottkys' formulas validity boundaries by examining semiconductor diodes electrical noise
PP-78 *Kęstutis Žilinskas* Instrumentation and technology for the *in situ* carrier lifetime contactless control under various irradiation conditions

PP-79 *Algimantas Časas* Numerical modeling of polarization in InGaN solar cells
PP-80 *Rimantas Belovas* Structure of 1-chloro-methyl-silacyclohexane: temperature-depending Raman and IR spectroscopy
PP-81 *Vladimir Kornijčuk* Noise characteristics and radiation spectra of multimode laser diodes during mode-hopping effect
PP-82 *Martynas Pareigis, Jonas Kausteklis* Two dimensional correlation spectroscopy and principal component analysis application for molecular compounds Raman and IR processing
PP-83 *Milda Pučetaitė* Infrared spectroscopy study of the molecules with internal hydrogen bonds isolated in the low temperature matrices
PP-84 *Aurimas Sakanas* Dielectric properties of RUBITHERM PX 21 latent heat powder
PP-85 *Oksana Solomenko* Electrical properties of microdischarge in air
PP-86 *Rimvydas Venckevičius* Terahertz imaging of the objects containing sucrose and tartaric acid
PP-87 *Tomas Žalys* Morphologilcal analysis of multicomponent kidney stones by means of infrared microscopy
PP-88 *Vytautas Butkus* Quantum coherence in simulations of 2D optical spectra of excitonically-coupled molecular aggregates
PP-89 *Patryk Drobiński* The radiation of a relativistic accelerated charge in a commoving frame
PP-90 *Andrius Gelžinis* Analysis of electronic excitation dynamics in a molecular dimer via hierarchical equations of motion
PP-91 *Rytis Kazakevičius* Generation of $1/f^{\beta}$ noise using the superposition of processes with two relaxations
PP-92 *Kęstutis Petravičius* Impurities superdiffusion in Si crystal lattice
PP-93 *Arūnas Radžvilavičius* Configurational entropy of Wigner clusters
PP-94 *Vytautas Rumbauskas* Investigation of diffusion parameters of metastable vacancies in crystal silicon
PP-95 *Radoslaw Strzalka* Application of the average unit cell concept to the 3D aperiodic Amman tiling
PP-96 *Egidijus Valma* The air refractive index gradient over Vilnius

AUTHOR INDEX

N

O

P

R

S

Š

T

U

V

W

Z

Ž